Titania-based nanocomposites for solar photocatalysis

Aditya Chauhan

St. John's College

University of Cambridge

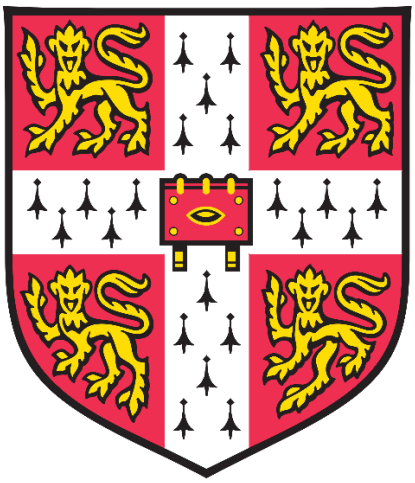

A thesis submitted in fulfilment of the requirements for the degree of

Doctor of Philosophy

June, 2019

Declaration of Authorship

I, Aditya Chauhan, declare that this thesis titled, “Titania-based nanocomposites for solar photocatalysis” and the work presented in it is my own. Furthermore, I confirm that:

- This thesis is the result of my own work and includes nothing which is the outcome of work done in collaboration except as declared in the Preface and specified in the text.
- It is not substantially the same as any that I have submitted, or, is being concurrently submitted for a degree or diploma or other qualification at the University of Cambridge or any other University or similar institution except as declared in the Preface and specified in the text. I further state that no substantial part of my dissertation has already been submitted, or, is being concurrently submitted for any such degree, diploma or other qualification at the University of Cambridge or any other University of similar institution except as declared in the Preface and specified in the text.
- It does not exceed the prescribed word limit for the relevant Degree Committee.

Titania-based nanocomposites for solar photocatalysis

Aditya Chauhan

Department of Materials Science and Metallurgy, University of Cambridge

This thesis explores several titania-based composites for photocatalytic water treatment and hydrogen evolution. For water treatment, TiO_2-C core-shell composites were prepared through controlled hydrolysis of titanium alkoxides followed by calcination in a non-oxygenating atmosphere. A total of nine TiO_2-C samples were synthesized by combining different alkoxides and solvents. The sub-micron sized composites displayed eight times faster photocatalytic activity for degradation of aqueous methylene blue under simulated sunlight compared to pristine TiO_2. Particle size of the best performing TiO_2-C catalyst was further reduced through hydrolysis with aqueous KCl. The resulting nanoparticles (~10 nm) displayed a comparable rate of photodegradation for methylene blue with only $1/5^{th}$ catalyst loading by weight. This nano-sized powder composite (nanocomposite) photocatalyst was also tested for photodegradation of other dyes, pharmaceuticals and Escherichia coli bacteria. The photo-activity was found to be at par or better than several state-of-art TiO_2-C materials reported in the literature and approximately twice as better as standard commercially available TiO_2 (P25).

Second part of the thesis explores three different nickel-based cocatalysts for TiO_2 for visible-light driven hydrogen evolution. Composites containing $Ni(OH)_2$, NiO, and Ni_2P were prepared and the effects of loading concentration and synthesis method on the rate of hydrogen evolution were studied. It was observed that hydrogen evolution could be achieved in the presence of a sacrificial electron donor (ethylenediaminetetraacetic acid disodium). Catalysts with $Ni(OH)_2$ and Ni_2P displayed significant photoactivity, in which highest rate of hydrogen production was achieved with TiO_2-Ni_2P nanoparticles. The prepared catalyst also displayed excellent long-term stability under continuous illumination tested for seven days.

The final section of this thesis reports on the synthesis and visible-light activity of a hybrid $Bi_{0.5}Na_{0.5}TiO_3$-BiOCl (BNT-BiOCl) ferroelectric photocatalyst. The parent ferroelectric BNT microparticles were prepared by solid-oxide reaction route and BiOCl growth on surface was achieved by treatment with dilute HCl. Despite a large bandgap and large particle size (>1 μm), the composite photocatalyst displayed a high rate of rhodamine B degradation under visible light. The high photoactivity was attributed to the heterojunction formed between the two phases, which improved charge separation.

Acknowledgements

At the outset I would like to express my gratitude to my research supervisor Prof. R.V. Kumar for his support and mentorship throughout the tenure of my PhD. His positive encouragement enabled me to freely explore the various aspects of being an independent researcher and helped me to learn and grow as a human being.

My thanks to the Cambridge International and Commonwealth Trust and Science and Engineering Research Board, India for funding my PhD program.

I would also like to thank my colleagues in the Materials Chemistry group for all the support and help I received along the way. A special mention to Chris, Peter and Mike for helping me get started and setup in the lab.

A special word of thanks to my friends Dr. Aditya Sadhanala and Arfa Karani for help with access to the instrumentation at the Kapitza hub and Cavendish laboratory, without whom this research would have taken considerably longer. My gratitude also goes out to Dr. Shahab Ahmad and Dr. Michael De Volder for access to valuable instrumentation in the nanomanufacturing group at the Institute for Manufacturing.

I would like to acknowledge Liam Bird, Dr. Giorgio Divitini and Simon Griggs for their help with acquiring electron microscopy images; Gauthaman Chandrabose and Chris Amey for help with XPS measurements and data interpretation; Dr. Rahul Vaish for access to research facilities at IIT Mandi and a very fruitful collaboration; and Sundar Thirumalai for valuable discussions and result inputs. I would also like to thank my friend and housemate Arjun Vijeta for providing invaluable help and access to the hydrogen production and measurement setup in the Reisner lab at the Chemistry Department.

My gratitude also goes out to all different people and staff members throughout the department and my college, who made my PhD at Cambridge as accommodating as possible.

A special word of thanks to all the life-long friends I made in Cambridge. My love and gratitude for my parents and sister for believing in me.

And finally, I would like to thank Mona (my angel) whose constant support was with me every step of my way. If it were not for you, I would still be struggling.

List of Publications

The following publications are largely based on the studies conducted as a part of the research work reported in this thesis.

1. A. Chauhan, M. Rastogi, P. Scheier, C. Bowen, R. V. Kumar, R. Vaish. Janus nanostructures for heterogeneous photocatalysis, *Appl. Phys. Rev.* **2018**, *5*, 041111.
2. A. Chauhan, S. Thirumalai, R. V. Kumar. In-situ fabrication of TiO_2-C core-shell particles for efficient solar photocatalysis, *Mater. Today Commun.* **2018**, *17*, 371-379.
3. A. Chauhan, H. S. Kushwaha, R. V. Kumar, R. Vaish. $Bi_{0.5}Na_{0.5}TiO_3$-BiOCl composite photocatalyst for efficient visible light degradation of dissolved organic impurities, *J. Environ. Chem. Eng.* **2019**, *7*, 102842.
4. A. Chauhan, M. Sharma, S. Kumar, S. Thirumalai, R. V. Kumar, R. Vaish. TiO_2@C core@shell nanocomposites: a single precursor synthesis of photocatalyst for efficient solar water treatment, *J. Hazard. Mater.* **2020**, *381*, 120883.

Table of Contents

List of Figures

List of Tables

List of Abbreviations and Symbols

Ab	Absorbed light (intensity)
$\alpha(E)$	Absorption coefficient of a semiconductor
N	Avogadro's number
E_g	Bandgap
c_{BET}	BET constant
E_{BE}	Binding energy of an electron
k_B	Boltzmann's constant
ΔG^0	Change in Gibb's free energy
ΔE^0	Change in reaction potential
C	Concentration (molar)
cb	Conduction band
e^-	Electron
E	Energy of the incident photon
Es	Energy state of an electron
p	Equilibrium pressure (gas)
E_F	Fermi level
R	Gas constant
h^+	Hole
θ	Incident angle (X-ray)
I	Incident energy (light)
d_{pl}	Interplanar (lattice) spacing
E_{KE}	Kinetic energy of an electron
$h\nu$	Photon (energy)

k	Rate constant
n	Order of chemical reaction
k_B	Boltzmann constant
Re	Reflected light (intensity)
p_0	Saturation pressure (gas)
T	Temperature
Tr	Transmitted light (intensity)
vb	Valence band
λ	Wavelength
ϕ	Work function
AM 1.5G	Air mass coefficient 1.5G
BE	Binding energy
BET	Brunauer-Emmett-Teller
BG	Brilliant green
BJH	Barret-Joyner-Halenda
BQ	Benzoquinone
CFU	Colony forming units
CNTs	Carbon nanotubes
DRS	Diffuse reflectance spectroscopy
DS	Diclofenac sodium salt
DSC	Differential scanning calorimetry
E. coli	Escherichia coli
EDX	Energy dispersive X-ray spectroscopy
EIS	Electrochemical impedance spectroscopy
FTIR	Fourier-transform infrared spectroscopy

GC	Gas chromatography
GC-MS	Gas chromatography mass spectroscopy
GDP	Gross domestic product
GO	Graphene oxide
HER	Hydrogen evolution reaction
HOMO	Highest occupied molecular orbital
IEA	International Energy Agency
IPA	Isopropanol
IS	Ibuprofen sodium salt
ITO	Indium tin oxide
LSPR	Localized surface plasmon resonance
LUMO	Lowest unoccupied molecular orbital
MB	Methylene blue
MO	Methyl orange
MSM	Department of Materials Science and Metallurgy
MWCNTs	Multi wall CNTs
Na-EDTA	Sodium ethylenediaminetetraacetic
NHE	Normal hydrogen electrode
OER	Oxygen evolution reaction
PBS	Phosphate buffer saline
REDOX	Reduction and oxidation
rGO	Reduced graphene oxide
Rh B	Rhodamine B
ROS	Reactive oxygen species
SEM	Scanning electron microscopy

SWCNTs	Single wall CNTS
TBA	Tert-butanol
TCD	Thermal conductivity detector
TEM	Transmission electron microscopy
TGA	Thermogravimetric analysis
TPM	Transient photocurrent measurement
UV/Vis	Ultraviolet/visible
XPS	X-ray photoelectron spectroscopy
XRD	X-ray diffraction
XRF	X-ray fluorescence spectroscopy

Chapter 1

Introduction

1.1 Overview

The global population crossed the 7 billion mark in 2012, compared to roughly 6 billion at the turn of the century (2000), of which developing countries accounted for 97% growth.[1] As the developing nations continue to fuel their technological and infrastructural advancement, it places an ever-increasing burden on the energy supplies of the world. Contrastingly, the developed world still accounts for a larger share of per-capita energy consumption, owing to the higher standards of living (Figs 1.1 and 1.2).

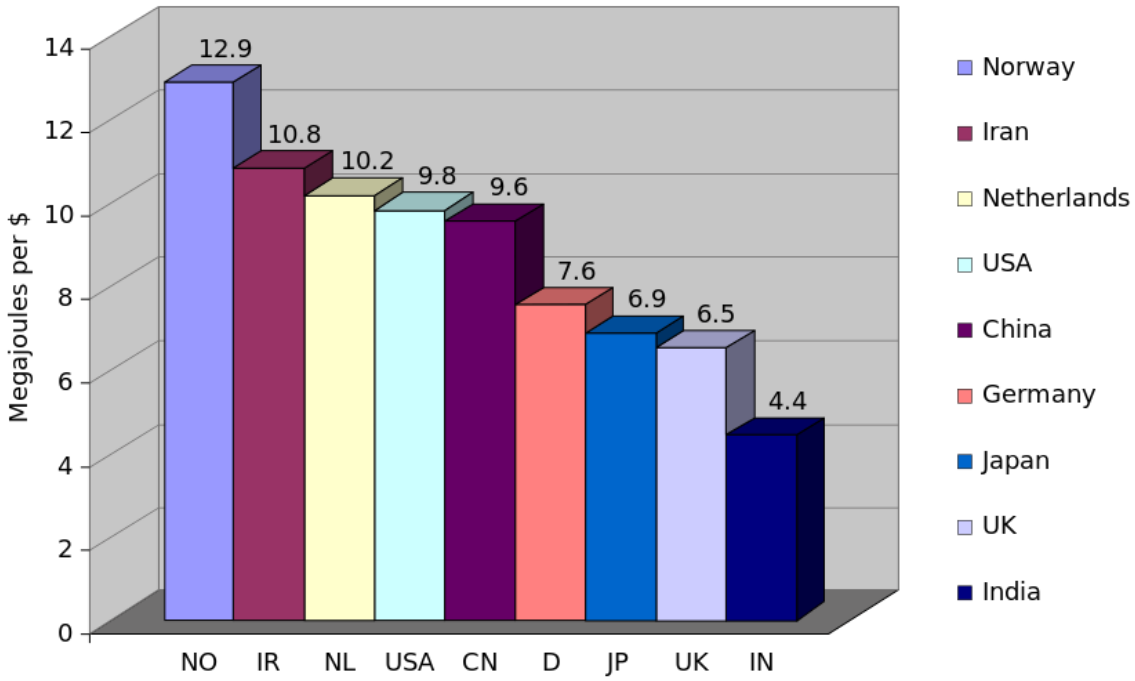

Figure 1.1: The graph shows the price per unit energy consumption for selected countries. Adapted from with permission from Ref.[2]

However, this trend is unsustainable as most of the energy required to provide for and maintain a high standard of living (including basic amenities like shelter, clean water and electricity) is drawn from fossil reserves. The International Energy Agency (IEA) estimated that the global energy consumption in 2013 was 18.0 terawatts (Fig 1.3),[3] of which a large portion (40.7%)

came from oil, natural gas (15%), and coal (10%), whereas renewable energy only accounted for 3.5%.[3]

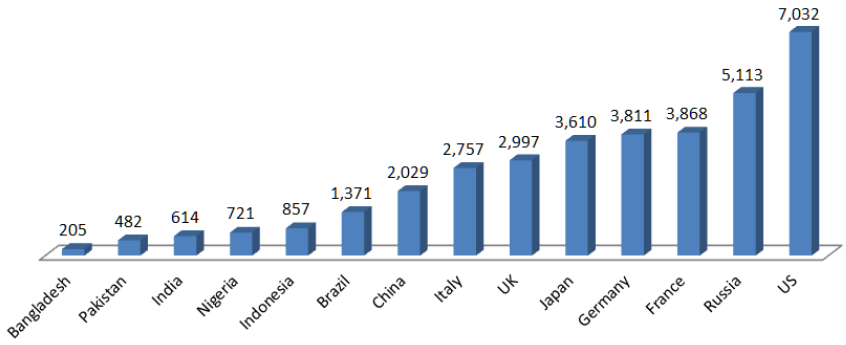

Figure 1.2: The graph shows the per capita energy consumption by several countries of the world in kilograms of oil equivalent, for 2011; adapted from Ref.[4]

IEA world energy outlook shows a trend which indicates that the global energy consumption could increase at a rate of 10% annually because of developing countries. At this rate the planet is expected to run out of oil in approximately 30 years, and coal will be the only source of fossil fuel left after 2042.[5]

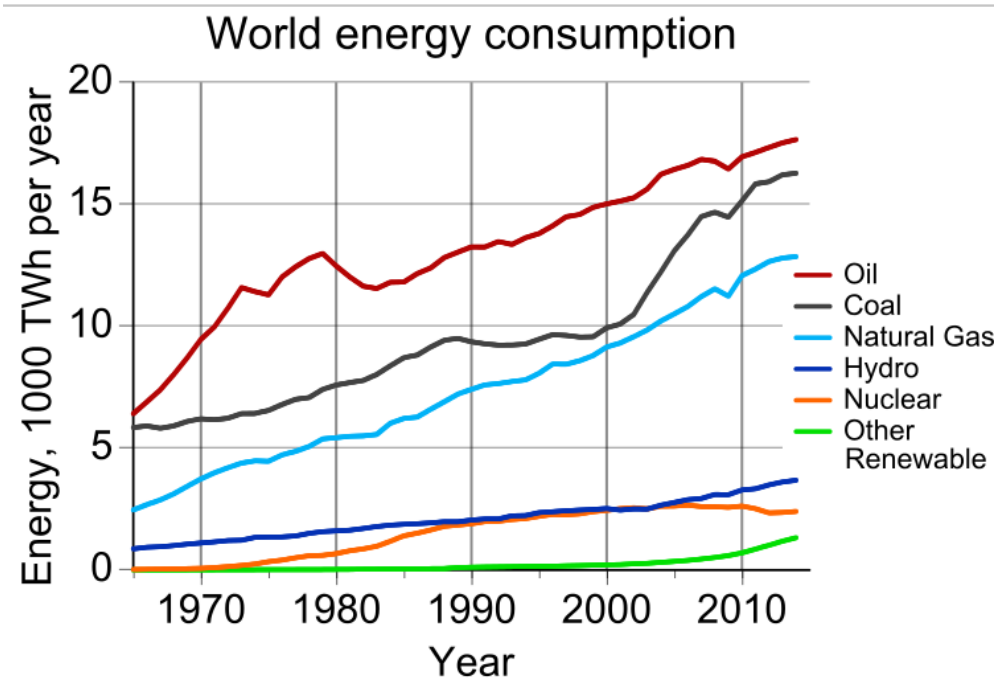

Figure 1.3: The graph shows the increase in global energy consumption as a function of time. Adapted from Ref.[3]

However, even before the global fossil reserves are depleted humanity could face a global and irreversible catastrophe in the form of climate change. Global warming due to the green-house effect is a major problem associated with rapid consumption of fossil fuels. Various

anthropogenic activities, chiefly burning of carbon-based fuels for energy production, release large amounts of carbon dioxide and other greenhouse gases into the atmosphere annually. According to a recent study published by Le Quéré et al. the global carbon emissions rose by approximately 2.7% in 2018 compared to 9.9 gigatons in 2017, marking it the year with the highest carbon emissions. According to the latest report by the International Institute for Applied Systems Analysis, the current emission trends will cause irreversible changes to the environment even if the global warming is somehow limited to 1.5 ^{o}C.[6] Effects of such extreme climate change include loss of entire ecosystems, food shortages owing to altered precipitation pattern, increased frequency of extreme weather events, and rise in sea level leading to loss of habitat in the coastal areas. Thus, there is an urgent need to create clean and renewable sources of energy and develop technology for active carbon capture from the atmosphere.

With regards to clean renewable energy, several technologies such as wind, geothermal, hydroelectric, and photovoltaic already have a strong presence. However, the total contribution from all these sources is still limited. Our planet receives about 1.74×10^{5} terawatt of solar energy every day at the upper atmosphere.[7] Of this 30% is reflected back and the rest reaches the earth's surface in the form of terrestrial radiation. The total energy received from the sun on the surface of the earth in one hour was more than that consumed by the entire human population in 2002.[8] Even by today's energy consumption rate, the total incident solar energy received by our planet in a day is more than the annual global consumption. Thus, it is easy to conclude that the future of humanity relies on efficient tapping and utilization of this abundant form of energy. However, solar energy is rather dilute and highly dependent on geographical and atmospheric conditions. Hence, techniques need to be developed which can directly utilize unconcentrated solar energy for various applications. Space and water heating, cooking, process heating, electricity generation and photocatalysis are all examples of such applications.

Heterogeneous photocatalysis is a technique that employs suitable semiconducting materials to harness and convert electromagnetic energy of the UV/visible region into chemical potential.[9] Photocatalysis can be used for several applications including air[10] and water treatment,[11] chemical synthesis,[12] solar fuel production[13] and active carbon capture.[14] Such technology requires minimum infrastructure, has low upfront and operational cost, is robust and easy to use, and can be powered by free and abundant solar energy, all of which make photocatalysis a lucrative prospect.

Photocatalysis in itself cannot be used to solve the pollution and energy problems of the world. Furthermore, the current state-of-art materials are still far from the efficiency level required to rival established technologies. However, there have been few recent attempts towards

successful commercialization of photocatalysis. CaluTech, a USA based firm, have developed photocatalytic strips employing UV light for indoor air-purification.[15] The developed system claims to successfully remove several gaseous pollutants, allergens, and pathogens at levels typically encountered in a domestic setting. Similarly, LIGHT2CAT was an EU funded research project with the aim of developing light-sensitive concrete to be used as building material for reducing NO_x pollution.[16] The team successfully modified commercial concretes with visible light active TiO_2 (4 wt.%), which were observed to be 15% more active than pristine concrete under warm white light. Finally, these modified concretes were used as building material in several European cities leading to 5-20% reduction in environmental NO_x concentration over a year. Furthermore, Panasonic has already presented a solar water-purification prototype capable of very high processing and flow speeds.[17] The technology employs zeolites which trap and release TiO_2 nanoparticles on-demand, thereby eliminating the need for permanent immobilization of photocatalysts. Finally, Syzygy Plasmonics, a USA based start-up focused on development of (photocatalytic) clean synthesis has already raised USD 5.8 million.[18] These examples indicate that the field of photocatalysis continues to grow and improve rapidly and it will soon be able to provide a competitive advantage large enough to warrant its integration into the established systems.

1.2 Aims and thesis structure

TiO_2 has been extensively investigated for photocatalytic applications owing to its abundance, stability and low toxicity.[19] However, pristine TiO_2 is highly inefficient and needs to be suitably modified to improve its performance under visible light, which accounts for nearly 45% of the total solar energy. Hence, this study is primarily focused on developing suitable modifications and cocatalysts for improving the photocatalytic response of TiO_2 (anatase phase) under full solar spectrum. In this regard, two applications namely water treatment and hydrogen evolution have been explored. The thesis itself is structured as follows:

- Chapter 2 provides an overview of the fundamentals of photocatalysis including semiconductor-light interactions and various reduction-oxidation processes. The chapter also provides a brief literature review of the current state-of-art materials. This is followed by a description of how photocatalysis can be employed for water treatment and hydrogen production. Finally, the chapter concludes with the introduction of TiO_2 and its reported composites with carbon and nickel, which are the two main configurations explored in this study.
- Chapter 3 lists the different chemicals and reagents used in this study. The chapter also provides a brief description of the various characterization techniques and tests

used in this study. Details regarding the experimental setup and actual measurement conditions, which are common to all studies, have also been provided.

- Chapter 4 reports on the effect of different solvent-precursor combinations on the shape, size and morphology of the as-prepared TiO_2-C core-shell particles. Nine different samples were prepared using a combination of three different alkoxides (precursor) and alcohols (solvents). The materials were thoroughly characterized and tested for their photocatalytic activities.
- Chapter 5 builds on the results obtained in chapter 4 and reports on the preparation of TiO_2-C nanoparticles (termed as nanocomposites) through optimized synthesis parameters. The as-prepared powder photocatalyst was tested for degradation of a broad-spectrum of water-borne pollutants including dyes, pharmaceutical compounds, and model pathogen (bacteria). Photoelectrochemical analyses were also performed to elucidate the reason for improved catalytic activity.
- Chapter 6 reports the synthesis and preliminary analysis of various TiO_2 and Ni-based composite nanoparticles (also termed as nanocomposites) for visible-light driven hydrogen evolution. Three different compounds were prepared and tested for their cocatalytic properties. It was observed that selection of appropriate Ni-based co-catalyst along with proper synthesis and loading conditions could considerably improve the hydrogen evolution activity of TiO_2 under visible light, without compromising the stability of the composite.
- Chapter 7 deviates away from semiconducting TiO_2 and reports on the synthesis and catalytic activity of $Bi_{0.5}Na_{0.5}TiO_3$-BiOCl composite particles. The combination of a parent ferroelectric phase ($Bi_{0.5}Na_{0.5}TiO_3$) with an active catalyst (BiOCl) was investigated for visible light degradation of rhodamine B. Finally, mechanisms responsible for the improved catalytic activity and dye degradation are also discussed.
- Chapter 8 summarizes the salient results and observations of the entire study, followed by an outline of areas requiring further research and some possible future work.

Reference:

1 Carl Haub, (2012).
2 US Department of Energy, (2007).
3 International Energy Agency, (2014); International Energy Agency, (2015).
4 The World Bank, (2011).
5 Shahriar Shafiee and Erkan Topal, Energy Policy **37** (1), 181 (2009).
6 O Hoegh-Guldberg, D Jacob, M Taylor, M Bindi, S Brown, I Camilloni, A Diedhiou, R Djalante, K Ebi, and F Engelbrecht, (2018).

[7] Vaclav Smil, in *General energetics: energy in the biosphere and civilization* (John Wiley & Sons, 1991).
[8] Oliver Morton, Nature **443** (7107), 19 (2006); Nathan S Lewis and Daniel G Nocera, Proceedings of the National Academy of Sciences **103** (43), 15729 (2006).
[9] Juan Carlos Colmenares and Y-Jun Xu, Green Chemistry and Sustainable Technology (2016).
[10] Ranjit K. Nath, M. F. M. Zain, and M. Jamil, Renewable and Sustainable Energy Reviews **62**, 1184 (2016).
[11] Shuying Dong, Jinglan Feng, Maohong Fan, Yunqing Pi, Limin Hu, Xiao Han, Menglin Liu, Jingyu Sun, and Jianhui Sun, RSC Advances **5** (19), 14610 (2015).
[12] Shao-Hai Li, Siqi Liu, Juan Carlos Colmenares, and Yi-Jun Xu, Green Chemistry **18** (3), 594 (2016).
[13] Akira Fujishima and K Honda, Nature **238** (5385), 37 (1972); Ronghao Zhang, Hong Wang, Siyang Tang, Changjun Liu, Fan Dong, Hairong Yue, and Bin Liang, ACS Catalysis **8** (10), 9280 (2018).
[14] Bing Liu, Liqun Ye, Ran Wang, Jingfeng Yang, Yuexing Zhang, Rong Guan, Lihong Tian, and Xiaobo Chen, ACS Applied Materials & Interfaces **10** (4), 4001 (2018).
[15] CaluTech.
[16] EuropeanUnion, (2016).
[17] Panasonic, (2014).
[18] Noah Long, (2019).
[19] Oluwafunmilola Ola and M. Mercedes Maroto-Valer, Journal of Photochemistry and Photobiology C: Photochemistry Reviews **24**, 16 (2015); Rachel Fagan, Declan E. McCormack, Dionysios D. Dionysiou, and Suresh C. Pillai, Materials Science in Semiconductor Processing **42**, 2 (2016); Rohini Singh and Suman Dutta, Fuel **220**, 607 (2018).

Chapter 2

Heterogeneous photocatalysis: principles, materials and application

2.1 Fundamentals of photocatalysis

The term 'photocatalysis' can be deconstructed into two individual terms of 'photoreaction' and 'catalysis'. Hence, the term photocatalysis can be defined as the process of catalysing a desired photoreaction. The catalyst employed in this case can either be of similar (homogeneous) or different (heterogeneous) phase than the reactants. Consequently, photocatalysis can be broadly divided into two major categories of homogeneous and heterogeneous catalysis. The majority of homogeneous photocatalysts are based on ozone and photo-phenton systems with a primary function of producing hydroxyl $OH^{\bullet}$ radicals.[1] Examples of mechanism for hydroxyl formation in ozone-based systems are as follows:[2]

$$O_3 + h\nu \rightarrow O_2 + O \quad (2.1)$$

$$O + H_2O \rightarrow OH^{\bullet} + OH^{\bullet} \quad (2.2)$$

$$O + H_2O \rightarrow H_2O_2 \quad (2.3)$$

$$H_2O_2 + h\nu \rightarrow OH^{\bullet} + OH^{\bullet} \quad (2.4)$$

Similarly, (Fe^{2+}-based) photo-phenton systems operate on the following mechanism:[3]

$$Fe^{2+} + H_2O_2 \rightarrow OH^{-} + OH^{\bullet} + Fe^{3+} \quad (2.5)$$

$$Fe^{2+} + OH^{\bullet} \rightarrow Fe^{3+} + OH^{-} \quad (2.6)$$

$$Fe^{3+} + 2H_2O + h\nu \rightarrow OH^{\bullet} + Fe^{2+} + H_3O^{+} \quad (2.7)$$

Homogeneous photocatalysis based on such systems has several advantages including high mass transfer rates, high efficiency and utilization of visible light (upto 450 nm) for photo-phenton systems.[1] However, each set of systems has its drawbacks which limits its wide-scale applicability. Ozone in higher concentrations is potentially harmful to biological life-forms and its production requires the use of deep UV which is carcinogenic. Further, as only a minor fraction of the incident solar energy is UV (<5%), artificial sources are required for its production. Similarly, photo-phenton based systems have a stringent set of requirements regarding pH, concentration of hydrogen peroxide and a need for removal of iron after reaction completion.[4]

In this regard, semiconductor based heterogeneous photocatalysis may offer a better route for direct conversion of incident electromagnetic energy into catalytically active species that are capable of performing reduction and oxidation reactions.[5] This chapter provides a detailed overview of the underlying processes, mechanism for production of photogenerated charge carriers and subsequent reduction and oxidation (REDOX) reactions. However, before the photochemistry of a semiconductor can be explored, it is important to elucidate the nature of semiconducting materials and the origin of the bandgap.

2.1.1 Electronic band-structure in solids and semiconductors

The basic and most fundamental building block of any element is its atom. An atom is made up of a dense, positively charged nucleus of protons and neutrons. The nucleus is surrounded by a cloud of orbiting electrons which keep the atom electrically neutral. The protons define the atomic number of the element and, hence, an element's place in the periodic table. However, protons themselves do not participate in classical chemical reactions, which are limited exclusively to the outermost orbiting electrons. This is especially relevant in all reactions pertaining to photochemistry and photocatalysis, in which the changes in the state of outmost electrons govern the various REDOX reactions.

The motion of an electron around the nucleus is defined as its atomic orbital and indicates the area where the probability of locating that electron is the highest. In an isolated atom, each atomic orbital has a discreet energy level and can be shared by a maximum of two electrons with opposing spin. When two or more atoms are grouped together, the atomic orbitals from the neighboring atoms begin to overlap. According to Pauli's exclusion principle, no two electrons can occupy the same set of quantum numbers. Hence, this overlap leads to splitting of energy levels known as molecular orbitals. Molecular orbital theory employs linear combination of atomic orbitals to define the 'new' orbitals which arise due to chemical bonding between two atoms. The bonding orbital is located in between a given pair of atoms and hence, possesses relatively lower energy with respect to the individual atomic orbitals. Similarly, anti-bonding orbitals contain electrons directly behind each nucleus and therefore, possess slightly higher energy. Fig 2.1 shows the evolution of molecular orbitals from atomic orbitals during the bonding process of two hydrogen atoms.

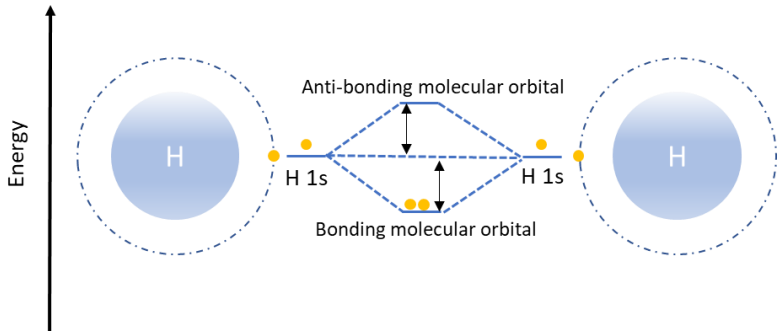

Figure 2.1: Evolution of bonding and anti-bonding molecular orbitals in a di-hydrogen molecule.

When a sufficiently large number of atoms come together, these molecular orbitals are spread over a range of energy levels. Furthermore, since the difference in energy between each individual molecular orbital is very small, the collection of these molecular orbitals can be approximated as a continuum and is defined as an energy band. Energy band containing the anti-bonding orbitals is known as the conduction band (cb). Similarly, the energy band consisting of bonding orbitals is known as valence band (vb). Finally, the difference between the highest energy state of the bonding orbitals and the lowest energy state of the anti-bonding molecular orbitals may be defined as the band gap. Fig 2.2 illustrates the evolution of band structures as a function of number of molecular orbitals/participating atoms.

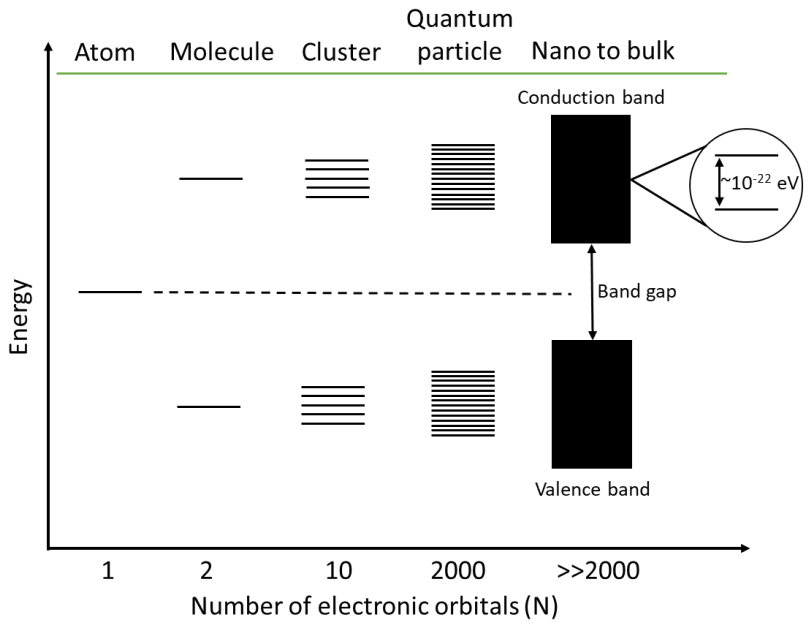

Figure 2.2: Evolution of band structure as a function of electronic orbitals. Adapted with permission from Ref.[6]

For any given material, the probability $f(Es)$ for an electron to occupy an energy state Es can be determined using Fermi-Dirac distribution as follows:[6]

$$f(Es) = \frac{1}{1+e^{(Es-E_F)/k_B*T}} \tag{2.8}$$

In which, E_F is the Fermi level, k_B is the Boltzmann constant and T is the temperature in Kelvin. In band theory of solids, E_F is defined as the energy level which has the probability of being 50% occupied at any given time, in a state of thermal equilibrium. Additionally, from the nature of equation (2.8), it can be easily concluded that the probability $f(Es)$ increases with increase in temperature T. Electrons which occupy energy beyond E_F can be readily employed for conduction. Hence, E_F along with position of molecular orbitals is vital in determining the electrical nature of a solid whether it is a conductor, a semiconductor or an insulator.[7] Materials in which E_F lies within a delocalized (occupied) band are readily able to conduct electric current and are termed as metals/conductors. Similarly, for materials which have E_F located within a large bandgap are termed as insulators. Semiconductors are materials in which the E_F is located within a band gap where the probability of electrons occupying $Es > E_F$ is non-negligible at room temperature. Fig 2.3 illustrates the placement of band positions with respect to Fermi level for different category of solids.

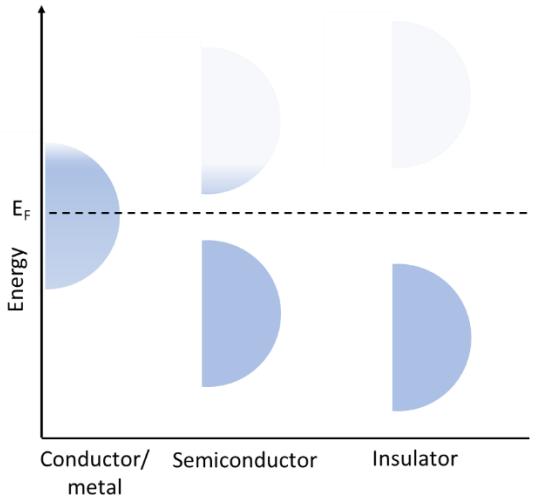

Figure 2.3: Fermi level positions with respect to occupied molecular orbitals in metals, semiconductors and insulators.

In semiconductors, the value of bandgap at operational temperatures is sufficiently small such that it can be easily overcome by activation. The energy required to move an electron from highest occupied molecular orbital (HOMO) to lowest unoccupied molecular orbital (LUMO) can be provided externally through electromagnetic interaction. With respect to photocatalysis

at room temperature, the upper limit of a band gap is restricted at ~3.4 eV, correlating to the most energetic photons of the incident solar spectrum (UV-B). Table 2.1 provides an overview of the band gaps and respective cb and vb positions with respect to normal hydrogen electrode (NHE), for common semiconductors employed in photocatalysis. Hence, when the semiconductor is excited with a photon of energy greater than its band gap, it may excite an electron from the conduction band to the valence band, leaving a hole in its place. This electron-hole pair is known as a photogenerated charge carrier and forms the basis of all photocatalysis. The associated photochemistry of a semiconductor, as well as factors affecting its catalytic performance can now be discussed.

Table 2.1: Band gap, conduction band, and valence band edge (v/s NHE) of common semiconducting materials.[8]

Semiconductor	**Valence band edge (V)**	**Conduction band edge (V)**	**Bandgap (eV)**
TiO_2 (anatase)	2.7	-0.5	3.2
TiO_2 (rutile)	2.7	-0.3	3.0
Cu_2O	0.85	-1.16	2.0
WO_3	2.7	-0.1	2.8
gC_3N_4	1.16	-1.53	2.2
Ag_3PO_4	2.49	0.04	2.45
$BiVO_4$	2.1	-0.3	2.4
CdS	1.5	-0.9	2.5
Ta_3N_5	1.35	-0.75	2.1
TaON	1.75	-0.75	2.5

2.1.2 *Heterogeneous photocatalysis*

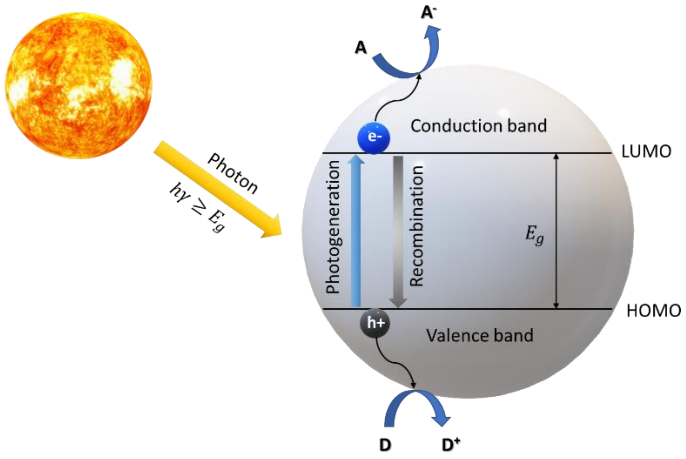

Figure 2.4: The process of photogenerated charge carrier production, annihilation and migration in a typical semiconductor. Surface adsorbed acceptor (A) and donor (D) species may react with the electron and hole pair to initiate photochemical reactions.

In heterogeneous photocatalysis, when a photon with energy greater or equal to the bandgap (E_g) of the semiconductor interacts with the material; it initiates non-equilibrium photophysical and photochemical processes[9]. This photon can excite an electron from the highest occupied molecular orbital to lowest unoccupied molecular orbital. The process lasts for a few femtoseconds and is followed by the relaxation of the generated holes and electrons to the top and bottom of vb and cb, respectively on a similar time-scale:[9,10]

$$semiconductor + h\nu \rightarrow e^{-}(cb) + h^{+}(vb) \qquad (2.9)$$

Depending on the band positioning and band bending configuration, these charge carriers can migrate to the surface of the catalyst and initiate REDOX reactions. The migration itself could be completed on a scale of microseconds, whereas the reactions themselves are much slower (millisecond timescale).[9] Alternately, if the electron/hole does not have sufficient time or energy to migrate, the charge pair may recombine to produce a phonon (heat). Depending upon the surrounding medium, these electrons and holes can be used to reduce and oxidize surface adsorbed acceptor and donor chemical species, respectively. Fig 2.4 gives a graphical representation of the processes involved in an aqueous photocatalytic reaction. Once the charge carriers successfully migrate to the surface, holes can oxidize adsorbed water at the surface to produce hydroxyl radicals ($OH^{\bullet}$). These hydroxyl radicals can have an oxidation potential of upto 2.70 V (vs NHE)[11,12] and can subsequently oxidize dissolved organic species producing mineral salts, CO_2, and H_2O.[11] Equations (2.10)-(2.16) summarize the main REDOX and the

subsequent chemical reactions that take place at the surface of a photocatalyst in an aqueous medium.

$$H_2O + h^+ \rightarrow OH^\bullet + H^+ \quad (2.10)$$

$$OH^\bullet + pollutant \rightarrow intermediate\ products \rightarrow H_2O + CO_2 \quad (2.11)$$

$$O_2 + e^- \rightarrow O_2^- \quad (2.12)$$

$$O_2^- + 2OH^\bullet \rightarrow H_2O_2 + O_2 \quad (2.13)$$

$$O_2^- + H^+ \rightarrow OOH^\bullet \quad (2.14)$$

$$OOH^\bullet + OOH^\bullet \rightarrow H_2O_2 + O_2 \quad (2.15)$$

$$H_2O_2 \rightarrow 2OH^\bullet \quad (2.16)$$

Electrons in the conduction band can be rapidly trapped by molecular oxygen absorbed on the surface, which is reduced to form a superoxide radical anion (O_2^-). This superoxide anion can further react with (H^+) to generate a hydroperoxide radical ($OOH^\bullet$). These reactive oxygen species (ROS) can also contribute to the oxidative pathways, such as the degradation of a pollutant; see equation (2.11). Thus, both the photocatalytic oxidation and reduction reactions generate powerful radicals for degradation of pollutants that are prone to mineralization in an aqueous medium. Alternately, the photogenerated electrons and holes may also be used for a variety of applications including water splitting[13], solar fuel production[14], chemical synthesis[15] and oxidation of air-born pollutants.[16] All of which can be powered through sunlight.

2.1.3 Factors affecting semiconductor photocatalysis

Not all incident photons interacting with a semiconductor result in the generation of a charge pair. The ratio of charge carriers produced to the number of photons intercepted (at a certain wavelength) is known as the quantum efficiency of the semiconductor. Moreover, a majority of the generated charge pairs could either be trapped as ions or may recombine to generate heat (phonon) in the process[17]. The semiconductor-photon interaction itself is dependent on a number of factors including the average cross-section and surface area of the particle as well as the wavelength of incident light. The absorption coefficient $\alpha(E)$ of an idealized semiconductor is given by:[9]

$$\alpha(E) = \alpha_0 \sqrt{\frac{E - E_g}{E_g}} \text{ (direct semiconductor)} \quad (2.17)$$

Or

$$\alpha(E) = \alpha_0 \left(\frac{E-E_g}{E_g}\right)^2 \text{(indirect semiconductor)} \quad (2.18)$$

In which α_0 indicates the intrinsic absorption of the semiconductor and E is the energy of the incident photon. Equations (2.17) and (2.18) indicate that photons with smaller wavelength are absorbed closer to the surface, whereas visible light (400-800 nm) can penetrate much deeper into the material (up to a few microns) before generating a charge-pair. Hence, care must be taken while selecting the morphology of the designated catalyst. A lower particle size increases the surface area, thereby increasing the number of incident photons and reducing the migration distance of electron and holes. However, a larger cross-section improves the photon to charge pair conversion ratio. Apart from the issue of photogeneration, other important factors are life-time of the charge pair and their migration ability within the material.

To design an efficient and stable photocatalyst for utilization of solar energy, several critical requirements must be satisfied. Primarily, the semiconductor responsible for light harvesting must possess a band gap large enough to provide energetic electrons, so that $E_g >> 1.23$ eV, and typically $E_g > 2.0$ eV.[18,19] However, the band gap must also be sufficiently small to allow for efficient absorption overlap with the solar spectrum, so that $E_g < 3.2$ eV.[18,19] The selection of an appropriate band gap is a trade-off between the low band gap (lower REDOX potential, high absorption) and the higher band gap (higher REDOX potential, reduced absorption). For example, to efficiently generate $OH^{\bullet}$ radicals an E_g of ≥2.7 eV is required. Furthermore, suitable band positions located above and below the hydrogen and oxygen evolution energy levels are also important to initiate and sustain several reactions, such as water splitting or hydrogen evolution.[20] Secondly, there must be a mechanism to efficiently drive the charge separation and transportation process. Finally, there should be suitable provisions to protect the catalyst from unwanted galvanic reactions, such as dissolution of components into ions or plating from the ions in the solution to form surface layers, which can deteriorate or destabilize the material over prolonged periods of use. It is generally accepted that pure or intrinsic semiconductors cannot satisfy the above criteria.[21] Hence, techniques such as band-engineering through doping, sensitizers, cocatalysts and creation of heterojunction are often employed. Barring a few exceptions, all heterogeneous catalysts can be broadly classified into the following categories: (a) doped semiconductor; (b) semiconductor-semiconductor; (c) molecule-semiconductor; (d) nano-hybrid; and (e) metal-semiconductor. Each one of these categories has its own set of advantages and disadvantages, which will be described in the following section.

2.2 Current materials: advantages and disadvantages

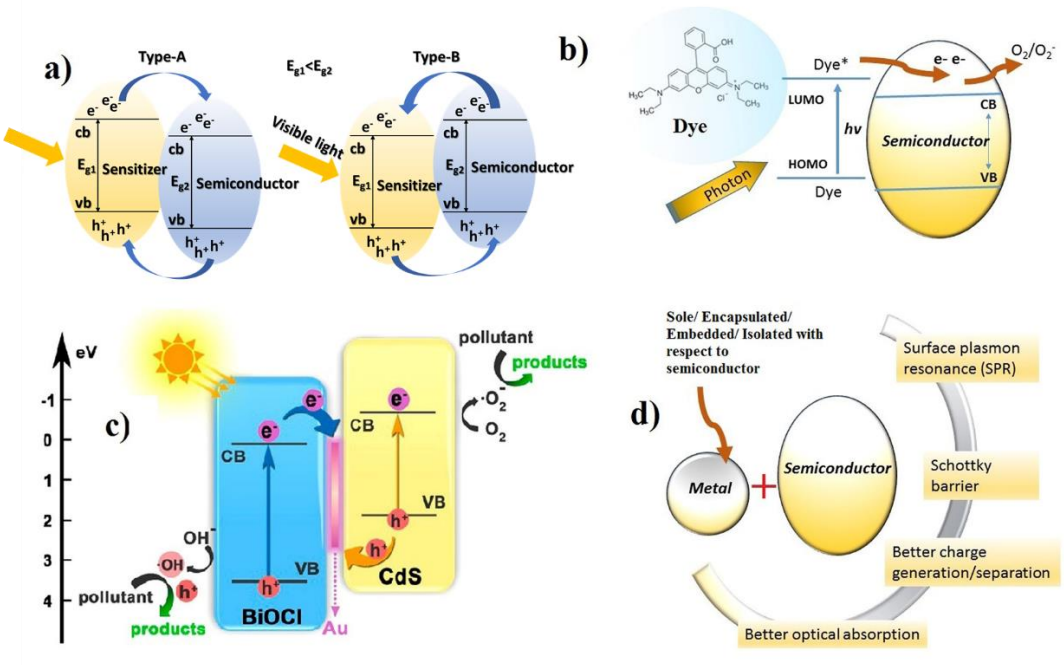

Figure 2.5: Typical photocatalytic behavior corresponding to a) semiconductor-semiconductor b) molecule-semiconductor c) multifunctional or nano hybrid and d) metal-semiconductor type catalyst. (Figure reproduced with permissions from Ref. [22] © Sustainable Chemistry and Engineering, ACS publications, 2017).

2.2.1 Doped semiconductor

Doping is the process of introducing controlled (small) amounts of impurity in an intrinsic semiconductor leading to the creation of additional electronic orbitals between HOMO and LUMO states. These energy states are known as band tails and appear close to the energy band corresponding to the dopant type. Dopants which are electron donors create band tails near cb while acceptor type impurities introduce energy states near vb. Creation of band tails practically lowers the band gap of the material, thereby allowing the material to absorb lower energy wavelengths. Additionally, if the dopant-site boding energy is relatively small, thermal energy at room temperature is enough to ionize all of the dopant atoms.[23] This leads to a higher availability of charge carriers which can partially compensate the high recombination rates. Finally, un-occupied electronic orbitals act as trap sites for electron/hole, which prevents recombination and enables the other species to successfully migrate to the surface. Co-doping of two or more ions is also reported where such mechanism imparts favourable overpotentials or band positions desired for certain REDOX reactions.[24] TiO_2 is most widely studied semiconductor with respect to doped photocatalysts. Examples include doping with metals (Cr,

Eu), non-metals (N, C), and self-doped (Ti^{3+}) catalysts.[23,25] Doping is an established science and has been successfully employed in several fields of semiconductor technology such as transistors (p-n junction). However, doping creates trap states which may act as recombination centres for photogenerated charge carriers along with lowering the reduction/oxidation potential of generated radicals. As doping alone is unable mitigate all the drawbacks associated with semiconductor photochemistry, creation of heterostructures is employed.

2.2.2 Semiconductor/semiconductor

As the name implies, a semiconductor/semiconductor (S/S) catalyst is composed of two different semiconducting materials with different band gaps but with an overlap of either the cb or vb positions, see Fig 2.5a. This allows the lower band gap semiconductor to absorb in the visible region and pump energetic charge carriers into its partner. Furthermore, the resulting difference in Fermi energy creates a Schottky junction at the interface which effectively resists charge recombination.[26] This Schottky or heterojunction can be of two types. A junction can be labelled as type-A when the conduction band of the sensitizer is located higher than that of the base semiconductor. In this case, the photogenerated electrons are transferred from the cb of the sensitizer to that of the catalyst. This high availability of electrons makes such an arrangement ideal for carrying out reduction reactions with chemisorbed acceptor type species. In an aqueous medium, this can give rise to superoxide radicals and can also be employed for hydrogen production. However, a higher availability of holes is of benefit for pollutant degradation, which can be achieved in the type-B junction. A type-B junction is created when the valence band of the sensitizer is lower than that of the primary catalyst. Such an arrangement allows some of the electrons from the vb of catalyst to be transferred to sensitizer. This creates an imbalance of charge which allows preservation of available holes in the catalyst vb to be used for oxidation reactions. Finally, depending upon the nature of the REDOX reactions and pollutants, a co-catalytic effect can also be observed. An example of such an arrangement includes titania and nickel/cobalt compounds,[27] TiO_2-CdS,[28] TiO_2-ZnO[29] and CdS-CdSe[30] among others. Hence, this combination offers advantages which can overcome some of the associated problems described above. However, the lower band gap semiconductors are generally less stable in a corrosive environment and prone to galvanic reactions at its surface, which reduces catalyst lifetime.[31] Surface passivation can be used to improve chemical stability but often results in reduced performance;[32] hence, the issue of chemical stability still needs to be addressed.[33]

2.2.3 Molecule/semiconductor

Another approach to acquire surface passivation, photosensitization and a cocatalyst effect involves binding the host semiconductor to co-catalytic molecules, see Fig 2.5b.[34] Fig 2.5b shows how the molecular catalyst helps to sensitize the semiconductor towards visible light absorption and allows rapid charge transfer between the surrounding dielectric medium and the depleted charge carriers on the catalyst surface. The molecular catalysts, which can be organic or inorganic in nature, act in a similar manner to that in a dye-sensitized solar cells.[35] A good example is chlorophyll, which is responsible for the green pigmentation in plants and aids photosynthesis.[35] Catalytic molecules are often used to suppress recombination of photogenerated charge carriers and facilitate rapid charge transfer. Furthermore, this step can also enable protection of the photocatalyst from oxidation, thereby prolonging the operational lifetime.[36] Molecular cocatalysts can be further subdivided into two individual classes depending upon the nature of interaction between the molecules and the host semiconductor. Type 1 catalysts include an arrangement in which the molecules are simply anchored to the semiconductor surface.[37,38] In contrast, Type 2 catalysts are created if there exists a distinct chemical bonding between the molecules and semiconducting phase.[39] Molecular catalytic systems possess several advantages over traditional heterogeneous materials; these systems are highly selective towards the adsorption/desorption of reactant species and products. This characteristic enables the desired REDOX reaction to proceed at a much faster rate. Furthermore, a better surface distribution requires lower loading percentages as opposed to other catalyst classes.[40] Finally, these systems have highly reduced REDOX overpotentials, which allows them to operate at efficiencies that are superior to bulk or nano-scale systems.[40,41]

Molecular systems are also employed as sensitizers to enable large band gap semiconductors to absorb and utilize visible light.[42] The dye reacts to visible light by producing electrons, which are then injected into the conduction band of the semiconductor, see Fig 2.5b. In return, the oxidized dye can be returned to its original state by accepting electrons from the donor species in the reaction. However, this mechanism places a limitation on the speed of REDOX reactions and the dye is exposed to potentially unwanted galvanic reactions. In some instances, these molecules also exhibit synergistic effects.[39,43] For example hydrogenases, including [Ni-Fe] or [Fe-Fe] hydrogenases, have been widely studied as cocatalysts for photogeneration of H_2.[44-46,47] However, there are limits in terms of the long-term stability of the catalyst or cost-effective production techniques.[47] Furthermore, the degradation products of the dye(s) are often toxic/carcinogenic in nature and present a disposal hazard. Hence, until the issue of long-term stability and recyclability of dye is addressed, large scale deployment cannot be realized.

2.2.4 Multifunctional or nano-hybrids

As the name suggests, this category includes multi-component and nano-scale architectures. However, their distinguishing feature is that each component serves a specific purpose in the overall structure. Since a designated shape, geometry and chemical composition are obtained, several benefits can be achieved simultaneously. These include desired REDOX reactions, efficient photogenerated charge transfer, enhanced catalytic activity and prolonged stability. Photocatalyst systems based on BiOCl-Au-CdS,[22] CdS-Au-TiO_2[48] and CdS-Pt-TiO_2[49] are example of such heterostructures. The photocatalytic performance of such materials far exceeds that of TiO_2 alone. Integration of multiple semiconductors or cocatalysts with an appropriate architecture allows functionality unattainable within a single material. For example, Fig 2.5c shows the BiOCl-Au-CdS system, where BiOCl is a large band gap catalyst that is sensitized by the lower band gap CdS through an Au junction which facilitates rapid charge transfer and prevents the photodegradation of CdS in the process. This methodology has been used to address some critical and fundamental challenges in the field of photocatalysis. The modular approach associated with fabrication of nano-architectures makes it the most appealing method for producing catalysts with specialized or tailored properties. This makes them a promising candidate for development of competitive photocatalytic technology. However, since the fabrication of nano-structures is often a multi-step and bottom-up approach, the difficulty and cost of fabrication scales with complexity and number of participating heterostructures. Additionally, majority of these nanomaterials are fabricated through wet chemistry, which requires the use of high purity precursors. Hence, the overall cost of production for such catalysts is exceptionally high. If the economics of fabrication can be resolved, this technique is potentially lucrative for wide-scale applications.

2.2.5 Metal/semiconductor

Nobel or rare-earth metals which are bonded with traditional semiconductors, have been reported to provide several benefits including band-bending, surface plasmonic resonance, Schottky junction and enhanced scattering and absorption.[17,44,50,51] As described by Zhang et al, the metal can be in solo, embedded, encapsulated or isolated form, as in Fig 2.5d.[52] Noble metals (Au, Ag, and Pt) are often used owing to their inertness in chemically aggressive environments. This is important, as the sole purpose of these photocatalysts is to retain the metallic characteristic, whereas oxidation of the element will give rise to semiconductor-semiconductor type catalyst, as in Fig 2.5a.

When the metal clusters form a close-contact with the host semiconductor, it gives rise to a Schottky junction.[53] However, unlike traditional semiconductor bonding, this junction allows for the separation of photogenerated charge carriers by acting as an electron reservoir.[53,54] This lowers the probability of recombination, thereby allowing for more charged species to migrate to the surface and initiate catalysis. Secondly, these metals often have their own co-catalytic properties.[55] Hence, their incorporation also attempts to reduce the overpotential for surface photochemical reactions. Finally, the abundant availability of free conducting electrons at the metal/water dielectric interface allows these metal clusters to display surface plasmon resonances (SPR).[56] Localized SPR, or LSPR, is observed when the interacting light has a wavelength comparable to the cluster size.[52] In the presence of a suitable dielectric medium, such as water, this generates a resonance in the surface electrons of the metal which results in a very high energy transfer. These 'hot-electrons' can easily overcome the forbidden zone of the Schottky junction and can be used for surface reduction reactions, while the metal itself can replace the lost electrons from the surface adsorbed species. LSPR is highly dependent on the size and shape of the metal cluster employed and hence, can be easily tuned to absorb specific wavelengths. This allows superior control over the light absorption characteristics of the metal/semiconductor pair without the need to alter their chemistry. LSPR and plasmonic catalysis is a growing field and there already exist several reviews on the topic.[52,56,57] In brief, the most commonly employed nanoclusters are based on Ag, Au, and Pt, while the semiconductors used for evaluation have included TiO_2, CdS and Fe_2O_3.[52,56] Several morphologies can be obtained, and a classification involves either asymmetric, axis-symmetric or core-shell structures. However, the use of noble metals and wet-chemistry techniques, often employed to fabricate these catalysts, makes them expensive and places them at a commercial disadvantage. This can be overcome by simplifying the fabrication process and shifting the focus to employ more earth-abundant elements, such as copper. Also, LSPR is only useful when the host semiconductor is insensitive or weakly sensitive to incident light. If the incident photons are energetic enough to trigger significant photogeneration in the primary catalyst, LSPR is not observed and the metal cluster is only employed as an electron reservoir. Hence, such configuration is highly selective with respect to incident wavelengths and care must be taken while designing such catalysts.

2.3 Selected applications for photocatalysis

2.3.1 Water treatment

Even though pure water does not have any nutrients or caloric value, it is essential for supporting all known life forms on our planet. Water in its pure form is a transparent, tasteless,

colourless and odourless liquid which covers about 71% of earth's surface.[58] However, 96.5% of all surface water is contained in the ocean and consequently unfit for human consumption. Of the remaining 3.5% fresh water, 1.74% is stored as permafrost (snow, ice and glaciers) while the remaining ~1.69% is potable ground water which is used to support the entirety of global population (7.6 billion people).

According to WHO, an average human being needs a minimum of 20 L potable water per day just to meet the basic hygiene and food requirements.[59] Water is also required for other purposes such as food production, cleaning, cooking and industrial processes. Hence, it is very important to ensure that a minimum acceptable quality of water is always available for everyone. However, even in 2018 approximately 844 million people (~11% of global population) lack access to clean water.[60] Water pollution has been linked to more than 14000 deaths each day and is considered as one of the leading causes of death and diseases in the world.[61] Furthermore, the majority of the population affected by this global water crisis is concentrated in developing economies. An estimated 580 people in India die daily due to polluted water, while 90% of the water in major cities of China is severely polluted. Growing economies, population and industry in these areas are all responsible for such dangerous levels of water pollution. Other practices such as surface run-off, agricultural discharge, lack of proper sanitation and water treatment plants also contribute to polluting of fresh water sources. Fig 2.6 shows a map of the world depicting the percentage of population with access to improved water sources.

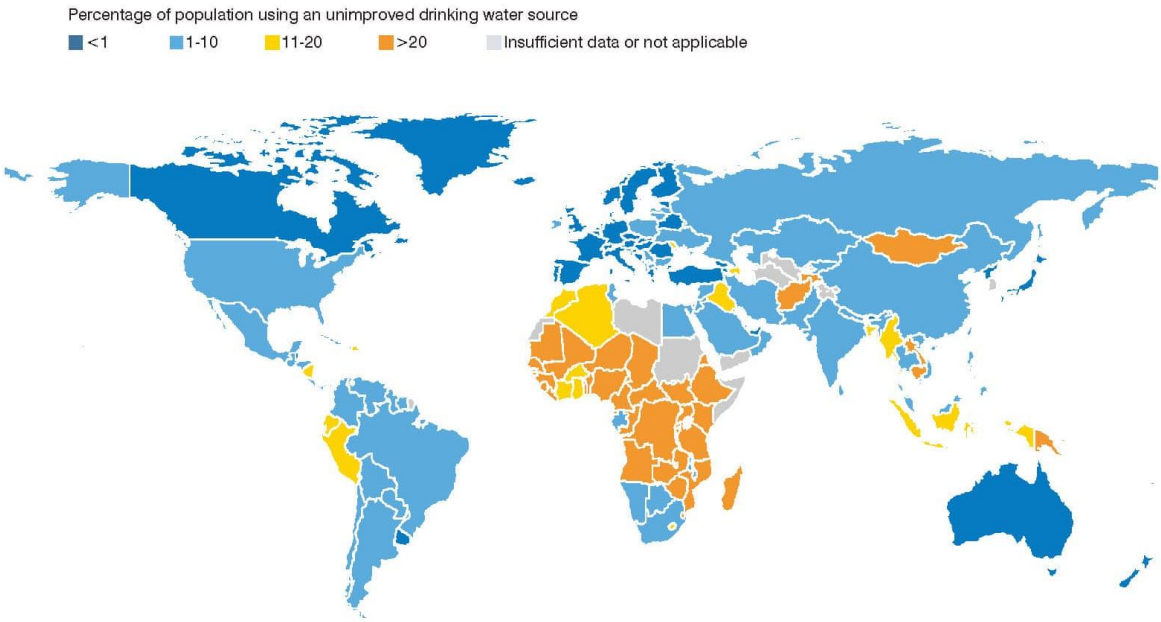

Figure 2.6: Global population (%) with access to improved water sources. Reproduced with permission from Ref. [60]

Contaminants or pollutants encompass a wide spectrum of pathogens and chemical compounds, a majority of which may be naturally occurring in water bodies. Hence, a pollutant can be defined as any substance above/below a certain concentration such that its presence/absence can pose an environmental and biological hazard. Nevertheless, water pollutants can be mainly classified as biological (pathogens) or chemical (compounds). Pathogens are micro-organisms (bacteria, virus and worms) responsible for causing and spreading disease in plants, animals and human beings. A few common examples include E. coli, Salmonella and Norovirus. Conversely, any chemical compound which is toxic or causes adverse effects can be classified as a chemical pollutant including detergents, insecticides, pesticides, pharmaceuticals and industrial by-products including textile dyes. Traditional methods for pollutant removal such as chemical treatment and mechanical filtration are energy and cost intensive, with any direct return on investment recouped only in the longer run.[62] However, one key challenge in employing such systems is the vast infrastructure required for the collection and redistribution of pollutant and treated products, respectively.[63] The problem is further aggravated due to the generation of chemical by-products which demand specialized disposal.[64] Hence, it would be economically and energetically beneficial if in-situ treatment of a majority of pollutants could be undertaken with minimum energy input and unwanted by-products. Of the currently available and researched technologies, solar photocatalysis is potentially capable of meeting these stringent requirements.[65,66]

Primarily, photocatalytic water treatment relies on the generation of powerful ROS such as hydroxyl radicals, superoxides, and peroxides (section 2.1.2) which can oxidize/mineralize a variety of organic, inorganic and biological contaminants. Most dissolved pollutants can be degraded through attack with these ROS provided their reduction/oxidation potential lies within the band edges of the employed semiconductor. The advantage of employing photocatalysis for water treatment lies in its simple construction, portability, need for minimum infrastructure and availability of free and abundant solar energy.[67] Another important aspect favouring the development of photocatalytic water treatment plants is the non-selectivity of ROS towards chemical and biological pollutants.[65] Hence, a single treatment can be applied to remove and/or inactivate a host of pollutants. Therefore, suitable development and integration of photocatalytic water treatment is being viewed as an important step towards the development of a cleaner and sustainable future.

Aqueous dye degradation is one of the most commonly employed tests for discerning the catalytic activity of any semiconductor. Organic dyes are employed in a variety of industries including textile and printing, but a large portion of untreated dye solution is often released as

an industrial effluent. The presence of dyes even in low concentrations can affect the quality of water adversely.[65] As majority of these dyes are not biodegradable, chemical treatment is often used for their removal. Photocatalysis can be used to mineralize/degrade aqueous dye solutions in the presence of actual or simulated sunlight.[68] If sufficient time is provided, most organic pollutants can be oxidized to produce carbon dioxide and water as the ultimate products. The presence of aqueous dyes can be easily identified due to their absorbance in the visible region. However, there are other classes of chemical compounds which are invisible to the naked eye. Cosmetics, pharmaceuticals (prescription and non-prescription) and agricultural products like fertilizers/insecticides can lead to disastrous effects such as eutrophication, endocrine disruption and development of anti-microbial resistance.[65] These are often hard to detect by the naked eye as they do not absorb in the visible region. Further, since these chemicals originate from a non-point source unlike industrial discharge, their collection and treatment is challenging. In this regard, non-selectivity of ROS generated in aqueous photocatalysis can lend a strategic advantage towards their elimination using natural sunlight.[69] The final category of pollutants consists of microbes such as bacteria, virus and fungi, which can spread water-borne diseases upon coming in contact with contaminated water.[70] Unlike chemical pollutants and industrial discharge, growth of microbes in wastewater is mainly linked to improper handling of sewage and sanitation products. Direct release of untreated sewage into water bodies gives these microbes an ideal environment for unchecked growth, in which they can multiply rapidly and disturb the ecosystem of the whole region. This problem can be further aggravated by the presence of fertilizers and pharmaceuticals, which can lead to eutrophication, and mutation of these pathogens to develop resistance to antibiotics. Photocatalytic treatment of waste water for the removal of microbial impurities has already been investigated on a large scale.[70] Photocatalytic disinfection of pathogens proceeds either through generation of ROS or metal ion formation. The ROS and metal ions attack the outer membrane and cell wall affecting the permeability of cell. Breach of the cell wall is followed by lipid peroxidation of the cytoplasmic membrane ultimately causing the cell to deactivate.[70,71] Fig 2.7 gives a graphical representation of the possible mechanisms by which photocatalytic bacterial inactivation can be accomplished.

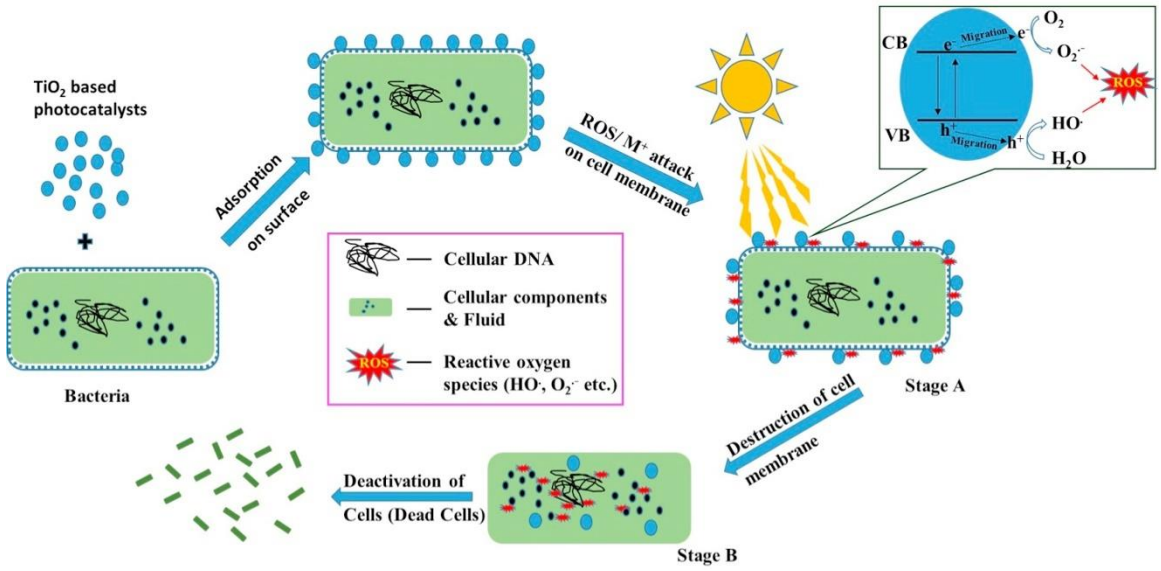

Figure 2.7: Possible mechanism for photocatalytic inactivation of bacteria. Reproduced with permission from Ref.[70]

TiO_2 (anatase) has been widely investigated as a potential catalyst for removal of disinfection and removal dissolved impurities from large water bodies because of its non-toxic nature, chemical and physical stability and a suitably high cb potential.[70,72] However, owing to its high band gap, charge recombination and poor activity in the visible light, there is a huge body of science dedicated towards the development of other candidate materials for photocatalytic water treatment using visible light.[65] Nevertheless, owing to its inherent advantages and economic viability, TiO_2-based materials remain one of the strongest contenders for the development of practical photocatalytic water treatment technology.[66]

2.3.2 Hydrogen production

Hydrogen is one of the cleanest fuels available and can be generated using abundant solar energy and water. Currently, majority of the hydrogen is produced through catalytic decomposition of fossil fuels or electrolysis of water using electricity which is often produced using fossil fuels.[73] However, these are not cost-effective methods and the hydrogen so produced is generally used for industrial applications rather than utilization as a fuel.[73,74] Furthermore, utilization of fossil fuels for hydrogen production is not a sustainable method. Water splitting can be used to generate large quantities of pure hydrogen in a sustainable manner. This can be accomplished through various techniques all of which utilize solar energy, as explained in Fig 2.8. However, energy conversion from one form to another appends to the irreversibility of the process and hence, the compounded efficiency of these models is low. Therefore, it would be very economical if we could utilize solar energy for direct splitting of

water. Heterogeneous photocatalysis presents an efficient method for the same. However, the prohibitively high cost of noble-metal cocatalysts and the lack of economical and stable systems has long prevented this concept from commercialization.

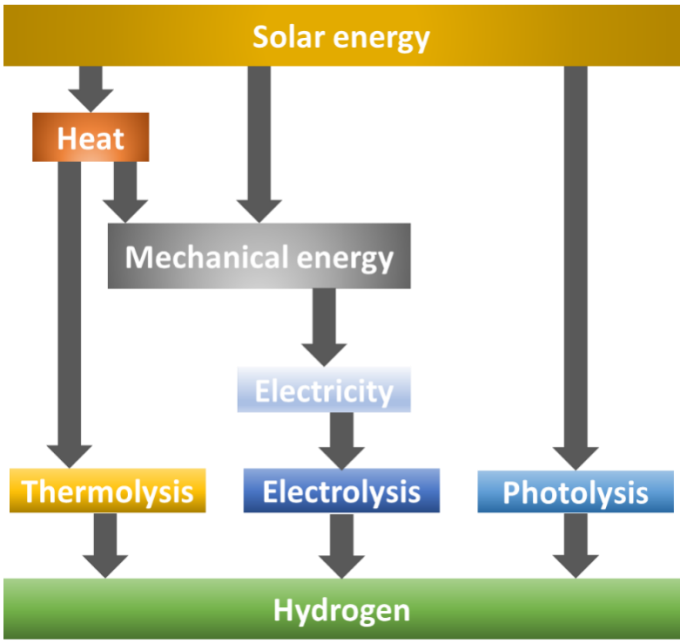

Figure 2.8: Methods of (solar) hydrogen production.

UV-assisted water splitting on a TiO_2-based photoanode was first demonstrated by Fujishima and Honda, in 1972.[75] This work was further built upon by Bard who laid the foundation for particle based heterogeneous photocatalysis.[15] Since then, a variety of semiconductors including ZnO[76], CdS[77], GaP[78] and ZnS[79] have been tested for solar hydrogen production. The ability to control the structure and functionality of semiconductor particles at nanoscale has enabled the use of cheaper earth-abundant materials with a significantly improved quantum efficiency. However, development of competitive photocatalytic technology requires a solar-to-hydrogen conversion efficiency of 15%[80] which is much higher than what can be achieved using current-state-of-the-art photocatalysts. However, this target could be readily achieved by a smart combination of photovoltaic technology and efficient electrocatalysts,[81] photoelectrocatalysis under concentrated sunlight,[82] and a reduced component cost.[83] For photocatalytic systems, the target could be met by efficient upconversion of NIR light which could participate in photocatalysis.[84]

Photocatalytic water splitting or photolysis is not a single step process but rather made up of two half reactions namely the hydrogen evolution reaction (HER) and oxygen evolution reaction (OER). Equations (2.19) and (2.20) describe the mechanisms for each half reactions

for the HER and OER respectively, whereas equation (2.21) gives the overall Gibb's free energy (ΔG^o) and REDOX potential (ΔE^o) of the whole process.[51]

$$2H^+ + 2e^- \rightarrow H_2(g)(\Delta E^o = -0.41\ V\ ) \quad (2.19)$$

$$2H_2O(l) \rightarrow O_2(g) + 4H^+ + 4e^-(\Delta E^o = +0.82\ V) \quad (2.20)$$

$$H_2O(l) \rightarrow H_2(g) + \frac{1}{2}O_2(g)(\Delta G^o = +237.2\ kJmol^{-1};\ \Delta E^o = +1.23\ V) \quad (2.21)$$

Equations (2.19) to (2.21) indicate that the OER is the limiting factor, requiring four electron oxidation of two water molecules. To achieve successful water splitting the lowest edge of the cb (LUMO) should be slightly below the reduction potential of H^+/H_2 (0 V against NHE at pH 7). Similarly, the highest edge of vb (HOMO) should be higher than the oxidation potential of H_2O/O_2 (1.23 V against NHE). Further, the minimum energy required to achieve water splitting places the lower limit of the band gap (E_g) to be >1.23 eV (absorbing <1000 nm wavelength). In theory, any semiconductor fulfilling these requirements will be able to achieve un-assisted splitting of pure water (pH 7) in the presence of energetic photons. However, in practical application the energy required to achieve water splitting is significantly more owing to several factors including sluggish reaction kinetics, imperfect crystal geometry, surface adsorption, recombination and back reactions. The difference between the minimum required energy and the practical requirements of a given system is known as its overpotential. Hence, for practical photocatalytic water splitting E_g of the material should lie in the range of 1.5-2.5 eV (Fig 2.9).

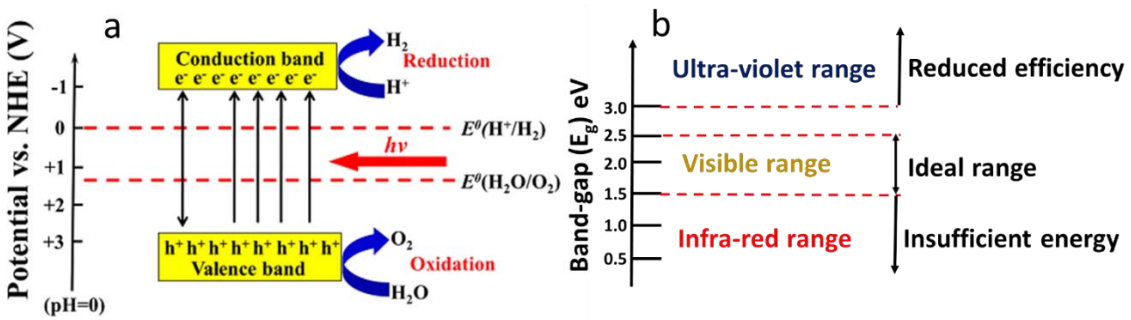

Figure 2.9: (a) Required positions of the conduction and valence band for efficient HER and OER reactions and, (b) band-gap energy of the semiconductor materials with respect to the electromagnetic spectrum.

An ideal semiconductor should be able to achieve pure water splitting with H_2 and O_2 gas being the only end products of the reaction in a strict stoichiometric ratio of 2:1. Even though TiO_2 is one of the most investigated photocatalytic materials, its cb edge of -0.5 V versus NHE makes it a poor catalyst for hydrogen production. Hence, other candidate materials have been

investigated for the purpose of solar hydrogen production including halides, nitrides and sulphides of transition metals.[85,86] Recently, CdS has emerged as one of the most important hydrogen evolution photocatalysts. It has a narrow band gap of 2.4 eV which allows it to absorb visible light along with an ideal cb edge of -0.9 V (vs RHE) enabling generation of energetic electrons for water reduction.[87] However, CdS suffers from fast photocorrosion attributed to autooxidation of Cd-S bonds from cb electrons resulting in its poor stability.[88] Hence, CdS is often employed with metal nanoparticles or other cocatalysts which can act as an electron sink.[89] Further details about techniques adopted to improve the efficiency and stability of these semiconductors have already been discussed in section 2.2. Alternately, several good reviews are available in the literature dealing with recent advances and challenges in the field of photocatalytic water splitting.[45,80,85-87] However, even with advance nanostructured and noble-metal cocatalysts, solar water splitting is a difficult task as intermediates for both HER and OER reactions are unstable and tend to undergo fast recombination to form water. Hence, most water splitting reactions are performed in the presence of sacrificial agents to suppress the backward reaction and isolate either H_2 and O_2 gas as the end product. For HER, the sacrificial agents traditionally consist of alcohols, which are consumed during the reaction. However, other compounds such as alkali carbonates[90], sulphates and sulphides have also been reported.[91] In case of the OER, nitrates of silver and iron have been employed as sacrificial electron traps to suppress the formation of hydrogen.[91] In order to achieve complete water splitting without the need for sacrificial agents the semiconductor must contain sites for both hydrogen and oxygen evolution, and these reaction sites must be physically separated. There have been a few reported examples of such system which are capable of achieving pure water splitting by inclusion of sites for both hydrogen and oxygen evolution. One of the landmark examples in this field has been reported by Duonghong et al. who fabricated colloidal TiO_2 particles co-deposited by ultrafine Ru_2O and Pt particles.[92] Pt being an electron reservoir acted as a site for hydrogen evolution while Ru_2O facilitated hole transport from the vb of TiO_2 to the particle surface. Consequently, a high quantum yield of 30% was reported under UV (300 nm) illumination. Recently, a few studies have reported the fabrication of 'Janus' particles for overall water splitting. The term 'Janus' is derived from the two-faced god in Roman mythology and, in materials science, is often used to identify biphasic heterodimer geometries which exhibit a clear anisotropic distinction between the two constituent phases. Zheng et al. fabricated a hollow carbon nitride nanosphere functionalized with Pt and Co_2O_3 nanoparticles on its interior and exterior surfaces, respectively.[13] Janus nanospheres with an optimized loading concentration (1 wt.%) of cocatalysts could achieve almost stoichiometric (H_2/O_2=2.1) water splitting in the absence of sacrificial agent under UV illumination (λ>300 nm). In another

recent study, authors reported the fabrication of a Janus z-scheme based on γ-MnS and Cu_7S_4.[93] The bare Janus catalyst could achieve a quantum efficiency of 18.8% for hydrogen evolution under visible light in the presence of sacrificial agents. To achieve complete water splitting the Janus particles were deposited with MnO_x cocatalyst for oxygen evolution. These modified Janus particles displayed an apparent quantum efficiency of 5.5% (420 nm) for overall water splitting without the need of any sacrificial agents. To date this remains one of the few studies dealing with photocatalytic overall water splitting using visible light. However, for preliminary investigations, the use of sacrificial agents remains a popular method.[51]

2.4 Titania-based photocatalysts

Titanium dioxide or titania (TiO_2) is one of the oldest known photoactive oxide semiconductors. The first reported photoactive effects of TiO_2 date back to 1920, when Renz reported darkening of the material under UV radiation.[94] However, it was only after the discovery of water-splitting activity of TiO_2 photoanode, reported in 1972, that TiO_2 based photocatalysis came into limelight.[75] According to Scopus, as of the submission of this thesis, over 50,000 articles have been published in the field of photocatalysis out of which ~32,000 (63%) are based on TiO_2 in a direct or indirect manner. Presently, TiO_2 has become the 'gold standard' for comparison of photoactivity for novel catalysts and still remains one of the most heavily investigated oxide photocatalyst till date.[23] There are several reasons responsible for the success of TiO_2-based materials in the field of photocatalysis. Primarily, titanium is fourth most abundant metal in earth's crust which translates to high availability and economy of production.[95] Titania in mineral form is evenly distributed over the globe which allows competitive production free from geo-political influence.[96] Fig 2.10 gives a graphical description of the global titania reserves. Processed TiO_2 is mined and used for a variety of application including production of pigments, plastics, cosmetics, optical and hydrophobic surfaces among others. The oxide industry itself is estimated to be worth USD 13.2 billion[97]. Furthermore, processes required for production, purification, size control and chemical modification of TiO_2 is an established body of knowledge. Apart from this, TiO_2 also possesses several other advantages including low toxicity, high thermal and physical stability, resistance to corrosion and photodegradation and chemical inertness in a wide range of acidic and basic media. All these factors have contributed heavily towards rapid development of TiO_2 based photocatalysts.

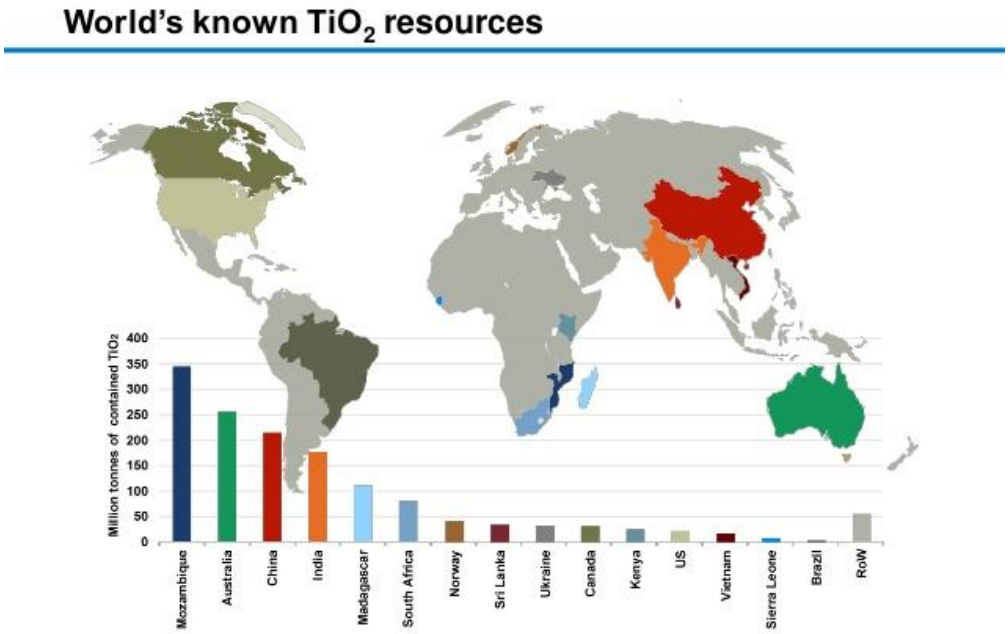

Figure 2.10: World map depicting global titania reserves. Adapted from Ref.[96]

The most abundant forms of titania are rutile, anatase and brookite. Of these, only rutile is stable at room temperature, whereas both anatase and brookite are metastable and revert back to rutile phase when heated to 600-800 ºC.[98] Of these, only anatase has been primarily investigated for photocatalytic applications. Anatase TiO_2 is a brilliant white mineral possessing tetragonal crystal structure and an optical band gap of 3.2 eV. Comparatively, rutile TiO_2 is also a tetragonal crystal and has a slightly lower band gap of 3.0 eV. However, the band positions for anatase are favourably placed with respect to a variety of desired REDOX reactions including hydrogen evolution, which makes it favourable to employ it as a photocatalyst.

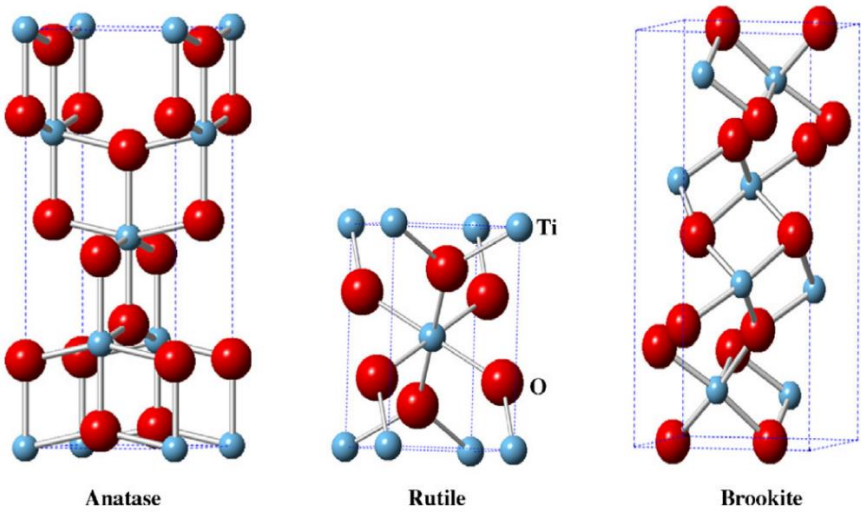

Figure 2.11: Crystal structure for polymorphs of TiO_2: anatase, rutile and brookite. Adapted with permission from Ref.[23]

However, pristine TiO_2 (anatase) has several disadvantages associated with its use. Primarily, its large band gap of 3.2 eV corresponds to absorption capacity of wavelength $\lambda \leq 380$ nm. This means that the material can only utilize UV radiation for photogeneration of charge carriers. UV radiation only constitutes ~5% of the total incident solar energy. Hence, TiO_2 is unable to employ a large fraction of the available energy, putting it at a significant disadvantage. Moreover, the quantum efficiency of pure TiO_2 is low, meaning a large fraction of the incident photons are unable to produce charge carriers. Finally, majority of the charge carriers produced are lost due to the high recombination rate of unmodified anatase TiO_2. Hence, a large body of science has been dedicated to sensitizing TiO_2 towards visible light, improving charge carrier life-time and mitigating the high recombination rate.[23] The three primary methods for improving photocatalytic performance of titania include doping, sensitization, and creation of heterostructures. A brief overview of these methodologies has already been provided in section 2.2. However, different applications require production of TiO_2 composites with tailored properties. Recently, with the discovery of LSPR effects, a large number of noble-metal and titania based catalysts have been reported.[56,99] Given the high visible light activity and good co-catalytic effects of metal nanoparticles, this approach has developed rapidly over the last decade. However, the fabrication cost of such catalysts is high and hence, any attempts at large scale production are self-limiting in nature. Therefore, a practical approach for developing economically viable photocatalyst will involve modification of TiO_2 with earth abundant elements. In this regard, this study deals with development, optimization and investigation of two specialized TiO_2 nanocomposites. In this entire study, the term nanocomposite is used to denote nanoparticles of TiO_2 containing a cocatalyst, whereas the photocatalysts themselves are powders which were dispersed in an appropriate aqueous solution. First composition, which is a carbon-coated TiO_2 has been developed for water treatment through rapid degradation of dissolved impurities and inactivation of bacteria. The second composition focuses on development on nickel nanostructures for efficient solar hydrogen production. A brief literature review of both categories is presented below.

2.4.1 Carbon-TiO_2 composites

Carbon is the 15th most abundant element in Earth's crust and forms the basis of all life forms on our planet.[95] At present, carbon-based fossil fuels power most of our technology and transportation. Rapid release of stored carbon (in oxide form) is also the biggest source of air pollution in the world and the main gas responsible for climate change.[100] However, carbon might also be the solution to harnessing the free and abundant solar energy and mitigating the air and water-based pollution. Carbon, due to its unique bonding properties can exist as different

allotropes including amorphous, graphene and diamond. With contemporary advancement in fabrication and imaging techniques, researchers have successfully engineered these allotropes at their most fundamental level to produce exotic carbon nanomaterials including nanotubes[101] and fullerene.[102] Further functionalization of these nanostructures has allowed us to tap into a wide range of unprecedented physical and chemical attributes which are not encountered in any other material class. The scientific and technological ramifications have been huge, including the field of photocatalysis.[103] Primarily, there are three different methods for creating carbon and TiO_2-based photocatalysts. These include doping with carbon,[24,104] coating with carbon,[105-107] and mounting onto carbon nanostructures such as graphene,[108] reduced graphene oxide,[109] nanotube (CNT),[110] fullerene,[111,112] and recently carbon-nitride.[113]

Among the potential non-metallic dopants for TiO_2, carbon has received considerable attention. This can be credited to its low cost and toxicity, and demonstrated ability for both band gap reduction and improved absorption of visible light.[24,103,107,112] Furthermore, compared to the most investigated non-metallic dopant nitrogen (N), C seems to be beneficial.[24,114] C-modified TiO_2 has been investigated for a host of applications including photoelectrochemical water splitting[114,115], mineralization of dissolved pollutants[24,116] and anti-bacterial treatment.[104] However, modification attempts with elemental C have met with limited success and hence, only a few studies have been reported compared to other dopants. This can be partly credited to the incompatibility of C with TiO_2 lattice[24] along with the high temperature and pressure requirements to produce such materials. The commonly employed methods to produce TiO_2-C composites entail flame-pyrolysis[114], high temperature sintering[105], hydrothermal[117] or sol-gel approaches.[24] Furthermore, usually an external carbon source is required and offers little control over the degree or placement of C atoms. Carbon as a dopant can exist as both: a substitutional anion[114] or an interstitial cationic impurity.[118] As a substitutional anion it tends to form Ti-C bonding with an oxidation state of -4. Similarly, as a cation it exhibits an oxidation state of +4 as a carbonate in C-O configuration. However, in any carbon-based material both may be present with varying degrees.[119] This uncertainty has led to different studies reporting conflicting findings and claims over the mechanism for enhancement of photocatalytic activity, expressed either as band gap reduction or from enhanced absorption. The energy levels associated with Ti-C[120], O-Ti-C[117], C-O[121] and C-C[122] bonds all lie well within the HOMO and LUMO levels of pristine anatase TiO_2. Hence, the presence of either one of more of these states could directly contribute to the lowering of band gap and corresponding change in optical absorption characteristics. However, another theory states that inclusion of C into TiO_2 matrix could give rise to oxygen vacancy defects.[123] These defects act as colour centers and are

responsible for the change in absorption spectra without necessarily altering the band gap. These facts coupled with the exhaustive number of reported synthesis techniques has created much controversy and debate over the subject matter. Nevertheless, over the last 15 years a number of published studies have indicated the beneficial effects of incorporating C in titania based photocatalysis.

One of the seminal articles in the field dates back to 2002 in which Khan et. al demonstrated the high photoactivity of C doped photoanode for photoelectrochemical water splitting.[114] A maximum total conversion efficiency of 11% was reported, which was an order of magnitude higher than undoped electrode. However, it was in 2007 that an actual direct comparison of C-doped TiO_2 was made with both pristine and N-doped TiO_2 as a standalone photocatalyst.[24] Chen et al. systematically investigated the effects of both individual and co-doping of TiO_2 with N and C at varying percentages, prepared through sol-gel approach. Visible light degradation of methylene blue solution indicated that C-doped TiO_2 is significantly better than N-doped TiO_2, whereas the highest activity was displayed by the co-doped sample. However, sol-gel fabrication technique is time and cost-intensive and alternate economic methods are required for the production of photocatalysts. This issue was addressed by Dong et al. who reported a 'green' approach for the synthesis of C-doped TiO_2[117]. The process involved dissolving known quantities of $Ti(SO_4)_2$ and glucose in water as precursors for titania and carbon, followed by hydrothermal synthesis at 160 ^oC for 12 H. The fabricated mesoporous catalyst was reportedly 17.6 times better than P25 Degussa under visible radiation for degradation of gaseous toluene.

Apart from doping, another popular configuration is a carbon coating on TiO_2 particles to produce a core-shell configuration. A layer of graphitic carbon over a titania shell can impart several benefits unobtainable from doped configurations. These include improved surface absorptivity of chemical species in an aqueous environment and a higher surface area which leads to the generation of more active sites for potential REDOX reactions.[105] Another important advantage is that graphitic carbon may enhance absorption in the visible spectrum due to electronic coupling of π electrons with cb states of TiO_2.[107] Additionally, since carbon incorporation helps absorb visible light, a smaller particle size may be employed since the light does not need to travel further. Hence, with all these benefits, it is expected that a TiO_2-C core-shell structure would exhibit superior catalytic activity. An example in this regard was demonstrated by Shanmugam and coauthors who prepared core-shell structure through thermal dissociation of titanium(IV) oxyacetyl acetonate monohydrate under high-pressure using a custom made cell.[105] The carbon content in the prepared catalyst varied with calcination temperature between 32.8% to 36.7% (900 ^oC to 700 ^oC). All catalysts performed better than

P25 for visible light degradation of methylene blue. However, the large carbon content and high temperature and pressure required for the synthesis makes the approach less than ideal. This method was further improved upon by Zhang et al. who surface functionalized P25 with a few molecular thick layer of graphitic carbon.[107] The functionalization was carried out by hydrothermal treatment of P25 in a glucose solution. Under UV radiation, the particles performed twice as better than untreated P25 for formaldehyde degradation, while also displaying significant activity in visible light. Recently, other forms of TiO_2-C core-shell structures have also been reported including nano-graphene covered TiO_2[106] and inverse TiO_2-C configuration.[124] However, to the best of our knowledge, a single method for facile, in-situ production of TiO_2-C core-shell particles has not yet been reported.

All other configurations of carbon-titania catalyst can be classified as mounting of TiO_2 on functionalized and unfunctionalized nano-carbon structures. Since the available configurations and preparation techniques differ vastly, it is not possible to provide an exhaustive review of the same. Hence, only a brief description will be provided. Ever since Iijima broke ground for their development,[125] CNTs have rapidly developed from being a scientific curiosity to having a host of practical applications such as structural support, functional probes, and energy storage and conversion.[101] CNTs have also been widely investigated in the field of heterogeneous photocatalysis due to several inherent advantages. Both single wall (SWCNT) and multi wall (MWCNT) possess exceptionally high surface area in the range of 400-900 m^2g^{-1} and 200-400 m^2g^{-1}, respectively.[126] Thus, combination with CNT increases the available REDOX sites manifold. Additionally, depending on the rolling vector, CNTs can be made to display all manners of electrical characteristics from conducting to insulating.[127] This combined with the ability to functionalize its surface area makes CNTs highly advantageous for selective catalysis.[128] CNTs have also been reported to suppress recombination of photogenerated charge carriers in TiO_2, through the formation of a Schottky junction as well as acting as an electron sink.[129,130] There have also been reports where CNTs have been employed as photosensitizers allowing TiO_2 to absorb photons in the visible region.[131] The reported TiO_2-CNT configurations include TiO_2 dispersed on SWCNT and MWCNT,[129] SWCNT and MWCNT on larger TiO_2 particles,[129] TiO_2 coated CNTs[131] and intermixed nanotubes[132] among others.

However, in the field of heterogeneous photocatalysis attention has recently shifted from CNT to its fundamental form of graphene[133] and its derivatives graphene oxide (GO)[134] and reduced GO (rGO).[135] Individual graphene sheets have a staggeringly high surface area of 2600 m^2g^{-1} owing to their two-dimensional structure.[136] Moreover, carefully prepared graphene sheets demonstrate a concomitantly high electron mobility of up to 15000 $m^2v^{-1}s^{-1}$ making them

exceptional conductors and an excellent electron sink.[137] Their monoatomic thickness allows them to retain high transparency[138] and being chemically bonded to the surface hydroxyl groups of TiO_2 also allows narrowing of band gap.[139] This sensitizes TiO_2 towards visible light as well as forming a heterojunction thereby, greatly suppressing electron-hole recombination.[134] Furthermore, the surface can also be functionalized to impede or accelerate certain reactions with targeted REDOX sites.[140] Graphene can also be readily oxidized to produce GO which can be used as an on-demand semiconductor-semiconductor junction and further reduced to form rGO.[141] Hence, graphene can impart all the benefits of CNT at a much higher scale. Comparative analysis has revealed that indeed for the same amount of carbon percentage graphene-TiO_2 composite can readily outperform CNT-TiO_2 catalyst under similar conditions.[139] Other nano-carbon morphologies investigated for titania based heterogeneous photocatalysis include graphitic carbon nitride[142] and fullerene among others.[103] However, there are relatively fewer studies in this area.

2.4.2 Nickel-TiO_2 composites

One of the primary reasons for popularity of TiO_2 as a universal photocatalyst is owing to the ideal placement of its vb. A high oxidation potential (2.7 V vs NHE) allows TiO_2 to readily oxidize a host of organic and inorganic compounds. However, its low cb edge (-0.5 V vs NHE) limits its applicability with respect to reduction reactions. Furthermore hydrogen evolution relies exclusively on high availability of cb electrons to reduce surface absorbed protons into molecular hydrogen.[86,87] This requires a high electron transport/mobility on the surface of the semiconductor as well as a highly negative cb edge with respect to the reduction potential of H^+/H_2 (E^0=0.0 V). Hence, pure TiO_2 is not considered to be a good material for hydrogen evolution reaction and the use of a cocatalyst is necessitated. A cocatalyst can improve hydrogen production by either reducing the overpotential for hydrogen evolution or lowering the cb edge, or both. In this regard, noble metals such as Pt, Au, Ag and Pd are often employed. Noble metals are preferred cocatalysts owing to several major advantages. Primarily, these metals have a Fermi level significantly lower than TiO_2 which allows the formation of a heterojunction.[19] This not only improves separation of photogenerated charge carriers but also suppresses their recombination. This junction also imparts band-bending which lowers the cb potential, thereby reducing the amount of energy required for hydrogen evolution. Additionally, these metals also act as electron reservoirs and hence, act a preferential reduction sites for adsorbed atomic (H^+) and molecular species (H_3O^+). Finally, size selected metal nanoclusters can also benefit from LSPR which uses visible light and rapidly injects hot electrons into the semiconductor cb.[52,56] All these properties make them an ideal candidate for direct conversion

of solar energy into hydrogen fuel. However, given the high cost and low availability of these metals, their wide scale applicability remains doubtful. Hence, efforts have been made to develop cocatalysts with earth abundant materials including Fe, Co, Mo, Ni and their compounds.[51,86] Recent reports have shown that carefully nanostructured transition metal compounds are not only efficient and stable but can also compete, and in some instances, outperform noble metal composites.

In this regard, Ni and its selected compounds have shown promising results.[143] Nickel in both free standing and supported forms is already employed as an industrial catalyst for various processes including hydro-cracking, steam reforming, methane reforming and hydrogenation of organic compounds.[143] Its thermocatalytic properties and ability to store and release large amounts of hydrogen gas make it indispensable as a noble-metal free catalyst. Indeed, nanostructured nickel is one of the most investigated materials for electrochemical and photoelectrochemical splitting of water. However, studies involving its direct application in semiconductor photocatalysis have been limited. Moreover, a majority of these studies focus exclusively on CdS, owing to its excellent capacity for photocatalytic water splitting; with only a handful of studies involving TiO_2.[143] However, CdS is highly prone to photo-corrosion and its stability is only limited to lower pH values;[144] whereas, TiO_2 being an oxide is stable in a wide variety of acidic and basic medium and hence, is highly versatile. Therefore, it is important to explore potential cocatalysts for hydrogen production using TiO_2. In order for a material to be a good hydrogen evolution cocatalyst several requirements must be met. Primarily, it should display a suitable cb position for hydrogen evolution (< 0 V vs RHE). As initially proposed by Bard,[15] a particulate photocatalytic system is essentially a small short-circuited photoelectrochemical cell. Hence, a good electrocatalyst could potentially also be employed for photocatalysis. However, other requirements such as rapid and efficient electron transfer between the parent semiconductor and the cocatalyst, preferable position of molecular orbitals, morphology and interfacial interaction are all important. Hence, only a select few morphologies of nickel have been explored including: metallic nickel, nickel oxide, hydroxide, sulphide and phosphide.[143]

Even though bulk Ni offers a large activation energy, nano-structured Ni is considered a good catalyst for hydrogen evolution. Owing to its nano-sized geometry it possesses a high surface area. Exposed surface of these nanoparticles also provide a large number of sites for adsorption/release of hydrogen atoms and photochemical proton reduction. The small size also facilitates close contact, leading to enhanced charge migration and separation though the formation of a heterojunction. The rapid charge transfer also prevents photo-oxidation of

metallic nickel, although care must be taken with respect to pH of the operating solution. One good example of this setup was demonstrated by Tran et al. who reported hydrogen production activity of Ni nanocluster decorated commercial TiO_2 powders.[145] When employed for visible light hydrogen production using triethanolamine as a sacrificial agent, it was observed that pure TiO_2 displayed no activity. However, with a 0.3 wt.% loading of Ni a turnover frequency of 90 H^{-1} was observed. However, this number was found to be three times lower than Pt decorated particles. A study by Wang et al. explored the possibility of in-situ photo-deposition of metallic Ni particles onto TiO_2 surface from a $Ni(NO_3)_2$ solution.[146] Using an aqueous solution of methanol and 0.32 mol.% $Ni(NO_3)_2$, the authors reported an optimized hydrogen production rate of 2547 $\mu molh^{-1}g^{-1}$; corresponding to a quantum efficiency of 8.1% for 365 nm (UV) light. However, no direct comparison with Pt or hydrogen production under visible light was reported. Recently, Chen et al. reported a direct comparison of hydrogen evolution capacity of Ni (0.5 wt.%) and Au (2 wt.%) loaded P25 particles.[147] The photocatalytic hydrogen evolution was carried out under UV illumination with a variety of water-alcohol mixtures of differing concentrations. The Ni containing catalyst performed comparable to or even better than Au containing catalyst, depending upon the choice and concentration of alcohol used. However, there are conflicting theories whether the active component for improving hydrogen production is Ni^0 (metal) or Ni^{2+} (oxide). A study exploring this topic was reported by the same group who examined the role of the active Ni species responsible for hydrogen production.[14] Using UV illumination comparable to that present in natural sunlight and a water-ethanol mixture, the authors demonstrated that metallic Ni is the active cocatalyst even in NiO. The surface atoms of NiO, in UV, are first reduced to Ni^0 before any hydrogen evolution is observed. Hence, for similar loading percentages, NiO performs poorly with respect to metallic Ni. Nevertheless, NiO is an important p-type semiconductor and has been explored as an independent cocatalyst for improving charge separation with TiO_2[148] while also extending its activity in the visible region[149]. However, only one study has been reported direct evidence of visible light hydrogen production using NiO and TiO_2.[149]

Primarily, hydrogen production over NiO-TiO_2 composites has been attempted with UV radiation. One of the earliest studies in this direction was conducted by Sreethawong and co-workers.[150] The authors prepared a mesoporous TiO_2 supported NiO using sol-gel route and employed it for UV assisted degradation of methanol. Another similar study reported the effect of calcination temperature on the hydrogen evolution activity of (10 wt.%) NiO_x supported on TiO_2.[151] The authors prepared the catalyst through incipient impregnation of TiO_2 using $Ni(NO_3)_2$ solution followed by calcination in air. For UV assisted degradation of aqueous (20

vol.%) glycerol solution, the authors reported an optimized calcination temperature of 450 ºC. Compared to bare TiO_2, NiO_x loaded catalyst demonstrated three times higher hydrogen evolution. The authors reported that calcination is important for the formation of heterojunction between TiO_2 and NiO phases. However, at higher temperatures agglomeration of particles may occur which could lead to activity reduction. The same group later reported a detailed analysis of the effects of preparation and reaction conditions on the photocatalytic hydrogen production of NiO loaded TiO_2.[152] The authors reported that hydrogen production activity of the composite catalyst increases up to 2 wt.% NiO loading after which it decreases. The percentage loading was responsible for altering the band gap of the composite material, which contributed partially towards improving the photocatalytic activity; whereas pH was reported to be another major factor. However, the authors noted that glycerol was the only source for evolved hydrogen and little to no water splitting was observed. Aspect ratio and morphology of the catalyst may also play an important role in determining the overall activity of such photocatalysts. Li et al reported the fabrication and photocatalytic activity of bicomponent NiO/TiO_2 (anatase phase) nanofibers.[153] The catalyst was prepared by electrospinning a colloidal solution of $Ni(NO_3)_2$ and titanium butoxide followed by calcination in air. Using 25 vol.% aqueous methanol, the optimized fibres (0.25 wt.% NiO) achieved a hydrogen evolution of 337 μmol h^{-1} g^{-1}, which was seven times higher than pure TiO_2.

Other important nickel-based compounds reported for their excellent cocatalytic activity include $Ni(OH)_2$, NiS, and Ni_xP_y. Even through pure $Ni(OH)_2$ does not display any photocatalytic hydrogen production, its inclusion as a cocatalyst can drastically improve the performance of TiO_2. This was demonstrated in a study by Yu and co-workers in which the authors decorated commercial titania (P25) with $Ni(OH)_2$ nanoclusters.[154] The composite catalyst was prepared by a conventional precipitation method in which TiO_2 particles were suspended in Na(OH) solution, to which a solution of $Ni(NO_3)_2$ was carefully added. Due to the lack of any further processing, the precipitated clusters of $Ni(OH)_2$ were amorphous in nature. The composite catalysts were then utilized for hydrogen evolution with a water-ethanol mixture (33 vol% ethanol) under UV illumination (365 nm). Catalyst containing an optimal loading of 0.23 mol% could achieve hydrogen production of 3056 μmol h^{-1} g^{-1}, corresponding to a quantum efficiency of 12.4%. This value was an impressive 223 times larger than reported for bare TiO_2 alone. The high performance of the composite catalyst was attributed to the slightly lower reduction potential of Ni^{2+}/Ni (E^0=-0.23 V) with respect to cb of TiO_2. This enabled rapid electron transfer from TiO_2 cb to $Ni(OH)_2$ nanoclusters, which acted as active site for proton reduction. Furthermore, presence of UV reduced Ni^{2+} to metallic Ni that acted

as an electron reservoir thereby improving charge separation. However, such a compound lacks proper sites for hole trapping, which could be employed for oxygen evolution during complete water splitting reaction. In this direction Wang et al. performed a follow-up study, modifying $Ni(OH)_2$ containing TiO_2 with amorphous Ti acting as a hole trapping site.[37] The base TiO_2 was prepared by hydrothermal synthesis and later modified using controlled hydrolysis of $Ti(SO_4)_2$ to achieve a coating of amorphous Ti. This was followed by urea assisted precipitation of $Ni(OH)_2$ using a solution of $Ni(NO_3)_2$. When employed for photocatalytic hydrogen evolution, the optimized catalyst (0.1 wt.%) could achieve hydrogen production of 7280.04 μmol h^{-1} g^{-1} and a quantum efficiency of 20.71%.

As a p-type semiconductor, NiS has also been employed as an efficient cocatalyst for hydrogen production. NiS also has some unique properties such as accelerated absorption-desorption kinetics of surface adsorbed species along with improved electron transfer, which favor its wide-scale applicability. Zhang et al. reported the fabrication and photocatalytic activity of nanostructured NiS deposited on the surface of TiO_2.[155] The catalyst was synthesized by mixing together anatase powder with thiourea, glycol and $Ni(NO_3)_2$ followed by hydrothermal synthesis at 180 ^oC. For photocatalytic hydrogen evolution, 30 vol% lactic acid in water was used a sacrificial agent. The setup was irradiated for 4 h with an unfiltered Xe lamp, indicating that both UV and visible radiation were present. It was reported that individually pure TiO_2 and NiS could not display any appreciable photocatalytic activity. However, with an optimized loading concentration of 7 mol% NiS, the composite catalyst could achieve a hydrogen evolution rate of 698 μmol h^{-1} g^{-1}. NiS, similar to $Ni(OH)_2$, can rapidly trap photogenerated electrons from cb of TiO_2 and transfer them to metallic Ni nanoclusters formed on the surface of NiS due to photoreduction. However, NiS is also a potent cocatalyst for effectively trapping and re-release of hydrogen atoms which allows it to function more effectively than either Ni_3S_2 or NiS_2. This performance could be further improved by adopting a morphology with a better aspect ratio, as demonstrated by Huang and co-workers.[156] In this study, the authors fabricated a TiO_2 nanotube and NiS composite catalyst with a single step hydrothermal synthesis by mixing P25 nanoparticle with Na(OH), thiourea, glycol and $Ni(NO_3)_2$ solution. The resulting catalyst consisted of TiO_2 nanotubes having a diameter of 5-15 nm and a length of 60-100 nm, decorated by clusters of NiS. The photocatalytic experimental setup consisted of a quartz reactor illuminated by a Xe lamp, in which 25 vol% aqueous methanol solution served as the electron donor. Pure TiO_2 nanotube displayed a poor hydrogen evolution rate of 94 μmol h^{-1} g^{-1}. In contrast, even a 2 mol% loading of NiS improved this number to 3743

μmol h^{-1} g^{-1}. The optimized loading concentration was reported to be 8 mol% with the highest hydrogen evolution rate of 7486 μmol h^{-1} g^{-1}, two orders of magnitude higher than pure TiO_2.

These studies demonstrate the excellent co-catalytic capacity of Ni based compounds for hydrogen evolution in acidic medium. However, all of the studies involving Ni modified TiO_2 rely mainly on the availability of UV to assist with hydrogen production, which is not desirable for a practical photocatalyst. To the best of our knowledge there are not studies for nickel-titania composites which report hydrogen production in visible light. One possible solution to this problem might be the use of an emerging new Ni based material. Ni_xP_y is used to denote a range of nickel phosphides with different oxidation states of Ni, of which Ni_2P is most investigated compound.[157-159] Ni_2P has been reported as the most effective noble metal free Ni based cocatalyst for both photocatalytic[157,159] and electrocatalytic[160] hydrogen evolution. This is often credited to the ameliorated charge separation, efficient charge transfer and ability to absorb in the visible region. Furthermore, it is the only Ni based compound with demonstrated and stable activity in visible light. However, only a limited number of studies have been conducted regarding the photocatalytic potential of Ni_2P, of which only one is reported with TiO_2.[159] Furthermore, the reported synthesis method primarily involves the use of unstable oleylamine, which makes the synthesis challenging while providing little control over the dispersion and morphology of the deposited Ni_2P particles. Given the recently reported promising results, this field warrants further investigation to realize its full potential and unlock the door to the development of a practical, effective and stable Ni based cocatalyst for solar powered hydrogen production and water splitting reactions.

References:

1 Michel Chanon, *Homogeneous photocatalysis*. (Wiley, 1997).

2 Chung-Hsin Wu and Chung-Liang Chang, Journal of hazardous materials **128** (2-3), 265 (2006).

3 Igor T Peternel, Natalija Koprivanac, Ana M Lončarić Božić, and Hrvoje M Kušić, Journal of hazardous materials **148** (1-2), 477 (2007).

4 Julia García-Montaño, Francesc Torrades, José A. García-Hortal, Xavier Domènech, and José Peral, Journal of Hazardous Materials **134** (1), 220 (2006).

5 Soonhyun Kim, Hyunwoong Park, and Wonyong Choi, The Journal of Physical Chemistry B **108** (20), 6402 (2004).

6 Michael R. Hoffmann, Scot T. Martin, Wonyong Choi, and Detlef W. Bahnemann, Chemical Reviews **95** (1), 69 (1995).

7 John Stringer, in *An Introduction to the Electron Theory of Solids*, edited by John Stringer (Pergamon, 1967), pp. 195; John Stringer, in *An Introduction to the Electron Theory of Solids*, edited by John Stringer (Pergamon, 1967), pp. 229.

8 Jiuqing Wen, Jun Xie, Xiaobo Chen, and Xin Li, Applied Surface Science **391**, 72 (2017).

[9] Franklin Feng Tao, William F Schneider, and Prashant V Kamat, *Heterogeneous catalysis at nanoscale for energy applications*. (John Wiley & Sons, 2015).
[10] Takashi Tachikawa, Mamoru Fujitsuka, and Tetsuro Majima, The Journal of Physical Chemistry C **111** (14), 5259 (2007).
[11] Nick Serpone and Ezio Pelizzetti, *Photocatalysis: fundamentals and applications*. (Wiley-Interscience, 1989).
[12] Sunil Kommineni, Jeffrey Zoeckler, Andrew Stocking, PS Liang, Amparo Flores, Rey Rodriguez, T Brown, R Per, and Anthony Brown, center for groundwater restoration and protection national water research institute (2000).
[13] Dandan Zheng, Xu-Ning Cao, and Xinchen Wang, Angewandte Chemie International Edition **55** (38), 11512 (2016).
[14] Wan-Ting Chen, Andrew Chan, Dongxiao Sun-Waterhouse, Toshihiro Moriga, Hicham Idriss, and Geoffrey I. N. Waterhouse, Journal of Catalysis **326**, 43 (2015).
[15] Harald Reiche and Allen J Bard, Journal of the American Chemical Society **101** (11), 3127 (1979).
[16] Sangman Hwang, Myung Churl Lee, and Wonyong Choi, Applied Catalysis B: Environmental **46** (1), 49 (2003).
[17] Anna Kubacka, Marcos Fernández-García, and Gerardo Colón, Chemical reviews **112** (3), 1555 (2011).
[18] Dionysios D Dionysiou, Gianluca Li Puma, Jinhua Ye, Jenny Schneider, and Detlef Bahnemann, *Photocatalysis: applications*. (Royal Society of Chemistry, 2016).
[19] Jingxiang Low, Jiaguo Yu, Mietek Jaroniec, Swelm Wageh, and Ahmed A Al-Ghamdi, Advanced Materials (2017).
[20] Shiyou Chen and Lin-Wang Wang, Chemistry of Materials **24** (18), 3659 (2012).
[21] Marye Anne Fox and Maria T Dulay, Chemical reviews **93** (1), 341 (1993).
[22] Qiaoying Li, Zhipeng Guan, Di Wu, Xiuge Zhao, Shenyuan Bao, Baozhu Tian, and Jinlong Zhang, ACS Sustainable Chemistry & Engineering **5** (8), 6958 (2017).
[23] Vinodkumar Etacheri, Cristiana Di Valentin, Jenny Schneider, Detlef Bahnemann, and Suresh C. Pillai, Journal of Photochemistry and Photobiology C: Photochemistry Reviews **25**, 1 (2015).
[24] Daimei Chen, Zhongyi Jiang, Jiaqing Geng, Qun Wang, and Dong Yang, Industrial & Engineering Chemistry Research **46** (9), 2741 (2007).
[25] S. Girish Kumar and L. Gomathi Devi, The Journal of Physical Chemistry A **115** (46), 13211 (2011).
[26] Huanli Wang, Lisha Zhang, Zhigang Chen, Junqing Hu, Shijie Li, Zhaohui Wang, Jianshe Liu, and Xinchen Wang, Chemical Society Reviews **43** (15), 5234 (2014); Prashant V Kamat, Accounts of Chemical Research **50** (3), 527 (2017).
[27] Shin-ichiro Fujita, Hiroki Kawamori, Daisuke Honda, Hiroshi Yoshida, and Masahiko Arai, Applied Catalysis B: Environmental **181**, 818 (2016); Monica Barroso, Alexander J. Cowan, Stephanie R. Pendlebury, Michael Grätzel, David R. Klug, and James R. Durrant, Journal of the American Chemical Society **133** (38), 14868 (2011).
[28] Gui-Sheng Li, Die-Qing Zhang, and Jimmy C Yu, Environmental science & technology **43** (18), 7079 (2009).
[29] DL Liao, CA Badour, and BQ Liao, Journal of Photochemistry and Photobiology A: Chemistry **194** (1), 11 (2008).
[30] Yuh-Lang Lee, Ching-Fa Chi, and Shih-Yi Liau, Chemistry of materials **22** (3), 922 (2009).
[31] Wolfgang Kautek and Heinz Gerischer, Surface Science **119** (1), 46 (1982).
[32] Hiroyuki Fujii, Michitaka Ohtaki, Koichi Eguchi, and Hiromichi Arai, Journal of Molecular Catalysis A: Chemical **129** (1), 61 (1998).
[33] Chuang Han, Min-Quan Yang, Bo Weng, and Yi-Jun Xu, Physical Chemistry Chemical Physics **16** (32), 16891 (2014); Chao Wang, Li Wang, Jun Jin, Jing Liu, Yu Li, Min Wu, Lihua Chen, Binjie Wang, Xiaoyu Yang, and Bao-Lian Su, Applied Catalysis B: Environmental **188**, 351 (2016).
[34] Miao Zhang, Chuncheng Chen, Wanhong Ma, and Jincai Zhao, Angewandte Chemie **120** (50), 9876 (2008).

[35] Andreas Kay and Michael Graetzel, The Journal of Physical Chemistry **97** (23), 6272 (1993).
[36] R. Comparelli, E. Fanizza, M. L. Curri, P. D. Cozzoli, G. Mascolo, and A. Agostiano, Applied Catalysis B: Environmental **60** (1), 1 (2005).
[37] J He, DW Shao, LC Zheng, LJ Zheng, DQ Feng, JP Xu, XH Zhang, WC Wang, W-H Wang, and F Lu, Applied Catalysis B: Environmental **203**, 917 (2017).
[38] Min Liu, Xiaoqing Qiu, Masahiro Miyauchi, and Kazuhito Hashimoto, Chemistry of Materials **23** (23), 5282 (2011).
[39] Guixia Zhao, Yubin Sun, Wei Zhou, Xiangke Wang, Kun Chang, Guigao Liu, Huimin Liu, Tetsuya Kako, and Jinhua Ye, Advanced Materials **29** (40), 1703258 (2017); Wooyul Kim, Guangbi Yuan, Beth Anne McClure, and Heinz Frei, Journal of the American Chemical Society **136** (31), 11034 (2014); Guixia Zhao, Hong Pang, Guigao Liu, Peng Li, Huimin Liu, Huabin Zhang, Li Shi, and Jinhua Ye, Applied Catalysis B: Environmental **200**, 141 (2017).
[40] Pengxin Liu, Yun Zhao, Ruixuan Qin, Shiguang Mo, Guangxu Chen, Lin Gu, Daniel M. Chevrier, Peng Zhang, Qing Guo, Dandan Zang, Binghui Wu, Gang Fu, and Nanfeng Zheng, Science **352** (6287), 797 (2016).
[41] Xiaogang Li, Wentuan Bi, Lei Zhang, Shi Tao, Wangsheng Chu, Qun Zhang, Yi Luo, Changzheng Wu, and Yi Xie, Advanced Materials **28** (12), 2427 (2016).
[42] Youngmin Cho, Wonyong Choi, Chung-Hak Lee, Taeghwan Hyeon, and Ho-In Lee, Environmental Science & Technology **35** (5), 966 (2001).
[43] Wentuan Bi, Xiaogang Li, Lei Zhang, Tao Jin, Lidong Zhang, Qun Zhang, Yi Luo, Changzheng Wu, and Yi Xie, Nature communications **6**, 8647 (2015).
[44] Zhenguo Yang, Jianlu Zhang, Michael CW Kintner-Meyer, Xiaochuan Lu, Daiwon Choi, John P Lemmon, and Jun Liu, Chemical reviews **111** (5), 3577 (2011).
[45] W Justin Youngblood, Seung-Hyun Anna Lee, Kazuhiko Maeda, and Thomas E Mallouk, Accounts of Chemical Research **42** (12), 1966 (2009).
[46] Daniel Streich, Yeni Astuti, Michele Orlandi, Lennart Schwartz, Reiner Lomoth, Leif Hammarström, and Sascha Ott, Chemistry – A European Journal **16** (1), 60 (2010); Masaki Ihara, Hirofumi Nishihara, Ki-Seok Yoon, Oliver Lenz, Bärbel Friedrich, Hitoshi Nakamoto, Kouji Kojima, Daisuke Honma, Toshiaki Kamachi, and Ichiro Okura, Photochemistry and photobiology **82** (3), 676 (2006).
[47] David J Evans and Christopher J Pickett, Chemical Society Reviews **32** (5), 268 (2003).
[48] Hiroaki Tada, Tomohiro Mitsui, Tomokazu Kiyonaga, Tomoki Akita, and Koji Tanaka, Nature materials **5** (10), 782 (2006).
[49] Hyunwoong Park, Wonyong Choi, and Michael R Hoffmann, Journal of materials chemistry **18** (20), 2379 (2008).
[50] Hailong Zhou, Yongquan Qu, Tahani Zeid, and Xiangfeng Duan, Energy & Environmental Science **5** (5), 6732 (2012); Michael G Walter, Emily L Warren, James R McKone, Shannon W Boettcher, Qixi Mi, Elizabeth A Santori, and Nathan S Lewis, Chemical reviews **110** (11), 6446 (2010); Yongquan Qu, Xing Zhong, Yujing Li, Lei Liao, Yu Huang, and Xiangfeng Duan, Journal of materials chemistry **20** (18), 3590 (2010).
[51] Xiaobo Chen, Shaohua Shen, Liejin Guo, and Samuel S Mao, Chemical reviews **110** (11), 6503 (2010).
[52] Xuming Zhang, Yu Lim Chen, Ru-Shi Liu, and Din Ping Tsai, Reports on Progress in Physics **76** (4), 046401 (2013).
[53] César Clavero, Nature Photonics **8** (2), 95 (2014).
[54] Song Bai, Xiyu Li, Qiao Kong, Ran Long, Chengming Wang, Jun Jiang, and Yujie Xiong, Advanced Materials **27** (22), 3444 (2015).
[55] Yan Li, Fangzhi Mou, Chuanrui Chen, Ming You, Yixia Yin, Leilei Xu, and Jianguo Guan, RSC Advances (2016); Kazuhiko Maeda, Kentaro Teramura, Daling Lu, Nobuo Saito, Yasunobu Inoue, and Kazunari Domen, Angewandte Chemie International Edition **45** (46), 7806 (2006).
[56] Wenbo Hou and Stephen B Cronin, Advanced Functional Materials **23** (13), 1612 (2013).

[57] Jiun-Jen Chen, Jeffrey CS Wu, Pin Chieh Wu, and Din Ping Tsai, The Journal of Physical Chemistry C **116** (50), 26535 (2012); Ewa Kowalska, Ryu Abe, and Bunsho Ohtani, Chemical Communications (2), 241 (2009); Jiangtian Li, Scott K Cushing, Joeseph Bright, Fanke Meng, Tess R Senty, Peng Zheng, Alan D Bristow, and Nianqiang Wu, Acs Catalysis **3** (1), 47 (2012).

[58] Peter H Gleick, Pacific Institute for Studies in Dev., Environment & Security. Stockholm Env. Institute, Oxford Univ. Press. 473p **9** (1993).

[59] RA Reed, Sam Godfrey, Sam Kayaga, Brian Reed, Jonathan Rouse, Julie Fisher, Karen Vilholth, and Frank Odhiambo, (WEDC, Loughborough University© World Health Organisation, 2013).

[60] Tom Slaymaker, (The Guardian, 2017), Vol. 2018.

[61] Philip J Landrigan, Richard Fuller, Nereus JR Acosta, Olusoji Adeyi, Robert Arnold, Abdoulaye Bibi Baldé, Roberto Bertollini, Stephan Bose-O'Reilly, Jo Ivey Boufford, and Patrick N Breysse, The Lancet (2017).

[62] Yu Jiang and Petra Hellegers, Journal of Environmental Management **184**, 504 (2016); Thomas H Tietenberg and Lynne Lewis, *Environmental and natural resource economics*. (Routledge, 2016).

[63] Allen V Kneese, *The economics of regional water quality management*. (Routledge, 2013).

[64] Qi Zheng, Xiaoqiu Yang, Wenchao Deng, X Chris Le, and Xing-Fang Li, Journal of Environmental Sciences **42** (4), 1 (2016); Hangzhou Xu, Haiyan Pei, Yan Jin, Hongdi Xiao, Chunxia Ma, Jiongming Sun, and Hongmin Li, Water research **111**, 382 (2017).

[65] Shuying Dong, Jinglan Feng, Maohong Fan, Yunqing Pi, Limin Hu, Xiao Han, Menglin Liu, Jingyu Sun, and Jianhui Sun, RSC Advances **5** (19), 14610 (2015).

[66] Seul-Yi Lee and Soo-Jin Park, Journal of Industrial and Engineering Chemistry **19** (6), 1761 (2013).

[67] Detlef Bahnemann, Solar Energy **77** (5), 445 (2004).

[68] Ioannis K Konstantinou and Triantafyllos A Albanis, Applied Catalysis B: Environmental **49** (1), 1 (2004).

[69] Jing An and Qixing Zhou, Journal of Environmental Sciences **24** (5), 827 (2012); Ioannis K. Konstantinou, Theophanis M. Sakellarides, Vasilis A. Sakkas, and Triantafyllos A. Albanis, Environmental Science & Technology **35** (2), 398 (2001); Guisheng Li, Ya Zhang, Ling Wu, Fang Wu, Rong Wang, Dieqing Zhang, Jian Zhu, and Hexing Li, RSC Advances **2** (11), 4822 (2012).

[70] P. Venkata Laxma Reddy, Beluri Kavitha, Police Anil Kumar Reddy, and Ki-Hyun Kim, Environmental Research **154**, 296 (2017).

[71] Ishrat Bano, R Vasant Kumar, and Abdul Hameed, International journal of environmental health research **23** (5), 407 (2013).

[72] Manoj Lazar, Shaji Varghese, and Santhosh Nair, Catalysts **2** (4), 572 (2012).

[73] Ibrahim Dincer, International Journal of Hydrogen Energy **37** (2), 1954 (2012).

[74] Zeke Barlow, Virginia Tech news (2013).

[75] Akira Fujishima and K Honda, Nature **238** (5385), 37 (1972).

[76] SR Morrison and T Freund, The Journal of Chemical Physics **47** (4), 1543 (1967); Kazuhiko Maeda, Tsuyoshi Takata, Michikazu Hara, Nobuo Saito, Yasunobu Inoue, Hisayoshi Kobayashi, and Kazunari Domen, Journal of the American Chemical Society **127** (23), 8286 (2005); Nezamaddin Daneshvar, Darioush Salari, and AR Khataee, Journal of Photochemistry and Photobiology A: Chemistry **162** (2), 317 (2004).

[77] Xu Zong, Hongjian Yan, Guopeng Wu, Guijun Ma, Fuyu Wen, Lu Wang, and Can Li, Journal of the American Chemical Society **130** (23), 7176 (2008); Qin Li, Beidou Guo, Jiaguo Yu, Jingrun Ran, Baohong Zhang, Huijuan Yan, and Jian Ru Gong, Journal of the American Chemical Society **133** (28), 10878 (2011); Ningzhong Bao, Liming Shen, Tsuyoshi Takata, and Kazunari Domen, Chemistry of Materials **20** (1), 110 (2007).

[78] Jianwei Sun, Chong Liu, and Peidong Yang, Journal of the American Chemical Society **133** (48), 19306 (2011).

[79] Jin-Song Hu, Ling-Ling Ren, Yu-Guo Guo, Han-Pu Liang, An-Min Cao, Li-Jun Wan, and Chun-Li Bai, Angewandte Chemie **117** (8), 1295 (2005); Jun Zhang, Jiaguo Yu, Yimin Zhang, Qin Li, and Jian Ru Gong, Nano letters **11** (11), 4774 (2011).
[80] Blaise A. Pinaud, Jesse D. Benck, Linsey C. Seitz, Arnold J. Forman, Zhebo Chen, Todd G. Deutsch, Brian D. James, Kevin N. Baum, George N. Baum, Shane Ardo, Heli Wang, Eric Miller, and Thomas F. Jaramillo, Energy & Environmental Science **6** (7), 1983 (2013).
[81] Yasunori Kikuchi, Takayuki Ichikawa, Masakazu Sugiyama, and Michihisa Koyama, International Journal of Hydrogen Energy **44** (3), 1451 (2019).
[82] Saurabh Tembhurne, Fredy Nandjou, and Sophia Haussener, Nature Energy **4** (5), 399 (2019).
[83] Deepak Yadav and Rangan Banerjee, Journal of Cleaner Production **183**, 1131 (2018).
[84] Dandan Li, Shu-Hong Yu, and Hai-Long Jiang, Advanced Materials **30** (27), 1707377 (2018).
[85] Takashi Hisatomi, Jun Kubota, and Kazunari Domen, Chemical Society Reviews **43** (22), 7520 (2014).
[86] Akihiko Kudo and Yugo Miseki, Chemical Society Reviews **38** (1), 253 (2009).
[87] Savio JA Moniz, Stephen A Shevlin, David James Martin, Zheng-Xiao Guo, and Junwang Tang, Energy & Environmental Science **8** (3), 731 (2015).
[88] Junze Chen, Xue-Jun Wu, Lisha Yin, Bing Li, Xun Hong, Zhanxi Fan, Bo Chen, Can Xue, and Hua Zhang, Angewandte Chemie International Edition **54** (4), 1210 (2015).
[89] Fukun Ma, Yongzhong Wu, Yongliang Shao, Yueyao Zhong, Jiaxin Lv, and Xiaopeng Hao, Nano Energy **27**, 466 (2016).
[90] Hironori Arakawa and Kazuhiro Sayama, Catalysis Surveys from Japan **4** (1), 75 (2000).
[91] Hui Liu, Jian Yuan, and Wenfeng Shangguan, Energy & Fuels **20** (6), 2289 (2006).
[92] Dung Duonghong, Enrico Borgarello, and Michael Graetzel, Journal of the American Chemical Society **103** (16), 4685 (1981).
[93] Qichen Yuan, Dong Liu, Ning Zhang, Wei Ye, Huanxin Ju, Lei Shi, Ran Long, Junfa Zhu, and Yujie Xiong, Angewandte Chemie **129** (15), 4270 (2017).
[94] Carl Renz, Helvetica Chimica Acta **4** (1), 961 (1921).
[95] (Israel Science and Technology Directory, 2018), Vol. 2018.
[96] David McCoy, in *Feedstock pressure on titanium sponge market* (https://www.slideshare.net, 2013).
[97] Zach Schonbrun, (https://www.bloomberg.com, 2018), Vol. 2018.
[98] Norman Neill Greenwood and Alan Earnshaw, (1984).
[99] L Gomathi Devi and R Kavitha, Applied Surface Science **360**, 601 (2016).
[100] Intergovernmental Panel On Climate Change, Agenda **6** (07), 333 (2007).
[101] Ray H Baughman, Anvar A Zakhidov, and Walt A De Heer, science **297** (5582), 787 (2002).
[102] Mildred S Dresselhaus, Gene Dresselhaus, and Peter C Eklund, *Science of fullerenes and carbon nanotubes: their properties and applications*. (Elsevier, 1996).
[103] Rowan Leary and Aidan Westwood, Carbon **49** (3), 741 (2011).
[104] Guomin Wang, Hongqing Feng, Liangsheng Hu, Weihong Jin, Qi Hao, Ang Gao, Xiang Peng, Wan Li, Kwok-Yin Wong, Huaiyu Wang, Zhou Li, and Paul K. Chu, Nature Communications **9** (1), 2055 (2018).
[105] Sangaraju Shanmugam, Alexandra Gabashvili, David S. Jacob, Jimmy C. Yu, and Aharon Gedanken, Chemistry of Materials **18** (9), 2275 (2006).
[106] Hyoung-il Kim, Gun-hee Moon, Damián Monllor-Satoca, Yiseul Park, and Wonyong Choi, The Journal of Physical Chemistry C **116** (1), 1535 (2012).
[107] Li-Wu Zhang, Hong-Bo Fu, and Yong-Fa Zhu, Advanced Functional Materials **18** (15), 2180 (2008).
[108] Yongye Liang, Hailiang Wang, Hernan Sanchez Casalongue, Zhuo Chen, and Hongjie Dai, Nano Research **3** (10), 701 (2010).
[109] Ping Wang, Jin Wang, Xuefei Wang, Huogen Yu, Jiaguo Yu, Ming Lei, and Yonggang Wang, Applied Catalysis B: Environmental **132**, 452 (2013).
[110] Karran Woan, Georgios Pyrgiotakis, and Wolfgang Sigmund, Advanced Materials **21** (21), 2233 (2009).

[111] Ze-Da Meng, Lei Zhu, Jong-Geun Choi, Ming-Liang Chen, and Won-Chun Oh, Journal of Materials Chemistry **21** (21), 7596 (2011).
[112] Min-Quan Yang, Nan Zhang, and Yi-Jun Xu, ACS applied materials & interfaces **5** (3), 1156 (2013).
[113] Hongjian Yan and Haoxin Yang, Journal of alloys and compounds **509** (4), L26 (2011); Zhenwei Tong, Dong Yang, Tianxiong Xiao, Yao Tian, and Zhongyi Jiang, Chemical Engineering Journal **260**, 117 (2015).
[114] Shahed U. M. Khan, Mofareh Al-Shahry, and William B. Ingler, Science **297** (5590), 2243 (2002).
[115] Jong Hyeok Park, Sungwook Kim, and Allen J Bard, Nano letters **6** (1), 24 (2006).
[116] Ganesh B. Markad, Sudhir Kapoor, Santosh K. Haram, and Pragati Thakur, Solar Energy **144**, 127 (2017).
[117] Fan Dong, Haiqiang Wang, and Zhongbiao Wu, The Journal of Physical Chemistry C **113** (38), 16717 (2009).
[118] Shanmugasundaram Sakthivel and Horst Kisch, Angewandte Chemie International Edition **42** (40), 4908 (2003).
[119] De-en Gu, Yun Lu, and Bang-chao Yang, Chemical Communications (21), 2453 (2008).
[120] Shih-Wei Hsu, Tien-Syh Yang, Ta-Kun Chen, and Ming-Show Wong, Thin Solid Films **515** (7-8), 3521 (2007).
[121] Myoung Joo Kim, Kwang-Dae Kim, Wei Sheng Tai, Hyun Ook Seo, Yuan Luo, Young Dok Kim, Byung Cheol Lee, and Ok Kyung Park, Catalysis letters **135** (1-2), 57 (2010).
[122] YJ Chen, JM Wu, CS Lin, GY Jhan, MS Wong, S-C Ke, and HH Lo, Journal of Vacuum Science & Technology A: Vacuum, Surfaces, and Films **27** (4), 862 (2009).
[123] Nick Serpone, (ACS Publications, 2006).
[124] Guozhi Zhang, Feng Teng, Changhui Zhao, Lulu Chen, Peng Zhang, Youqing Wang, Chengshi Gong, Zhenxing Zhang, and Erqing Xie, Applied Surface Science **311**, 384 (2014).
[125] Sumio Iijima, nature **354** (6348), 56 (1991).
[126] Philippe Serp, *Carbon nanotubes and nanofibers in catalysis*. (John Wiley & Sons, Inc.: Hoboken, NJ, 2009); Philippe Serp, Massimiliano Corrias, and Philippe Kalck, Applied Catalysis A: General **253** (2), 337 (2003).
[127] Edward A. Laird, Ferdinand Kuemmeth, Gary A. Steele, Kasper Grove-Rasmussen, Jesper Nygård, Karsten Flensberg, and Leo P. Kouwenhoven, Reviews of Modern Physics **87** (3), 703 (2015).
[128] Philippe Serp and José Luís Figueiredo, *Carbon materials for catalysis*. (John Wiley & Sons, 2009).
[129] Yuan Yao, Gonghu Li, Shannon Ciston, Richard M Lueptow, and Kimberly A Gray, Environmental science & technology **42** (13), 4952 (2008).
[130] Yongsheng Chen, John C Crittenden, Stephen Hackney, Larry Sutter, and David W Hand, Environmental science & technology **39** (5), 1201 (2005).
[131] O Akhavan, M Abdolahad, Y Abdi, and S Mohajerzadeh, Carbon **47** (14), 3280 (2009).
[132] Ruey-An Doong and Li-Fen Chiang, Water Science & Technology **58** (10) (2008).
[133] Xuan Pan, Yong Zhao, Shu Liu, Carol L Korzeniewski, Shu Wang, and Zhaoyang Fan, ACS applied materials & interfaces **4** (8), 3944 (2012).
[134] Chao Chen, Weimin Cai, Mingce Long, Baoxue Zhou, Yahui Wu, Deyong Wu, and Yujie Feng, Acs Nano **4** (11), 6425 (2010).
[135] Wenqing Fan, Qinghua Lai, Qinghong Zhang, and Ye Wang, The Journal of Physical Chemistry C **115** (21), 10694 (2011).
[136] Sasha Stankovich, Dmitriy A Dikin, Geoffrey HB Dommett, Kevin M Kohlhaas, Eric J Zimney, Eric A Stach, Richard D Piner, SonBinh T Nguyen, and Rodney S Ruoff, nature **442** (7100), 282 (2006).
[137] Kostya S Novoselov, Andre K Geim, Sergei V Morozov, DA Jiang, Y_ Zhang, Sergey V Dubonos, Irina V Grigorieva, and Alexandr A Firsov, science **306** (5696), 666 (2004).
[138] Rahul Raveendran Nair, Peter Blake, Alexander N Grigorenko, Konstantin S Novoselov, Tim J Booth, Tobias Stauber, Nuno MR Peres, and Andre K Geim, Science **320** (5881), 1308 (2008).

[139] Hao Zhang, Xiaojun Lv, Yueming Li, Ying Wang, and Jinghong Li, ACS nano **4** (1), 380 (2009).
[140] Prashant V Kamat, The Journal of Physical Chemistry Letters **1** (2), 520 (2009).
[141] Graeme Williams, Brian Seger, and Prashant V Kamat, ACS nano **2** (7), 1487 (2008).
[142] Ze'ai Huang, Qiong Sun, Kangle Lv, Zehui Zhang, Mei Li, and Bing Li, Applied Catalysis B: Environmental **164**, 420 (2015).
[143] You Xu and Rong Xu, Applied Surface Science **351**, 779 (2015).
[144] Allen P. Davis and C. P. Huang, Water Research **25** (10), 1273 (1991).
[145] Phong D. Tran, Lifei Xi, Sudip K. Batabyal, Lydia H. Wong, James Barber, and Joachim Say Chye Loo, Physical Chemistry Chemical Physics **14** (33), 11596 (2012).
[146] Wenguang Wang, Shengwei Liu, Longhui Nie, Bei Cheng, and Jiaguo Yu, Physical Chemistry Chemical Physics **15** (29), 12033 (2013).
[147] Wan-Ting Chen, Andrew Chan, Dongxiao Sun-Waterhouse, Jordi Llorca, Hicham Idriss, and Geoffrey I. N. Waterhouse, Journal of Catalysis **367**, 27 (2018).
[148] Cha-Jung Chen, Chi-Hung Liao, Kai-Chien Hsu, Yi-Ting Wu, and Jeffrey C. S. Wu, Catalysis Communications **12** (14), 1307 (2011).
[149] Anna Iwaszuk, Michael Nolan, Qiliang Jin, Musashi Fujishima, and Hiroaki Tada, The Journal of Physical Chemistry C **117** (6), 2709 (2013).
[150] Thammanoon Sreethawong, Yoshikazu Suzuki, and Susumu Yoshikawa, International Journal of Hydrogen Energy **30** (10), 1053 (2005).
[151] Ruixia Liu, Hiroshi Yoshida, Shin-ichiro Fujita, and Masahiko Arai, Applied Catalysis B: Environmental **144**, 41 (2014).
[152] Shin-ichiro Fujita, Hiroki Kawamori, Daisuke Honda, Hiroshi Yoshida, and Masahiko Arai, Applied Catalysis B: Environmental **181**, 818 (2016).
[153] Lingling Li, Bei Cheng, Yuanxu Wang, and Jiaguo Yu, Journal of Colloid and Interface Science **449**, 115 (2015).
[154] Jiaguo Yu, Yang Hai, and Bei Cheng, The Journal of Physical Chemistry C **115** (11), 4953 (2011).
[155] Lu Zhang, Baozhu Tian, Feng Chen, and Jinlong Zhang, International Journal of Hydrogen Energy **37** (22), 17060 (2012).
[156] Jiasheng Huang, Zhisheng Shi, and Xinfa Dong, Journal of Energy Chemistry **25** (1), 136 (2016).
[157] Zijun Sun, Huafei Zheng, Jingshi Li, and Pingwu Du, Energy & Environmental Science **8** (9), 2668 (2015).
[158] Deqian Zeng, Wanjie Xu, Wee-Jun Ong, Juan Xu, He Ren, Yuanzhi Chen, Hongfei Zheng, and Dong-Liang Peng, Applied Catalysis B: Environmental **221**, 47 (2018).
[159] Yubin Chen and Zhixiao Qin, Catalysis Science & Technology **6** (23), 8212 (2016).
[160] Eric J Popczun, James R McKone, Carlos G Read, Adam J Biacchi, Alex M Wiltrout, Nathan S Lewis, and Raymond E Schaak, Journal of the American Chemical Society **135** (25), 9267 (2013); Zonghua Pu, Qian Liu, Chun Tang, Abdullah M Asiri, and Xuping Sun, Nanoscale **6** (19), 11031 (2014).

Chapter 3

Materials and methods

3.1 Materials

Details for the different precursor, reagents and other compounds used in this study are provided in Table 3.1.

Table 3.1: Data for materials used in this study.

Material	Provider	Assay
TiO_2-C core-shell particles		
titanium IV butoxide	Acros Organics	99%
titanium IV isopropoxide	Acros Organics	>98%
titanium ethoxide	Sigma-Aldrich	97%
1-butanol	Acros Organics	anhydrous
isopropanol	Acros Organics	anhydrous
ethanol	Acros Organics	anhydrous
potassium chloride	Fisher Scientific	extra pure, SLR
P25 Degussa	Sigma-Aldrich	>99%
$Bi_{0.5}Na_{0.5}TiO_3$-BiOCl composites		
bismuth nitrate pentahydrate	Fisher Scientific	99%
bismuth carbonate	Fisher Scientific	99%
sodium carbonate	Fisher Scientific	99%
titanium dixode (anatase nanopowder; <25 nm)	Sigma-Aldrich	99.70%
Nickle-titania nanocomposites		
titanium dixode (anatase nanopowder; <25 nm)	Sigma-Aldrich	99.70%
nickel (II) acetate tetrahydrate	Sigma-Aldrich	>98%
ammonia solution (35%)	Fisher Scientific	N/A
sodium hydroxide (anhydrous pellets)	Sigma-Aldrich	>97%

sodium hypophosphite monohydrate	Sigma-Aldrich	>99%
Model pollutants		
brilliant green	Sigma-Aldrich	>90%
methyl orange	Sigma-Aldrich	85%
methylene blue	Sigma-Aldrich	>82%
rhodamine B	Sigma-Aldrich	>95%
diclofenac (sodium salt)	Alfa Aesar	>98%
ibuprofen (sodium salt)	Sigma-Aldrich	>98%
Escherichia coli (bacterial strain JM109)	Promega	N/A
Electrochemical and photochemical measurements		
sodium sulphate	Sigma-Aldrich	>99%
nafion	Sigma-Aldrich	~5 wt.% solution

Since different methods have been used to synthesise each material, detailed procedures for the preparation of individual catalysts are described separately in each chapter. However, the description of the common characterization techniques used throughout this study is provided in the following sections.

3.2 Characterization techniques: phase and morphology

A successful and thorough characterization of any (new) material is crucial to gain important insight into its structure-property relationship. Characterization also acts as a fundamental pillar upon which the reproducibility of scientific data is based. Hence, when reporting on the fabrication of a (new) compound it is important to include relevant information about its phase, microstructure, and chemical composition. Thereafter, based on the intended application, further tests might be required to ascertain other aspects such as electronic, optical, electrical or mechanical properties. There are several established and standardized techniques which can be employed to directly probe and analyse these attributes. In this regard, this chapter aims to provide a brief overview of the various characterization techniques employed in the course of this study. Details which are common to all investigations have been included at the appropriate places in the following subsections, whereas any deviation relevant to a particular study has been dealt with separately.

3.2.1 Powder X-ray diffraction (XRD) analysis

As several TiO_2-based and other composite materials were prepared in this study, identification of the constituent phases and crystal structure of the prepared samples is an important first step for confirming a successful synthesis. As all the photocatalysts in this study are polycrystalline powders, powder XRD analysis was used for phase identification. A key advantage of X-ray or any other diffraction technique is that they can be used to differentiate between compounds having similar chemical composition but different crystal structure.[1] Hence, XRD patterns serve as fingerprints for identification of various crystal structures and phases in a material. X-rays are unique in the sense that their wavelength is comparable to the lattice spacings of most crystalline materials.[1] Hence, when these X-rays are reflected from the internal planes of any crystal, depending upon the difference in path length, either constructive or destructive interference is obtained. A constructive interference results in a sharp rise in intensity of the reflected X-rays, which can be identified as a 'peak' against the background of destructive reflection. The condition for constructive interference can be determined by using Bragg's law:[1,2]

$$n\lambda = 2d_{pl} * sin\theta \qquad (3.1)$$

In equation (3.1), 'n' is an integer and 'θ' is the incident angle with respect to the plane of reflection, whereas the symbols 'd_{pl}' and 'λ' denote the interplanar spacing and the wavelength of incident radiation, respectively. Hence, in a polycrystalline sample, the position 'θ' of the peak is used to identify a certain set of parallel planes, whereas the intensity ratio of reflections with respect to other peaks can be used to evaluate the relative concentration/orientation of the sample.

In this study, the powder XRD patterns for all samples were acquired using a Bruker D8 Gen 10 theta/theta system employing Cu-K_α radiation (λ=1.5406 Å), unless otherwise specified. For sample preparation, equal amounts of powder (~0.2 g) were weighed and placed in a special single crystal (Si) holder having sample diameter of 10 mm. To achieve a flat surface that is level with the surface of sample holder, the powder was pressed with a clean glass slide and all excess powder was scraped off. The XRD setup was configured with a slit mount of 4.0^o and a slit size of 9.5 mm. The diffraction data was collected with a step-size of 0.03^o and a dwell time of 1 sec. The scanning range for all samples was limited from 10^o to 80^o (2θ), unless otherwise specified. The obtained diffraction patterns were analysed using HighScore Plus software (PANalytical X'Pert).

3.2.2 Scanning electron microscopy (SEM) imaging

In photocatalysis, the particle size and morphology have a significant bearing on the photo-activity of a catalyst. Hence, electron microscopy was employed to image the different micro and nano-sized morphological aspects of the different samples prepared in this study. SEM is a versatile and powerful tool for acquiring information about the microstructure of a large variety of materials and has become ubiquitous as a characterization technique in materials science. Unlike electromagnetic radiation, electrons can be accelerated to achieve a very small (de Broglie) wavelength,[3] which can be scanned across a surface to produce high-resolution images of a material at micro or nanometre level. Interaction of an accelerated electron beam with a sample produces various signals such as secondary electrons, back-scattered electrons, transmitted electrons and X-rays.[1] Each of these signals provide a unique set of information about the shape and configuration of the sample. For example, secondary electrons can be used to image the surface morphology, whereas X-ray generation can be used to detect the distribution of various elements, thereby revealing the approximate chemical composition. The latter technique is known as energy dispersive X-ray spectroscopy and is covered in section 3.3.

In this study, the SEM images were acquired using two separate instruments namely FEI Nova NanoSEM and FEI Helios Nanolab. For image acquisition, catalyst samples containing no carbon were prepared as follows: a double adhesive conductive carbon tape was applied to an aluminium stub and a small quantity of the powdered sample was transferred to the exposed surface of the carbon tape. Alternately, for carbon-containing TiO_2 copper tape was used instead, and the powdered samples were immobilized using silver paste (adhesive). The stub-mounted samples were sputtered with a Pt target for 5 min to achieve a conductive coating with a thickness of approximately 10 nm. Information about the actual imaging conditions such as the spot size, accelerating voltage and working distance is provided in the images itself. Part of the SEM images used in this study were acquired with help of Mr. Simon Griggs (MSM), whereas the rest were provided by Mr. Sundararajan Thirumalai (MSM) and Mr. Moolchand Sharma (IIT Mandi).

3.2.3 Transmission electron microscopy (TEM) imaging

Transmission electron microscopy was employed to image samples for which sufficient resolution could not be obtained using SEM alone. As the name implies, in a TEM sample images are produced by transmitted electrons rather than secondary or back-scattered electrons. This places a limit on the overall sample thickness that can be imaged directly using a TEM. However, a TEM is capable of achieving a much higher resolution (~0.1 nm), which is limited

only by lens aberrations.[1] Images produced using data derived from transmitted electrons in known as a bright-field image in which areas with higher mass density appear darker. Similarly, a dark-field image is generated using data from diffracted electrons and is darker for areas with low mass density. A TEM is a versatile instrument and is often coupled with other sensors and techniques such as energy-dispersive X-ray spectroscopy or high-angle annular dark-field imaging to obtain data about the local chemical composition of a material at nanoscale. The TEM images used in this study were provided by Dr. Giorgio Divitini (MSM), Mr. Moolchand Sharma (IIT Mandi), and Mr. Gauthaman Chandrabose (Open University). The TEM images were acquired using FEI Tecnai F20, JEOL JEM 2100, and FEI Technai G2 microscopes. For images acquired in the department, powdered samples were directly deposited onto holey-carbon film TEM grids (Cu 400 mesh; EM resolutions U.K.) and imaged under bright-field mode with an acceleration voltage of 200 kV. For both TEM and SEM images, individual acknowledgement is provided at the end of each chapter.

3.3 Characterization techniques: chemical composition

The surface of a photocatalyst is pivotal to its overall performance as it is where both photon absorption and subsequent REDOX reactions take place. Hence, accurate determination of the chemical makeup of a catalyst's surface is of prime importance. The following techniques were used to determine the composition, oxidation states, chemical species and nature of bonding in the prepared samples.

3.3.1 Energy dispersive X-ray (EDX) spectroscopy

EDX analysis was used to determine the average elemental composition at the surface of the prepared photocatalysts. As the interaction volume in EDX analysis is based on the mass density of the material and the incident beam energy, it is usually employed for qualitative rather than quantitative measurement. This is especially true in case of large-area particulate analysis as the interaction volume can vary a lot over the distances. EDX spectroscopy is based on the principle that interaction of accelerated electrons with an atom can eject electrons from the inner orbitals.[1,4] This causes an electron from the outer shell to migrate to an empty orbital and the difference in energy can result in the production of X-rays. Since each element has a distinct set of atomic orbitals and allowed transitions, it results in a unique X-ray emission spectrum. Hence, EDX spectroscopy can be used to precisely map the presence and quantity of individual elements on a sample. In this study, the EDX spectra of different samples was acquired in-situ during electron microscopy imaging using an EDX detector. Maps were acquired by using area scans and analysed using the ESPIRIT imaging software (Bruker).

However, owing to the high-magnification and heterogeneity of the samples, the EDX spectrum can change with respect to the area of imaging. Hence, all EDX images and data presented in this study are only used to provide qualitative information about the presence of particular elements and not the actual composition.

3.3.2 X-ray photoelectron spectroscopy (XPS)

XPS analysis was used to identify the oxidation states and hence, determine the overall chemical composition of the surface of the prepared photocatalysts. The term X-ray photoelectron is used to describe an electron ejected from the inner shell of an atom after absorbing an incident X-ray photon. If the energy of the incident X-ray photon is known, the binding energy (E_{BE}) of the emitted electron can be calculated as:[5]

$$E_{BE} = E - E_{KE} - \phi \qquad (3.2)$$

In equation (3.2), the symbols E, E_{KE}, and ϕ denote the energy of the incident X-ray photon, kinetic energy of the ejected electron and work function which is dependent on the material and spectrometer, respectively. Hence, an XPS spectra provides a measure of the number of ejected electrons as a function of binding energy. Since each element produces a set of characteristic XPS peaks, this can be used to identify the presence of that element in the sample; whereas the location and ratio of peaks with respect to binding energy reveals the oxidation state and ratio of different chemical species.[1,5] Hence, XPS is considered as a very powerful tool to study the surface composition, electronic state and chemistry of a variety of samples in physical sciences. However, as the technique relies on detection of ejected electrons, it has a probe-depth limitation of ~10 nm and requires a high vacuum to operate.[5] In this study, the majority of the XPS spectra were acquired using an ESCALAB 250Xi instrument (Thermo Fisher, U.K.), equipped with an Al-Kα X-ray source ($h\nu$ = 1486.6 eV). Prior to XPS measurements, the sample chamber was initially pumped down to 10^{-9} mbar and flooded twice with He (BIP) to remove any stray gases escaping from the samples. The acquired spectral data was corrected for charge compensation with respect to the C 1s orbital of adventitious carbon (284.8 eV). Data acquisition and peak-fitting for all samples were performed by Mr. Chris Amey at the Cavendish laboratory, University of Cambridge. XPS data for some samples, which could not be analysed with the above instrument, were provided by Mr. Gauthaman Chandrabose (Open University) by employing a Kratos XSAM800 system (Shimadzu) equipped with a dual anode Mg-Kα X-ray source ($h\nu$ = 1253.6 eV). Mr. Gauthaman Chandrabose also did the processing and peak-fitting (deconvolution) of the raw XPS data.

3.3.3 Raman spectroscopy

Even though EDX and XPS can reveal important information about the surface chemistry, it often does not provide the complete picture such as the presence of distinct electronic states in chemical bonds. Owing to the unique nature of photocatalysts prepared in this study (carbon containing core-shell structured TiO_2 and ferroelectric $Bi_{0.5}Na_{0.5}TiO_3$-supported BiOCl), additional characterization techniques such as Fourier-transform infrared and Raman spectroscopy were used to acquire information about the constituent molecules and chemical bonds. In Raman spectroscopy, the working principle is based on inelastic or Raman scattering of monochromatic electromagnetic radiation by polarizable molecules.[6] An incident photon of energy comparable to the vibrational energy of the molecule can be used to excite it to a higher (vibrational) energy. If the molecule returns to its original level, no net change is observed in the frequency of the scattered photon and the phenomenon is known as elastic scattering. Conversely, if the final molecular vibration is different than the initial a concomitant shift in the frequency of the scattered photon is observed. This is known as inelastic or Raman scattering and can be classified as either Stokes (shift to lower frequency) or anti-Stokes (shift to higher frequency).[6] As each type of molecule has a defined number of vibration modes and unique frequencies, by measuring the shift in frequency with respect to certain wavenumbers the presence of certain molecules or chemical species and be identified. In order for a vibration mode to be Raman active, the first derivative of polarizability with respect to vibration at the equilibrium position should not be zero.[1] In other word, if a particular molecule displays a change in polarizability with respect to certain vibration, then that mode is Raman active. Hence, Raman spectroscopy is especially useful for identification of molecules/vibrational modes which are infrared inactive.

In this study, the samples were analysed using confocal Raman spectroscopy (Renishaw InVia) at 5× magnification in ambient atmosphere. Samples were prepared by transferring a small amount of powdered sample onto a clean glass slide. This was then pressed using another glass slide to immobilize the powder and create a relatively flat surface for measurement. The illumination source was a 532 nm diode laser which was coupled with a diffraction grating of 1800 mm^{-1}.

3.3.4 Fourier-transform infrared (FTIR) spectroscopy

FTIR and Raman spectroscopy were used to provide complementary data about the molecular composition and chemical structure of the prepared photocatalysts. However, there is a fundamental difference between the two techniques. For a vibration mode to be infrared active,

the derivative of dipole moment with respective to the vibration at the equilibrium position should be non-zero.[1,7] In other words, if the dipole distance changes as a consequence of shifting centre of charges, then that particular mode is infrared active. Another difference in Raman and FTIR techniques is the method of data acquisition. In FTIR, the material is simultaneously probed with photons of multiple frequencies. The actual absorption (or transmission) spectrum is obtained by Fourier transformation of the raw data. Since IR absorption occurs at resonant frequencies, the position and intensity of an FTIR peak can be used to identify the nature and relative concentration of a certain species in a material. FTIR data used in this study was provided by Dr. Himmat Singh Kushwaha at IIT Mandi. The spectra were acquired on a K8002AA carry 660 (Agilent) FTIR spectrophotometer.

3.4 Characterization techniques: optical and electronic

In the field of photocatalysis, properties such as the band gap, absorption of the electromagnetic spectrum, and separation and transport of photogenerated charge carriers can be used to analyze and elucidate the photo-activity of the catalyst. Accurate determination of these attributes can be used to correlate or explain any change in the catalytic activity. In this study, the following optical and electronic characterization techniques were employed.

3.4.1 Diffuse reflectance spectroscopy (DRS)

The optical bandgap of the various samples prepared in this study was determined indirectly by using diffuse reflectance spectroscopy. When any material interacts with electromagnetic waves three phenomena, namely transmission (Tr), absorption (Ab), and reflection (Re), are observed. The relationship between the incident energy (I) of the light and can be expressed as:

$$I = Tr + Ab + Re \tag{3.3}$$

Depending upon the wavelength of incident light, bandgap and microstructural environment of the material, it is possible that no transmission takes place ($Tr = 0$). A good example of this condition would be polycrystalline transition-metal compounds under visible light. In such a case, by measuring the reflectivity of the sample with respect to a standard, information such as wavelength-dependent optical absorption and bandgap of the material can be determined. The total reflection from the surface of a material can be differentiated into two-types: (1) specular reflection, in which angle of incidence equals angle of reflection such as reflection encountered on polished surface; and (2) diffuse reflection, in which incident light is scattered randomly.[1] DRS is a quick and easy technique to determine optical absorption spectra of powdered samples. In this study, DRS spectra of the samples were acquired using USB-4000

Ocean Optics Spectrometer equipped with a DRS probe. The setup was calibrated to 100% reflectance under illumination by using $BaSO_4$ as the internal standard (Labsphere) and a tungsten-halide lamp as the illumination source; whereas, the baseline was measured by acquiring the reflectance spectrum in the dark. For data acquisition, the powdered samples were immobilized by compressing between two pre-cleaned glass slides. Acquired data was processed on OceanView software (Ocean Optics), which measured the change in reflectivity of the sample with respect to the internal standard as a function of wavelength. Several spectra were acquired for each sample and the average value was used to minimize the manual measurement error.

3.4.2 Transient photocurrent measurement

In semiconductor analysis, transient photocurrent measurements are used to quantify the magnitude of photogenerated charge carrier extraction in a given volume of sample.[8] When a semiconductor is illuminated with light it results in the production of photogenerated charge carriers. These charge carriers can either recombine to generate heat or migrate to the surface to participate in photocatalytic reactions. If the semiconductor is sandwiched between two conducting electrodes, these charge carriers can be extracted, and based on the principles of photovoltaic effect, a current can be made to flow in the external circuit.[9] In photocatalysis, the intensity of transient photocurrent is a direct measure of the extractable (usable) charge carriers and can also be used to provide useful information about the generation and recombination of charge carriers.[10] Usually, a higher photocurrent density indicates better performance.[8]

In this study, transient photocurrent measurements were performed on an AUT86543 electrochemical workstation (Metrohm Autolab B.V.). To fabricate the working electrode, a homogeneous catalyst ink solution was prepared by dispersing the catalyst (5 mg) in a solution of deionized water (1 mL), isopropyl alcohol (1 mL), and Nafion (20 μL; 5 wt.%). The catalyst ink was ultrasonicated for about 30 min to obtain a homogeneous dispersion. 500 μL of the catalyst ink was drop-cast onto a pre-cleaned indium tin oxide (ITO) glass substrate and allowed to dry under flowing N_2. The dried substrates were directly used as working electrodes. A custom-made LED setup (15 W; λ=420 nm; Phillips India) was used as the light source to provide chopped illumination. The transient photocurrent results used in this study were provided by Dr. Himmat Singh Kushwaha (IIT Mandi) and Mr. Moolchand Sharma (IIT Mandi).

3.4.3 Electrochemical impedance spectroscopy (EIS)

Impedance can be defined as the resistance to the flow of (alternating) current through a circuit. EIS is performed by applying AC voltage to a sample and measuring the current output with respect to different frequencies. This data can be represented using a complex-impedance plane plot and its fitting with respect to an equivalent electrical circuit can be used to observe and quantify various kinetic processes. In photocatalysis, the frequency dependent current or impedance data can be used to calculate the charge-transfer resistance between the semiconductor and the surrounding medium (electrolyte).[10,11] This data can be used to acquire useful information about the separation efficiency and transport characteristics of photogenerated charge carriers. Generally, semiconductor with a lower charge-transfer resistance indicates a better mobility and utilization of charge carriers. In this study, the EIS measurements were performed using a standard three-electrode cell setup on AUT86543. Ag/AgCl (saturated) and platinum wires were used as the reference and counter electrodes, respectively, with aqueous Na_2SO_4 (0.1 M) as the electrolyte. The procedure for fabrication of working electrode is the same as that described in section 3.4.2. The working electrodes had an exposed surface area of 1 cm^2 which was directly exposed to the electrolyte. The EIS measurements and processing of raw data were done by Mr. Moolchand Sharma (IIT Mandi).

3.5 Characterization techniques: other

To acquire information about the surface area and composition of the prepared samples, the following techniques were employed.

3.5.1 Nitrogen adsorption-desorption isotherms

Information about the apparent surface area and pore size distribution of the prepared photocatalyst were acquired through gas sorption isotherms. Nitrogen adsorption-desorption isotherms were acquired by measuring the amount of N_2 gas adsorbed on the surface of the photocatalyst being tested and the subsequent amount that desorbs at a constant temperature. A plot of adsorbed gas volume as a function of relative pressure can be used to calculate the surface area and characterize the porosity of a given material.

In this study, the gas sorption isotherms were acquired using TriFlex sorption equipment (Micromeritics), located at Institute for Manufacturing (IFM) courtesy of Dr. Michael De Volder. A carefully measured amount (~100 mg) of powdered sample was transferred into the sampling tube, which was connected to the instrument. Prior to isotherm measurement, the samples were degassed in-situ at 250 ^oC for 6 h. Raw isotherm data was converted to comma-

separated value format using 3Flex software (Micromeritics). Isotherms are plotted for the molar amount of gas absorbed or desorbed under isothermal conditions as a function of the equilibrium partial pressure. Brunauer–Emmett–Teller (BET) theory was used on the adsorption branch of the isotherm in the partial pressure range of less than 0.4 to calculate the specific surface area. The BET theory is an extension of Langmuir theory for monolayer adsorption and is based on the following assumptions: (1) gas molecules physically adsorb on a solid in layers infinitely; (2) gas molecules only interact with adjacent layers; and (3) the Langmuir theory can be applied to each layer. The resulting BET equation can be expressed as:[12]

$$\frac{1}{v[(p_0/p)-1]} = \frac{c_{BET}-1}{v_m c_{BET}}\left(\frac{p}{p_0}\right) + \frac{1}{v_m c_{BET}} \tag{3.4}$$

In equation (3.4) p_0 and p are the saturation and equilibrium pressure of the adsorbates at a given temperature, v_m and v are the monolayer and total adsorbed volume and, c_{BET} is the BET constant defined as:

$$c_{BET} = e^{\left(\frac{E_1-E_L}{RT}\right)} \tag{3.5}$$

in which E_1 is the heat of adsorption of the first layer, $E_L$is the heat of liquefaction, R is the gas constant and T is the temperature in Kelvin. Thus, data from sorption isotherms can be used to calculate the specific surface area (S_{BET}) using the following expression:

$$S_{BET} = \frac{v_m N}{aV} \tag{3.6}$$

In equation (3.6) a is the mass of the solid sample, V is the molar volume of the adsorbate gas and N is Avogadro's number. Furthermore, the volume pore size distribution was determined using the Barret-Joyner-Halenda (BJH) model, which assumes that critical relative pressure leads to condensation in pores according to the following equation:[13]

$$ln\frac{p}{p_0} = \frac{-2\gamma V\, cos\theta}{RT(r_p - t_c)} \tag{3.7}$$

In equation (3.7), γ corresponds to the surface tension at the liquid-vapour interface and θ is the contact angle between the liquid and pore wall, which is assumed to be zero for N_2. Furthermore, symbols r_p and t_c denote the pore radius and the thickness of the adsorbed layer, respectively. It is important to mention here that the specific surface area of the particles has been calculated in a dry state using gaseous N_2, which has a diameter of about 300 pm. Even though the water molecule is even smaller with an approximate diameter of 275 pm, the terminal hydroxyl groups at the surface of TiO_2 particles can lead to agglomeration depending

on the pH of the aqueous solution.[14] Hence, techniques such as stirring and ultrasonication are needed to achieve a homogeneous dispersion of the individual particles and ensure availability of active sites.

3.5.2 Thermal analysis

Additional information about the composition and important thermal events (such as calcination temperature) of the various photocatalysts prepared in this study were acquired through the following thermal analyses. Differential scanning calorimetry (DSC) is a technique that measures the difference in the amount of energy required to raise the temperature of a sample with respect to a reference, as a function of temperature. This data can be used to identify the temperature required to induce important physical and chemical transitions such as phase change and crystallization. Furthermore, if the mass of the material is known, data provided by DSC can be used to calculate the enthalpy of transformation. Hence, it is considered to be an important tool in the field of materials science. Data from DSC is often complimented by performing thermogravimetric analysis (TGA). TGA is another form of thermal analysis and is used to measure the change in mass of a given material as a function of temperature. This data can be used to acquire important information about various physical attributes such as thermal stability, phase change temperature, oxidation temperature and even some limited information about the material composition such as water and (combustible/volatile) organic content.

In this study, simultaneous DSC and TGA were used to determine the crystallization temperature and weight percentage (wt. %) of water in amorphous (hydrated) and carbon in calcined TiO_2 particles. To perform the thermal analysis, a carefully measured amount of powdered sample (~50 mg) was placed into a clean alumina crucible, which was loaded into a Q600 SDT thermal analysis instrument (TA instruments). The ramp rate for both heating and cooling cycles were fixed at 5 $^{o}C.min^{-1}$ and the holding time at peak temperature was 30 min. At least two runs were performed for each sample to ensure reproducibility.

3.6 Photocatalytic experiments: setup and methods

3.6.1 Illumination sources

The following equipment were used as illumination sources for various photocatalysis experiments.

3.6.1.1 Newport Oriel solar simulator

A Newport Oriel solar simulator (Class A flood exposure source) equipped with an AM 1.5G optical filter was used for generating artificial sunlight for aqueous dye degradation experiments

with TiO_2-C composite particles. The incident power at the surface of the liquid was calibrated at 100 $mW.cm^{-2}$ by using a standard Si solar cell (Fraunhofer-ISE RS-OD4), which is the roughly equal to the average solar intensity received on the surface of the earth.

3.6.1.2 Mercury-vapor lamp

A 125 W mercury-vapor lamp (Phillips, India) was used in conjunction with a long-pass filter (λ>400 nm; UQG Optics) for performing dye degradation experiments under visible light. The distance between the lamp and the surface of the liquid was kept fixed at 15 cm, which provided an equivalent (theoretical) illumination of 4.97×10^4 Lux.

3.6.1.3 OAI solar simulator

An OAI TC-100E solar simulator (TRISOL class AAA) equipped with an AM 1.5G optical filter was employed as a light source for anti-bacterial analysis with TiO_2-C composite particles. Access to this solar simulator, located at IIT Mandi, was provided by courtesy of Dr. Rahul Vaish for the anti-bacterial tests. The incident power at the sample surface was calibrated at 100 $mW.cm^{-2}$ by using a photovoltaic integrated measurement system (OAI Instruments).

3.6.1.4 LOT-Quantum design solar simulator

A LOT-Quantum design LS0816-H (LOT-QD GmBH) large area solar simulator was used for simultaneous photocatalytic hydrogen evolution testing of various nickel-titania composites. The output power at the liquid surface was calibrated to 1 Sun (100 $mW.cm^{-2}$) by using an optical power meter (1916-R, Newport). Access to this instrument for intermittent and continuous exposure experiments was provided by courtesy of Mr. Arjun Vijeta (ReisnerLab) at the department of chemistry, University of Cambridge.

3.6.2 Aqueous dye degradation

Photo-assisted degradation of aqueous dye solutions is one of the oldest and most frequently employed tests for measurement of a catalyst's performance. Generally, stock solutions are prepared by dissolving a known quantity of a certain dye in water, which can be degraded in the presence of a catalyst and proper irradiation. The relative change of concentration can be determined using various methods, of which ultraviolet/visible spectroscopy, either in absorption or transmission mode, is the most popular. The concentration of the stock solution is selected such that it corresponds to the linear working range of the testing spectrophotometer (for absorption analysis). Hence, by calibrating the change in intensity, the relative change in concentration can be measured as a function of irradiation time. This method is not only

straightforward but also enables relative comparison of performance between various materials. Hence, it remains a popular technique among the scientific community.

Photocatalytic degradation of dyes or other dissolved pollutants is often attempted with very dilute aqueous solutions and in the presence of rather large quantities of photocatalyst. Furthermore, (usually) the end product of such a reaction are CO_2 and water. Hence, the reaction itself can be classified as a first order or pseudo-first order, and the rate of degradation is directly proportional to the initial concentration of the pollutant as follows:

$$rate = -\frac{d[C]}{dt} = k[C]^n \tag{3.8}$$

In equation (3.8), k is the rate constant, $[C]$ is the concentration of the reactant, and n is the order of the reaction (=1 for first order reactions). Equation (3.8) can be rearranged as:

$$-\frac{d[C]}{[C]} = kdt \tag{3.9}$$

Integrating equation (3.9) within the limits $t = 0$ to t gives the rate law of the first order reaction as follows:

$$\ln[C] = -kt + \ln[C_0] \tag{3.10}$$

In which, C_0 is the initial concentration whereas C is the concentration after time t. The terms in equation (3.10) can be rearranged to yield the following:

$$-\ln\left(\frac{C}{C_0}\right) = k \times t \tag{3.11}$$

The log form represented in equation (3.11) is widely used to determine the degradation rate of various aqueous pollutants in a photocatalytic reaction. However, it only holds true under the following assumptions: (1) the initial (molar) concentration of the pollutant is sufficiently low, (2) the generated (by)products do not affect the equilibrium point of the reaction, (3) the heterogeneous catalyst is present in large quantities, and (4) there is no significant reduction in the number of active catalytic sites. Equation (3.11) holds true for most dilute aqueous solutions and can be used to calculate the rate constants with sufficient accuracy. However, performance evaluation through dye degradation also has its shortcomings. Coloured dye molecules have been reported to produce a sensitization effect in some photocatalysts, which enables visible light absorption.[15] This can lead to an apparent increase in the degradation rate. Furthermore, dye properties such as light absorption, degradation mechanism, and production of intermediates varies for different catalysts, which can lead to inconsistent results. Finally, decomposition of pure/single dye solutions has limited practical applicability outside laboratory

trials. Therefore, dye degradation is not a standardized benchmark for performance evaluation, but rather an indicator of the catalytic activity. In this study, degradation of aqueous solutions of various dyes were performed to evaluate the performance of various photocatalysts. Furthermore, degradation of two pharmaceutical compounds namely diclofenac and ibuprofen were also tested similarly as these are transparent to the visible light and hence cannot induce any sensitization. Degradation of the dyes and pharmaceutical compounds was confirmed by the change in their absorbance peak in the visible and UV regions respectively. Stock solution of various concentrations were prepared for each compound by dissolving a known quantity in 1 L deionized water under constant stirring and stored in the dark for further use. The concentration of each compound was selected based on relevant data reported in literature, solubility in water, and the absorbance peak produced by the spectrophotometer (linear range). Before each degradation experiment, 50 mL of the stock solution was mixed with a known quantity of powder photocatalyst. The mixture was kept stirred in dark for at least 30 min to achieve absorption-desorption equilibrium. Each experiment was performed until either complete dye degradation was achieved, or five data points could be recorded at equal intervals, to accurately determine the degradation rate constant. After the experiments, all remaining liquids were disposed of in accordance with the department's chemical disposal policy. A schematic of the dye degradation setup employed in this study is provided in Fig 3.1.

Figure 3.1: Schematic of the dye degradation setup.

3.6.3 Ultraviolet/visible (UV/Vis) spectroscopy

UV/Vis absorption spectroscopy is an indispensable characterization tool in analytical chemistry for both quantitative and qualitative measurements. Theoretically, any compound with bonding and non-bonding electrons can absorb photons from both ultraviolet (250-400 nm) and visible (400-750 nm) spectra and be excited to higher anti-bonding orbitals.[16] Hence, by identification of the wavelength corresponding to the maximum absorption and calibrating it with respect to a known solution, the change in concentration of a compound can be easily ascertained. This method for quantitative determination is based on the Beer-Lambert law:[16]

$$A = \log_{10}\left(\frac{I_0}{I}\right) = a_{mol} \times L_{path} \times C \qquad (3.12)$$

In equation (3.12), the symbols A, I_0, and I denote absorbance, intensity of the incident light and intensity of the transmitted light, respectively. Similarly, a_{mol}, L_{path}, and C correspond to molar absorptivity (extinction coefficient), path length through the sample, and concentration of the compound, respectively. The extinction coefficient is a fundamental property of a compound in a given solvent and is usually considered to be a constant at a given temperature and pressure. Therefore, if the path length of the absorbing liquid is fixed, the change in absorbance becomes directly proportional to the change in concentration. This method is used by spectrophotometer to determine the relative change in concentration of any compound.

In this study, UV/Vis absorption spectroscopy was used to determine the change in concentration of aqueous dye and pharmaceutical compounds as a function of time (degradation rate). During the photocatalytic degradation experiments, 1 mL sample aliquots were drawn from the reaction mixture at fixed intervals using a micropipette. The dye mixture was centrifuged at 8000 rpm for 4 min to separate any stray catalyst particles. The supernatant (0.8 mL) was pipetted into a fresh centrifuge tube and the process was repeated. Finally, the clear supernatant (0.5 mL) was pipetted into a clean quartz cuvette providing a path length of 1 cm and analysed using an Agilent/HP 8453 spectrophotometer in the absorbance mode. Stock solution was used to determine the initial absorbance, whereas the concentration at zero min was acquired using the dye solution after establishing absorption-desorption equilibrium in the dark. Similarly, the baseline of the instrument was calibrated using deionized water (solvent). All absorbance data were acquired within the manufacturer-specified linear limits of the instrument.

3.6.4 Hydrogen evolution

Solar water-splitting for production of hydrogen as a renewable fuel is another attractive application for photocatalysis. Details regarding semiconductor-based photocatalytic water splitting have already been discussed in section 2.3.2. In practice, photocatalytic splitting of water for hydrogen production is plagued with several shortcomings such as sluggish kinetics, recombination, and side reactions.[17] Hence, most photocatalysts for hydrogen evolution are tested in the presence sacrificial electron donors. These sacrificial agents provide the necessary electrons to drive the hydrogen evolution reaction, act as hole traps to prevent oxygen evolution and are consumed in the process. In this study, hydrogen evolution was tested using sodium ethylenediaminetetraacetic acid (Na-EDTA) as the sacrificial agent. 3 mL of the freshly prepared aqueous stock solution (0.1 M; pH 4.5) of Na-EDTA was mixed with 5 mg catalyst powder under constant stirring in a borosilicate glass vial. Thereafter, the vials were sealed with a septum and bubbled with an inert gas chromatography (GC) standard (2% CH_4 in N_2) for 30 min in dark. The sample mixtures were placed in a temperature-regulated rack at 25 ^oC and illuminated using a solar simulator (incident energy 100 $mW.cm^{-2}$) through coupled AM 1.5G and long-pass ($\lambda \geq 420$ nm) filters. After the reaction completion, a gas sample (20 µL) was drawn from the headspace of the vials using a gas-tight syringe and analysed using a GC coupled with a thermal conductivity detector. A schematic representation of the hydrogen production setup used in this study is provided in Fig 3.2. Both intermittent (4 h) and continuous illumination experiments (upto 168 h) were performed to assess the rate of hydrogen production and long-term stability of the catalyst.

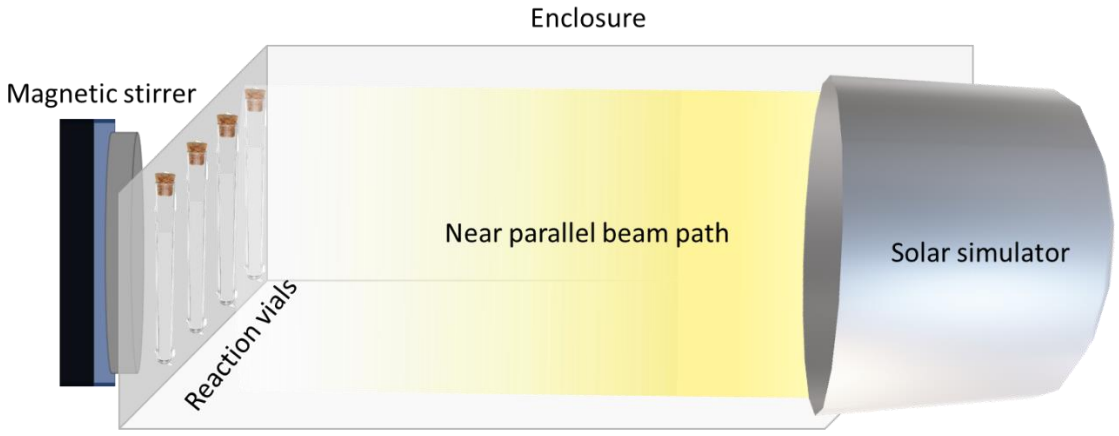

Figure 3.2: Schematic of the hydrogen production setup.

3.6.5 Gas chromatography (GC)

As the name implies, GC is a type of chromatography technique in which the mobile phase is a gas that is either non-reactive (H_2/N_2) or inert (He/Ar) in nature. GC used in conjunction with mass-spectrometry (GC-MS) is considered to be one of the most versatile and powerful characterization techniques in physical sciences for identification of specific compounds. GC in isolation can be used to detect and quantify the presence of even trace amounts of gas or any compound that can be volatilized without decomposition. The mixture of compounds to be tested is injected into a long-tubing known as the column, which houses the stationary phase on a solid-support. The column itself is located inside a thermally-regulated oven for precise temperature control. When a mixture to be identified is made to flow through the column, each individual compound in the mixture is fractionated depending on its interaction with the stationary phase. Hence, individual compounds can be detected based on their retention time. In this study, an Agilent 7890A Series GC was used for quantitative measurement of the hydrogen gas produced during photocatalytic experiments. In all characterizations, N_2 was used as the carrier gas and the oven temperature was fixed at 45 ^oC. The GC itself was setup with a 5 Å molecular sieve in conjunction with a thermal conductivity detector (TCD) column. A TCD consists of a temperature-controlled cell that houses an electrically heated filament. In principle, as the thermal conductivity of all compounds are different, by comparing the increase or decrease in the thermal conductivity of the filament with respect to a reference the presence of a particular compound can be identified. For quantitative measurements, approximately 20 µL sample was drawn from the headspace of the vials using a gastight syringe (Hamilton; GASTIGHT) and the produced hydrogen was determined by comparing the area under the peak for CH_4 (2%) which served as an internal standard.

3.6.6 Bacterial inactivation

The term water disinfection implies removal, inactivation or killing of pathogenic microorganisms present in water to render it fit for human consumption. Photocatalysis has long been investigated and reported for its ability to oxidize dissolved organic impurities. However, photocatalysts have also been explored for their biocidal properties.[18,19] The powerful reactive oxygen species (ROS) produced by TiO_2 and other high bandgap semiconductors can also be employed for inactivation of a host of pathogens that are commonly present in large water bodies.[18] Photocatalysts have also been reported for destruction of cancer cells[20] and treatment oral bacteria present in humans.[21] Hence, photocatalysis is considered to be a potential solar-powered solution for non-centralized water-treatment applications, especially in places which lack proper sanitation infrastructure such as many developing countries.

In order to assess the bactericidal activity of any potential photocatalyst, two bacterial strains namely gram-negative Escherichia coli (E. coli) and gram-positive Lactobacillus acidophilus are used as model pollutants. The rate of inactivation/death of any bacterial culture is dependent on a number of factors such as the individual strain, growth mechanism and the type of agar plate employed. However, there appears to be a common consensus for the mechanism responsible for inducing cell death in microorganisms in the presence of photocatalysts. Bacteria are single cellular organisms and are often classified as the most primitive life-form on earth. The species forms a sub-classification of the prokaryotic microorganisms. Bacteria can be further classified as either gram negative or positive depending on their ability to retain the crystal violet strain used in gram-staining method. The gram-positive bacteria have a thick peptidoglycan layer that retains the crystal-violet dye upon gram staining whereas, gram-negative bacteria have a thinner peptidoglycan layer which does not retain the dye molecules. The gram-negative bacteria also have an outer membrane consisting of polysaccharides in its outer leaflet and phospholipids in its inner leaflet. The article by Maness et al was one of the first to establish that lipid peroxidation might be responsible for cell death.[22] In the presence of sunlight and water, semiconductors such as TiO_2 produce ROS (mainly hydroxyl and superoxide radicals) that attack the outer membrane and cell wall of the bacteria. This initial attack affects the permeability of the cell thereby allowing the ROS to penetrate further into the cell, finally leading to phospholipid peroxidation of cytoplasmic membrane resulting in disruption of cell respiratory functions and ultimately cell death. The process generates malondialdehyde as a by-product, which also serves as an indicator for photocatalytic activity. Alternately, the remaining bacteria can be salvaged and loaded onto an agar plate to measure the colony forming units (CFU).

In this study, gram-negative E. coli (Bacterial Strain JM109, Promega) was used as a representative bacterium to assess the anti-bacterial activity of the prepared photocatalysts. The photocatalytic bacterial inactivation test was performed as follows: 1 mL of bacterial suspension containing 1×10^6 cells.mL^{-1} was diluted with 3 mL phosphate buffer saline (PBS) to obtain the working bacterial suspension. To this bacterial suspension 100 µL of photocatalyst suspension (10 mg.mL^{-1} in PBS) was added. Thereafter, all test-tubes were separately kept under dark and illuminated conditions for a specified period of time (120 min). All test-tubes were shaken at 100 rpm during the experiments to ensure uniform distribution of particles and bacterial cells.[23] Aliquots of 100 µl were drawn at specific time intervals (0, 30, 60, 90, and 120 min) and spread over solidified Luria Broth agar plates after dilution. The colony forming units

per mL (CFU.mL^{-1}) were then calculated for each plate and represented as percentage survival with respect to control sample.

To assess the effect of photocatalysis on morphology and survival of bacterial cells, SEM micrographs were acquired for photocatalyst and control-treated bacterial cells after 60 min. Sample preparation for SEM analysis was performed according to a previously described procedure.[24] The cells were collected with centrifugation followed by fixation using 4% glutaraldehyde and kept at 4 ^{o}C for 6 h. The metabolically fixed cells were serially dehydrated over silicon wafer surface using 20%, 40%, 60%, 70% and 100% (v/v) ethanol followed by acetone. The dehydrated cells were sputter coated with gold and mounted for SEM analysis. All photocatalytic anti-bacterial studies were performed by Mr. Sandeep Kumar at IIT Mandi who also provided the results for these experiments.

3.6.7 Scavenger tests

Photocatalytic oxidation or reduction of dissolved organic species is dependent on several factors such as the dye-catalyst interaction, formation of reaction intermediates and the nature of ROS produced.[15] Equations (2.10) to (2.16) in section 2.1.2 give an overview of the main photocatalytic reduction/oxidation reactions. Even though hydroxyl ions are the most powerful and abundant radical in heterogeneous photocatalysis, other species such as superoxide anion radical (O_2^-), hydrogen peroxide (H_2O_2), holes (h^+), and singlet oxygen ($^1O_2$; spin-paired molecule) may also play an important role in the degradation of a compound.[25] Hence, scavenger tests are employed to quantify the generation and relative contribution of different ROS and to determine the possible degradation pathway. As the name suggests, scavengers are compounds which react with/consume a specific ROS and, thereby, quench the photocatalytic reaction. The incorporation of specific scavenging agents and the degree of reduction of the apparent rate constant is useful to determine the role of individual ROS in the overall degradation. In this study, the following compounds were used as scavenging agents: isopropanol (IPA) and tert-butanol (TBA) for $OH^{\bullet}$; Na-EDTA and sodium oxalate for h^+, and para-benzoquinone (BQ) for O_2^-. The relative concentration of each of the compound to be used were determined from published literature.[26] Concentrated solution of individual scavenging agents were produced by dissolving a known quantity in 100 mL of deionized water. A few drops of the concentrated solution were added to the (50 mL) mixture of powered catalyst and dye solution to achieve the final concentrations of 0.01 M for each compound. Thereafter, the solution was stored in the dark for 30 min to establish absorption-desorption equilibrium before performing the photocatalytic experiment. The reduction in apparent rate constant compared to

standard experiment was used to determine the role of different ROS and a degradation mechanism was proposed.

References:

[1] Yang Leng, *Materials characterization: introduction to microscopic and spectroscopic methods*. (John Wiley & Sons, 2009).

[2] HP Meyers and HP Myers, *Introductory solid state physics*. (CRC press, 1997).

[3] Richard Phillips Feynman, *QED: The strange theory of light and matter*. (Princeton University Press, 2006).

[4] Joseph I Goldstein, Dale E Newbury, Joseph R Michael, Nicholas WM Ritchie, John Henry J Scott, and David C Joy, *Scanning electron microscopy and X-ray microanalysis*. (Springer, 2017).

[5] John F Watts and John Wolstenholme, An Introduction to Surface Analysis by XPS and AES, by John F. Watts, John Wolstenholme, pp. 224. ISBN 0-470-84713-1. Wiley-VCH, May 2003., 224 (2003).

[6] Herman A Szymanski, *Raman spectroscopy: theory and practice*. (Springer Science & Business Media, 2012).

[7] Barbara H. Stuart, *Infrared Spectroscopy: Fundamentals and Applications*. (John Wiley & Sons, Chichester, England, 2005).

[8] Yuan Liu, Changsheng Xie, Jie Li, Tao Zou, and Dawen Zeng, Applied Catalysis A: General **433-434**, 81 (2012).

[9] Christopher R. McNeill, Inchan Hwang, and Neil C. Greenham, Journal of Applied Physics **106** (2), 024507 (2009).

[10] Fangfang Duo, Yawen Wang, Xiaoming Mao, Xiaochao Zhang, Yunfang Wang, and Caimei Fan, Applied Surface Science **340**, 35 (2015).

[11] Ying Wang, Jiaguo Yu, Wei Xiao, and Qin Li, Journal of Materials Chemistry A **2** (11), 3847 (2014).

[12] Stephen Brunauer, P. H. Emmett, and Edward Teller, Journal of the American Chemical Society **60** (2), 309 (1938).

[13] Elliott P. Barrett, Leslie G. Joyner, and Paul P. Halenda, Journal of the American Chemical Society **73** (1), 373 (1951).

[14] Gang Li, Lu Lv, Haitao Fan, Junyan Ma, Yanqiang Li, Yong Wan, and X. S. Zhao, Journal of Colloid and Interface Science **348** (2), 342 (2010).

[15] Ioannis K. Konstantinou and Triantafyllos A. Albanis, Applied Catalysis B: Environmental **49** (1), 1 (2004).

[16] Brian M. Tissue, in *Characterization of Materials* (John Wiley & Sons, 2012), pp. 1.

[17] Dionysios D Dionysiou, Gianluca Li Puma, Jinhua Ye, Jenny Schneider, and Detlef Bahnemann, *Photocatalysis: applications*. (Royal Society of Chemistry, 2016).

[18] Zheng Huang, Pin-Ching Maness, Daniel M. Blake, Edward J. Wolfrum, Sharon L. Smolinski, and William A. Jacoby, Journal of Photochemistry and Photobiology A: Chemistry **130** (2), 163 (2000).

[19] Yongzhang Fan, Rongmei Liu, Wei Du, Qingyi Lu, Huan Pang, and Feng Gao, Journal of Materials Chemistry **22** (25), 12609 (2012); Weiwei He, Hyun-Kyung Kim, Wayne G. Wamer, David Melka, John H. Callahan, and Jun-Jie Yin, Journal of the American Chemical Society **136** (2), 750 (2014).

[20] M. Kalbacova, J. M. Macak, F. Schmidt-Stein, C. T. Mierke, and P. Schmuki, physica status solidi (RRL) – Rapid Research Letters **2** (4), 194 (2008).

[21] Naoki Suketa, Takashi Sawase, Hideki Kitaura, Mariko Naito, Koumei Baba, Koji Nakayama, Ann Wennerberg, and Mitsuru Atsuta, Clinical Implant Dentistry and Related Research **7** (2), 105 (2005).

[22] Pin-Ching Maness, Sharon Smolinski, Daniel M. Blake, Zheng Huang, Edward J. Wolfrum, and William A. Jacoby, Applied and Environmental Microbiology **65** (9), 4094 (1999).
[23] Sandeep Kumar, Himmat S. Kushwaha, Vinay P. Singh, Rahul Vaish, Bouraoui Ilahi, and Niyaz A. Madhar, International Journal of Applied Glass Science **9** (4), 480 (2018).
[24] Qiaoqiao Yin, Linxiang Tan, Qingqing Lang, Xiaoxia Ke, Lijie Bai, Kaiyan Guo, Ru Qiao, and Song Bai, Applied Catalysis B: Environmental **224**, 671 (2018).
[25] Yoshio Nosaka and Atsuko Y. Nosaka, Chemical Reviews **117** (17), 11302 (2017).
[26] Mingcai Yin, Zhaosheng Li, Jiahui Kou, and Zhigang Zou, Environmental Science & Technology **43** (21), 8361 (2009); Guoting Li, K. H. Wong, Xiwang Zhang, Chun Hu, Jimmy C. Yu, R. C. Y. Chan, and P. K. Wong, Chemosphere **76** (9), 1185 (2009).

Chapter 4

Fabrication of TiO_2-C core-shell particles: effect of solvent and precursor

4.1 Introduction

Among heterogeneous semiconductor photocatalysts no other material has been investigated as extensively as TiO_2 (anatase).[1,2] This can be credited to several desirable attributes of TiO_2 such as economy of production, chemical and physical stability, low toxicity, and ease of fabrication.[3] Hence, it is still one of the most widely investigated photocatalytic material to date. However, pure TiO_2 suffers from several drawbacks:[3] (1) TiO_2 being a wide band gap semiconductor (3.2 eV) mainly absorbs in the UV region, which is less than 5% of the total solar energy and (2) suffers from fast recombination of photogenerated charge carriers. These characteristics have already been covered in detail in section 2.4. Other factors which affect the catalytic performance of TiO_2 are its particle size/surface area, crystallinity, and phases present. Significant efforts have been made to mitigate these aforementioned shortcomings and increase the catalytic efficiency of TiO_2.[1] Some of the popular methods include metal and non-metal doping, surface sensitization and coupling with narrow band-gap semiconductors.[1] The merits and demerits of each individual technique have also been provided in section 2.2, but all of which primarily focus on improving visible-light absorption of TiO_2.

From the view of enhancing light absorption, carbon (C) incorporation has been a popular technique.[4-7] Depending on the structure and fabrication strategy either doping or coupling with carbon can be attempted. Doping can result in generation of colour centres and mid-gap states which can improve (visible) light absorption. However, it can also lead to generation of trap sites, which restrict the mobility of charge carriers and also act as recombination centres.[8,9] Alternately, an external combination with nano-structured carbon can impart several benefits including band-gap shifting, enhanced absorption, and reduced trap sites.[4] Hence, various carbon-based structures have been investigated including amorphous C,[10] reduced graphene oxide (r-GO),[11] carbon nanotubes (CNTs)[12,13] and recently graphitic carbon nitride.[7] C-TiO_2 based morphologies reported so-far also include core-shell[5,12] and Janus morphologies.[10] A detailed literature overview of popular C-TiO_2 composites is provided in section 2.4.1. It can be observed that most of these studies employ an external carbon source and entail a two-step process for the final synthesis of these composite catalysts.

In this regard, it would be highly advantageous to develop a technique that not only enables facile synthesis of desired TiO_2-C composite photocatalysts but also allows a high-degree of control over the particle size and morphology. Hence, this chapter deals with the development of a method for in-situ preparation of TiO_2-C composite particles by using titanium alkoxide as a single precursor for both C and TiO_2. Parameters affecting the final particle geometry and chemistry can be placed in two broad categories of precursor (reagent) selection and synthesis technique. To prepare a material with high catalytic activity, optimization of both categories has been attempted. The first part of the study explores the hydrolysis of various titanium alkoxides in different media.

The term alkoxide is used to define the conjugate base of an alcohol, therefore alkoxides are good nucleophiles and generally not stable in protic solvents such as water. In the presence of water, metal alkoxides (MOR) undergo hydrolysis to produce the respective alcohols (ROH), whereas the ligand is precipitated (M_2O). The process can be described with the following equation:

$$2MOR + H_2O \rightarrow M_2O + 2ROH \qquad (4.1)$$

However, alkoxides can be easily dissolved in alcohols, which can be used as a reaction medium to perform controlled hydrolysis of the desired ligand. Hydrolysis of titanium alkoxides to produce TiO_2 is well explored.[14,15] However, the choice of solvent (alcohol) is usually determined by the nature of conjugate base, and often similar alcohols are used. According to the best of our knowledge, there exists no study in literature exploring the effect of different solvents on the hydrolysis of titanium alkoxides and its resultant particles. As the selection of different alcohols can affect the zeta-potential of the resultant solution, it is expected to have a direct bearing on the particle morphology and forms the first topic of investigation.

4.2 Material selection

Given the large number of alkoxides available only three model compounds were selected for in-depth analysis namely titanium IV butoxide, titanium IV isopropoxide and titanium ethoxide. These are the most commonly used precursors for wet-synthesis of TiO_2 nanoparticles. Consequently, 1-butanol, isopropanol and ethanol were used as solvents. For the purpose of simplification, the following reference codes have been adopted to designate the reagents: titanium IV butoxide (T1), titanium IV isopropoxide (T2), titanium ethoxide (T3). Similarly, the alcohols employed as solvents carry the following designation: ethanol (E), isopropanol (I) and butanol (B) unless specified otherwise.

4.3 Photocatalyst synthesis

First, amorphous TiO_2 particles were prepared through controlled hydrolysis of titanium alkoxides, according to a previously reported method.[15] Maret and coworkers initially proposed the method for fabrication of highly monodisperse colloidal TiO_2 particles. The authors suggested that the molar ratio between the titanium alkoxide and water in the final solution should be 1:3 as a minimum. Hence, this ratio was selected as a guideline for the synthesis of 1 gm calcined TiO_2 powder. Briefly, a known quantity of titanium precursor T1 (4.3 mL), T2 (3.7 mL) and T3 (3.11 mL) was added to 15 mL alcohol under inert conditions (glove box) and shaken vigorously for 5 min to achieve a clear solution. To this solution another 50 mL alcohol was added under magnetic stirring in ambient conditions. To ensure a homogeneous solution the stirring was continued for 10 min. Thereafter, water (1.5 mL) was added dropwise to the solution under vigorous stirring. Depending upon the alcohol and precursor used, precipitation started to occur after several seconds or minutes, as indicated by the colour change of the solution. The fastest hydrolysis was observed for T3, whereas T1 took several minutes before precipitation was observed. The stirring was discontinued after 30 minutes and the mixture was allowed to stand for a further 120 min to allow the reaction to complete. The suspended particles were recovered through centrifuging and washed repeatedly with designated solvent to remove any unreacted components. These particles, which were found to be amorphous, were then left to dry overnight in a vacuum furnace at 60 ^oC. As per the combination of alkoxide and alcohol, nine samples were prepared. The complete nomenclature for the samples has been provided in Table 4.1.

Table 4.1: Sample codes used in this work.

Sample code	Precursor	Solvent
T1-E	Titanium (IV) butoxide	Ethanol (C_2H_5OH)
T1-I	$Ti(OCH_2CH_2CH_2CH_3)_4$	Isopropanol [$(CH_3)_2CHOH$]
T1-B		Butanol (C_4H_9OH)
T2-E	Titanium isopropoxide	Ethanol (C_2H_5OH)
T2-I	$Ti[OCH(CH_3)_2]_4$	Isopropanol [$(CH_3)_2CHOH$]
T2-B		Butanol (C_4H_9OH)
T3-E	Titanium (IV) ethoxide	Ethanol (C_2H_5OH)
T3-I	$Ti(OC_2H_5)_4$	Isopropanol [$(CH_3)_2CHOH$]
T3-B		Butanol (C_4H_9OH)

Thereafter, the samples were calcined in a non-oxidizing atmosphere to preserve the residual carbon from the alkoxide precursor. To achieve this, a tube furnace was connected to a

compressed nitrogen gas supply. The amorphous powders were transferred into an alumina boat and placed in the furnace. The furnace was initially flushed with N_2 (100 mL.min^{-1}) for 30 min to ensure complete removal of air. Thereafter, the flow rate was decreased to 5 mL.min^{-1}. The calcination was performed at 500 ^{o}C for three hours and the ramp rate was fixed at 5 ^{o}C.min^{-1} for both heating and cooling steps. The as-prepared powders displayed a range of colour varying from dark grey to sharp black. A control sample (W) was prepared by similar calcination of amorphous T1-I (500 ^{o}C; 3 hr) in air. Fig 4.1 shows a digital (optical) photograph of the as-prepared samples.

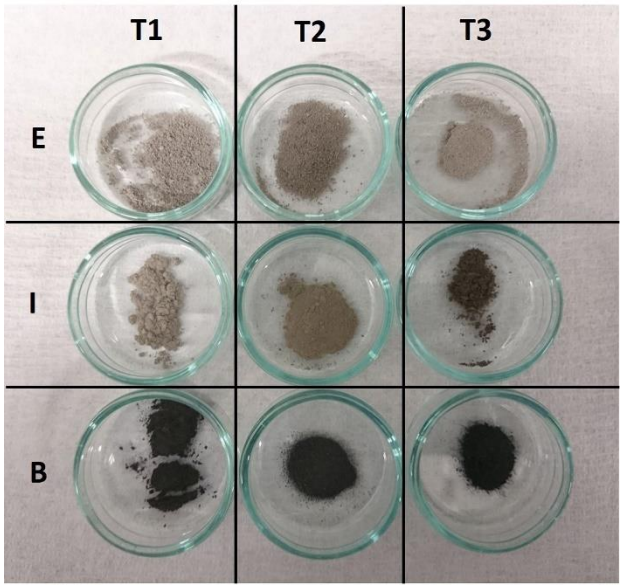

Figure 4.1: Optical photograph demonstrating the colour of calcined samples.

4.4 Characterization

The as-prepared samples were investigated using the following characterization techniques to determine their physical, chemical and optical properties.

4.4.1 Powder X-ray diffraction analysis

Fig 4.2 a, b and c displays the XRD patterns of T1-E, T1-I, and T1-B, respectively. Fig 4.2a utilizes the symbols (A) and (R) to indicate the peaks corresponding to anatase and rutile phase, respectively. The XRD patterns for the remaining six samples have been provided in Fig 4.3. The presence of strong and well-defined peaks indicate the crystalline nature of all samples understudy.

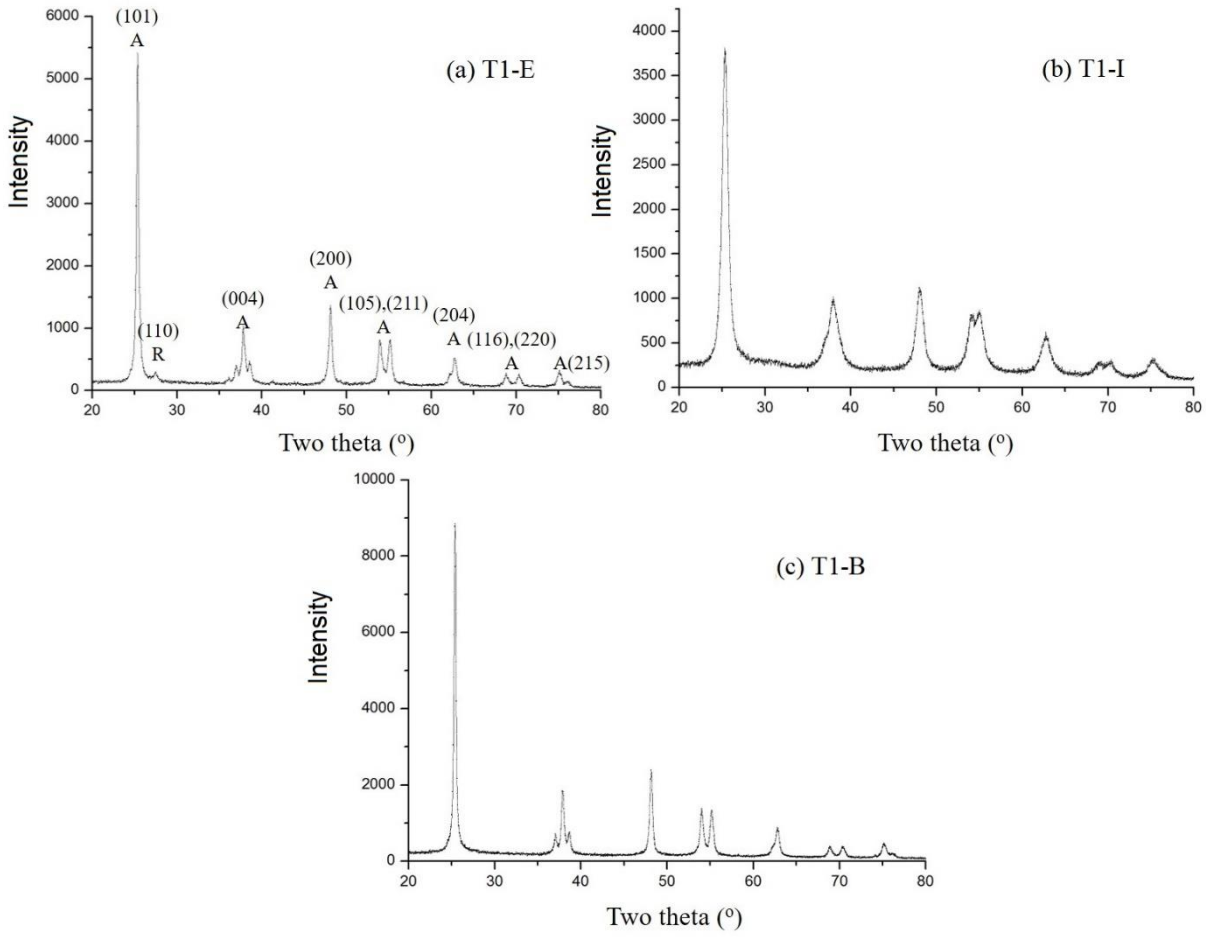

Figure 4.2: Powder XRD patterns for (a) T1-E, (b) T1-I and (c) T1-B (A-anatase; R-rutile).

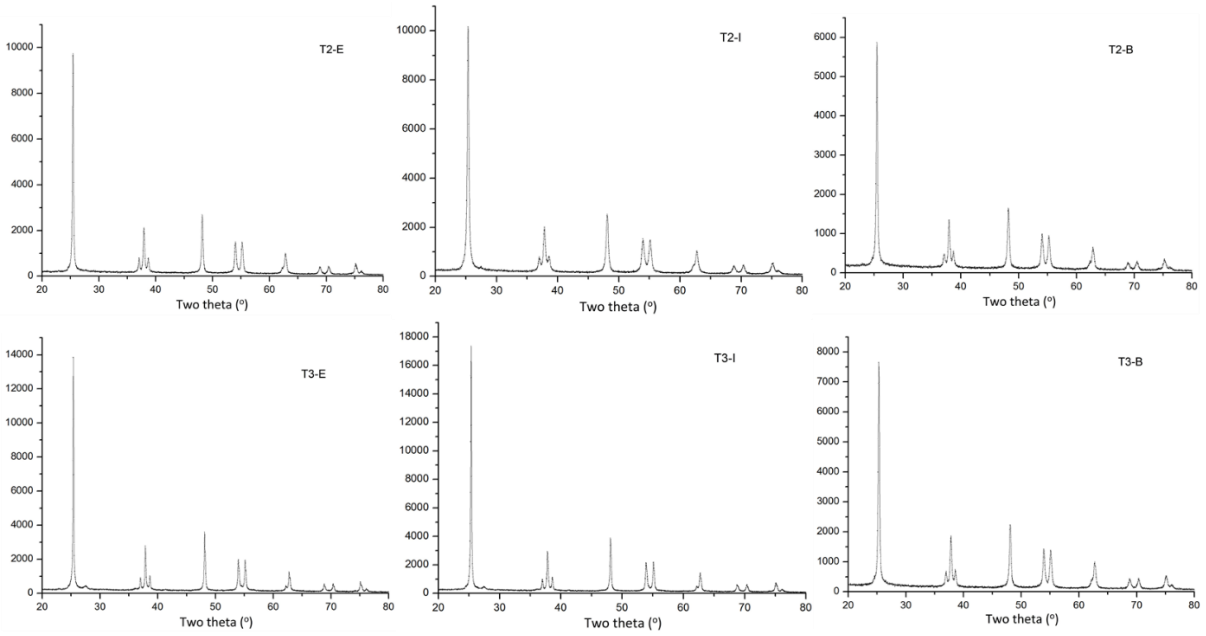

Figure 4.3: Powder XRD patterns for T2-E/I/B and T3-E/I/B

For all samples, major peaks could be indexed to anatase phase (JCPDS file No. 21-1272), whereas a few minor peaks associated with rutile phase (JCPDS file No. 03-0380) were also

observed. The rutile phase was particularly visible in T1-E, T3-E, and T3-I. The formation of a minor amount of rutile phase can be attributed to the relative high calcination temperature (500 ^{o}C) used in this study.[8] However, the presence of C can stabilize anatase even at higher temperature, which explains the low rutile content in the prepared samples.[16] For T1-I, the broadening observed for (101) peak and a high background could originate from its reduced crystallite size. As a preliminary test, Debye-Scherrer equation was employed to calculate the crystallite size of all samples by using (101) peak data. The calculation indicated that T1-I possessed the smallest crystallite size of ~1.59 nm, whereas the biggest size was observed for T3-E (8.15 nm). All calculated crystallite sizes are presented in Table 4.2. However, it is to be noted that the Debye-Scherrer equation is not an accurate method for determination of grain size in nanoparticles. Recently, Vorokh proposed that for particle sizes below 4 nm, the error in Scherrer formula increases non-linearly.[17] Furthermore, since the calculated crystallite sizes are comparable to the absolute error (~0.3 nm), these values are only representative and do not impart any quantitative insight. Another important observation that can be made from the XRD data is the lack of any additional peaks which could explain the colour change of the samples. This indicates that the phase/impurity/doping which is responsible for the colour change in the as-prepared samples is either amorphous in nature or below the detection limits of the instrument. Notably, the presence of interstitial carbon does not generate any additional peaks, especially at lower concentrations. However, it does induce a slight shift (~0.08) in the 101 peak owing to change of lattice parameters.[18] For the present study, no appreciable shift was observed with respect to pristine TiO_2, suggesting the absence of any bulk-doping.

Table 4.2: Experimental matrix summarizing the key quantifiable results.

Sample	**Surface area ($m^2.g^{-1}$)**	**Crystallite size (nm)**	**Rate constant *k* (min^{-1})**	**Surface-area normalized *k* ($min^{-1}.m^{-2}$)**	**Weight loss (%)**
T1-E	4.85	4.02	0.088	0.3629	2.3
T1-I	96.84	1.59	0.101	0.0209	4.0
T1-B	2.33	4.35	0.035	0.3004	0.54
T2-E	4.37	5.83	0.044	0.2014	1.32
T2-I	12.33	3.89	0.055	0.0892	0.76
T2-B	2.25	4.57	0.030	0.2667	0.63
T3-E	4.05	8.16	0.047	0.2321	3.4
T3-I	2.44	8.02	0.022	0.1803	0.5
T3-B	1.33	5.03	0.012	0.1805	0.5

4.4.2 Scanning electron microscopy imaging

Fig 4.4 displays the acquired SEM micrographs for T1-E, T1-I, and T1-B. Representative SEM images for all other samples are provided in Fig 4.5. It can be visualized that T1-E, T2-E, T2-B, T3-E and T3-I exhibit spheroidal geometry with an average agglomerated particle size ranging from 300 to 500 nm.

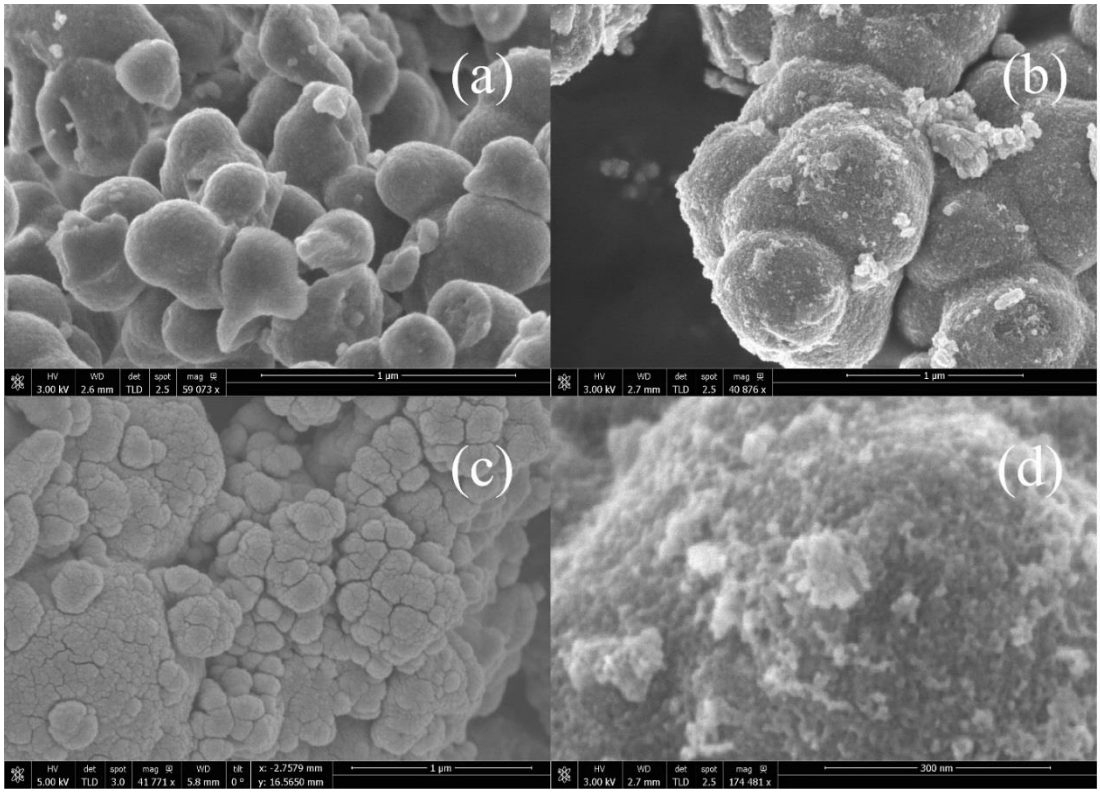

Figure 4.4: SEM images for (a) T1-E, (b) T1-I and (c) T1-B; (d) high magnification image for T1-I.

T1-I displays shapes resembling agglomerated spheres with an average size of ~500 nm. However, upon further magnification, it was observed that these spherical lumps are composed of a network of much finer particles and the surface displays a porous structure, Fig 4.4d. T1-B consists of irregular particles of varying sizes and a clear trend or average particle size could not be determined even under higher magnifications. Furthermore, the lack of observable necking between individual particles suggest that lumps observed in the SEM image of T1-B might be soft agglomerates. T2-I also exhibits a porous structure, as observed for T1-I. However, here the constituent smaller particles are observed to be more densely packed.

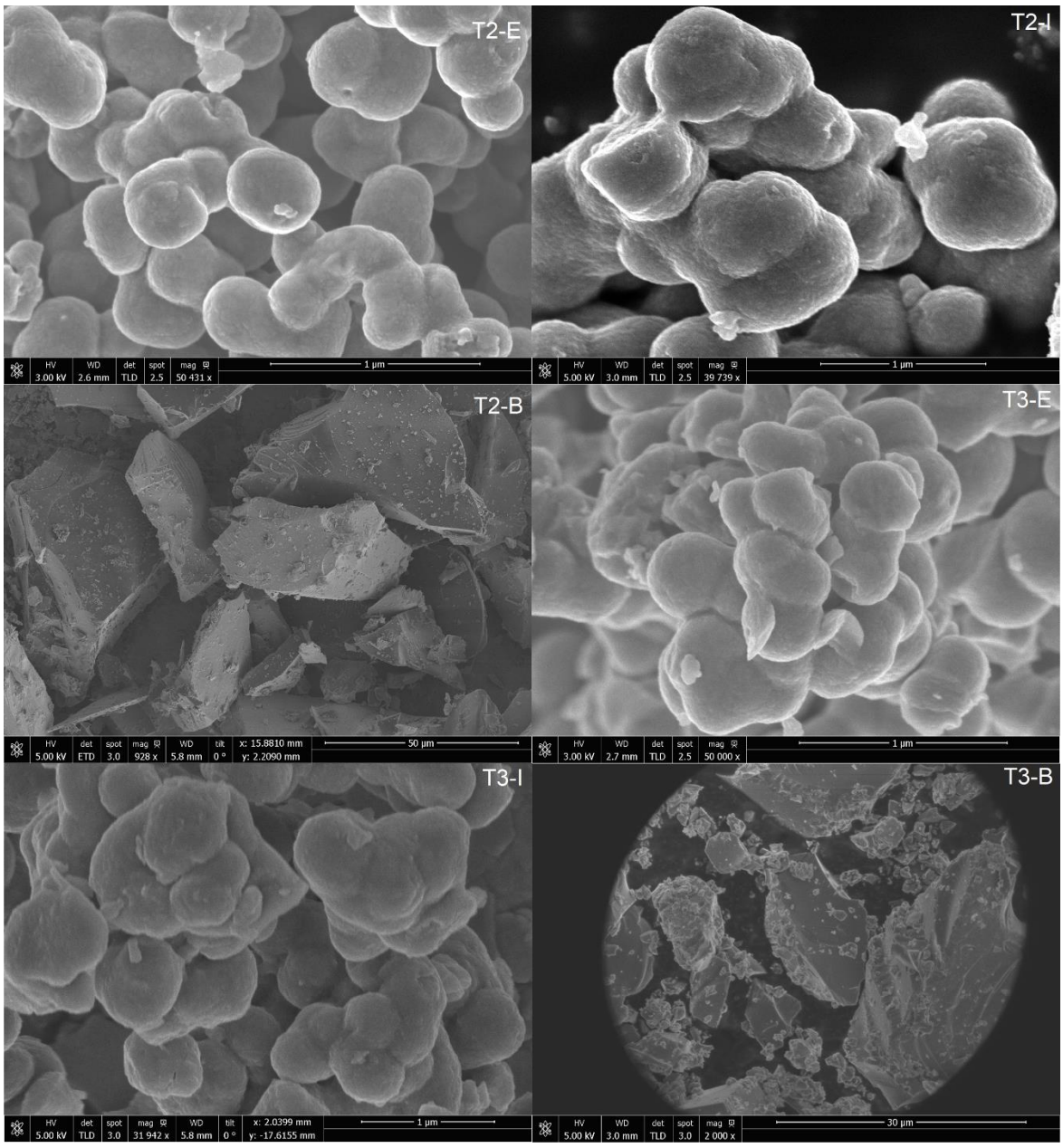

Figure 4.5: SEM images for T2-E/I/B and T3-E/I/B.

T3-B appears to be composed of irregularly shaped particles with sharp edges, whereas the flat part appears to be decorated with smaller particles. However, in case of T3-B, the particle size was found to be extremely large with an average cross-section of >10 µm. These images indicate that different combinations of the participating alkoxide and alcohols can greatly influence the particle size and geometry. Further, energy dispersive X-ray (EDX) spectrum was also acquired for all samples to determine the (elemental) composition. The EDX analysis could not be used to determine the percentage composition of the samples with a high accuracy, as the data shifted with respect to area of imaging. This is an expected feature as EDX analysis is typically used for qualitive measurements and the acquired depends on the interaction volume, which changes with respect to imaging area. Nevertheless, the presence of elemental C on the

surface of the samples could be easily identified, which can be used to explain the colour change of the samples. The representative EDX spectra for 3 samples (T1-B, T2-E and T3-B) is presented in Fig 4.6.

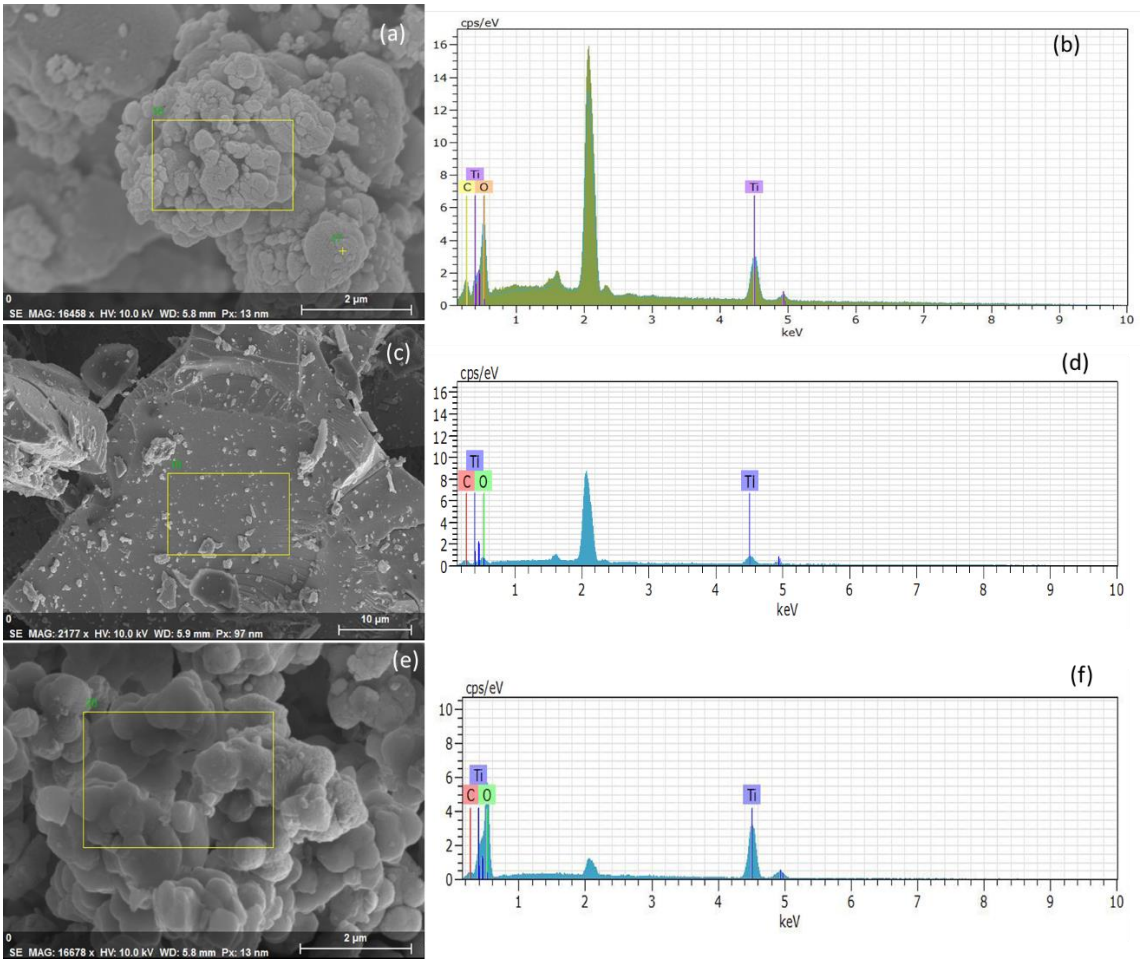

Figure 4.6 SEM image (left) and corresponding EDX spectrum (right) of the highlighted area for (a, b) T1-B, (c, d) T3-B and (e, f) T2-E.

4.4.3 X-ray photoelectron spectroscopy

To acquire an in-depth assessment of the chemical composition and electronic structure of the particle surface XPS was performed. The XPS survey spectrum for T1-E is provided in Fig 4.7a, in which the characteristic peaks for O 1s, Ti 2p, and C 1s could be easily identified. Furthermore, the survey data indicates that the catalyst surface is primarily composed of these three elements (O, Ti and C), which is in good agreement with the EDX results. The high-resolution spectra for these elements are provided in Fig 4.7b to d.

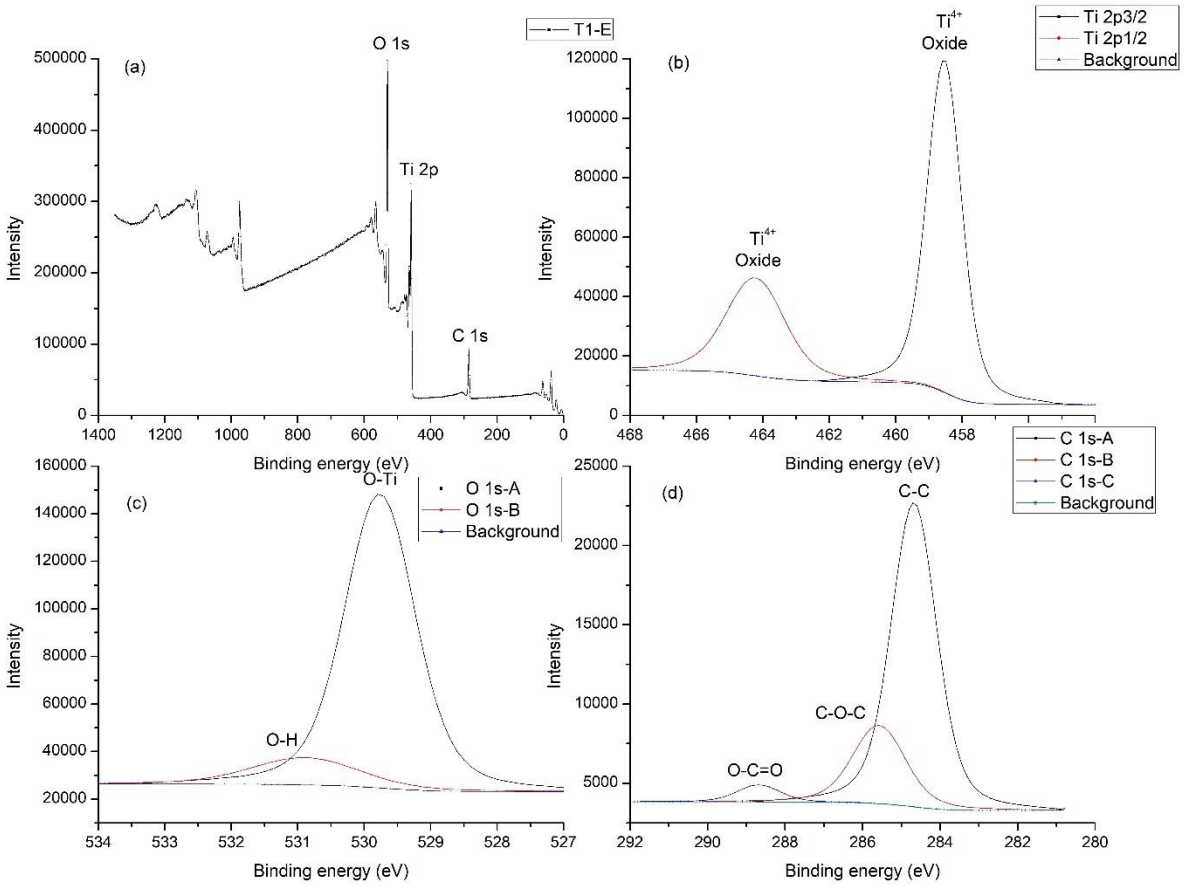

Figure 4.7: (a) XPS survey spectrum, and high-resolution (b) Ti 2p, (c) O 1s and (d) C 1s spectra of T1-E.

Similar peaks were observed for the remaining samples and, therefore, have not been shown. All spectra were acquired after charge compensation with respect to adventitious carbon (C 1s), which is inevitable for samples exposed to atmosphere. Fig 4.7b shows that the acquired Ti 2p spectrum contains two well-defined peaks at binding energies (BEs) of 458.5 and 464.3 eV. Both these peaks correspond to the presence of Ti^{4+} oxide, which is typical for TiO_2. Lack of any additional peaks indicates that the Ti atoms present on the surface are exclusively bonded to oxygen atoms. Similarly, the major peak in the O 1s spectrum is centred around BE of 529.8 eV, which corresponds to the presence of metal oxides. Since Ti was the only metal detected in the survey spectrum, this further corroborates the lack of any additional phases or dopants. However, a small and broad peak centred around ~530.9 eV can also be observed in the O 1s spectrum. This can be attributed to the presence of surface (terminal) hydroxyl groups and is a commonly reported impurity for photoactive TiO_2-based materials.[19] Finally, Fig 4.7d displays the C 1s spectra for T1-E. The largest peak corresponding to BE of 284.8 can be attributed to a few nm thick layer of adventitious carbon. The spectrum could be further convoluted into two additional peaks centred around BEs of 285.6 and 288.7 eV. These peaks correspond to the presence of carbonate phases. The presence of asymmetrical peaks indicate that the present

carbon lacks any long-range order. Analysis of the XPS spectra suggests that the majority of C is present on the surface of the catalyst, possibly bonded to the terminal oxygen groups, and does not contribute to interstitial doping in any significant way. Combined with the SEM imaging and XRD data, it can be suggested that the as-prepared catalysts display a (TiO_2-C) core-shell structure. As the depth of XPS analysis is only limited to a few nanometres, confocal Raman spectroscopy was applied to further confirm this hypothesis.

4.4.4 Raman spectroscopy

The acquired Raman spectra for T1-E/I/B are presented in Fig 4.8. Observations made from the Raman spectra are in good agreement with the results obtained from XRD, SEM, and XPS analysis. All five Raman active modes for anatase phase could be easily indexed including the E_g (147, 198, and 640 cm^{-1}), B_{1g} (398 cm^{-1}) and A_{1g} (515 cm^{-1}) bands. Notably, neither interstitial C nor stoichiometric Ti-C bonds can be identified using Raman spectroscopy. However, Raman spectra can be used to identify and even characterize the presence of free carbon.

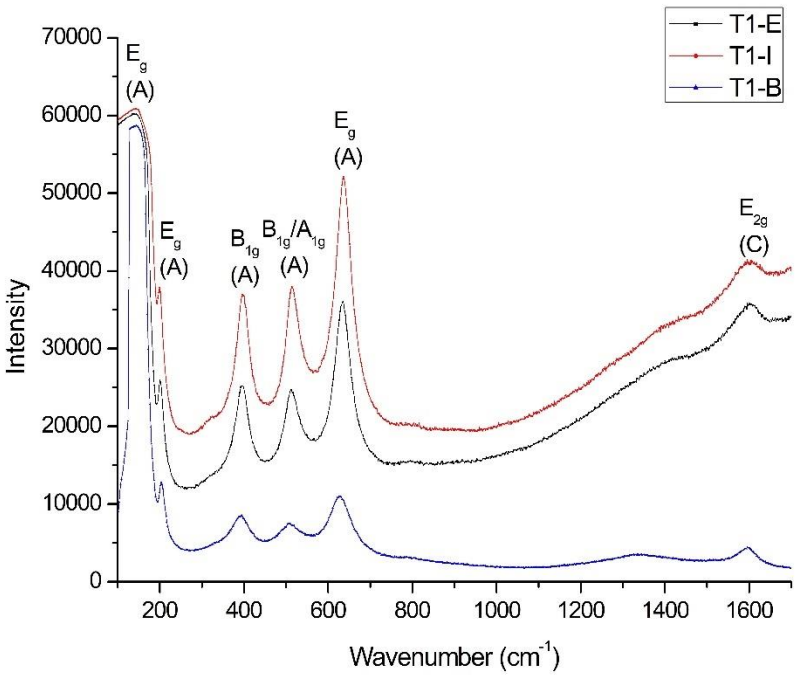

Figure 4.8: Acquired Raman spectra for the T1-E/I/B samples.

A small band is observed at 1590 cm^{-1} corresponding to the in-plane stretching vibration (E_{2g}) of carbon, which confirms the presence of sp^2-hybridized carbon on the surface of the particles. The lack of additional modes corresponding to D and D' bands suggest that the present carbon is amorphous in nature and lacks long-range order. Similar observations were also made in the acquired Raman spectra of the remaining samples (Fig 4.9)a.

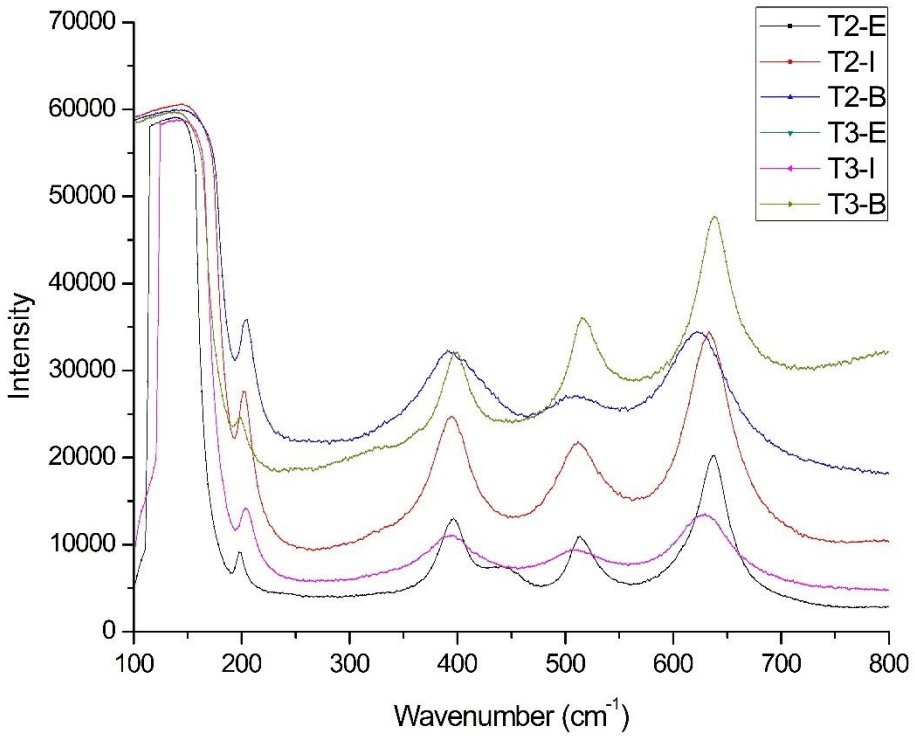

Figure 4.9: Acquired Raman spectra for the T2-E/I/B and T2-E/I/B samples.

4.4.5 Thermogravimetric analysis

All the analysis made until this point clearly indicate the presence of surface carbon. However, quantitative data regarding the amount of C present in the system is still needed. To determine the wt.% of carbon in the composites, all of the samples were analysed using TGA under the assumption that any surface carbon would oxidize in the presence of air upon heating to a sufficiently high temperature. This would result in a net weight loss of the powder which can be used to determine its relative amount. Therefore, all samples were heated in air up to a temperature of 600 ^{o}C and thereafter cooled down to room temperature. Fig 4.10 shows the heat flow and mass change of T1-E as a function of temperature. Similar plots were obtained for the remaining samples and the results are listed in Table 4.2. It was observed that all samples displayed a weight loss between 0.5% to 4%. However, no correlation could be established between the weight change and other parameters such as particle size or surface area. This suggests that the amount of carbon cannot be controlled by altering the morphology of the particles and is unique for each precursor-solvent composition.

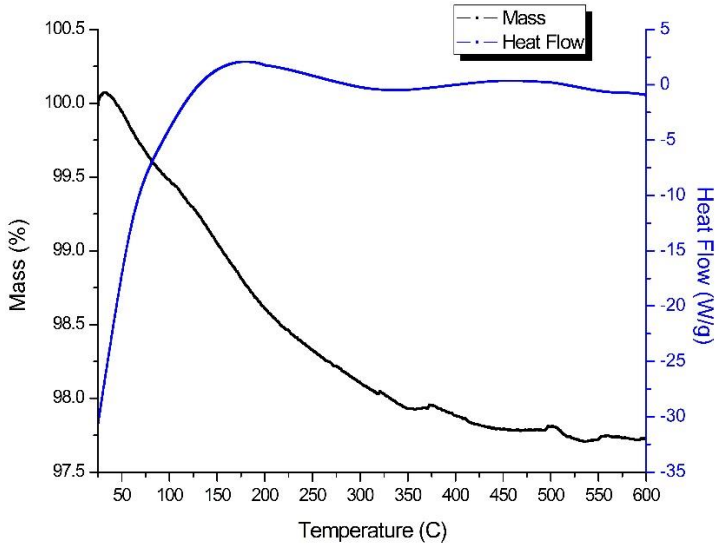

Figure 4.10: TGA graph depicting mass change and heat flow as a function of temperature for T1-E.

4.4.6 Diffuse reflectance spectroscopy

The photocatalytic properties of any material is directly dependent on its light harvesting ability and its effective surface area. Therefore, measurement of both these parameters is important to assess and compare the different catalytic performance. Hence, DRS measurements were performed on all samples understudy to observe their optical characteristics. Fig 4.11 shows the reflectivity of the as-prepared catalysts compared to a standard TiO_2 sample. Owing to the presence of surface carbon, all of the samples displayed a strong absorbance in the visible region. The small bump observed at λ=475 nm and the increased reflectivity at λ<330 nm are an artefact of measurement introduced by the imperfect reflection from the internal calibration standard. Compared to standard (commercial) TiO_2, approximately a 50% drop in reflectivity was observed. Furthermore, the characteristic transition curve for TiO_2 (~390 nm) was visible in all spectra indicating that carbon incorporation has not shifted the band gap of the base semiconductor; even though for some samples a slight red-shift of the transition point was apparent. This could be credited to an enhanced scattering of the photons by the external carbon shell after being reflected from the TiO_2 layer underneath. Alternately, the presence of rutile phase in some samples could also result in a reduced bandgap. In either case, the red-shift is only of the order of ~20 nm, suggesting that the prepared catalyst still possess a band gap of ~3.2 eV, thereby, making them UV active. Compared to pristine TiO_2, the improved absorption in the visible region should help to improve its catalytic performance.

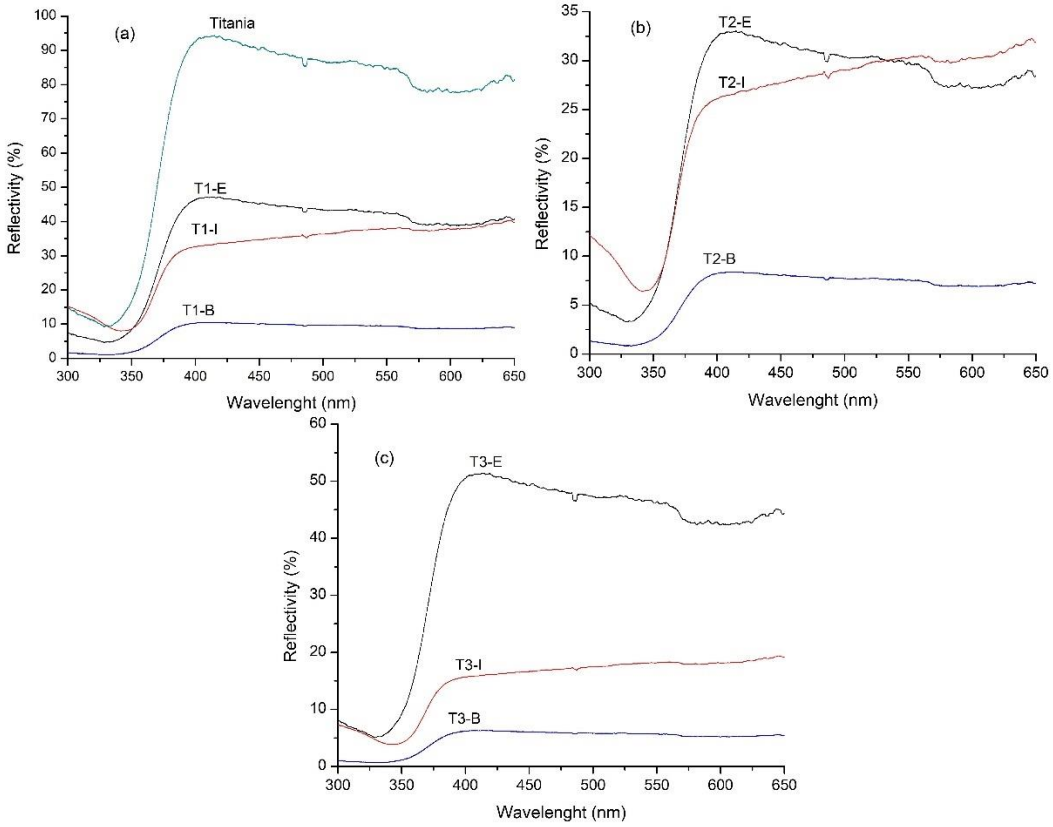

Figure 4.11: Diffuse reflectance spectra for (a) T1-E/I/B, (b) T2-E/I/B and (c) T3-E/I/B.

4.4.7 Nitrogen absorption-desorption isotherms

The DRS measurements were followed by specific surface area measurements through nitrogen absorption-desorption isotherms. Fig 4.12 displays the acquired sorption isotherms for all the samples under study. Except for T1-I and T2-I, all of the samples displayed plots closely resembling a type-II isotherm, indicating indefinite multilayer adsorption and a wide pore-size distribution. Contrarily, both T1-I and T2-I resemble a type-IV isotherm with a weak hysteresis observed between partial pressure values of 0.4 to 0.6. This corresponds to finite multilayer adsorption and indicates a relatively narrow pore-size distribution. The placement and nature of hysteresis suggest that both these samples have some degree of porosity with a large pore size distribution.

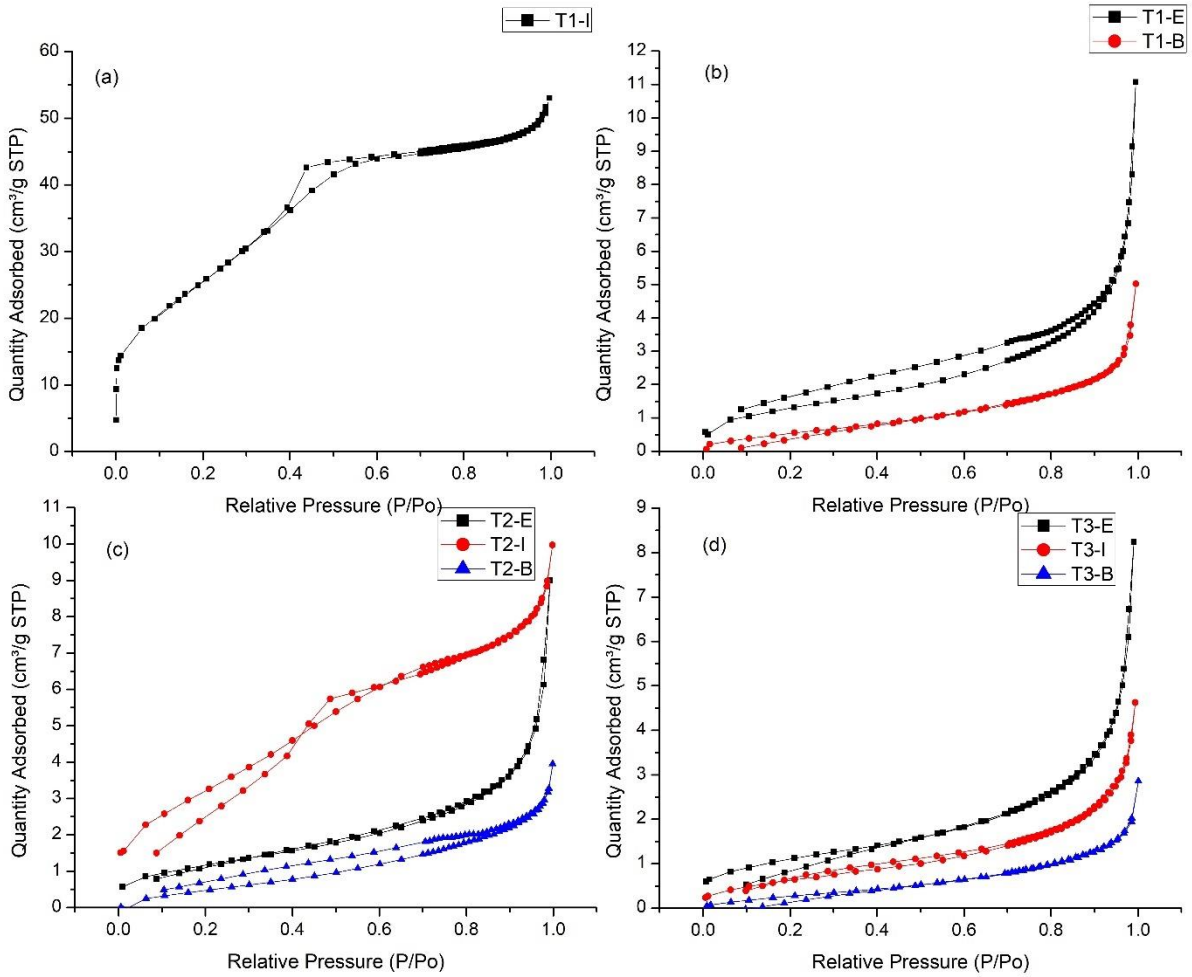

Figure 4.12: Nitrogen absorption-desorption isotherms for (a) T1-I, (b) T1-E/B, (c) T2-E/I/B and (d) T3-E/I/B.

Brunauer–Emmett–Teller (BET) theory was used to calculate the specific surface area and the obtained values are listed in Table 4.2. As expected from the isotherms, T1-I was found to possess an exceptionally high surface area of ~96.8 $m^2.g^{-1}$ compared to other samples. This could be attributed to the highly porous surface of T1-I, as also observed under SEM imaging. This was followed by T2-I displaying a surface area of ~12.3 $m^2.g^{-1}$, which also correlates well with the observation of a porous structure in its SEM image. The rest of the samples displayed a specific surface area ~4 $m^2.g^{-1}$ with T1-E, T2-E and T3-E possessing an effective surface area of 4.9, 4.4, and 4.1 m^2g^{-1}, respectively. The least specific surface area was observed for T3-B (1.3 $m^2.g^{-1}$), which could be attributed to its relatively large particle size.

4.5 Formation of TiO_2-C core-shell particles

Controlled hydrolysis of titanium precursors with the method described in this study yields amorphous hydrated titania particles. TGA analysis reveal that the hydrated amorphous particles are composed of ~20% water by weight and display onset of crystallization upon

heating to ~410 ^{o}C (Fig 4.13). The amorphous samples appear to lose water rapidly with increasing temperature and the weight stabilizes around 350 ^{o}C signalling a complete loss of water. TGA/DSC data indicates that calcination can be performed at ~420 ^{o}C to obtain anatase phase. However, a calcination temperature of 500 ^{o}C was selected in order to ensure complete crystallization of the amorphous precipitates. Calcining the amorphous particles in air resulted in powders with the distinct white colour associated with pristine TiO_2. Repeated washing and drying of precipitates further ensure that the carbon shell of the calcined samples originates from the residual organic precursor (alkoxide). Hence, a methodology can be proposed for the formation of the observed core-shell structure.

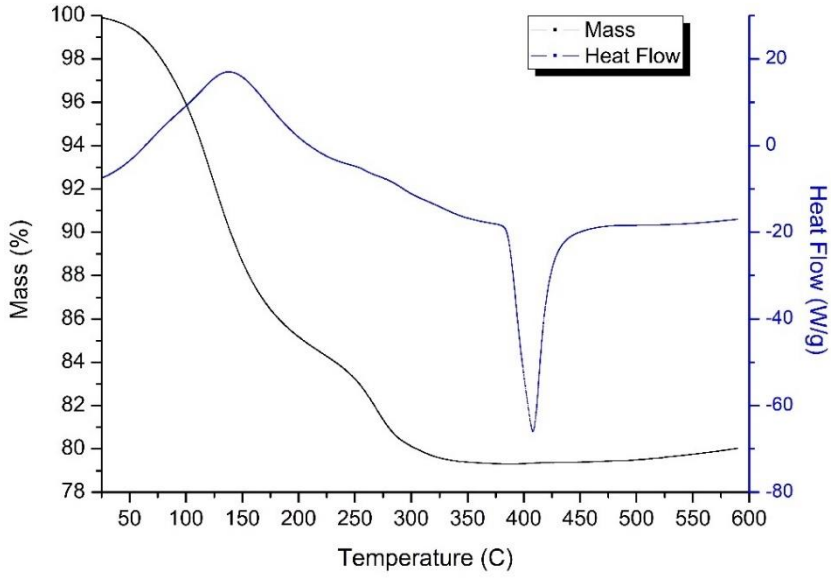

Figure 4.13: Simultaneous DSC and TGA plots for amorphous T1-E.

Calcination of the amorphous powders in an atmosphere devoid of oxygen allows preservation of residual carbon from the incomplete hydrolysis of the titanium alkoxide. Upon reaching crystallization temperature, compaction of the particles starts to occur, and the residual carbon permeates outwards owing to its lower density. Consequently, this residual carbon bonds with the terminal oxygen groups at the surface of individual crystallites and imparts a range of colour to the prepared TiO_2 samples (Fig 4.1). A schematic description of the whole process is provided in Fig 4.14.

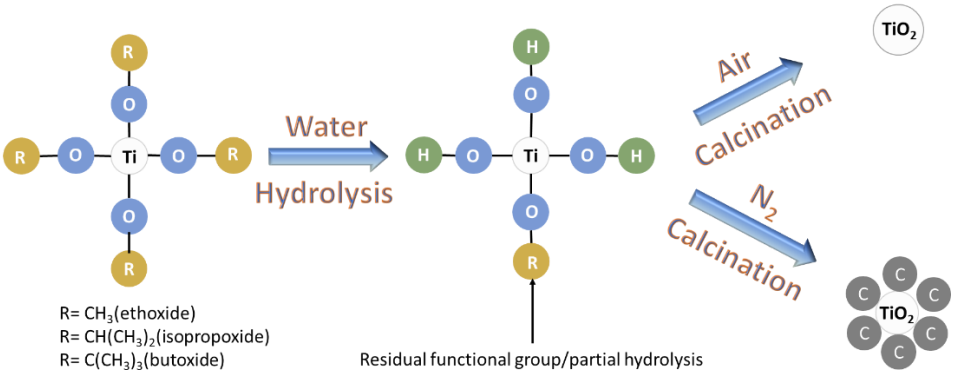

Figure 4.14: Formation mechanism for the TiO_2-C core-shell particles.

4.6 Dye degradation experiments

Finally, to assess the catalytic activity all samples were tested using sunlight-assisted dye degradation experiments. Methylene blue (MB) was selected as the model compound for the experiment with 50 mL of stock solution (10 $mg.L^{-1}$) mixed with 50 mg catalyst. It was observed that for the best catalyst, complete degradation could be achieved in less than 15 min. Hence, each experiment was designed to run for 12 min. Absorbance data was collected at λ=664 nm with respect to the untreated (initial) dye sample. Fig 4.15a and b displays the change in absorbance spectra and the corresponding profile for MB solution over T1-E, both in dark and illuminated conditions, respectively. Fig 4.15b can be used to clearly differentiate the change in absorbance due to absorption-desorption process and the onset of photocatalysis. The time-dependent degradation profiles were plotted for each sample and are provided in Fig 4.15a and b as both linear and logarithmic forms, respectively.

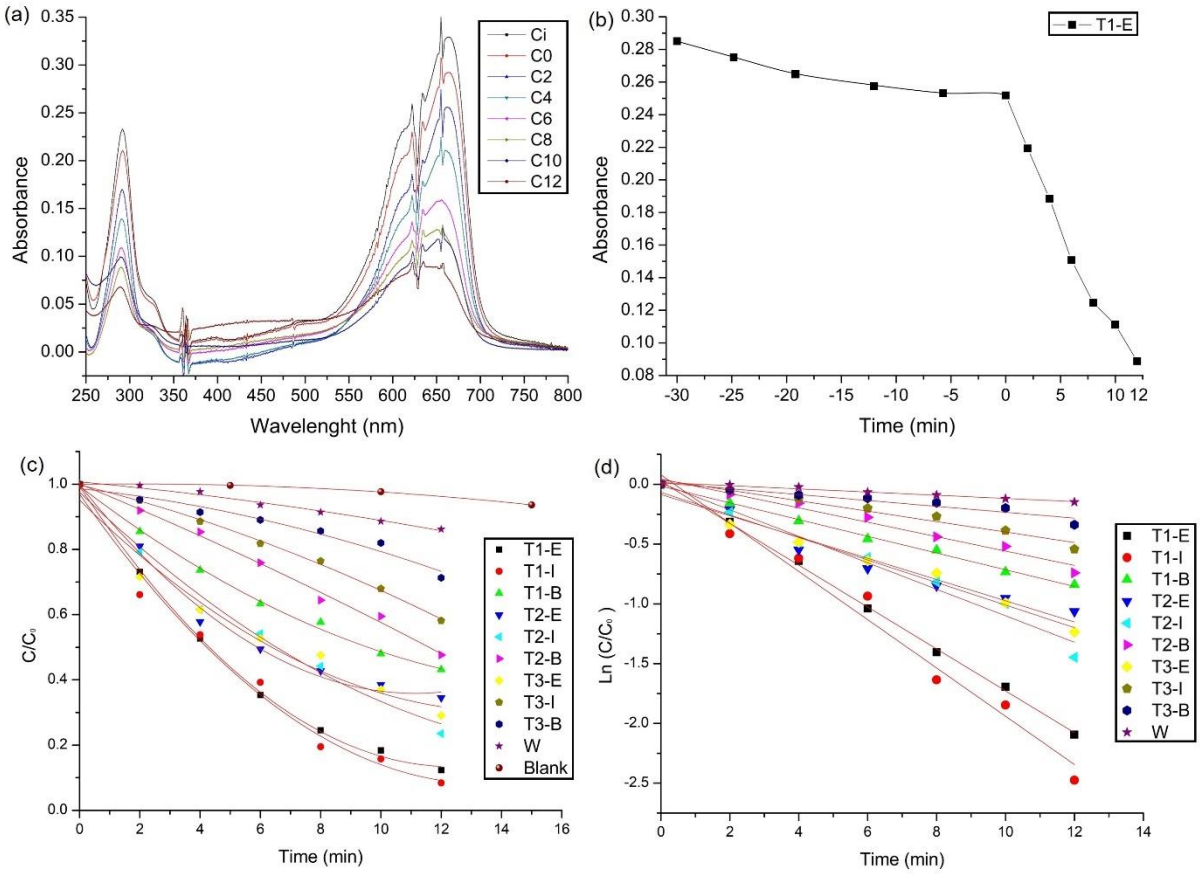

Figure 4.15: (a) Absorbance spectra and (b) corresponding change in absorbance of MB over T1-E. (c) Time-dependent degradation profiles for all samples and control experiments and (d) corresponding natural log plots (line of best fit provided as a guide only).

It can be clearly observed from Fig 4.15 that there is a correlation between the surface area of the prepared catalysts and the corresponding degradation rates. Within the measured time-period, the highest degradation of ~92% was achieved with T1-I, followed closely by T1-E (87%), T2-I (76%), and T3-E (70%), whereas T3-B displayed the lowest degradation of 28%. Control experiments were also performed by monitoring the degradation of dye in dark (with catalyst) and blank (illuminated without catalyst) conditions. Negligible degradation under these control experiments confirmed that mineralization was achieved primarily through photocatalysis. In order to firmly establish the benefit of carbon incorporation, the control sample (W) was further tested for MB degradation under similar conditions, in which no appreciable change in dye concentration was observed. These observations clearly indicate that incorporation of a carbon shell on the surface of TiO_2 particles significantly improves their photocatalytic properties.

The degradation of MB solution closely follows the first order kinetics which can be described by the following expression:

$$-\ln\left(\frac{C}{C_0}\right) = k \times t \qquad (4.1)$$

In which C_0 is initial concentration, C is the concentration at time t and k is the apparent reaction rate constant. Hence, the rate constant can be estimated by measuring the slope of a line having the best fit with the data points. Table 4.2 lists the determined rate constants for all samples understudy. T1-I displayed the highest reaction rate constant of 0.101 min^{-1} followed closely by T1-E (0.087 min^{-1}) and T2-I (0.055 min^{-1}). A direct comparison of the rate constants for T1-I and W (0.012 min^{-1}) indicates that for particles with similar morphology, carbon incorporation improves the photocatalytic activity by 8.35 times. Even with a significantly reduced surface area of sample T2-I, the activity of carbon coated sample is still 4.58 times higher than pristine TiO_2.

4.7 Discussion

Upon arranging the samples according to their measured surface areas an important observation can be made. With the exception of T3-I, all other samples, using isopropanol as a solvent have shown a relatively high surface area post calcination. Conversely, employing butanol as a solvent produces the lowest specific surface area particles. Similarly, among precursors, particles synthesized using titanium butoxide possess a higher surface area followed by isopropoxide and ethoxide. This observation could be credited to two major factors. The first being the relative molecular weight and viscosity of the different titanium organometallic precursors. For a given alcohol, the rate of polycondensation (hydrolysis) of any titanium alkoxide is dependent on the molecular weight and nature of the conjugate base.[20] Hence, increasing the molecular weight and viscosity of alkoxide reduces the rate of hydrolysis. This slower mixing increases the number of nucleation sites giving rise to a higher number of smaller particles. Alternately, a lower molecular weight precursor (ethoxide) tends to hydrolyse more rapidly resulting in fewer nucleation sites. Hence, the latter reaction results in lesser particles with a relatively larger cross-section. Another important factor which could determine the particle formation and growth is the zeta-potential of the initial colloidal solution. It has been previously reported that the particle size of TiO_2 during precipitation can be controlled by carefully varying the zeta-potential.[15] It is quite possible that depending upon the alcohol used, the zeta-potential of the nucleated particles might be significantly different. Further work has been undertaken to analyse and confirm the role of changing zeta-potential on the size and surface area of the calcined particles.

Degradation profile for all samples in this study has a good correlation with their specific surface area. This is to be expected as the photocatalysis is mainly a surface phenomenon and

hence, a larger surface area would equate to faster degradation. However, the degradation profile is not directly proportional to the specific surface area of the respective samples. T1-I has the highest specific surface area of 96 $m^2.g^{-1}$ and achieves ~91% degradation in 12 min. The second-highest degradation rate is observed for T1-E (~87%) despite having a significantly lesser surface area (4.9 $m^2.g^{-1}$) than both T1-I and T2-I (12.3 $m^2.g^{-1}$). In order to explain this phenomenon, SEM images of the samples can be helpful. In each of the above three samples, the average particle size is of the order of 500 nm, indicating that the samples are polycrystalline. In samples T1-I and T2-I, the individual particles are porous in nature. It can be theorized that at the inception of crystallization, the primary crystallites for T1-I and T2-I are relatively smaller. Given their larger surface energy, upon calcination, these primary particles form agglomerates resulting in a porous structure, which explains the large surface area observed in the BET analysis. However, given the black colour and opaque nature of the samples, only the sites directly exposed to irradiation participate in photocatalysis. Therefore, despite having a significantly larger surface area and high porosity, the materials are unable to deliver concomitant degradation rates. A succinct summary of some key findings in this study is tabulated in Table 4.2. Furthermore, Table 4.2 also lists the area-normalized rate constants for all powders understudy. From this new parameter, it can be observed that T1-E has the highest area-normalized *k* of 0.018 $min^{-1}.m^{-2}$ followed closely by T1-B (0.015 $min^{-1}.m^{-2}$) and T2-B (0.013 $min^{-1}.m^{-2}$). The now differing values of *k* indicate that there might other factors such as enhanced surface adsorption, increased trap sites or efficient separation of photogenerated charge carriers, which could determine the overall mechanism for photocatalysis. It also indicates that for the same amount of surface area present, T1-E has the highest rate constant of all the prepared samples. Contrary to the direct rate constant, the surface normalized *k* does not display a correlation with either the surface carbon percentage, crystallite size, or specific surface area. Furthermore, given the small sample size, such a correlation would be unable to provide much insight. Prima facie it appears that the catalyst prepared using titanium butoxide and ethanol produces a higher number of active sites per unit area. One possible explanation is that the molecular mass and nature of conjugate base affects the creation of catalytically active sites during calcination. However, the underlying mechanism for this still remains unclear and would need further investigation. Nevertheless, it is evident that for a given surface area, T1-E is the most active photocatalyst, and this number could be further improved by reducing the primary particle size of the catalyst. This is an important observation and hence, this configuration was selected for a follow-up study dealing with size optimization and in-depth investigation of catalytic performance of these core-shell particles.

4.8 Conclusions

In this chapter, we report a facile method for in-situ preparation TiO_2-C core-shell composites through controlled hydrolysis of titanium alkoxides. To study the effect of preparation conditions on the size and morphology of the resulting particles three different combinations of titanium precursors (ethoxide, isopropoxide, and butoxide) along with three alcohols (ethanol, isopropanol, and butanol) were investigated. The hydrolysed particles were amorphous in nature, contain 20 wt.% water, and exhibit onset of crystallization at ~420 ^oC. Upon calcination in an oxygen-free atmosphere, the residual carbon from organic precursor diffuses outwards to form a shell around the titania particles. XRD, XPS, SEM and Raman analysis of the samples indicate that the Ti atoms are exclusively bonded to O atoms, the samples do not display any evidence for bulk doping, and carbon is present as a thin coating on individual TiO_2 crystallites. SEM images revealed that depending upon the combination of alkoxide and solvent, different particle geometries and sizes, ranging from 300 nm to 50 µm, can be prepared. BET and XRD analysis indicate that for a given alcohol, samples prepared using titanium butoxide possessed the largest surface-area and smallest crystallite size.

The largest surface area of 96.8 $m^2.g^{-1}$ was reported for sample designated as T1-I with a correspondingly high *k* of 0.101 min^{-1} for sunlight-assisted mineralization of MB dye. However, the highest activity per unit surface area was recorded for T1-E sample with an effective *k* of 0.018 $min^{-1}.m^{-2}$. Compared to a controlled sample calcined in air, the photocatalytic activity was improved by eight times through carbon incorporation. DRS analysis reveals that carbon-containing samples are 60% to 90% less reflective than commercial titania in the visible spectrum. However, a significant change in bandgap was not observed, suggesting that the material can efficiently utilize both UV and visible light. Results indicate that the as-prepared TiO_2-C composites possess a core-shell structure and can be employed for efficient solar photocatalysis. Further improvement of catalytic performance could be obtained by reducing the particle size, which has been dealt with in chapter 5. However, it is important to note that further research is required to understand the role of solvent-alkoxide combination on the nature and placement of residual carbon such that further optimization can be attempted.

4.9 Acknowledgements

Some of the SEM images used in the study were acquired by Sundararajan Thirumalai, the rest were acquired with the support of Mr. Simon Griggs, both at MSM.

References:

[1] Rimeh Daghrir, Patrick Drogui, and Didier Robert, Industrial & Engineering Chemistry Research **52** (10), 3581 (2013).

[2] S Girish Kumar and L Gomathi Devi, The Journal of physical chemistry A **115** (46), 13211 (2011); Meng Ni, Michael KH Leung, Dennis YC Leung, and K Sumathy, Renewable and Sustainable Energy Reviews **11** (3), 401 (2007); Ioannis K Konstantinou and Triantafyllos A Albanis, Applied Catalysis B: Environmental **49** (1), 1 (2004); Li Liang, Kaining Li, Kangle Lv, Wingkei Ho, and Youyu Duan, Chinese Journal of Catalysis **38** (12), 2085 (2017); Ruiwen Yang, Jinghua Cai, Kangle Lv, Xiaofeng Wu, Wenguang Wang, Zhihua Xu, Mei Li, Qin Li, and Weiqing Xu, Applied Catalysis B: Environmental **210**, 184 (2017).

[3] Kazuya Nakata and Akira Fujishima, Journal of Photochemistry and Photobiology C: Photochemistry Reviews **13** (3), 169 (2012); Kazuhito Hashimoto, Hiroshi Irie, and Akira Fujishima, Japanese journal of applied physics **44** (12R), 8269 (2005).

[4] Anupama Surenjan, Balaji Sambandam, Thalappil Pradeep, and Ligy Philip, Journal of Environmental Chemical Engineering **5** (1), 757 (2017).

[5] Guozhi Zhang, Feng Teng, Changhui Zhao, Lulu Chen, Peng Zhang, Youqing Wang, Chengshi Gong, Zhenxing Zhang, and Erqing Xie, Applied Surface Science **311**, 384 (2014).

[6] Ruili Liu, Yingjie Ren, Yifeng Shi, Fan Zhang, Lijuan Zhang, Bo Tu, and Dongyuan Zhao, Chemistry of Materials **20** (3), 1140 (2007).

[7] Zhao Lu, Lei Zeng, Wulin Song, Ziyu Qin, Dawen Zeng, and Changsheng Xie, Applied Catalysis B: Environmental **202**, 489 (2017).

[8] Qi Xiao and Linli Ouyang, Chemical Engineering Journal **148** (2), 248 (2009).

[9] Yiseul Park, Wooyul Kim, Hyunwoong Park, Takashi Tachikawa, Tetsuro Majima, and Wonyong Choi, Applied Catalysis B: Environmental **91** (1), 355 (2009).

[10] Beatriz Jurado-Sánchez, Sirilak Sattayasamitsathit, Wei Gao, Luis Santos, Yuri Fedorak, Virendra V Singh, Jahir Orozco, Michael Galarnyk, and Joseph Wang, Small **11** (4), 499 (2015).

[11] Ping Wang, Jin Wang, Xuefei Wang, Huogen Yu, Jiaguo Yu, Ming Lei, and Yonggang Wang, Applied Catalysis B: Environmental **132**, 452 (2013); Ganganagappa Nagaraju, Gunter Ebeling, Renato V Goncalves, Sergio R Teixeira, Daniel E Weibel, and Jairton Dupont, Journal of Molecular Catalysis A: Chemical **378**, 213 (2013).

[12] Kan Zhang, Feng Jun Zhang, Ming Liang Chen, and Won Chun Oh, Ultrasonics sonochemistry **18** (3), 765 (2011).

[13] K Byrappa, AS Dayananda, CP Sajan, B Basavalingu, MB Shayan, K Soga, and M Yoshimura, Journal of Materials Science **43** (7), 2348 (2008).

[14] Gerko Oskam, Abhinav Nellore, R. Lee Penn, and Peter C. Searson, The Journal of Physical Chemistry B **107** (8), 1734 (2003); Mou Pal, J. García Serrano, P. Santiago, and U. Pal, The Journal of Physical Chemistry C **111** (1), 96 (2007).

[15] S Eiden-Assmann, J Widoniak, and G Maret, Chemistry of Materials **16** (1), 6 (2004).

[16] Lixia Yang, Shenglian Luo, Shaohuan Liu, and Qingyun Cai, The Journal of Physical Chemistry C **112** (24), 8939 (2008).

[17] AS Vorokh, Nanosystems: Physics, Chemistry, Mathematics **9** (3), 364 (2018).

[18] AT Rajamanickam, P Thirunavukkarasu, and K Dhanakodi, Journal of Materials Science: Materials in Electronics **26** (6), 4038 (2015).

[19] Hongwei Bai, Zhaoyang Liu, and Darren Delai Sun, Journal of Materials Chemistry **22** (36), 18801 (2012); Eunyoung Bae and Teruhisa Ohno, Applied Catalysis B: Environmental **91** (3), 634 (2009).

[20] Bulent E Yoldas, Journal of Materials Science **21** (3), 1087 (1986).

Chapter 5

Optimized TiO_2-C core-shell nanocomposites for solar water treatment

5.1 Introduction

Results obtained in chapter 4 have already demonstrated that TiO_2-C core-shell structure can be successfully prepared without the need for multi-step fabrication techniques or an external C source. Furthermore, it was also observed that C-modification can lead to a significant improvement in the photocatalytic activity of TiO_2. The sample prepared by using titanium (IV) butoxide with isopropanol as the solvent displayed a high activity for degradation of methylene blue dye. This ameliorated performance could be attributed to its outstanding surface area (96.8 $m^2.g^{-1}$), which was more than an order of magnitude higher than catalysts synthesized from other combinations (listed in Table 4.2). However, the sample prepared using titanium (IV) butoxide and ethanol delivered the best performance per unit surface area.

Notably, the average particle size of all samples reported in chapter 4 was in the range of 0.5 to >5 µm. It has already been discussed that for a wide bandgap semiconductor such as TiO_2, the majority of the photon absorption and charge generation occurs near the surface (equations 2.17 and 2.18). Therefore, the larger particle size of the prepared TiO_2-C samples is actually a major limiting factor that needs to be addressed. This is further confirmed by the fact that the as-prepared TiO_2-C composites did not display a change in the bandgap suggesting effective UV utilization. Hence, reducing the particle size and increasing the specific surface area of the catalyst is expected to significantly improve its performance. Furthermore, in-depth characterization of the core-shell composites is required to explain the underlying mechanism for improved photo-response. Finally, it is important to test the efficacy of a practical photocatalyst for a broad spectrum of water-borne pollutants including pharmaceuticals and pathogens.

In this regard, this chapter reports the optimized synthesis parameters for producing highly photoactive TiO_2-C core-shell nanocomposites. In-depth characterization of the optimized catalyst has been performed to highlight and explain the underlying mechanism for the improved photo-response. Finally, the as-prepared nanocomposites were tested for remediation of a variety of common water pollutants including gram-negative Escherichia coli (E. coli) bacteria. A comparative analysis of the results reported in this study with those reported in the literature is also provided.

5.2 Material selection

Table 4.2 provides the key quantifiable results of the dye degradation tests performed in chapter 4. From the table, it can be easily visualized that sample designated as T1-E provides the highest degradation rate constant normalized with respect to surface area. As T1-E was fabricated by controlled hydrolysis of titanium (IV) butoxide in ethanol, the same combination was selected.

5.3 Photocatalyst synthesis

The fabrication method reported in chapter 4 (section 4.3) was slightly modified to prepare TiO_2-C core-shell nanocomposites. The synthesis procedure is the same as described in section 4.3, except that precipitation was performed in the presence of aqueous KCl (1.5 mL; 0.5, 0.2 and 0.1 M). Barringer and Bowen first reported the synthesis of monodisperse TiO_2 particles by hydrolysis of titanium alkoxides in alcoholic solutions.[1] The authors reported that highly monodisperse particles could be obtained if the molar ratio of alkoxide to water in the final solution was ≥3. It was also observed that the alkoxide itself has a direct bearing on the average size and morphology of the particles. This study forms the basis for all hydrolysis analysis reported thereafter. However, the authors noted that only a slight reduction in particle size can be obtained even if the concentration of water used for hydrolysis is increased considerably. Hence, the study did not report on the possibility of size control of particles. Furthermore, in our study it was observed that increasing the water of hydration led to complete hydrolysis and did not result in the traditional C-coated structures. In the same direction, Maret and coworkers discovered that inclusion of surfactants and ionic salts in low concentrations can be a useful tool to control the zeta potential of ethanoic solution, which in turn can be used to control the size of the primary precipitates.[2] Addition of alkali salts to the precursor solution has a two-fold effect: 1) primarily it increases the zeta potential which prevents Brownian aggregation and, therefore, formation of larger particles; 2) with increasing salt concentration, more cations bind to the water in the hydration shell thereby restricting or even preventing hydrolysis. Further tests confirmed that no residual cation or anionic elements/compounds were observed in the calcined particles. Hence, given the ease of application and the greater degree of control, precipitation of nanoparticles was performed with dilute KCl solutions.

It was observed that the reaction mixture containing 0.5 M KCl did not produce any precipitation even after extended time periods. The solution was allowed to stand for several days, which resulted in the formation of a pale yellow-coloured transparent gel. However, no direct precipitation was observed. Upon using 0.2 M KCl solution, a white turbid solution was

obtained indicating hydrolysis. However, the resulting particles could not be separated from the solution even after centrifuging for >20 min (at 4500 rpm) suggesting that the particles are colloidal in nature. Finally, experiment performed with 0.1 M KCl produced particles which could be recovered by centrifuging at 4500 rpm for 10 min resulting in a clear supernatant. In this last experiment, the effective concentration of KCl in the final solution was calculated to be approximately 2.1 mM. The precipitates were washed several times with ethanol to remove any trace reactants and salts and dried overnight at 60 ^{o}C in a vacuum oven. A measured quantity of the powder was spread evenly in an alumina boat and calcined at 450 ^{o}C for 3 h under Ar flow (5 mL.min^{-1}) in a tube furnace with a ramp rate of 5 ^{o}C.min^{-1}. As opposed to previous synthesis conditions (500 ^{o}C, N_2) a lower temperature and Ar gas were selected based on results acquired from TGA analysis of amorphous powders (Fig 4.14). These conditions were adopted to avoid any high-temperature induced sintering/cluster formation and thereby preserve the nanostructure of the primary precipitates. Prior to calcination, the sample in the furnace was purged with Ar for 30 min (100 mL.min^{-1}) to ensure a completely oxygen-free environment. The as-prepared catalyst was dark-grey in colour and is designated as TC. The control sample was prepared in a similar manner by calcination in air and is designated as TA.

5.4 Characterization

5.4.1 Powder X-ray diffraction analysis

Powder XRD patterns for both the primary catalyst (TC) and the control sample (TA) are presented in Fig 5.1. The strong diffraction lines and well-defined peaks indicate a high-degree of crystallinity in both the samples. However, the presence of peak broadening indicates a smaller crystallite size compared to catalysts prepared by salt-free precipitation (Fig 4.2). All the peaks for TC could be clearly indexed to anatase phase (JCPDS card No. 21-1272) indicating phase purity of the sample. However, for TA a small peak corresponding to the orthorhombic brookite phase (121) could also be observed (JCPDS card No. 39-1360). It has been previously reported by Zhang and Banfield that during calcination of amorphous (hydrated) titania nanoparticles, the thermodynamics of anatase to rutile transformation is highly dependent on the crystallite size of the precursor.[3] Anatase is the most stable phase for crystallite size below 11 nm, whereas brookite phase can be obtained if the crystallite size is between 11 to 35 nm.

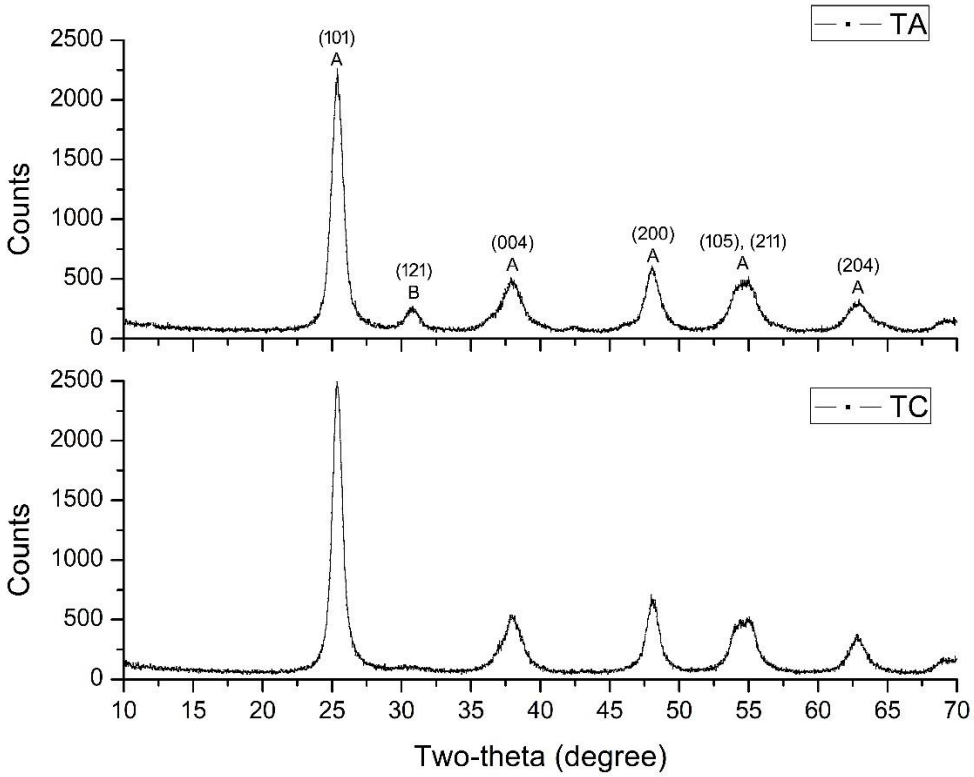

Figure 5.1: Powder X-ray diffraction patterns for the calcined TA and TC samples.

Since in this study the size of the primary precipitates for both TC and TA are same, it is likely that calcination in air has favoured the formation of unstable brookite phase in the control sample (TA). As a preliminary test, the crystallite size of the two samples was calculated by using the Scherrer equation for (101) XRD peak data, which was fitted using Gaussian function in Origin software. The average crystallite size for both the samples was calculated to be approximately 1.79 nm. However, as the calculated value is similar for both samples and comparable to the absolute error (~0.3 nm) it cannot be considered as a reliable indicator of crystallite size.[4] Notably, no peaks corresponding to TiC or other polymorphs of carbon could be observed within the detection limits of the instrument. This can be attributed to the absence of bulk doping and the low concentration of carbon in the samples, which is in good agreement with our previous observations.

5.4.2 Scanning and transmission electron microscopy imaging

SEM imaging was used to study the morphology and average particle size of the prepared catalysts. Fig 5.2 shows the SEM images for both samples at various magnifications.

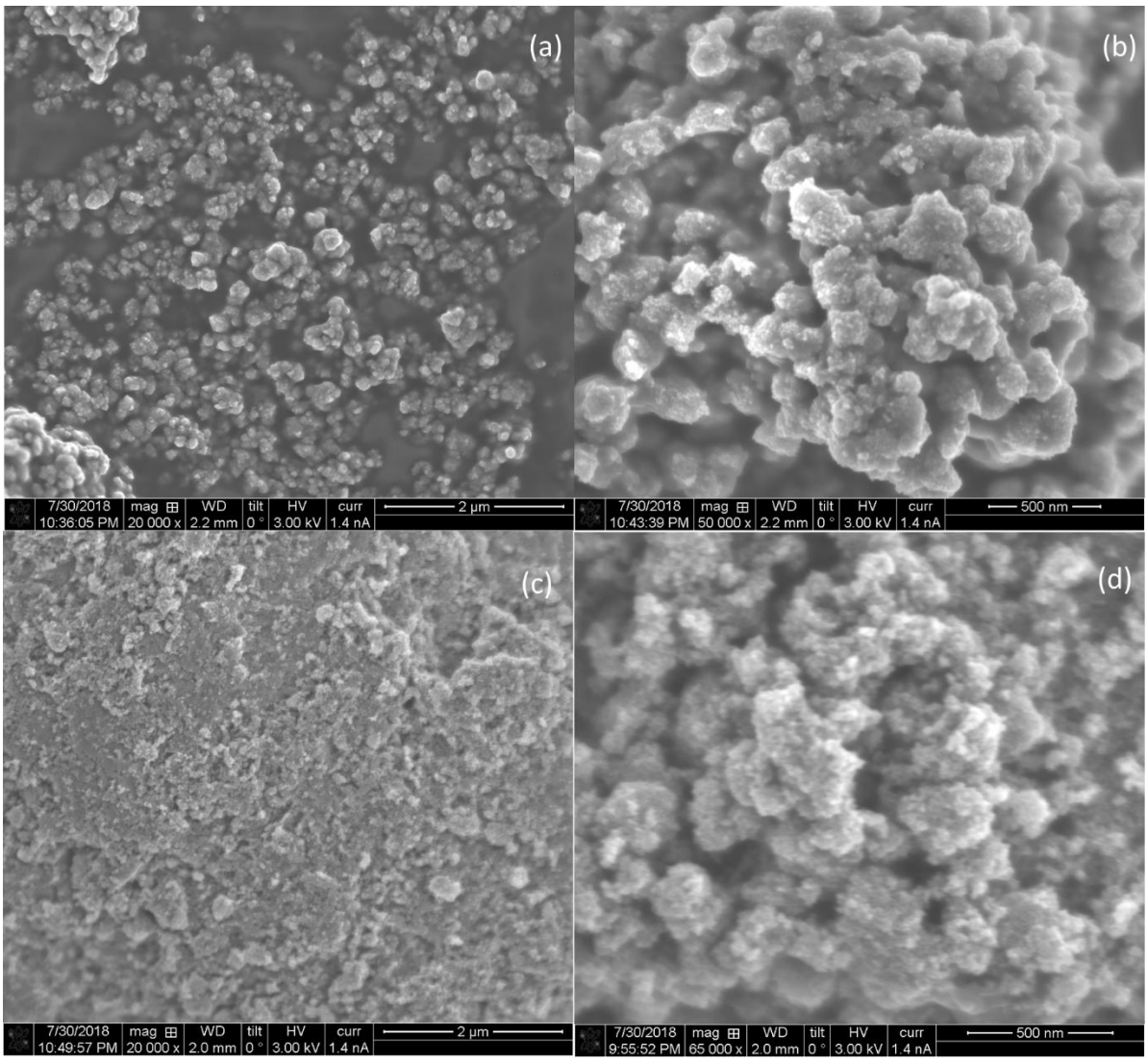

Figure 5.2: SEM images for (a, b) TC and (c, d) TA samples at different magnifications.

The images reveal that both samples form agglomerates of irregular shape and size, and a clear pattern could not be observed. Furthermore, owing to the extremely small particle size and charging of the samples higher magnification images could not be obtained, thereby limiting the information provided in the SEM images. To accurately determine the average particle/crystallite size and elemental composition of the catalyst TEM imaging was employed. Fig 5.3a and c shows the low magnification TEM images for TC and TA, respectively. The TEM images reveal that both the catalysts form an average cluster size of roughly 100 nm across, consisting of much smaller individual particles.

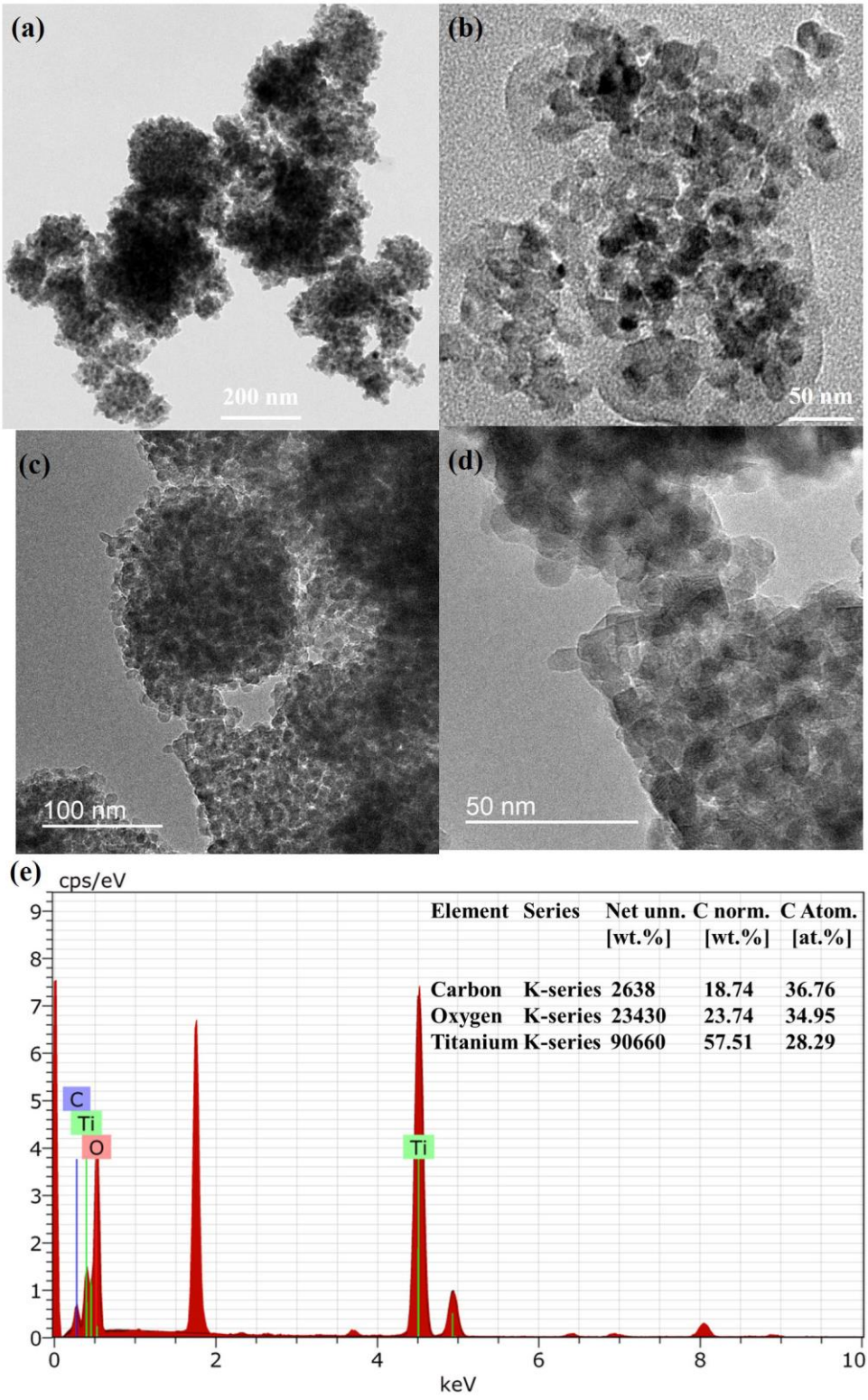

Figure 5.3: TEM images for (a, b) TC and (c, d) TA at different magnifications. (e) Representative EDX spectra for TC under area scans.

The HR-TEM images for TC and TA (Fig 5.3b and d) reveal that the average crystallite size is around 10 nm for both samples. This value is significantly larger than that predicted using the (101) XRD peak data and further confirms the limitation of Scherrer formula for size

determination of nanoparticles. To determine the presence of different elements in the as-prepared TC catalyst, energy dispersive X-ray spectroscopy (EDX) was performed using large area scans. Fig 5.3e shows a typical EDX spectrum for TC, clearly revealing the presence of C along with Ti and O atoms. However, as the relative composition changed with respect to each individual analysis, an accurate composition could not be determined. The HR-TEM images also reveal that the individual TiO_2 particles for both TC and TA are highly crystalline and display no apparent distortion of the lattice, which is commonly attributed to the inclusion of C in the TiO_2 matrix. This suggests that C may be present as a thin coating on the surface of the individual particles and eliminates the possibility of a bulk-doping. However, further characterization is required to confirm this hypothesis.

5.4.3 X-ray photoelectron spectroscopy

XPS analysis was performed to investigate the chemical composition and electronic structure of the catalyst surface and the acquired XPS spectra are presented in Fig 5.4. Fig 5.4a displays the survey spectrum for TC, in which the peaks corresponding to O 1s, C 1s and Ti 2p orbitals could be easily indexed, thereby, confirming the presence of these elements. Fig 5.4b shows the high-resolution Ti 2p spectra with two symmetrical peaks located at binding energies (BEs) of 464.2 and 458.5 eV. The presence of symmetric peaks and a splitting energy difference of 5.7 eV confirms the presence of Ti^{4+} oxide (TiO_2). No additional peaks corresponding to metallic (Ti^0) or self-doped (Ti^{3+}) species were observed. It has been previously reported that doping or interstitial incorporation of foreign elements like C and N can shift the Ti 2p peaks to lower binding energies by ~0.5 eV with respect to pure anatase TiO_2.[5] As the acquired Ti 2p spectrum for TC displays a lack of any shift in BEs of these orbitals, it suggests the absence of C or any other heteroelement doping. This observation is further supported by the O 1s spectrum presented in Fig 5.4c, which can be deconvoluted into two peaks. The sharp peak corresponding to BE of 529.7 eV can be attributed to the Ti-O bonding, whereas the smaller and broader peak centred around ~530.9 eV indicates the presence of either hydroxide or carbonate species on the sample surface. This is a commonly reported impurity on the surface of photoactive TiO_2.[5,6] The high-resolution XPS spectrum for C 1s has been presented in Fig 5.4d. The main band can be deconvoluted into three individual peaks centred around 284.8, 286 and 288.5 eV, corresponding to C-C, C-O and C=O species, respectively. Even though the scans have been performed after charge compensation with respect to carbon, a large portion of the peak centred at 284.8 eV could originate from (atmospheric) adventitious carbon with no means for further resolution. The other two peaks located at BEs of 286 and 288.5 eV can both be attributed to the presence of carbonate phase. It has been previously reported that the presence of a C 1s

band at ~288.5 eV indicates substitutional doping of C in TiO_2 matrix, in which some of the C atoms can displace Ti atoms and form bonds with the lattice O.[5,6] However, in such a case the BEs for Ti 2p orbitals would be shifted to lower energies and a strong O 1s peak corresponding to C-O would be observed beyond 531.5 eV. Since the acquired XPS data for TC does not support this observation, it is safe to assume that the majority of C is present as free/amorphous carbon bonded with the terminal oxygen groups at the surface.

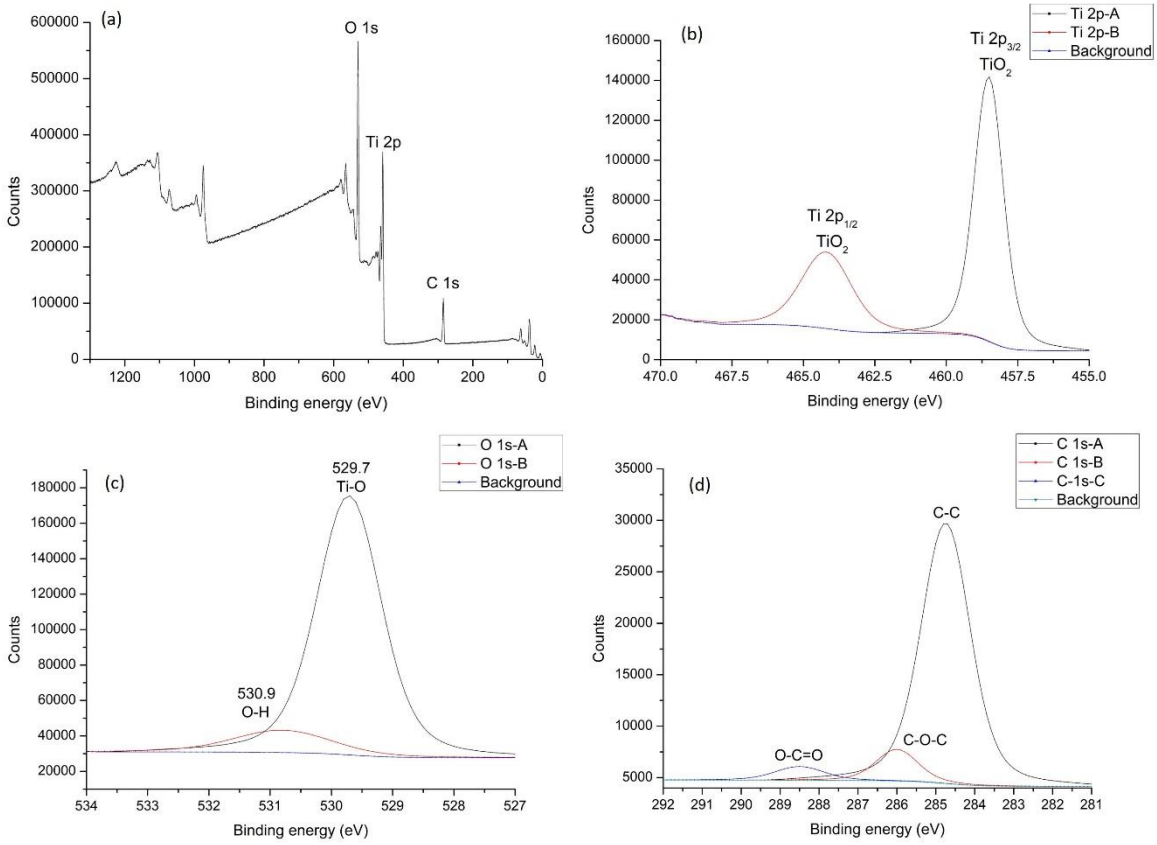

Figure 5.4: (a) XPS survey spectrum and the corresponding high-resolution XPS spectra of (b) Ti 2p, (c) O 1s and (d) C 1s orbitals of calcined TC samples.

5.4.4 Raman spectroscopy

The prepared samples were further analysed using Raman spectroscopy and the acquired spectra is presented in Fig 5.5. The presence of a strong band at 147, 198, and 640 cm^{-1} can be correlated to the E_g mode of the anatase phase. Similarly, bands corresponding to 398 and 515 cm^{-1} can be attributed to the B_{1g} and A_{1g} modes of the anatase phase. No additional modes corresponding to either rutile or brookite phase were observed suggesting the phase purity of anatase phase in TC, within the detection limit of the instrument. Similar observations were made in the Raman spectrum of TA along with a small band around 450 cm^{-1}, which can be

attributed to the brookite phase and is in good agreement with the XRD results. The presence of surface carbon in TC was confirmed by the observation of a peak at 1590 cm^{-1} corresponding to the in-plane stretching vibration (G band) of carbon. This G-band (~1590 cm^{-1}) clearly indicates the presence of sp^2-hydridized graphitic carbon. Additionally, the inset of Fig 5.5 clearly shows the redshift of E_g band in TC compared to TA, which can be attributed to the electronic interaction between the TiO_2 and carbon layers on the surface.[7,8] The Raman spectrum of crystalline graphitic carbon usually contains a D-band (at ~1350 cm^{-1}). This D-band is associated with the presence of defects in long-range ordered graphene layers and its intensity is dependent on the number of graphene layers present on the material.[9] The absence of a strong D-band in the acquired Raman spectrum suggests that the C-shell coating of TC composite lacks sufficient long-range order, which makes the C-shell appear to be amorphous in nature.[10,11] Additionally, the intensity ratio of the D and G peaks [I(D)/I(G) ≈0] along with the G peak position indicates that the present carbon is indeed amorphous in nature with a high sp^2 content[10,12]. However, owing to the high background of TiO_2 and the overall low carbon content in the nanocomposites, it is difficult to accurately determine the volume ratio of sp^2/ sp^2 carbon in the mixture.

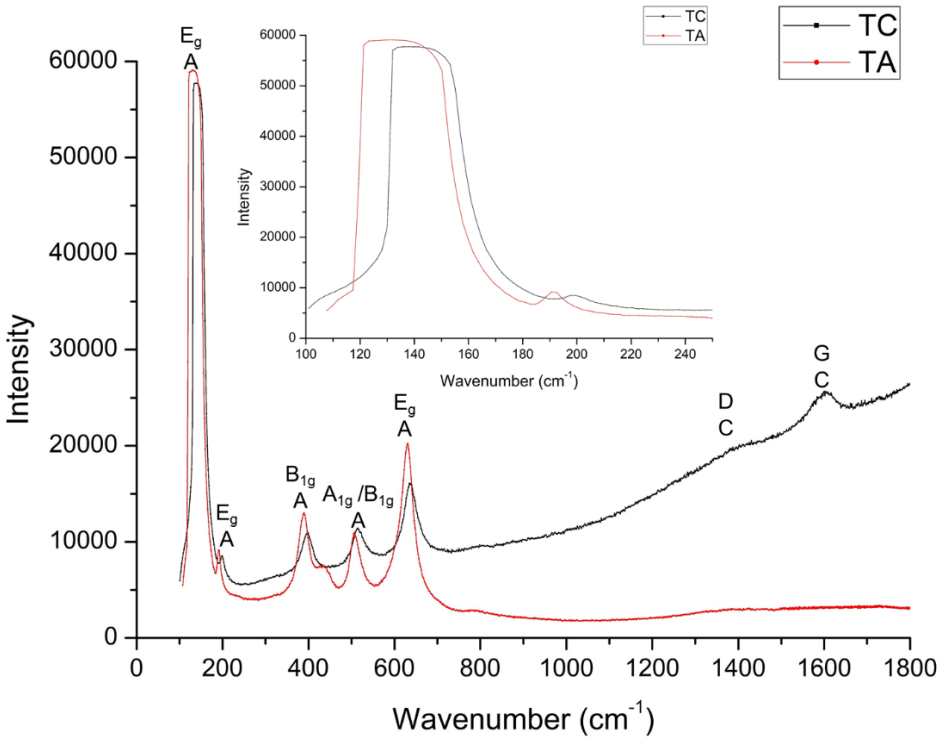

Figure 5.5: Acquired Raman spectra for the as-prepared TC and TA powders.

5.4.5 Thermogravimetric analysis

To quantitatively determine the amount of carbon (wt.%) present in the sample thermogravimetric analysis was performed. The catalyst was heated in air up to 800 ^{o}C to achieve complete oxidation of the surface carbon. Fig 5.6 shows the weight change of the sample as a function of temperature and the highlighted area shows the associated y-error. The graph displays a sharp drop in the weight of the sample from 0-200 ^{o}C, which can be partially attributed to the removal of adsorbed moisture. However, at 200 ^{o}C a shift in the heat flow is encountered indicating a possible loss of water from the hydroxyl defects in the sample. Another sharp transition in the heat flow can be observed at ~620 ^{o}C, potentially attributed to the onset of carbon oxidation. The sample was further heated to 800 ^{o}C and held at this for 30 min, after which it was slowly cooled to room temperature. Analysis of the TGA data indicates that TC contains ~2.2 wt.% carbon which could be directly oxidized in air. This value is in excellent agreement with that observed for the T1-E sample, which displayed a weight change of ~2.3% (Table 4.2). This data suggests that the mechanism for partial hydrolysis of titanium alkoxide does not change in the presence of aqueous KCl and that the amount of surface C is possibly invariant for a certain combination of alkoxide and alcohol synthesis. However, further testing is required to fully confirm this hypothesis.

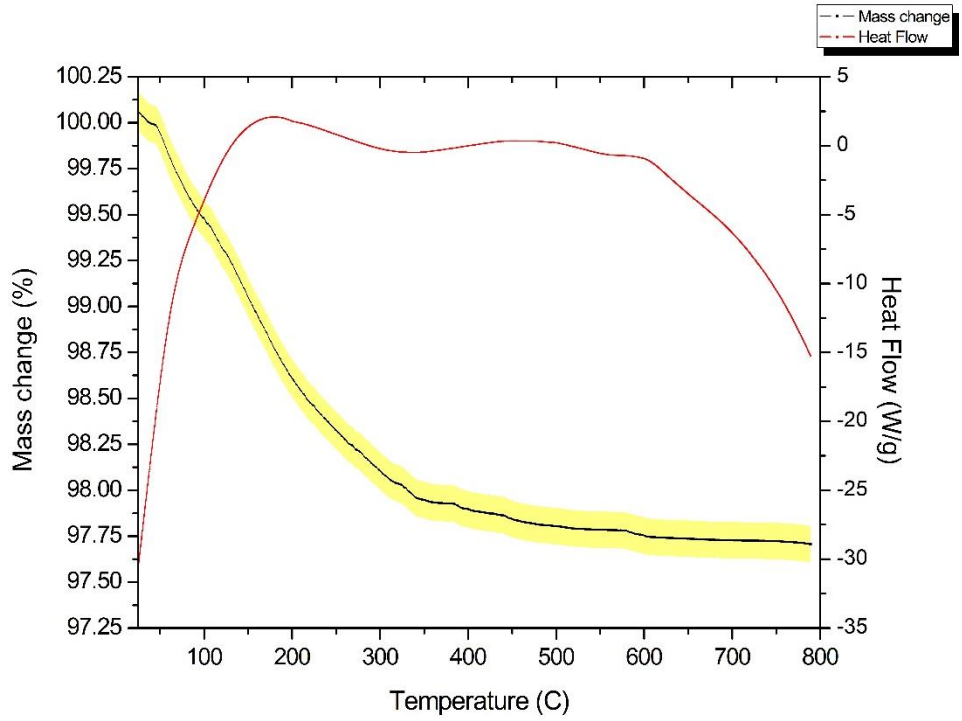

Figure 5.6: Graph depicting mass change and heat flow as a function of temperature for TC.

5.4.6 Diffuse reflectance spectroscopy

Fig 5.7 shows the DRS spectra of TC and TA in the wavelength range of 250 to 650 nm. From the presented data it can be clearly observed that the core@shell structure of TiO_2 allows it to better absorb in the visible region. The reflectivity of TC in the wavelength range of λ>400 nm is almost half that of TA, which is consistent with the DRS data observed for the sub-micrometre sized particles (section 4.4.6). The characteristic absorption edge of TiO_2 is still clearly visible in TC, as indicated by the sharp drop in reflectivity at approximately ~380 nm; even though compared to TA a slight red-shift in the band gap (~0.05 eV/ 20 nm) can be observed. As bulk or interstitial incorporation of carbon is associated with a significant reduction of the bandgap, the presented data further supports the theory that majority of carbon in the sample is present at the surface.

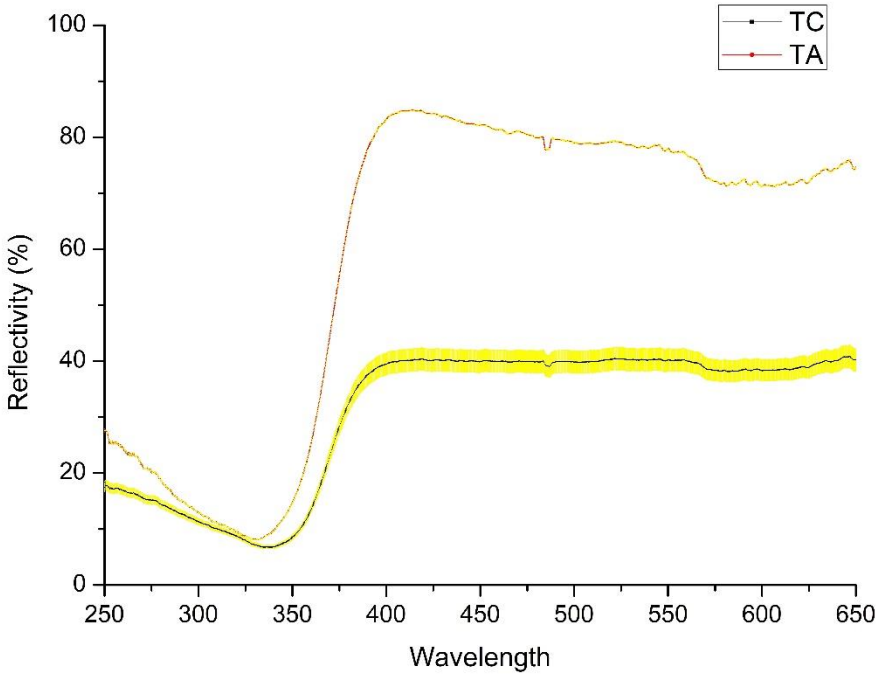

Figure 5.7: Diffuse reflectance spectra for TC and TA.

5.4.7 Nitrogen absorption-desorption isotherms

As photocatalysis is essentially a surface phenomenon, the average surface area and pore size of the catalyst has a direct bearing on its catalytic properties. Hence, nitrogen absorption-desorption isotherms were acquired for both TC and TA and are presented in Fig 5.8a and b. The isotherms for both TC and TA can be categorized as type IV owing to the lack of a clear saturation even in the higher relative pressure region. TC displays two distinct hysteresis regions in the relative pressure range of 0.5-0.8 and 0.9-1.0. Hysteresis in the pressure range of

0.5-0.8 suggests the presence of mesopores with a broad size distribution, whereas the second region (0.9-1.0) can be approximated to a H1-type hysteresis indicating the presence of well-ordered micropores with a smaller size distribution. Contrarily, for TA the distinct hysteresis region is observed in the partial pressure range of 0.6-0.9 with an H2-type geometry suggesting that the mesopores in TA have a larger average size and a narrower size distribution compared with TC.

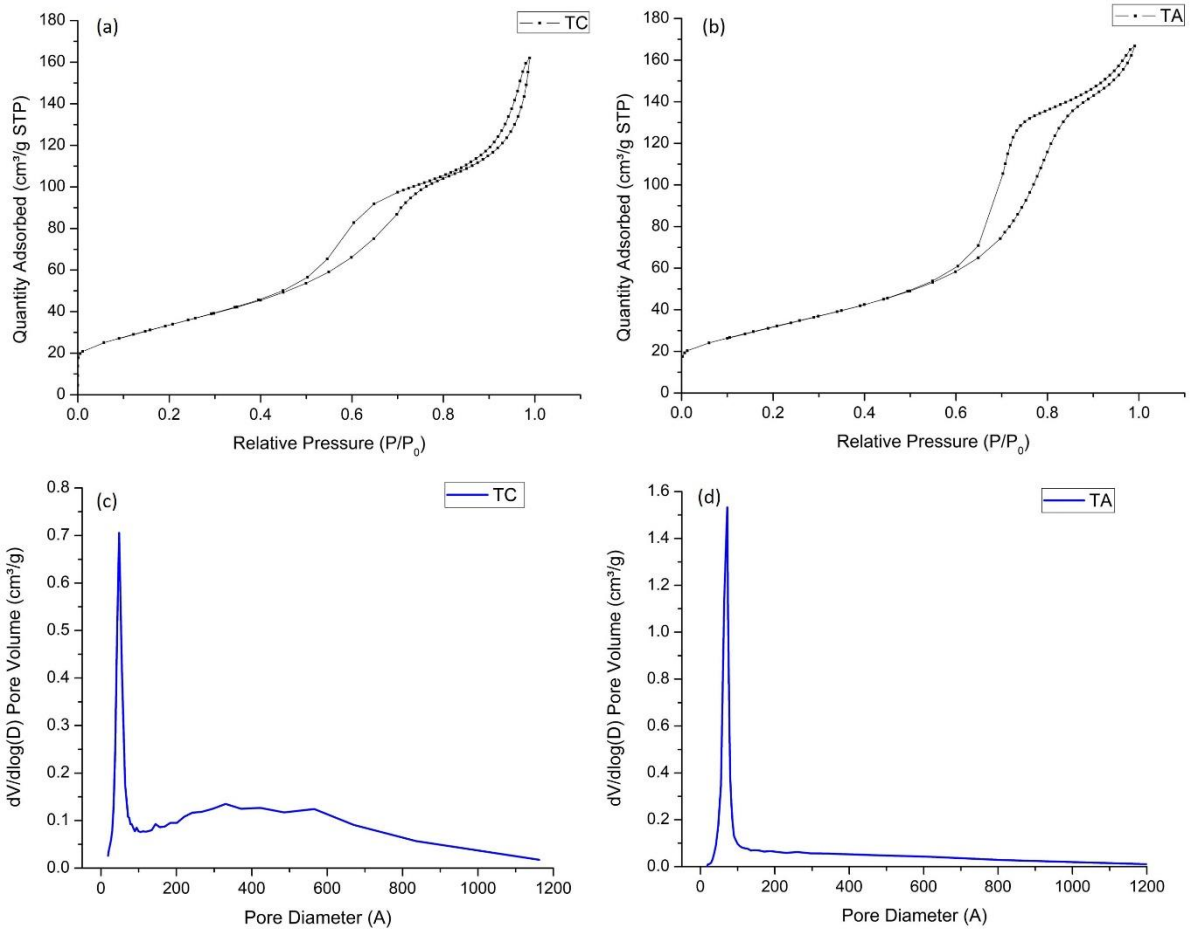

Figure 5.8: (a, b) Nitrogen absorption-desorption isotherms and (c, d) the derived pore-size distribution plots for TC (left) and TA (right).

To further analyse the size and distribution of porosity in the two samples, the desorption branch of the isotherms was analysed using Barret-Joyner-Halenda (BJH) theory and the resulting pore-size distribution is plotted in Fig 5.8c and d. It was observed that the first pore mode for TC is located at 47.78 Å with a broad pore-size distribution, whereas the first pore mode for TA is observed to be at 72.23 Å with a narrow distribution of pores. The Brunauer–Emmett–Teller (BET) theory was used to calculate the specific surface area of both as-prepared catalysts. It was observed that TC possesses a slightly higher surface area of ~123 $m^2.g^{-1}$ compared to ~116 $m^2.g^{-1}$ for TA. The specific surface area for both samples is significantly higher compared

to commercial TiO_2 powders (P25; 56 $m^2.g^{-1}$) and 25 times larger than salt-free samples (Table 4.2).[13] This can be credited to the optimized synthesis parameters which help to produce well-dispersed nanoparticles (~10 nm) and prevent agglomeration. The small discrepancy between the surface areas of TC and TA can be explained based on the calcination process. In the absence of an oxygenating environment the presence of residual carbon can interfere with the growth process of the nucleated crystallites, consequently leading to the creation of smaller and numerous particles. However, in an oxygenating environment this free carbon is oxidized before the onset of crystallization of amorphous TiO_2. Hence, some agglomeration and growth of particle size is possible.

5.5 Formation of TiO_2@C nanocomposites

The mechanism for formation of the carbon-coated TiO_2 particles to produce a core@shell structure has been previously discussed and will only be reported here briefly.[13] Essentially, controlled hydrolysis of titanium alkoxide followed by calcination in an inert atmosphere allows the heavier TiO_2 to condense during the crystallization process, whereas decomposition of the residual alkoxy group produces amorphous C, which permeates outwards and is deposited on the surface of the calcined particles as a thin layer. The addition of salt (KCl) helps to control the zeta potential of the primary and calcined particles by limiting coagulation of the amorphous precipitates and the rate of hydrolysis.[2] Alternately, calcination in the presence of oxygen produces pristine TiO_2 with a varying mixture of crystalline phases (anatase/rutile/brookite) depending upon the size of the primary precipitates. A graphical representation of the whole process is presented in Fig 5.9. By a careful selection of the water amount (for hydrolysis), salt concentration, calcination time/temperature and the inert gas, well-dispersed nanoparticles of TiO_2 can be obtained with a thin outer layer of carbon. This presence of surface carbon can impart a host of benefits for photocatalysis including enhanced surface area, improved visible-light response, efficient generation/separation of charge carriers and better adsorption of dye molecules.

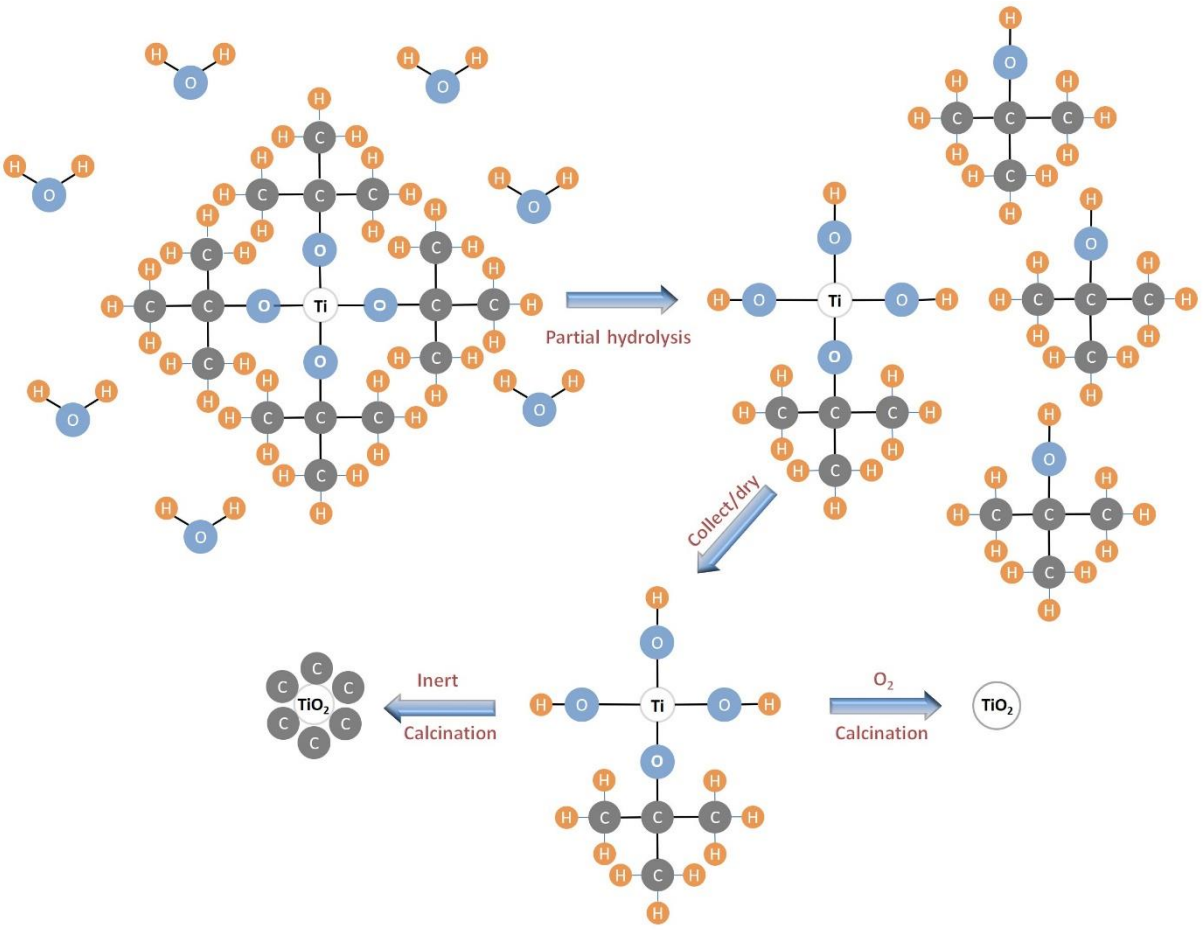

Figure 5.9: Graphical depiction of the controlled hydrolysis process used for fabrication of pristine and TiO_2@C core@shell nanoparticles.

5.6 Photocatalytic tests

5.6.1 Dissolved impurities

The experimental setup and preparation technique for photocatalytic degradation experiments is identical to that described in section 4.5. The photocatalytic activity of the as-prepared and control catalyst was initially determined by monitoring sunlight-assisted degradation of aqueous methylene blue (MB) as a function of time. Initially, 50 mg of catalyst was added to 50 mL stock solution of MB dye (5 $mg.L^{-1}$). However, in this case the dye was mineralized within 3 min and no reliable data could be obtained. Hence, to generate meaningful data points the catalyst amount was limited to 10 mg and the experiment was repeated. UV/Vis adsorption data for the dye (supernatant) was collected at 3 min intervals until 5 data points were obtained. The plot of dye concentration as a function of time is provided in Fig 5.10a. It was observed that ~66% degradation of MB was achieved in 15 min by TC compared to ~37% degradation over TA, Fig 5.10b. No appreciable degradation was observed for blank (no catalyst) or in dark suggesting photocatalysis as the primary means for degradation. The experiment was repeated

with brilliant green (BG, 5 mg.L^{-1}) dye, for which ~91% degradation was achieved over TC compared to only ~74% with the control sample (TA). These two tests clearly indicate that the TiO_2@C core@shell structure of TC helps to significantly improve the photocatalytic properties. However, the rate of photo-mineralization is observed to be dependent on the dye molecule. To further confirm this hypothesis additional tests were performed with methyl orange (MO; 5 mg.L^{-1}) and rhodamine B (Rh B; 5 mg.L^{-1}) under similar conditions. The degradation percentage was significantly lower for MO (~34%) and least for Rh B at ~33%. However, upon increasing the catalyst amount to 50 mg and repeating the experiment ~89% Rh B could be degraded in 9 min, whereas the dye was completely mineralized in <12 min (Fig 5.10c). For comparative analysis, the test was repeated with 50 mg P25 Degussa, which could produce only ~77% degradation of Rh B in a similar time frame (9 min). The advantage of TC compared to P25 can be credited to its high surface area and the presence of carbon on the surface, which improves visible-light absorption and charge separation.

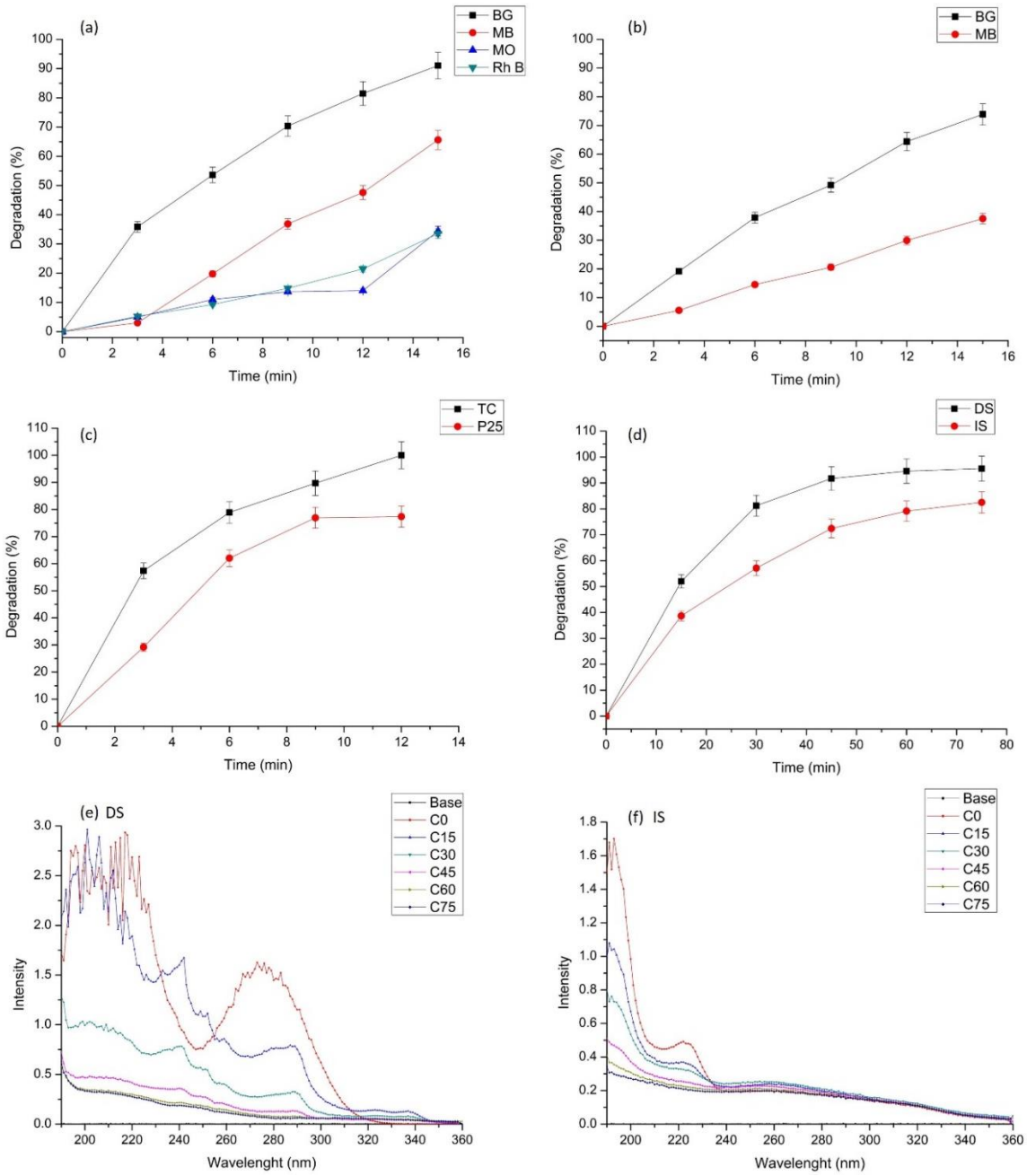

Figure 5.10: Time-dependent photocatalytic dye degradation plots using (a) TC and (b) TA. (c) Rh B degradation plots for TC and P25 Degussa. (d) Time-dependent absorbance spectra for (e) Diclofenac (DS) and (f) Ibuprofen (IS) sodium salts using TC.

The logarithmic plots of relative concentration profiles and the calculated degradation rate constants for all photocatalytic experiments in this study have been provided in Fig 5.11 and Table 5.1, respectively.

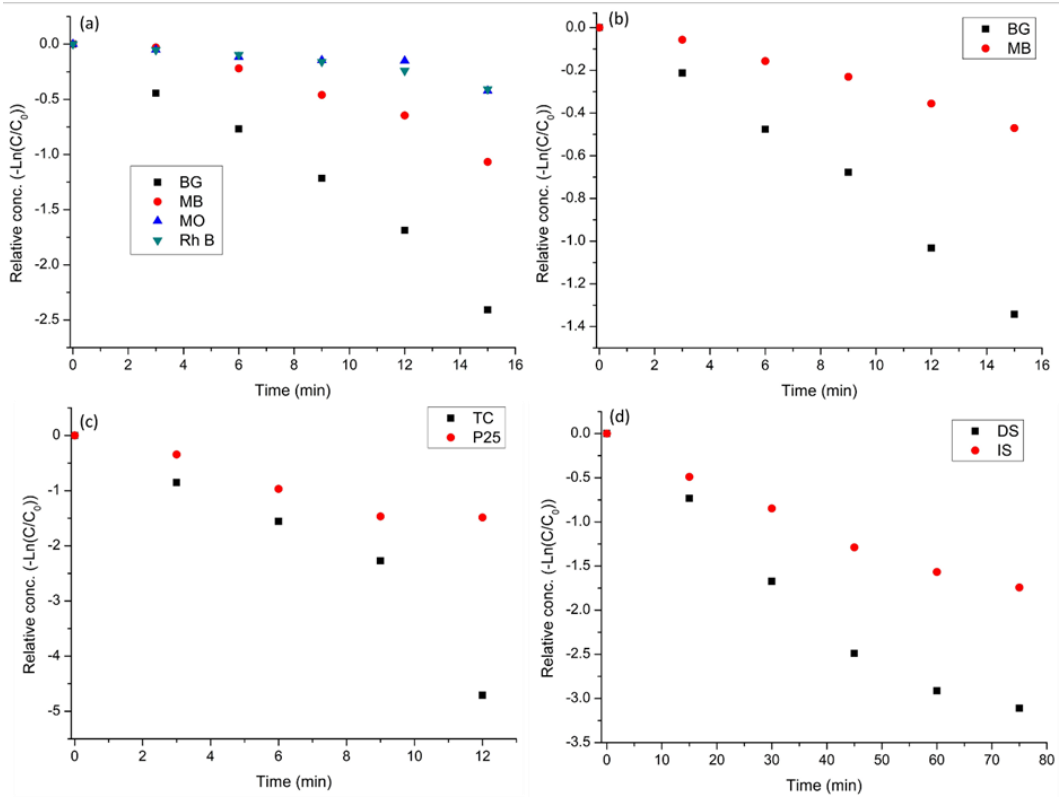

Figure 5.11: Time-dependent concentration plots for various dyes with (a) TC and (b) TA samples. (c) Concentration plot for Rh B over TC and P25 Degussa. (d) Concentration plots of DS and IS over TC.

It can be argued that coloured dyes can sensitize TiO_2 rendering it slightly active in the visible region. Furthermore, a practical photocatalyst will be seldom employed only for mineralization of coloured dyes. Hence, the photocatalytic study was extended to include two model pharmaceutical compounds namely ibuprofen and diclofenac. Both ibuprofen and diclofenac are nonsteroidal anti-inflammatory compounds. However, their unchecked presence in the environment can be fatal to other organisms such as the Indian vulture crisis caused by the rampant use of diclofenac, which resulted in near extinction of Gyps vultures in the subcontinent.[14] The stock solution for IS (10 $mg.L^{-1}$) and DS (50 $mg.L^{-1}$) were prepared according to their respective solubility in water. 50 mg of catalyst was added to 50 mL of pharmaceutical stock solution and the setup was illuminated as in previous experiments. Samples were collected at 15 min intervals and the experiment was allowed to run for 75 min.

Table 5.1: Summary of key data for photocatalytic dye and pharmaceutical degradation experiments.

Sample	Amount (mg)	Dye	Run time (min)	Absorbance wavelength (nm)	Degradation (%)	Rate constant[a] (min^{-1})	R^2 value
TC	10	BG[b]	15	626	91	-0.1544	0.991
	10	MB[b]	15	626	65.62	-0.0707	0.939
	10	MO[b]	15	462	34.41	-0.0232	0.792
	10	Rh B[b]	15	552	33.54	-0.0254	0.932
	50	Rh B[b]	12	552	100	-0.361	0.914
	50	DS[c]	75	277	95.54	-0.0436	0.958
	50	IS[d]	75	193	82.5	-0.0236	0.979
TA	10	BG[b]	15	626	73.86	-0.0893	0.991
TA	10	MB[b]	15	626	37.54	-0.0316	0.987
P25	50	Rh B[b]	12	552	77.38	-0.1365	0.943

[a] Rate constant calculated using the following expression: $-\ln\left({C}/{C_0}\right) = k \times t$, in which k is the rate constant, C_0 is the initial absorbance and C is the absorbance after time t.

[b] Compound concentration 5 $mg.L^{-1}$.

[c] Compound concentration 50 $mg.L^{-1}$.

[d] Compound concentration 10 $mg.L^{-1}$.

The UV/Vis absorption spectra for DS indicates that highest absorption lies below λ=224 nm. However, given the poor signal/noise ratio in that region, the absorbance data was collected with respect to λ=277 nm. It can be clearly visualized from Fig 5.10e that the absorbance spectra of DS changes as progressive oxidation of DS produces reaction intermediates, which were also mineralized subsequently. Measuring absorbance with respect to 224 nm indicates that ~95% mineralization was achieved within 60 min and did not change after that suggesting reaction completion. The corresponding relative concentration profile is provided in Fig 5.11d. It can be observed that this number is limited by the baseline compensation of the instrument and the wavelength used. In case of IS, the UV/Vis absorbance spectrum was much clearer (Fig 5.10f). Hence, λ=193 nm was selected for monitoring the change in absorbance. Similar to DS, ~83% degradation could be achieved in 60 min and no further change in absorbance was observed (Fig 5.10f). From Table 5.1 it can be clearly observed that for similar amounts of catalyst and dissolved compounds, the degradation rate constant can vary largely depending on the dye molecule. The highest rate constant of -0.1544 min^{-1} was observed for BG, whereas it was reduced to -0.0254 min^{-1} for Rh B. Data also shows that TC is approximately twice as efficient as TA for photo-degradation of BG (1.72×) and MB (2.237×). This confirms the beneficial

effects of the carbon shell coating for visible light absorption. Furthermore, optimized fabrication leads to a higher surface area which allows it to easily outperform commercial P25 (2.64×). Scavenger analyses were performed with aqueous Rh B to determine the relative contribution of various REDOX species in the overall degradation process. Benzoquinone (BQ), tert-butanol (TBA), and sodium oxalate were used as scavenging agents for superoxide (O_2^-), hydroxyl ion ($OH^\bullet$), and photogenerated holes (h^+), respectively. The percentage degradation achieved in the presence of different scavenging agents is shown in Fig 5.12.

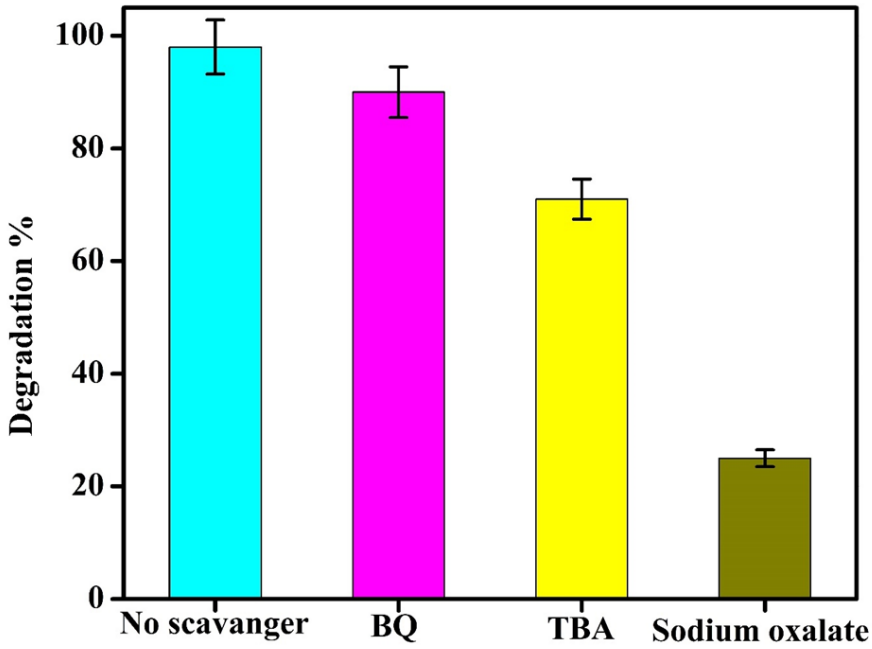

Fig 5.12: Scavenger analysis for determination of different REDOX species generated during photocatalytic degradation of Rh B in the presence of TC.

Scavenger tests reveal that photogenerated holes are the primary REDOX species followed by hydroxyl radicals, whereas superoxide anions contribute very little to the overall degradation process. However, considering the abundance of water molecules adsorbed on the surface of the photocatalyst at any given time compared to the relatively fewer pollutant molecules; it can be theorized that the photogenerated holes are primarily used for the production of hydroxyl ions, which subsequently lead to pollutant degradation.

5.6.2 Antibacterial analysis

As a final indicator of its versatile applicability, TC was employed as an anti-bacterial material for inactivation of gram-negative *E. coli* bacteria. For complete details of the experimental procedure please refer to section 3.6.6. The results of the photocatalytic antibacterial analysis are presented in Fig 5.13.

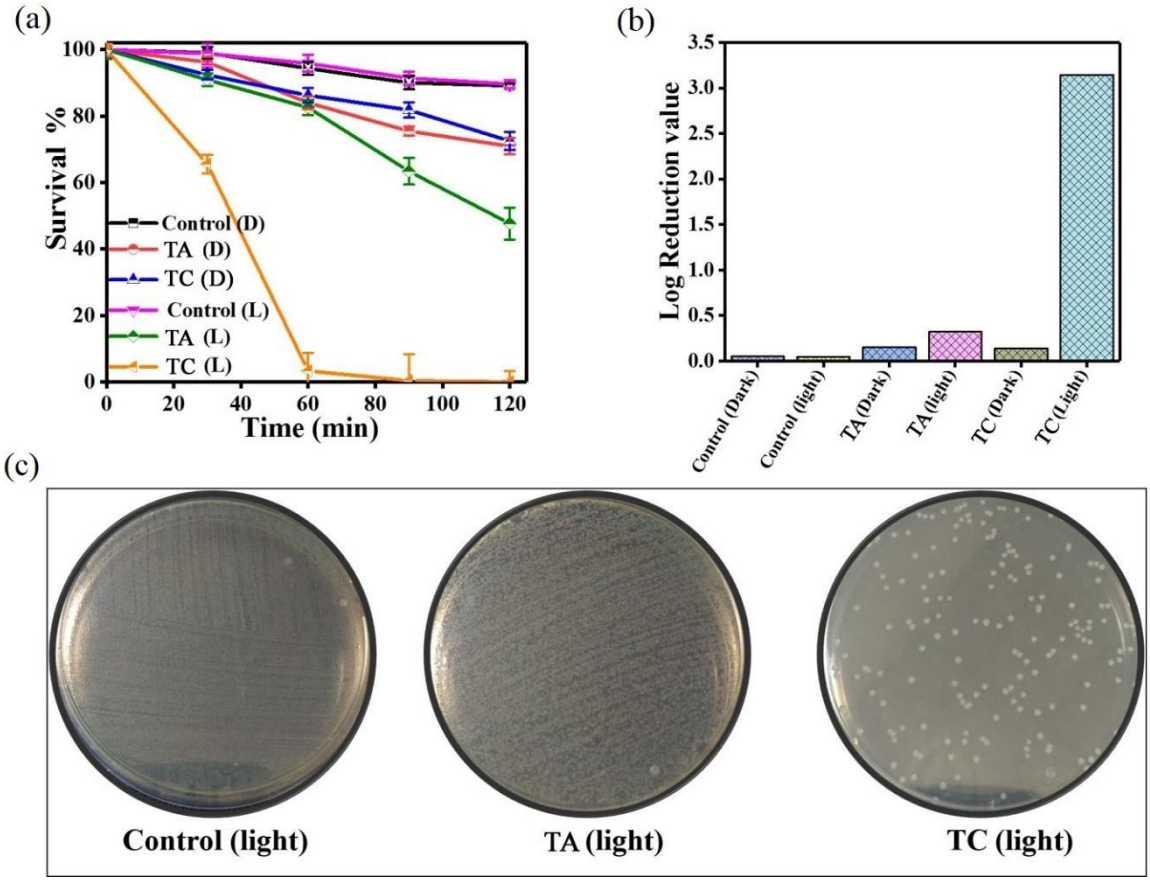

Figure 5.13: (a) Percentage survival and (b) Log reduction value of E. coli bacteria under various conditions. (c) Post illumination optical photographs of the bacterial assays.

Control tests indicate that the survival rate for the bacterial assay is significant in dark conditions, even though ~20% inactivation was observed (Fig 5.13a). Similar inactivation rates were also observed in the dark for both TC and TA suggesting that loss of homeostasis could be responsible. However, when the setup was illuminated with simulated sunlight almost 100% bacterial inactivation was achieved over TC in 60 min, whereas only 50% inactivation was achieved over TA even after 120 min. This loss in survival rate over TA can be credited to the presence of ~5% UV component in the simulated sunlight, which leads to a minor production of photogenerated charge carriers resulting in bacterial death. Fig 5.13c shows the optical photographs of the bacterial assay post-illumination for TC, TA and blank samples without dilution. The FE-SEM micrographs of the bacteria before and after treatment with TC are presented in Fig 5.14. Results from the cumulative analyses indicate that the as-prepared TC is a simple and effective photocatalyst, which can be used for a host of water treatment applications and works through oxidation of various dissolved organic impurities and pathogens.

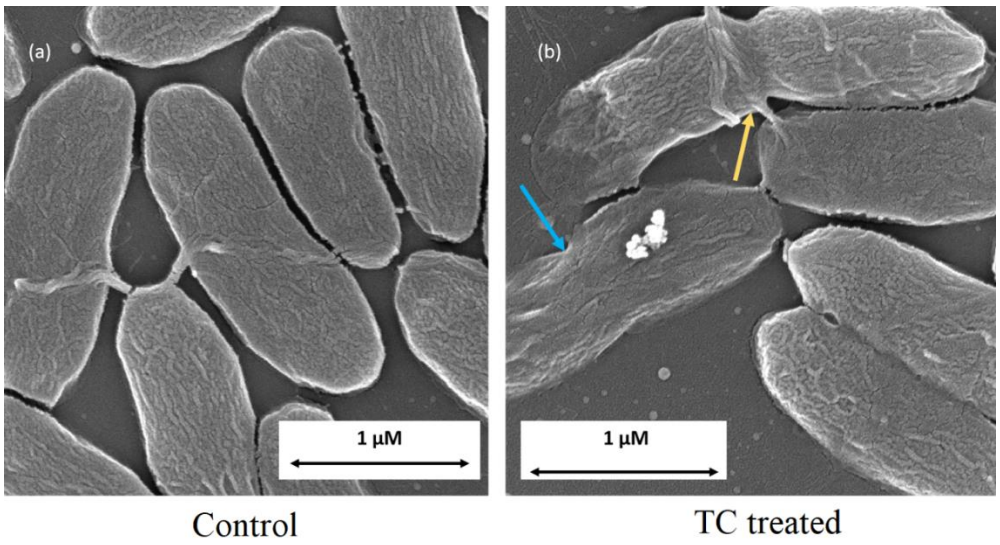

Figure 5.14: FE-SEM images of the bacterial assay after 60 min exposure to visible light over (a) control (blank) and (b) TC.

5.7 Discussion

As the DRS data already indicates, the presence of carbon helps to improve the visible light absorption in TC (Fig 5.7). The decreased reflectivity of the carbon-containing TC can be attributed to the increased electric surface charge of the composite. The presence of a thin layer of carbon on the surface of individual TiO_2 particles results in a good electronic contact between the two phases.[8] The presence of sp^2-hydridized carbon on the TiO_2 surface, which is expected to have a two-fold effect: 1) The overlapping orbital/electronic interaction helps to improve separation of the photogenerated charge carriers, as evident from the improved photocurrent response; and 2) the carbon atoms on the surface can also provide a sensitization effect as evident from DRS analyses. To confirm this hypothesis transient photocurrent under chopped illumination and EIS measurements were performed for both samples. The results for transient photocurrent measurement are plotted in Fig 5.15.

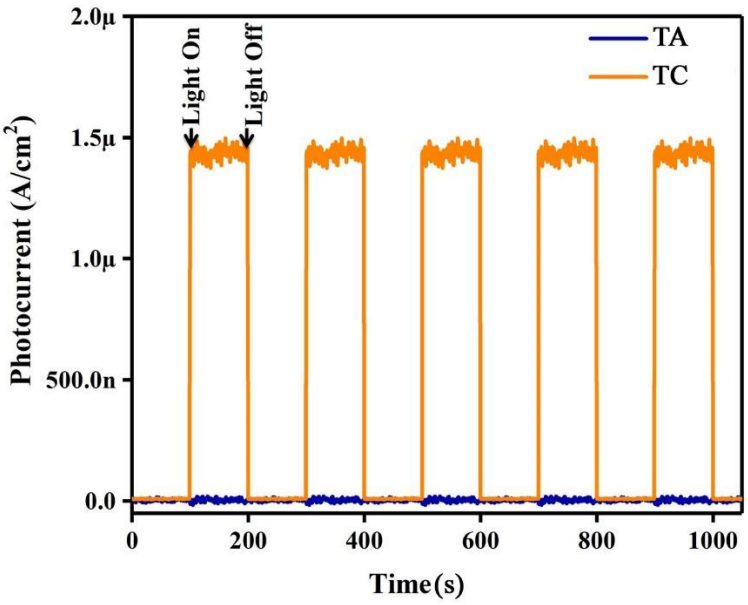

Figure 5.15: Transient photocurrent measurements for TC and TA.

From Fig 5.15 it can be clearly observed that a fast and uniform photocurrent is generated in the TC containing electrode. Furthermore, a stable current density of ~1.4 µA.cm^{-2} was reproduced for 10^3 seconds. Compared to the negligible current observed with air calcined TA, the photocurrent density of TC is several orders of magnitude higher. This demonstrates the excellent separation efficiency of photogenerated charge carriers in TC, which can be attributed to the electronic overlap between the sp^2-hybridized carbon and TiO_2 phases. The results from photocurrent measurements were complimented by performing EIS study on both TC and TA samples. EIS data can not only reveal the separation efficiency of photogenerated charge carriers but also provide valuable information regarding charge transfer kinetics at the electrode/electrolyte interface. Hence, EIS data was acquired under dark and illuminated conditions and is presented in Fig 5.16.

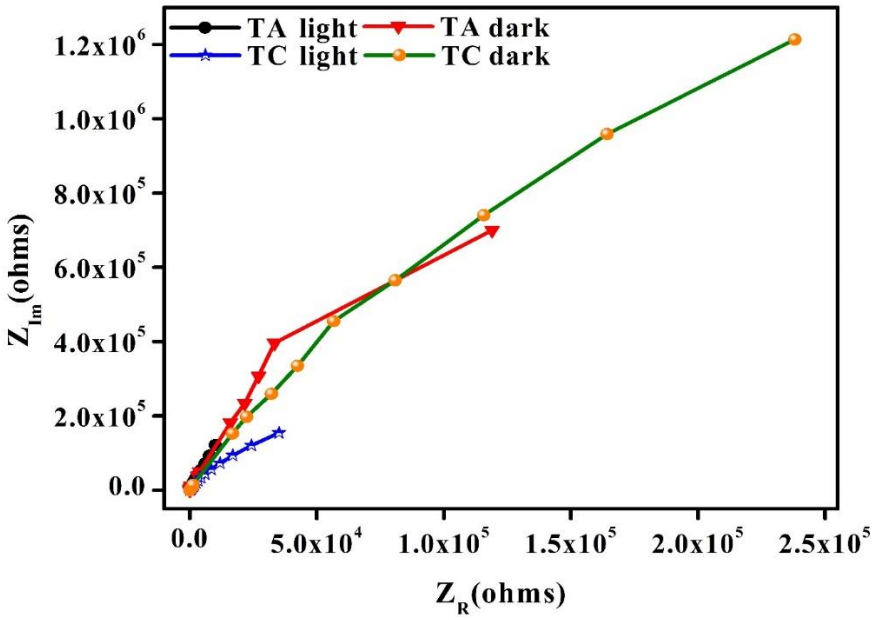

Figure 5.16: EIS complex plane plots for TA and TC under dark and illuminated (visible light) conditions.

The presence of only one arc in the EIS plots for both samples indicates that charge transfer at the catalyst/liquid interface is the rate limiting step in the photocatalytic activity. The EIS plots for TA exhibited a similar radius under illuminated and dark conditions confirming that pristine TiO_2 is insensitive to the visible light used in the experiment. However, the charge transfer resistance decreased considerably for TC, as indicated by the decreased radius under visible light. Furthermore, the corresponding EIS plots for TC were observed to have a smaller arc radius than those obtained for TA. Both these observations indicate that the presence of a carbon shell not only helps to reduce the surface charge transfer resistance but also sensitizes TiO_2 to absorb and utilize visible light.

Table 5.2 provides a comparative analysis of selected C-modified TiO_2 photocatalysts reported in the literature. Owing to the vast difference in illumination source, incident energy, light absorbed, surface area, and aqueous suspension of the catalysts between different studies, a direct comparison is not possible. However, it can be easily observed almost all C-modifications require an external carbon source and multi-step processing, which is eliminated in the proposed methodology. Furthermore, even with lower catalyst loading concentrations the photocatalytic performance of TC is either comparable or better than the state-of-the-art catalysts reported in literature; in which TC is the only catalyst reported to be effective for such a broad spectrum of water-borne pollutants. The photocatalytic activity of TC is observed to be even better than Ag-loaded TiO_2, which was recently reported by our group.

Table 5.2: Table provides a brief overview of photocatalytic performance of selected C-modified TiO_2 nanostructures reported in literature.

Material	Catalyst conc. ($g.L^{-1}$)	Dye	Dye conc. ($mg.L^{-1}$)	Light source	Time[a] (min)	Precursor	Year	Ref
C-doped mesoporous TiO_2	1	Rh B	5	500 W metal-halogen (>420 nm)	>300	Glucose	2007	[15]
TiO_2@C nanofiber	0.3	Rh B	5	150 W Xe (>400 nm)	360	Glucose	2011	[16]
C-coated TiO_2 nanocrystals	0.33	Rh B	N/A	Solar simulator	40	Pluronic F127	2014	[17]
C-coated (001) microspheres	0.2	MB	10	250 W metal-halogen (visible)	360	Glucose	2014	[17]
TiO_2@C peapods	0.15	Rh B	19.16	300 W Xe	60	Glucose	2015	[18]
C-modified TiO_2 nanotubes	N/A	MB	12	160 W Hg-vapor	240	Carbamide solution	2015	[19]
TiO_2@C nanobelts	0.5	Rh B	4.79	Hg-vapor	30	Poly(acrylic acid)	2016	[7]
TiO_2@C hollow sphere	0.625	Rh B	20	500 W Hg-vapor	120	Glucose	2016	[20]
C-doped TiO_2 single crystal nanorods	0.2	Rh B	9.58	350 W Xe	40	Polystyrene spheres	2017	[21]
Graphene-carbon nanodot-TiO_2 ternary composite	0.2	MB	3	50 W metal-halogen (100 $W.m^{-2}$)	90	Graphite, graphene oxide	2017	[22]
TiO_2@C nanocomposites	0.1	MB	5	Solar simulator	42[b]	-	This work	
TiO_2@C nanocomposites	1	MB	5	Solar simulator	<3	-	This work	
TiO_2@C nanocomposites	0.1	Rh B	5	Solar simulator	117[b]	-	This work	
TiO_2@C nanocomposites	1	Rh B	5	Solar simulator	<12	-	This work	
TiO_2-Ag (3 mol.%)	1	MB	5	150 W Xe	21[b]	N/A	2017	[23]

[a] Time required to achieve complete degradation.

[b] Estimated time required for >95% degradation based on observed rate constant.

To provide a quantitative direct comparison, different photocatalysts need to be evaluated using the same experimental setup and conditions. This represents a very stringent set of requirements and requires that all variables including spectrum/intensity of the light source, and

depth/absorptivity of the aqueous suspension must be measured and reported. However, this is usually not the case and unless a standardized testing/reporting protocol is developed other methods of indirect comparison must be adopted. Finally, the presented results indicate that the nanocomposites still primarily employ UV light for generation of charge carriers. Hence, suitable cocatalysts/sensitizers should be explored to further improve their performance.

5.8 Conclusions

This chapter reports the synthesis of TiO_2@C core@shell nanocomposite as an efficient photocatalyst for solar water-treatment applications. Partial hydrolysis of titanium alkoxide followed by calcination in an inert atmosphere enables the fabrication of highly monodisperse TiO_2 particles with a thin coating of amorphous carbon, which is bonded with the terminal oxygen groups. The presence of surface carbon improves visible-light absorption, provides a small red-shift of the band gap, and drastically improves the separation efficiency and transport of photogenerated charge carriers. Even in low concentrations, the as-prepared catalyst can be employed for rapid degradation of a variety of water contaminants including azo dyes, pharmaceutical compounds and *E. Coli* bacteria. The facile preparation technique, high catalytic activity and a wide range of applicability makes the proposed catalyst a strong contender for practical solar water treatment applications; especially in combination with suitable membranes which enable facile recovery and reuse of such nanocomposites.[24]

5.9 Acknowledgements

I would like to acknowledge the following people for the various help and input received towards the completion of this study. Mr. Sundararajan Thirumalai (MSM) for providing the SEM images. Dr. Giorgio Divitini (MSM) for his help in acquiring the first set of TEM images. Mr. Moolchand Sharma (IIT Mandi) for providing the second set of TEM images, and the results from transient photocurrent and EIS measurements. Mr. Sandeep Kumar (IIT Mandi) for providing results of the antibacterial analysis, and Dr. Rahul Vaish for access to research facilities at IIT Mandi.

References:

1 Eric A. Barringer and H. Kent Bowen, Journal of the American Ceramic Society **65** (12), C (1982).
2 S. Eiden-Assmann, J. Widoniak, and G. Maret, Chemistry of Materials **16** (1), 6 (2004).
3 Hengzhong Zhang and Jillian F. Banfield, The Journal of Physical Chemistry B **104** (15), 3481 (2000).

[4] AS Vorokh, Nanosystems: Physics, Chemistry, Mathematics **9** (3), 364 (2018).
[5] Hongwei Bai, Zhaoyang Liu, and Darren Delai Sun, Journal of Materials Chemistry **22** (36), 18801 (2012).
[6] Eunyoung Bae and Teruhisa Ohno, Applied Catalysis B: Environmental **91** (3), 634 (2009).
[7] Jianming Zhang, Mitra Vasei, Yuanhua Sang, Hong Liu, and Jerome P. Claverie, ACS Applied Materials & Interfaces **8** (3), 1903 (2016).
[8] Li-Wu Zhang, Hong-Bo Fu, and Yong-Fa Zhu, Advanced Functional Materials **18** (15), 2180 (2008).
[9] Duhee Yoon, Hyerim Moon, Hyeonsik Cheong, Jin Sik Choi, Jung Ae Choi, and Bae Ho Park, J. Korean Phys. Soc **55** (3), 1299 (2009).
[10] Andrea C. Ferrari and Denis M. Basko, Nature Nanotechnology **8**, 235 (2013).
[11] Mildred S. Dresselhaus, Ado Jorio, Mario Hofmann, Gene Dresselhaus, and Riichiro Saito, Nano Letters **10** (3), 751 (2010).
[12] Andrea C. Ferrari, Jhon Robertson, Andrea Carlo Ferrari, and John Robertson, Philosophical Transactions of the Royal Society of London. Series A: Mathematical, Physical and Engineering Sciences **362** (1824), 2477 (2004); C. Casiraghi, A. Hartschuh, H. Qian, S. Piscanec, C. Georgi, A. Fasoli, K. S. Novoselov, D. M. Basko, and A. C. Ferrari, Nano Letters **9** (4), 1433 (2009); A. C. Ferrari, J. C. Meyer, V. Scardaci, C. Casiraghi, M. Lazzeri, F. Mauri, S. Piscanec, D. Jiang, K. S. Novoselov, S. Roth, and A. K. Geim, Physical Review Letters **97** (18), 187401 (2006); A. C. Ferrari and J. Robertson, Physical Review B **64** (7), 075414 (2001); A. C. Ferrari and J. Robertson, Physical Review B **61** (20), 14095 (2000); Andrea C. Ferrari, Solid State Communications **143** (1), 47 (2007).
[13] Aditya Chauhan, Sundararajan Thirumalai, and Ramachandran Vasant Kumar, Materials Today Communications **17**, 371 (2018).
[14] J. Lindsay Oaks, Martin Gilbert, Munir Z. Virani, Richard T. Watson, Carol U. Meteyer, Bruce A. Rideout, H. L. Shivaprasad, Shakeel Ahmed, Muhammad Jamshed Iqbal Chaudhry, Muhammad Arshad, Shahid Mahmood, Ahmad Ali, and Aleem Ahmed Khan, Nature **427**, 630 (2004); Rhys E Green, IAN Newton, Susanne Shultz, Andrew A Cunningham, Martin Gilbert, Deborah J Pain, and Vibhu Prakash, Journal of Applied ecology **41** (5), 793 (2004).
[15] Wenjie Ren, Zhihui Ai, Falong Jia, Lizhi Zhang, Xiaoxing Fan, and Zhigang Zou, Applied Catalysis B: Environmental **69** (3), 138 (2007).
[16] Peng Zhang, Changlu Shao, Zhenyi Zhang, Mingyi Zhang, Jingbo Mu, Zengcai Guo, and Yichun Liu, Nanoscale **3** (7), 2943 (2011).
[17] Ting Xia, Wei Zhang, Zhihui Wang, Yuliang Zhang, Xiangyun Song, James Murowchick, Vincent Battaglia, Gao Liu, and Xiaobo Chen, Nano Energy **6**, 109 (2014).
[18] Liang Peng, Huijuan Zhang, Yuanjuan Bai, Yangyang Feng, and Yu Wang, Chemistry – A European Journal **21** (42), 14871 (2015).
[19] Yinchang Li, Yongqian Wang, Junhan Kong, Hanxiang Jia, and Zhengshu Wang, Applied Surface Science **344**, 176 (2015).
[20] Yan Zhuang, Jianhua Sun, and Mingyun Guan, Journal of Alloys and Compounds **662**, 84 (2016).
[21] Jian Shao, Weichen Sheng, Mingsong Wang, Songjun Li, Juanrong Chen, Ying Zhang, and Shunsheng Cao, Applied Catalysis B: Environmental **209**, 311 (2017).
[22] Ganesh B. Markad, Sudhir Kapoor, Santosh K. Haram, and Pragati Thakur, Solar Energy **144**, 127 (2017).
[23] Michael Coto, Giorgio Divitini, Avishek Dey, Satheesh Krishnamurthy, Najeeb Ullah, Cate Ducati, and R. Vasant Kumar, Materials Today Chemistry **4**, 142 (2017).
[24] M. Coto, S. C. Troughton, J. Duan, R. V. Kumar, and T. W. Clyne, Applied Surface Science **433**, 101 (2018); Lei Liu, Zhaoyang Liu, Hongwei Bai, and Darren Delai Sun, Water Research **46** (4), 1101 (2012).

Chapter 6

Nickle-titania nanocomposites for visible light hydrogen production

6.1 Introduction

Ever since the discovery of UV-assisted water splitting on a TiO_2-based photoanode,[1] efficient solar hydrogen production has been a dream of the (photocatalytic) scientific community. Over four decades of research in this area has led to the discovery and development of many novel photocatalyst, and significant progress has been made with respect to the stability, economy and efficiency of hydrogen production.[2-4] Nevertheless, even as of yet the state-of-art materials are no closer to meeting the requirements for commercial or large-scale deployment. This can be partly attributed to economic factors and easy availability of conventional forms of energy including fossil fuels. However, with increasing concerns over the long-term detrimental impact of carbon emissions on the environment and climate, this field has received renewed interest in the past few years. The basics of semiconductor-assisted photocatalytic water splitting, including the underlying processes, has already been discussed in section 2.3.2. Briefly, the interaction between an energetic photon and a semiconductor with a suitable bandgap and band edges can result in the production of an electron (e^-) and a hole (h^+) in the conduction (cb) and valence (vb) bands, respectively. These photogenerated charge carriers can migrate to the surface of the photocatalyst and react with adsorbed water molecules to initiate REDOX reactions at the surface to produce hydrogen and oxygen. The whole process can be summarized as follows:[5]

$$semiconductor + hv \rightarrow e^-(cb) + h^+(vb) \quad (6.1)$$

$$2H^+ + 2e^- \rightarrow H_2(g)(\Delta E^o = 0\ V) \quad (6.2)$$

$$2H_2O(l) \rightarrow O_2(g) + 4H^+ + 4e^-(\Delta E^o = +1.23\ V) \quad (6.3)$$

$$H_2O(l) \rightarrow H_2(g) + \frac{1}{2}O_2(g)(\Delta G^o = +237.2\ kJmol^{-1};\ \Delta E^o = +1.23\ V) \quad (6.4)$$

Equations (6.2) and (6.3) represent the hydrogen (HER) and oxygen (OER) evolution reactions, respectively; whereas, equation (6.4) represents the overall water splitting with all potential measured against NHE. The symbols ΔE^o and ΔG^o represent the required potential and Gibb's free energy for the reaction, respectively. Equation (6.4) indicates that any semiconductor with a bandgap ≥1.23 eV and suitable band positions should, in theory, be able to achieve water splitting. However, owing to limited catalytic sites and sluggish reaction kinetics, the actual

bandgap should lie in the range of 1.5-2.5 eV (Fig 2.9). Furthermore, suitable band edges are required to initiate and sustain both the HER and the OER.

Few intrinsic semiconductors satisfy the required criteria for hydrogen production. Among these TiO_2,[3] CdS,[6] and recently discovered graphitic carbon nitride (gC_3N_4)[7] have been extensively studied. CdS has established its presence as the one of the leading semiconductors for photocatalytic hydrogen evolution owing to its narrow band gap (2.4 eV) and ideal cb edge of -0.9 V (Table 2.1). However, pure CdS is unstable and suffers from fast photo-corrosion, bulk recombination and poor quantum efficiency.[8] In contrast, gC_3N_4 has a bandgap of ~2.7 eV with an exceptionally high cb potential of -1.53 V.[9] This combined with its unique advantages of metal-free composition, low toxicity, economy of production and high thermal and chemical stability make it an excellent candidate for photocatalytic water splitting. However, bulk gC_3N_4 suffers from various drawbacks including low surface area (~10 $m^2.g^{-1}$), low charge mobility, high recombination, poor reaction kinetics and small number of catalytically active sites.[9] There is active ongoing research to mitigate these issues and improve the photocatalytic activity of gC_3N_4.[10] Until these limitations persist, TiO_2 will remain a popular choice as base semiconductor for photocatalytic hydrogen evolution.[2,11] However, considering the drawbacks of pristine TiO_2 along with the high energy requirement for overall water splitting (ΔG^o=+237.2 $kJ.mol^{-1}$), the use of cocatalysts and sacrificial agents (electron donors) become indispensable.

Nanostructured Pt is the ideal cocatalyst for photocatalytic water splitting, but its prohibitively high cost limits any attempt at commercialization. Hence, there is a need to develop cocatalysts based on more earth-abundant materials. In this regard, nanostructured Ni has been extensively studied as a possible substitute for Pt in a variety of disciplines involving the HER such as electrocatalysis,[12] photoelectrocatalysis[13] and photocatalysis. Section 2.4.2 provides a detailed discussion and literature review on the various Ni-based compounds reported for photocatalytic hydrogen evolution. A common drawback of TiO_2-supported nanostructured-Ni cocatalyst is its poor or complete lack of activity in the visible spectrum. Owing to the high bandgap and poor cb potential of TiO_2, an ideal cocatalyst should not only improve the rate of hydrogen production but also sensitize TiO_2 to absorb in the visible spectrum. Hence, this chapter aims to explore various Ni-based compounds as cocatalysts for visible light hydrogen production over TiO_2. Even though TiO_2 is not an ideal material for solar water splitting, it is expected that the findings in this study will help the development of other suitable composite materials for solar hydrogen production.

6.2 Material selection

Reiche and Bard's work is one of the seminal articles in the field of photocatalytic hydrogen production.[14] The authors deposited Pt on TiO_2 powder and irradiated it in the presence of aqueous NH_4Cl saturated with CH_4, which resulted in the production of amino acids and hydrogen as a byproduct. The study was based on the premise that a particulate photocatalytic system is essentially a small short-circuited photoelectrochemical cell. This article is also credited with establishing the modern approach of particle-based photocatalysis. Thereafter, the field of photocatalysis, photoelectrocatalysis, and electrocatalysis have developed as separate disciplines with little overlap. Nevertheless, much of the fundamentals for development of cocatalyst for water splitting remains the same. Hence, it is quite possible that electrocatalysts developed to lower overpotential for (photo)cathodes in (photo)electrolysis can also be employed for photocatalytic hydrogen production. In this regard, this chapter aims to explore some established state-of-art Ni-based electrocatalysts as potential cocatalysts for TiO_2. Three compounds namely β-$Ni(OH)_2$, and its derivatives NiO, and Ni_2P were fabricated. Details regarding advantages, disadvantages and previous studies for all three compounds have already been provided in section 2.4.2 (Chapter 2).

6.3 Photocatalyst synthesis

6.3.1 TiO_2-β-$Ni(OH)_2$

TiO_2 nanocomposites with 1, 2.5, 5, and 10 wt.% $Ni(OH)_2$ were prepared using hydrothermal synthesis by slightly modifying a previously reported method.[15] In a typical synthesis, for the preparation of (2 gm) 1 wt.% photocatalyst, 0.21 mM of $Ni(CH_3CO_2)_2 \cdot 4H_2O$ was dissolved in 50 mL deionized water under vigorous stirring resulting in the formation of a clear green solution. To this solution, 1.98 gm of anatase TiO_2 (Sigma; <20 nm) was added and the mixture was allowed to stir for another 30 min. Thereafter, 1.0 M ammonia water was added dropwise under continuous stirring till the mixture attained a stable pH of 11. Addition of ammonia initially resulted in the precipitation of pale-green $Ni(OH)_2$, which later re-dissolved in the presence of excess ammonia to form Ni-NH_3 hexammine complex. This final solution, characterized as having a bright blue colour, was transferred to a stainless-steel autoclave (100 mL) and heated to 180 ^oC for 3 h. The heating and cooling ramp rates were fixed at 5 $^oC.min^{-1}$. After the autoclave cooled down to room temperature, the mixture was collected, washed with deionized water and centrifuged at 4500 rpm for 10 min. The resulting precipitates were repeatedly washed until the supernatant reached a stable pH value of ~7. The wet precipitates were dried overnight in an oven at 80 ^oC to finally obtain the nanocomposites. The as-prepared

nanocomposites were designated as TNH-1, 2.5, 5 and 10 corresponding to 1, 2.5, 5, and 10 wt.% $Ni(OH)_2$. As a control, pure β-$Ni(OH)_2$ samples were also prepared similarly by eliminating TiO_2 from the synthesis.

6.3.2 TiO_2-NiO

TiO_2-NiO samples were prepared by simply heating the TNH samples in air.[16] Carefully weighed amount of powder was transferred to an alumina boat, which was placed inside a muffle furnace. The temperature was slowly raised to 350 ^oC and held for 2 h. The heating and cooling ramp rates were fixed at 5 $^oC.min^{-1}$. After cooling to room temperature, the powder was collected without any further treatment. The corresponding samples were labelled as TNO-1, 2.5, 5 and 10.

6.3.3 TiO_2-Ni_2P

Ni_2P containing samples were prepared by reaction with $NaH_2PO_2 \cdot H_2O$.[15] Dried TNH samples were mixed with sodium hypophosphite such that the molar ratio was Ni^{2+}/P^{5+}=1:5. The powders were ground together using a mortar and pestle for 30 min to aid mixing and achieve physical homogeneity. The ground mixture was transferred to an alumina boat and heated to 275 ^oC for 2 h in a tube furnace under Ar atmosphere. The furnace was initially flushed with Ar (100 $mL.min^{-1}$) for 30 min with sample inside to ensure complete removal of air. Thereafter, the flow rate was decreased to 5 $mL.min^{-1}$ and the ramp rate for both heating and cooling legs was limited to 5 $^oC.min^{-1}$. After cooling to room temperature, the samples were repeatedly washed with deionized water until the supernatant achieved a stable pH value of ~7, and dried overnight at 80 ^oC. The corresponding samples were labelled as TNP-1, 2.5, 5 and 10. Pure Ni_2P was also prepared using pure β-$Ni(OH)_2$.

A second set of Ni_2P containing samples was also prepared by a simple precipitation technique followed by calcination in Ar atmosphere. A procedure similar to preparation of TNH samples was followed except the precipitation of $Ni(OH)_2$ was performed using 1.0 M NaOH solution. This prevented the redissolution of $Ni(OH)_2$ precipitate. The samples were washed repeatedly with deionized water until the supernatant achieved an approximate pH value of 7. The samples were then recovered and dried overnight at 80 ^oC. The dry powders were ground together with sodium hypophosphite (Ni^{2+}/P^{5+}=1:5) and calcined in an Ar atmosphere at 275 ^oC for 2 h. The samples prepared by this method were designated as TNP-1s, 2.5s, 5s and 10s, in which the suffix ‘s’ is used to indicate the salt-precipitation method.

6.4 Characterization

6.4.1 Powder X-ray diffraction analysis

Fig 6.1 shows the XRD patterns for the as-prepared pure samples along with the commercial (anatase) TiO_2 used in the synthesis.

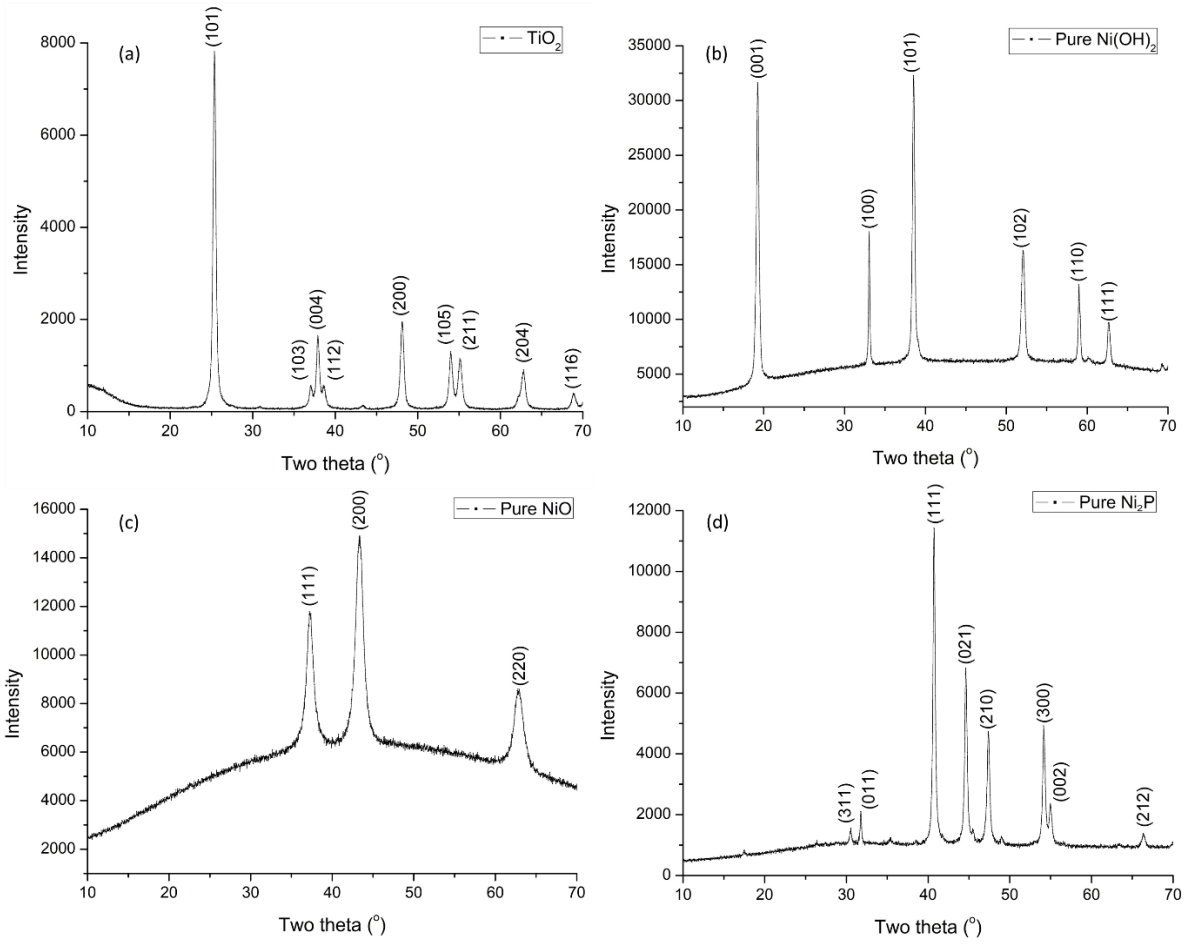

Figure 6.1: XRD patterns for phase pure (a) TiO_2, (b) β-$Ni(OH)_2$, (c) NiO and (d) Ni_2P.

The major peaks in all samples could be easily indexed to the respective JCPDS card numbers for anatase TiO_2 (21-1272), β-$Ni(OH)_2$ (14-0117), NiO (47-1049), and Ni_2P (03-0953). The XRD patterns were observed to be free of any additional or anomalous peaks indicating purity of the samples, within the detection limits of the instrument. Furthermore, all graphs display sharp, intense and well-defined peak shapes suggesting high crystallinity. Similarly, XRD patterns were also acquired for the 1, 2.5, 5 and 10 wt.% nanocomposites. In the XRD pattern for samples below 10 wt.% loading only peaks for TiO_2 could be observed. These samples did not display any reflections corresponding to the respective Ni compound, which could be attributed to the low concentration of the cocatalysts. Consequently, only XRD patterns for samples with 10 wt.% loading are displayed in Fig 6.2.

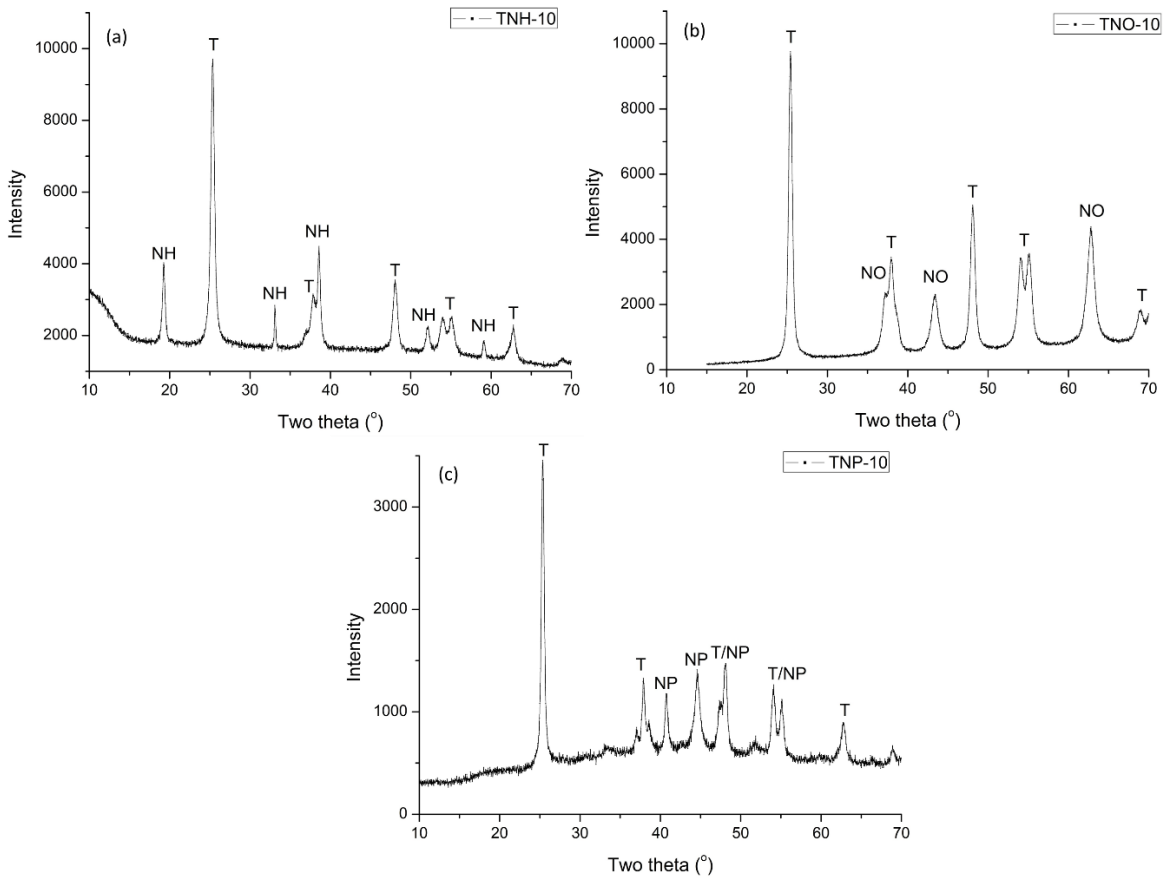

Figure 6.2: XRD patterns for (a) TNH-10, (b) TNO-10 and (c) TNP-10. The symbols T, NH, NO and NP denote peaks associated with TiO_2, β-$Ni(OH)_2$, NiO, and Ni_2P, respectively.

Fig 6.2 a, b and c displays the XRD patterns for TNH-10, TNO-10 and TNP-10, respectively. The XRD pattern for TNP-10s was similar to that observed for TNP-10 and, therefore, is not shown. Peaks corresponding to both anatase phase and the respective Ni compounds could be clearly indexed. This confirms that the suggested procedure resulted in successful fabrication of the desired composites. Owing to the small size of particles and the high background in the XRD patterns, information regarding the average crystallite size could not extracted reliably using the Debye-Scherrer method. Hence, the samples were inspected using electron microscopy imaging.

6.4.2 Transmission electron microscopy imaging

Fig 6.3 shows the low and high resolution TEM images for pristine β-$Ni(OH)_2$ and NiO.

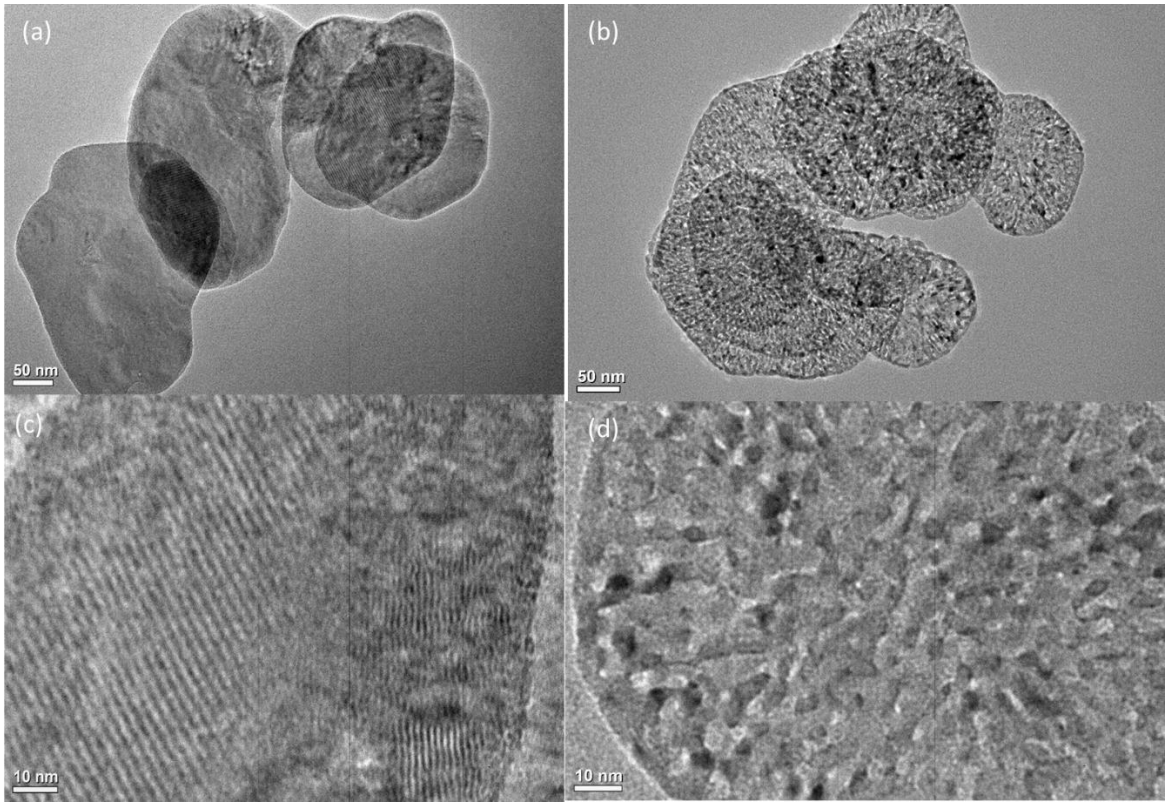

Figure 6.3: Low and high resolution TEM images for (a, c) β-$Ni(OH)_2$ and (b, d) NiO.

It can be clearly visualized from the images that hydrothermal synthesis leads to the production of two-dimensional (2D) plate-like β-$Ni(OH)_2$. This observation is in good agreement with that reported in the literature.[16] The individual platelets appear to have an average cross-section of ~200 nm. This 2D plate-like structure is preserved during calcination of $Ni(OH)_2$ in air, leading to the creation of highly mesoporous NiO. The as-prepared NiO appears to have limited or poor crystallinity owing to the abundance of pores. This could be a possible explanation for the high background observed in the XRD pattern for free-standing NiO. However, hydrothermal synthesis of $Ni(OH)_2$ in the presence of TiO_2 nanoparticles results in the formation of large clusters with an average cross-section well over 300 nm, which made it difficult to resolve individual phases (Fig 6.4a). Similarly, large sized particles were also observed for TNO samples (Fig 6.4b). Furthermore, a majority of the particles also displayed the evolution of rod-like structures in both TNH and TNP samples. The evolution of these nanorods can actually help to explain the formation these large clusters. The temperature used in the hydrothermal synthesis of β-$Ni(OH)_2$ (180 ^oC) is sufficiently large for initiating recrystallization of the anatase nanoparticles. This leads to agglomeration and growth of larger particles.

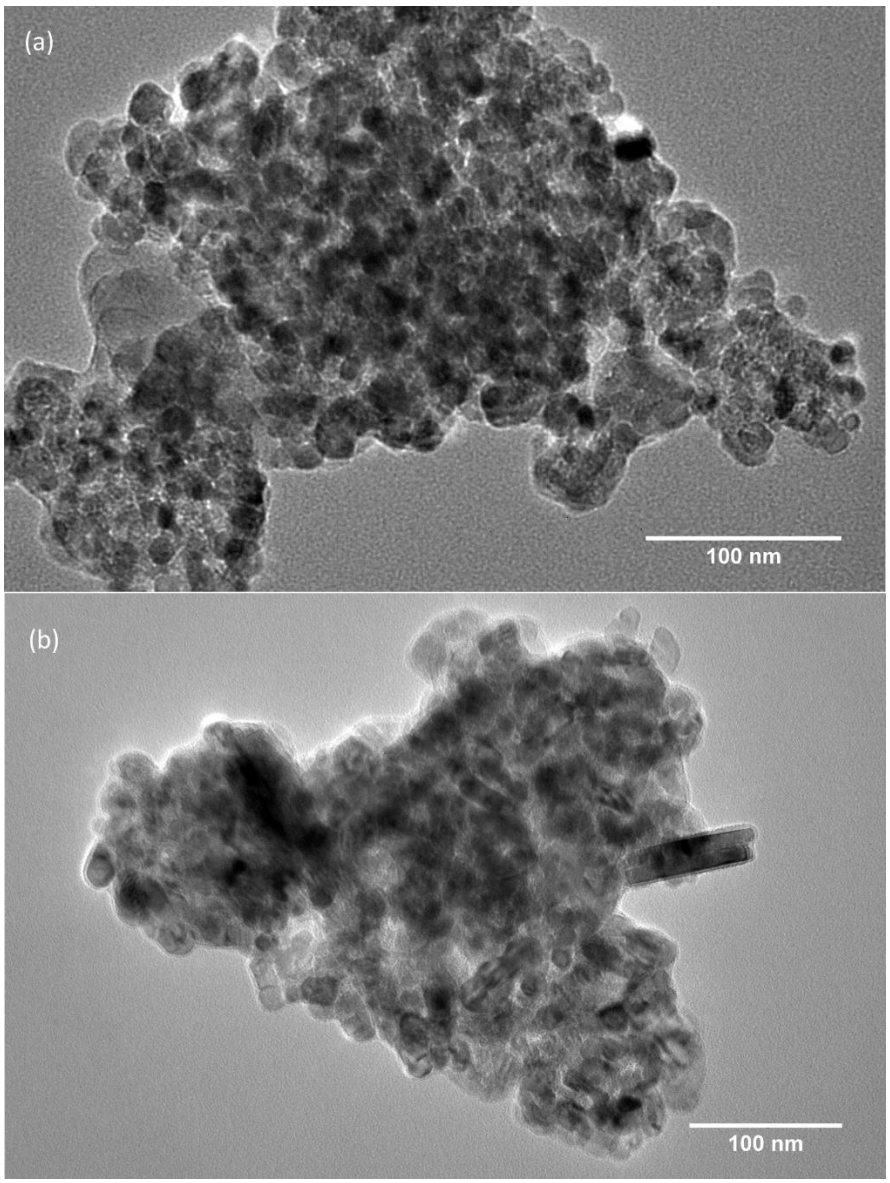

Figure 6.4: Representative TEM images for (a) TNH-5 and (b) TNO-5.

The evolution of TiO_2 nanorods from nanoparticles is actually a byproduct of the high pH (~11) of the Ni-hexammine precursor solution, as previously reported in literature.[17] TEM images of the TNP samples also displayed similarly large particles with an average cross-section >100 nm. However, the TNP samples prepared by salt-deposition method exhibited an average cluster size <100 nm, in which the individual anatase crystallites could be easily observed. This can be credited to the overall low-temperature processing of the salt-deposited TNP samples, which prevents agglomeration. The representative TEM images for both conventional and salt-deposited TNH samples have been provided in Fig 6.5.

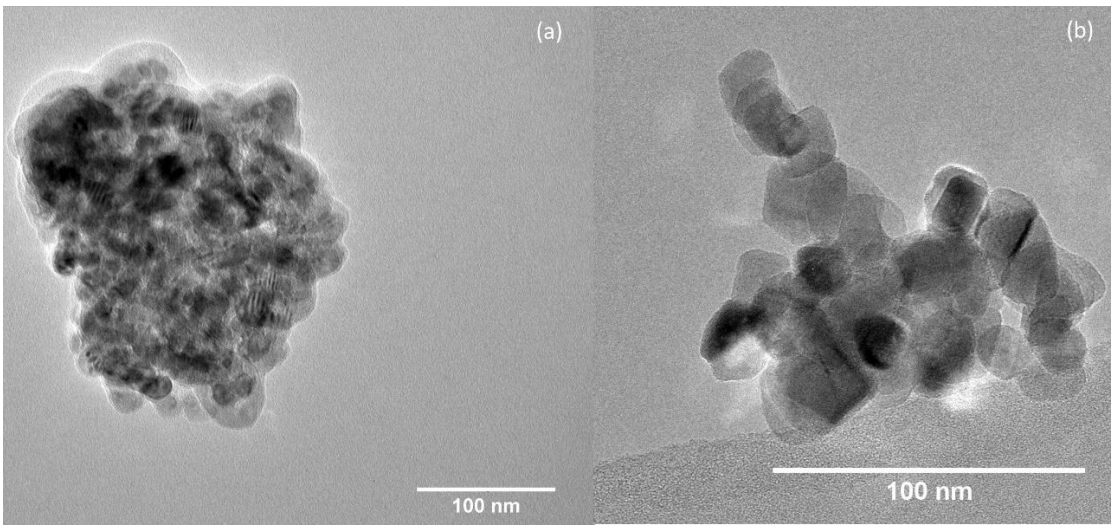

Figure 6.5: Representative TEM images for (a) TNP-5 and (b) TNP-5s.

Preliminary energy dispersive X-ray spectroscopy does indicate the presence of Ni and P in the respective samples. However, owing to the large variation between individual scans, further characterization is required to confirm the chemical composition.

6.4.3 X-ray photoelectron spectroscopy

Information about the surface chemistry and valence state of the participating elements was acquired using XPS. Samples with less than 5 wt.% Ni did not produce a clear Ni 2p spectra; whereas, for samples with 10 wt.% Ni the Ti 2p peaks could not be acquired, possibly owing to the shielding effect of Ni. Hence, high-resolution XPS spectra for only for 5 wt.% samples are provided here. Fig 6.6 a and b displays the XPS spectra for Ni 2p and O 1s orbitals for TNH-5.

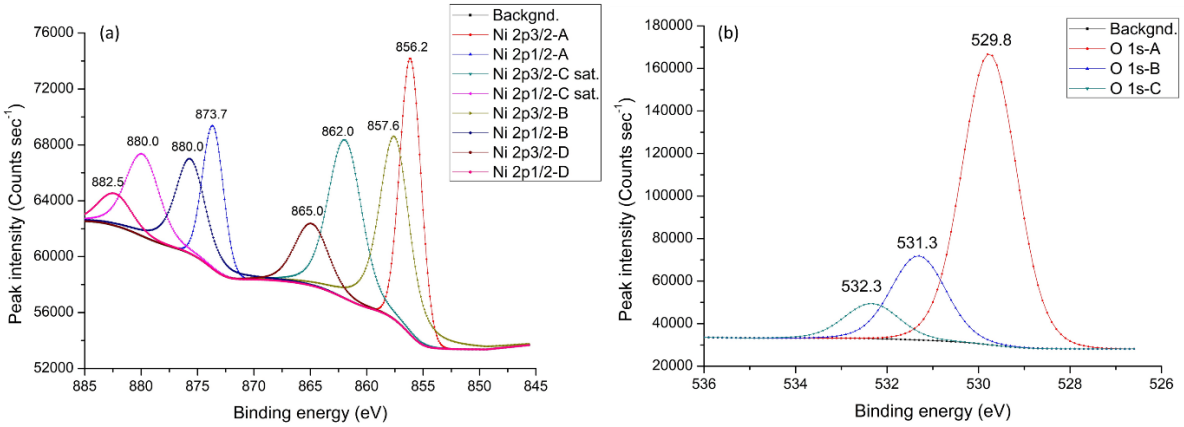

Figure 6.6: (a) Ni 2p and (b) O 1s XPS spectra of TNH-5.

The binding energy (BE) associated with the Ni $2p_{3/2}$ orbital in pure $Ni(OH)_2$ is located at 855.2 eV; whereas in the TNH-5 sample, this peak was observed at a BE of 856.2 eV.[18] This peak

shift to a higher BE could originate from sample charging. However, another plausible explanation could be delocalization of Ni antibonding orbitals owing to the formation of a heterojunction with TiO_2. This can be confirmed if a concomitant shift is observed in the BE of Ti 2p orbitals. However, as of yet a clean Ti 2p spectrum is not available. The absence of Ni 2p orbitals below 854 eV indicates the lack of any oxide or metallic Ni^0, thereby confirming that Ni is indeed present as a hydroxide. This is further confirmed by the splitting value of the BEs (Δ=17.5 eV) for Ni 2p orbitals, which is in a good agreement with that reported in literature for β-$Ni(OH)_2$.[18] The main peak of the O 1s orbital lies at a BE of 529.8, which is attributed to the presence of Ti-O. However, the presence of another peak centered at BE of 531.3 eV can be attributed to the presence of chemisorbed water (-OH). The relative intensity of this peak compared to O 1s-A suggests the origin to be Ni-O-OH rather than presence of surface impurity. However, the final (O 1s-C) peak could be attributed to the presence of either carbonate or physically adsorbed water on the surface. Corresponding Ni 2p and O 1s XPS spectra for TNO-5 are presented in Fig 6.7.

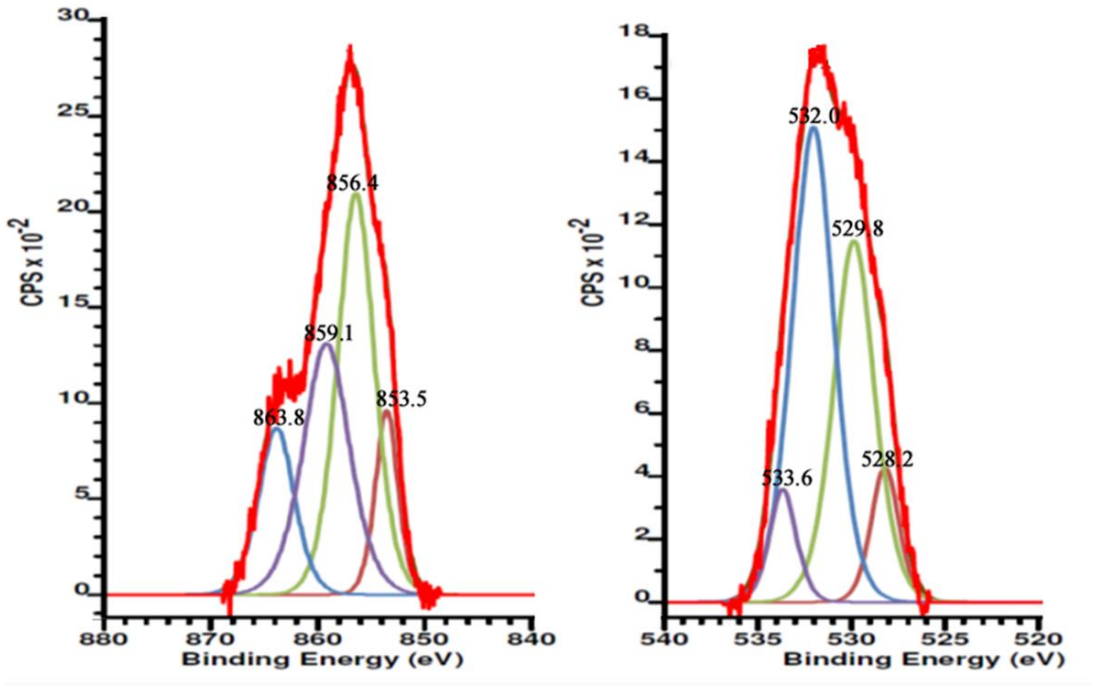

Figure 6.7: (a) Ni 2p and (b) O 1s XPS spectra of TNO-5.

The analysis of this sample was performed by Gauthaman Chandrabose (OU), who also provided Fig 6.7. Gauthaman has also done the processing and peak fitting of the XPS data for TNO-10 and other Ni-Ti composites. The deconvoluted Ni 2p spectra suggests the presence of Ni^{2+} (853.5 eV), Ni^{3+} (856.4, 863.8 eV) and Ni^0 (859.1 eV) species. However, further analysis is required to confirm the presence of metallic Ni^0. Similarly, deconvolution of O 1s spectra shows the presence of four peaks at 528.2, 529.8, 532.0 and 533.6 eV corresponding to Ni-O,

Ni-O-OH/Ti-O, -OH and physically adsorbed water, respectively. Finally, the Ni 2p and P 2p XPS spectra for TNP-5s is provided in Fig 6.8.

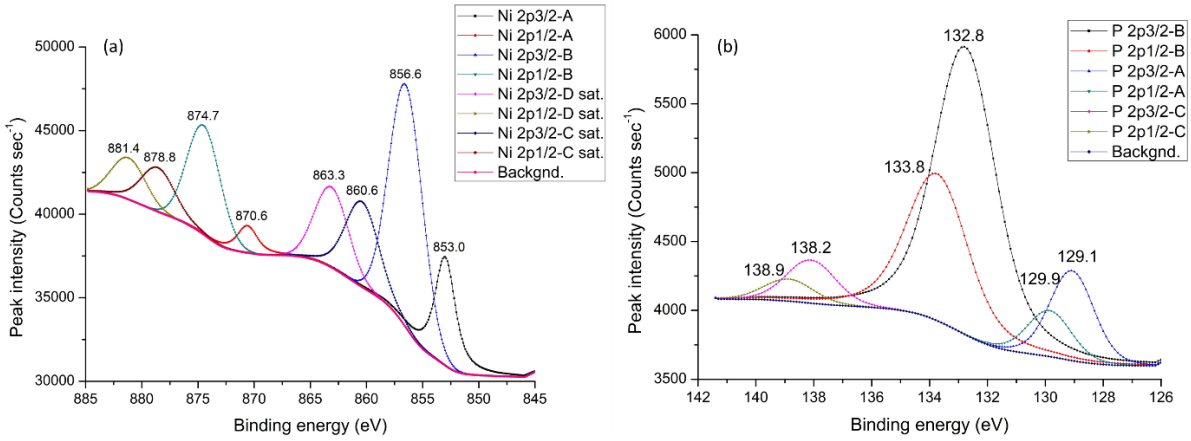

Figure 6.8: (a) Ni 2p and (b) P 2p XPS spectra of TNP-5s.

In the Ni 2p spectrum of TNP-5s, the peak observed at BE of 853.0 eV can be assigned to partially $Ni^{\delta+}$ and is a characteristic of Ni_2P.[19] The corresponding peak for $Ni^{\delta+}$ can be observed at 870.6 eV, resulting in a splitting energy difference of 17.6 eV. Both these observations further confirm the presence of Ni_2P. The peaks observed at 856.6 and 860.6 correspond to the Ni^{2+} (oxidized) and satellite Ni $2p_{3/2}$. The remaining peaks can also be classified similarly, corresponding to a splitting energy difference of 17.6 eV. In the P 2p core spectra, peaks located at 129.1 and 129.9 eV indicate the presence of $P^{\delta-}$ in Ni_2P. However, the spectra also suggest the presence of metal phosphate owing to the strong peaks located at BEs of 132.8 and 133.8 eV. The presence of peaks corresponding to phosphate in both Ni and P core spectra suggest that Ni_2P undergoes significant oxidation upon exposure to atmosphere. Unfortunately, reliable information about the origin and nature of peaks observed at 138.2 and 138.9 eV could not be found in literature, and further analysis might is required.

Preliminary investigation of the XPS spectra for all samples indicate that the intended Ni-compounds could be successfully synthesized. Hence, it is now possible to undertake hydrogen evolution experiments.

6.4.4 Photocatalytic hydrogen evolution

Complete details of the hydrogen evolution setup used in this study has been provided in section 3.6.4. Initially, 5 mg each of the phase pure samples along with TNH-1, TNO-1, TNP-1 and TNP-1s were added to 3 mL of deionized water, and the experiment was performed for a total duration of 4 h under constant stirring. No hydrogen evolution was observed over any of the samples upon using pure water. This could be attributed to the lack of a suitable cocatalyst

or active sites for the OER. Hence, the experiment was repeated using 3 mL aqueous solution of sodium ethylenediaminetetraacetic acid (Na-EDTA) (0.1 M, pH=4.5), which acts as a sacrificial electron donor. In the presence of Na-EDTA, a minor quantity of hydrogen evolution was observed for pure Ni_2P along with TNH-1, TNP-1 and TNP-1s. Hence, these samples were selected for further analysis, whereas the evolved hydrogen for pure Ni_2P (0.698 µM) was selected as reference.

Fig 6.9 displays the hydrogen evolution rate for different samples as a function of Ni-loading. It can be observed that photocatalytic hydrogen evolution follows the order: (salt precipitated) TNP-s>TNH>TNP. For 1 wt.% samples, the total evolved hydrogen is similar for all samples, which is approximately 0.16 µM for TNP-1s, 0.155 µM for TNH-1, and 0.147 µM for TNP-1. For samples containing $Ni(OH)_2$, the maximum rate of hydrogen production was observed for TNH-2.5 (0.342 µM). The rate and total hydrogen production was observed to decline with increasing $Ni(OH)_2$. However, the rate of hydrogen production increases significantly for TNP-s samples with increasing Ni loading. TNP-5s displayed a net hydrogen production of 0.981 µM, which increased to 0.993 µM for TNP-10s. This marginal increase of performance between samples with 5 and 10 wt.% loading suggest that over deposition of Ni_2P could be blocking light absorption for TiO_2. However, the net hydrogen production over regular TNP samples was consistently poor. This drastic difference between the catalytic activity of similar compounds suggests the importance of proper synthesis method. However, further analysis is required to confirm the underlying mechanism responsible for this improvement in catalytic activity (and lack thereof) for the different samples.

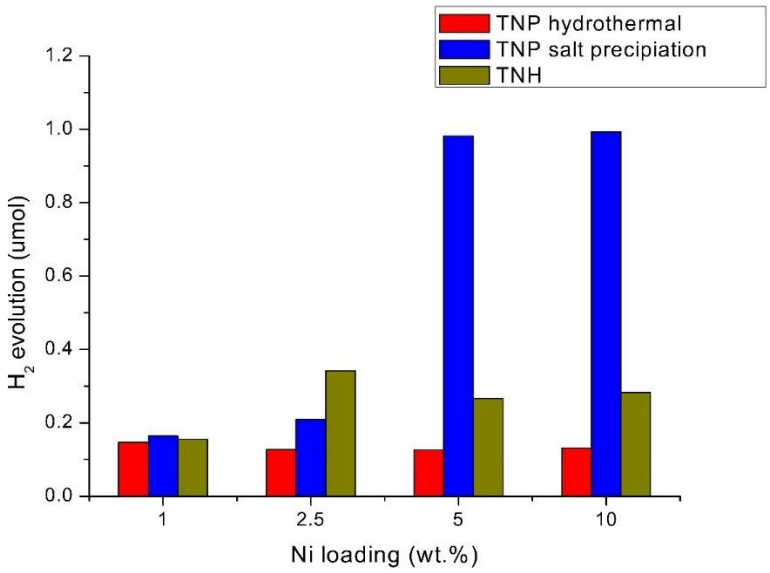

Figure 6.9: Hydrogen evolution as a function of Ni loading for various samples.

Considering the minor difference in activity between TNP-5s and 10s samples, the hydrogen production per unit Ni (wt.%) is higher in TNP-5s, which indicates that this is close to the optimum loading concentration. It is also important to determine the long-term stability of the as-prepared catalyst and ensure that auto-oxidation of Ni_2P is not responsible for the evolved hydrogen. Hence, to assess the photostability of the catalyst, an extended experimental run was performed under continuous illumination. A fresh vial was prepared using 3 mL (0.1 M) Na-EDTA and 5 mg TNP-5s. After purging the sample with the GC standard for 30 min, the mixture was illuminated continuously for seven days. During the test, gas samples were withdrawn from the headspace of the vials intermittently and tested for the amount of evolved hydrogen. Fig 6.10 displays the net hydrogen evolution over TNP-5s under continuous illumination for seven days. It can be observed from the graph that an almost linear rate of hydrogen evolution was observed over TNP-5s. After a total illumination period of 168 h, 50.8 µM of H_2 was evolved. These results demonstrate the excellent photostability of the prepared catalyst. Furthermore, to assess the photocatalytic performance, turnover number (TON) and turnover frequency (TOF) were calculated with respect to Ni_2P as follows:

$$TON = \frac{moles\ of\ hydrogen\ prouced}{moles\ of\ active\ catalyst} \tag{6.1}$$

$$TOF = \frac{TON}{reaction\ time} \tag{6.2}$$

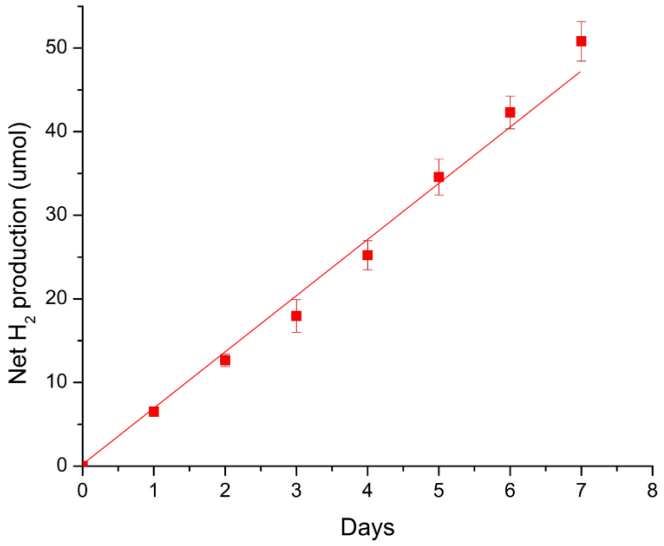

Figure 6.10: Net hydrogen evolution over TNP-5s for extended illumination.

Data from the extended illumination experiment reveals that TNP-5s has a stable TOF 0.179 $mol_{H2}.mol_{Ni2P}.h^{-1}$. Owing to the lack of reports on similar material systems, a comparative analysis with current state of the art cannot be provided. However, prima facie these numbers

are more than an order of magnitude smaller than recently reported Ni-TiO_2 based catalysts,[20] which is still lower than state of the art C_3N_4-based photocatalysts.[21]

6.5 Discussion

Even though the mechanism for increasing reaction kinetics is different for both electrocatalysis and photocatalysis, some of the underlying principles such as facilitating surface adsorption of proton and providing active sites for proton reduction to H_2 gas remain the same. Apart from this, other factors such as high surface area, electronic conductivity and improved reaction kinetics are also common in both fields. Furthermore, the ability of Ni to adsorb and release large quantities of hydrogen atoms prompted us to explore the possibility of using some established Ni electrocatalysts for photocatalytic hydrogen evolution. It has been previously reported that in the presence of UV light, most Ni compounds including NiO can be reduced to metallic Ni,[22] which in turn acts as a cocatalyst by promoting rapid electron transfer between TiO_2 and surface adsorbed hydrogen.[23] Hence, to avoid the formation of metallic Ni and evaluate the effect of different compounds all experiments were performed under visible light. Both 2D plate-like β-$Ni(OH)_2$ and Ni_2P have been extensively reported for electrocatalytic and photoelectrocatalytic water splitting, whereas NiO has been traditionally reported as a cocatalyst for photocatalytic hydrogen evolution. Literature review indicates that $Ni(OH)_2$ can serve as a precursor for both NiO[16] and Ni_2P,[15] hence TNH samples were fabricated first and used as starting materials for preparation of both TNO and TNP nanocomposites.

Preliminary results provided in this study indicate that pure TiO_2, NiO and $Ni(OH)_2$ are unable to generate hydrogen using visible light even in the presence of sacrificial agents. However, significant hydrogen production was observed pure Ni_2P. Similarly, no hydrogen production was observed for NiO decorated TiO_2, whereas TiO_2 nanocomposites with both $Ni(OH)_2$ and Ni_2P showed significant hydrogen evolution. In case of $Ni(OH)_2$, it has already been reported that the slightly lower reduction potential of Ni^{2+}/Ni (E^0=-0.23 V) with respect to cb of TiO_2 (E^0=-0.26 V) enables rapid electron transfer from TiO_2 cb to $Ni(OH)_2$ nanoclusters. This reduces $Ni(OH)_2$ to metallic Ni, which act as active site for proton reduction.[24] However, in such earlier studies $Ni(OH)_2$ used was amorphous in nature and UV light is required to enable reduction of $Ni(OH)_2$ to metallic Ni as the energetic electrons must originate in the cb of TiO_2. The presence of UV light and amorphous nature of $Ni(OH)_2$ in the earlier study could be responsible for the difference in activity of the TNH samples with that reported in literature. However, there are no reports available in the literature describing the hydrogen evolution activity of TiO_2-Ni_2P compounds in visible light.[153] Ni_2P has already been reported for its excellent stability and photoactivity in the visible region,[151,153] which is also reflected in the

results obtained in this study. The results also indicate that materials developed for improving the HER in electro and photoelectrolysis of water can also be used as suitable cocatalysts for photocatalytic hydrogen evolution. However, further research is required to uncover the mechanism(s) responsible for the ameliorated performance. Based on this information further optimization with respect to both loading and morphology can be undertaken.

6.6 Conclusions

This chapter reports the fabrication and assessment of various Ni-titania nanocomposites for visible light induced photocatalytic hydrogen evolution. Three different Ni compounds namely β-$Ni(OH)_2$, NiO and Ni_2P with different loading concentration (1, 2.5, 5 and 10 wt.%) were fabricated. Characterization techniques such as XRD, TEM and XPS were utilized to confirm the phase and morphology of the as-prepared composites. It was observed that hydrothermal synthesis leads to the production of large sub-micrometre sized particles, which can be avoided with salt precipitation technique. Photocatalytic experiments revealed that for $Ni(OH)_2$ 2.5 wt.% loading is optimum and leads to a hydrogen evolution rate of 17 $\mu mol.h^{-1}.g^{-1}$ under visible light, whereas no hydrogen production was observed for NiO containing compounds. TiO_2-Ni_2P composites prepared from β-$Ni(OH)_2$ also displayed poor photocatalytic activity. However, TiO_2-Ni_2P nanocomposites prepared by salt-precipitation method showed a high and stable hydrogen production rate. The highest hydrogen evolution rate of 60.5 $\mu mol.h^{-1}.g^{-1}$ was demonstrated by sample containing 5 wt.% Ni_2P, which could be sustained for 168 h under constant illumination. These results indicate that Ni_2P can be used as a stable and efficient cocatalyst for visible light hydrogen evolution. However, TiO_2 is not suitable for development of a stable and practical photocatalyst for hydrogen evolution, In this regard, the prospect of properly engineered C_3N_4 are much better as it offers better band positions, visible light absorption, quantum efficiency, and economy of production and operation. Finally, these preliminary results also serve as a proof of concept that electrocatalysts can potentially be employed for photocatalytic water splitting.

6.7 Planned work

The results presented here form a part of an ongoing investigation and the following is suggested future work. Further characterization such as electrochemical impedance spectroscopy, transient photocurrent measurement or photoluminescence emission spectroscopy will help to evaluate various features such as flat band potential and generation and transport of the photogenerated charge carriers for pristine and nanocomposite samples. To further evaluate the role of Ni compounds on the bandgap, techniques such as diffuse

reflectance spectroscopy and ultraviolet photoemission spectroscopy should be employed. TEM images have revealed a large variation in the particle size of the samples prepared by different techniques. Hence, determination of effective surface area and Ni loading between various samples is important to normalize and evaluate the relative performance. Finally, the effect of pH and sacrificial agents on the net hydrogen evolution will also be studied.

6.8 Acknowledgements

I would like to acknowledge the following people for the various help and input received towards the completion of this study. Mr. Gauthaman Chandrabose (OU) for providing the complimentary XPS data and the first set of TEM images. Dr. Giorgio Divitini (MSM) for his help in acquiring the second set of TEM images. Mr. Arjun Vijeta (Christian Doppler Laboratory, Cambridge) for his help with conducting the photocatalytic hydrogen production experiments.

References

1 Akira Fujishima and K Honda, Nature **238** (5385), 37 (1972).

2 Vignesh Kumaravel, Snehamol Mathew, John Bartlett, and Suresh C. Pillai, Applied Catalysis B: Environmental **244**, 1021 (2019).

3 Jingsheng Cai, Jiali Shen, Xinnan Zhang, Yun Hau Ng, Jianying Huang, Wenxi Guo, Changjian Lin, and Yuekun Lai, Small Methods **3** (1), 1800184 (2019).

4 Mohammad Ziaur Rahman, Kenneth Davey, and Shi-Zhang Qiao, Journal of Materials Chemistry A **6** (4), 1305 (2018).

5 Xiaobo Chen, Shaohua Shen, Liejin Guo, and Samuel S Mao, Chemical reviews **110** (11), 6503 (2010).

6 Ningzhong Bao, Liming Shen, Tsuyoshi Takata, and Kazunari Domen, Chemistry of Materials **20** (1), 110 (2008); Qin Li, Beidou Guo, Jiaguo Yu, Jingrun Ran, Baohong Zhang, Huijuan Yan, and Jian Ru Gong, Journal of the American Chemical Society **133** (28), 10878 (2011); Zhigang Chai, Ting-Ting Zeng, Qi Li, Liang-Qiu Lu, Wen-Jing Xiao, and Dongsheng Xu, Journal of the American Chemical Society **138** (32), 10128 (2016).

7 Xinchen Wang, Kazuhiko Maeda, Arne Thomas, Kazuhiro Takanabe, Gang Xin, Johan M. Carlsson, Kazunari Domen, and Markus Antonietti, Nature Materials **8**, 76 (2008); Shaowen Cao and Jiaguo Yu, The Journal of Physical Chemistry Letters **5** (12), 2101 (2014).

8 Lei Cheng, Quanjun Xiang, Yulong Liao, and Huaiwu Zhang, Energy & Environmental Science **11** (6), 1362 (2018).

9 Jiuqing Wen, Jun Xie, Xiaobo Chen, and Xin Li, Applied Surface Science **391**, 72 (2017).

10 Amene Naseri, Morasae Samadi, Ali Pourjavadi, Alireza Z. Moshfegh, and Seeram Ramakrishna, Journal of Materials Chemistry A **5** (45), 23406 (2017).

11 J. F. Guayaquil-Sosa, Benito Serrano-Rosales, P. J. Valadés-Pelayo, and H. de Lasa, Applied Catalysis B: Environmental **211**, 337 (2017); Hui-Jie Hou, Xiao-Hu Zhang, De-Kang Huang, Xing Ding, Sheng-Yao Wang, Xiang-Long Yang, Sheng-Qing Li, Yong-Gang Xiang, and Hao Chen, Applied Catalysis B: Environmental **203**, 563 (2017); Tumelo W. P. Seadira, Gullapelli Sadanandam, Thabang Ntho, Cornelius M. Masuku, and Michael S. Scurrell, Applied Catalysis B: Environmental **222**, 133 (2018).

[12] Ali Eftekhari, International Journal of Hydrogen Energy **42** (16), 11053 (2017).
[13] Lucas-Alexandre Stern, Ligang Feng, Fang Song, and Xile Hu, Energy & Environmental Science **8** (8), 2347 (2015); Zhifeng Liu and Xuan Wang, International Journal of Hydrogen Energy **43** (29), 13276 (2018); Mengyuan Zhang, Rajini P. Antony, Sing Yang Chiam, Fatwa Firdaus Abdi, and Lydia Helena Wong, ChemSusChem **0** (0).
[14] Harald Reiche and Allen J Bard, Journal of the American Chemical Society **101** (11), 3127 (1979).
[15] Jiayuan Li, Jing Li, Xuemei Zhou, Zhaoming Xia, Wei Gao, Yuanyuan Ma, and Yongquan Qu, ACS Applied Materials & Interfaces **8** (17), 10826 (2016).
[16] Zhen-Hua Liang, Ying-Jie Zhu, and Xian-Luo Hu, The Journal of Physical Chemistry B **108** (11), 3488 (2004).
[17] Zewei Yang, Bing Wang, Hao Cui, Hao An, Yang Pan, and Jianping Zhai, The Journal of Physical Chemistry C **119** (29), 16905 (2015).
[18] Abdelnaby M. Elshahawy, Kuan Hung Ho, Yating Hu, Zhen Fan, You Wei Benedict Hsu, Cao Guan, Qingqing Ke, and John Wang, CrystEngComm **18** (18), 3256 (2016).
[19] Ali Han, Huanlin Chen, Zijun Sun, Jun Xu, and Pingwu Du, Chemical Communications **51** (58), 11626 (2015); Deqian Zeng, Wanjie Xu, Wee-Jun Ong, Juan Xu, He Ren, Yuanzhi Chen, Hongfei Zheng, and Dong-Liang Peng, Applied Catalysis B: Environmental **221**, 47 (2018).
[20] Yi Wei, Gang Cheng, Jinyan Xiong, Feifan Xu, and Rong Chen, ACS Sustainable Chemistry & Engineering **5** (6), 5027 (2017).
[21] Jixiang Xu, Yinhong Qi, Chao Wang, and Lei Wang, Applied Catalysis B: Environmental **241**, 178 (2019).
[22] Wan-Ting Chen, Andrew Chan, Dongxiao Sun-Waterhouse, Toshihiro Moriga, Hicham Idriss, and Geoffrey I. N. Waterhouse, Journal of Catalysis **326**, 43 (2015).
[23] Phong D. Tran, Lifei Xi, Sudip K. Batabyal, Lydia H. Wong, James Barber, and Joachim Say Chye Loo, Physical Chemistry Chemical Physics **14** (33), 11596 (2012).
[24] Jiaguo Yu, Yang Hai, and Bei Cheng, The Journal of Physical Chemistry C **115** (11), 4953 (2011).

Chapter 7

Other avenues: photocatalysts with internal electric field

7.1 Introduction

TiO_2 or titania (anatase phase) is one of the oldest and most investigated material in the field of photocatalysis.[1] It is chemically and physically stable, economic to produce, easily available and non-toxic, which makes it highly desirable for photocatalytic applications. Over the years P25 Degussa (mixture of anatase and rutile phases) has come to be regarded as the 'gold standard' in photocatalysis owing to its excellent photoactivity.[2] Hence, the performance of other materials is often evaluated relative to it. However, owing to its large band gap (~3.2 eV) it is only active in the ultraviolet (UV) region, which accounts for only (approximately) 5% of the available energy in the solar spectrum.[2] Majority of the incident electromagnetic energy is contained in the visible spectrum (44%), which remains untapped. Hence, pristine TiO_2 needs to be modified such that it can harness visible light energy. Modification of TiO_2 usually entails band engineering[3], doping (metal/non-metal) and formation of heterogeneous multi-component materials.[4] However, as discussed in previous section, each of these techniques has its own set of advantages and limitations and may not always be a practical solution. In this regard, replacing TiO_2 with an alternate/better material as the base semiconductor can be an effective approach. The selection of a new semiconductor can be tailored to specific applications. For example, in reactions requiring water splitting (hydrogen production) the base material should have a conduction band edge much lower than reduction potential of NHE. Similarly, oxidation of water-borne pollutants can benefit from a higher valence band edge. Notably, non-TiO_2 heterogeneous catalysts have shown promise for rapid growth and improvement, and exhibit excellent stability.[5] One such emerging material in this field is bismuth oxychloride (BiOCl).[6-13] BiOCl is a wide bandgap (3.6 eV) semiconductor which is active in the UV region.[12] Primarily, its high bandgap puts it at a disadvantage compared to anatase (3.2 eV). However, it possesses a remarkably high quantum efficiency and the ability to form heterojunction with its native oxide, chloride or sulphide compounds, which renders it visible light active.[6,7,9,10,13] These potential advantages have sparked a flurry of research into the field of Bi-based multi-component catalysts over the past few years. Many studied have reported various Bi-based compounds such as Bi/BiOCl[12], $BiPO_4$/BiOCl[13], Bi_2O_3/BiOCl[10,11], BiOCl/$BiVO_4$[9], Fe(III)-modified BiOCl[8], BiOCl/$Bi_2Sn_2O_7$[7], and $Bi_{24}O_{31}Cl_{10}$/BiOCl[6] among others. However, majority of these studies have been limited to different compounds of Bi which are independently

sensitive to visible light, but unstable and (potentially) toxic. Hence, it is highly desirable to develop a stable support for BiOCl that can also help to improve its sensitivity to visible light. Previous research has demonstrated that ferroelectrics form an interesting new field of photocatalytic materials owing to their unique advantages of Stern-layer formation and band-bending.[14,15] $Bi_{0.5}Na_{0.5}TiO_3$ (BNT) is an established Bi-based ferroelectric material which is explored for its excellent piezoelectric and pyroelectric properties.[16,17] Even though pristine BNT is a poor photocatalyst,[15] the Bi-rich phase in BNT can be used for growth of BiOCl on its surface. In this regard, this study reports a suitable combination of BNT with BiOCl through a heterojunction. The resulting composite material (BNT/BiOCl) exhibits unprecedented visible light photocatalytic activity.

Ferroelectric materials possess spontaneous (remnant) polarization (below Curie temperature), which is stable under a wide range of environmental conditions including those that are chemically aggressive.[18] This bulk polar vector draws holes towards the negative potential and electrons towards the positive potential regions of the grain, respectively. Consequently, a space-charge region is created which imparts several beneficial features including: (i) Stern-layer formation, (ii) band bending, (iii) enhanced chemisorption on the surface, (iv) bond bending of polar species, and most importantly (v) effective charge separation and enhanced life-time of photogenerated electron-hole pairs.[19] Owing to selective potential surface availability, ferroelectric materials are ideal for separation REDOX sites, thus, prevent recombination and back reactions . Based upon these facts, it can be concluded that despite lacking any evident sensitizing effect or photoactivity, presence of BNT could be potentially beneficial to enhance the catalytic properties of BiOCl. Hence, this chapter reports the development of a facile method for fabricating a stable BNT/BiOCl composite photocatalyst. The composite was characterized for its phases, structural and optical properties. It was observed that the as-prepared composite catalyst is visible-light active despite a large bandgap. Furthermore, the material displays excellent and stable photocatalytic activity, which makes it a strong contender for solar-water treatment applications.

7.2 Photocatalyst synthesis

Pure BiOCl catalyst was prepared according to a previously reported study.[20] Briefly, 3 mmol of $Bi(NO_3)_3 \cdot 5H_2O$ was added to 50 mL deionized water and stirred for 60 min. The resulting turbid solution was transferred to an autoclave (100 mL) and heated at 160 ^oC for 24 h under autogenous pressure. The synthesized BiOCl particles were recovered using a centrifuge (4400 rpm, 10 min), washed several times with ethanol and water, and dried overnight in a vacuum furnace at 80 ^oC.

BNT powder was prepared through a conventional solid-state reaction technique. Briefly, powders of $BiCO_3$, Na_2CO_3 and TiO_2 were weighed in stoichiometric ratios and ground using mortar-pestle for 2 h to aid mixing and obtain physical homogeneity. The ground powders were then transferred to an alumina crucible and calcined at a temperature of 800 ^oC for 2 h. The ramp rate during both heating and cooling processes was kept at 5 $^oC.min^{-1}$. The calcined powders were ground again for 2 h to break any agglomeration encountered during the calcination process.

BNT powder obtained in the previous step was separated into four batches. The first batch, marked as 'zero', was kept as a reference sample whereas the rest of the batches were treated with dilute HCl (50 mL, 0.1 M) for 15, 30 and 60 min and designated as 5%, 10%, and 15% BNT-BiOCl, respectively. Post-treatment powders were recovered by centrifuging at 4400 rpm for 10 minutes and washed several times with ethanol and water to remove any residual ions. The wash-cycles were continued until the supernatant achieved a pH of ~7.0. Subsequently, the treated powders were dried over-night (~10 h) in a vacuum furnace (held at 80 ^oC) to finally obtain the composite catalysts.

7.3 Growth and formation of BNT-BiOCl

Fig 7.1(a) provides a schematic description of the various processes leading to the formation of BiOCl on the surface of $Bi_{0.5}Na_{0.5}TiO_3$ in the presence of dilute HCl. Literature review indicates that BNT is attacked in the presence of concentrated HCl, which triggers the nucleation-dissolution-recrystallization process.[21,22,23] In the present scenario, Bi^{3+} ion reacts with the Cl^{-1} to produce $BiCl_3$, which dissolves in presence of excess HCl (step 1). This is followed by an immediate hydrolysis of $BiCl_3$ to form precipitates of BiOCl on the surface of BNT (step 2). This initial layer serves as a nucleus for further growth of BiOCl, as progressively more Bi is leached away from the surrounding area and deposited onto the seed layer (step 3). The process continues until either Bi^{3+}/Cl^{-1} ions are depleted or the whole surface is passivated by the formation of BiOCl, which prevents further leaching of BNT.

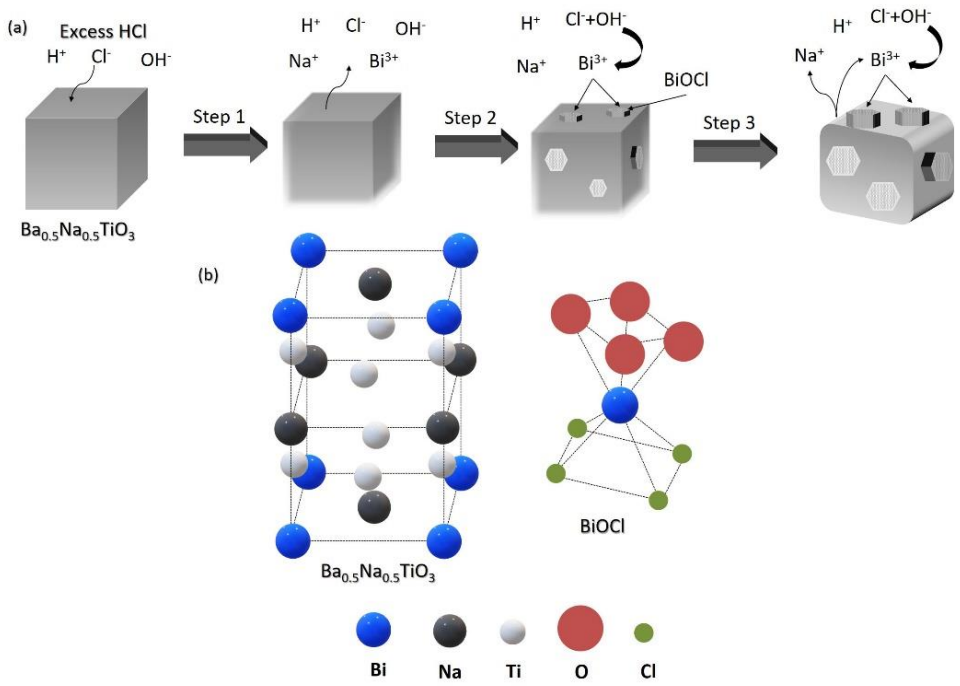

Figure 7.1: (a) Step-wise formation and growth of anisotropic BiOCl on the surface of $Bi_{0.5}Na_{0.5}TiO_3$. (b) Representative unit cells for $Bi_{0.5}Na_{0.5}TiO_3$ and BiOCl.

In the present study, excess HCl serves as both an acidic medium and as a source of aqueous Cl^{-1} ions. A detailed description of this mechanism was provided by Li et al. for Bi_2O_3 film,[21] and recently verified by Singh and Vaish with $SrO\text{-}Bi_2O_3\text{-}B_2O_3$ glass ceramic containing $SrBi_2B_2O_7$ nanocrystals[23]. In case of Li et al. NaCl was used as a source of Cl^{-1} ions required for BiOCl synthesis.[21] At a pH of 2.0 dense and uniform BiOCl films could be obtained within 30 min. However, the recent results by Singh and Vaish suggests that a much smaller time scale (~5 min) can be sufficient to initiate the growth of BiOCl. Once the initial layer is deposited, the growth rate for the subsequent layers increases considerably with time until complete conversion is achieved. The following characterization data not only supports this theory but also confirms the successful formation of BiOCl on the surface of BNT.

7.4 Characterization

The physical, chemical, and optical properties of the as-prepared catalysts were characterized using the following techniques.

7.4.1 Powder X-ray diffraction analysis

Fig 7.2 displays the acquired X-ray diffractograms for all samples under study. For the pristine samples, the peaks could be easily indexed to tetragonal structure of BNT (JCPDS card no. 46-0001) and BiOCl (JCPDS card no. 06-0249), in which the lack of any excess or anomalous

peaks confirmed the phase purity of the samples (within the detection limit). Similar analyses were conducted for the treated catalyst (15-60 min) and are compared with the XRD pattern for pure samples. It can be observed that with increasing treatment time, the peaks progressively start resembling that of pure BiOCl (peak evolution at 25˚ and 33˚). However, the underlying BNT peaks (position) remain clearly visible and unaltered. The lack of distinct peaks corresponding to BiOCl phase in the XRD patterns of 15- and 30-min samples could be attributed to its low weight percentage, which is below the detection limit of the instrument. The peak positions for the evolved BiOCl on the acid-treated samples is in good agreement with the pristine BiOCl. However, the relative peak intensity of the composite powders does not match well with the prepared BiOCl. This could be attributed to the different/random orientation of BiOCl on the BNT particles compared to pure (two-dimensional) BiOCl, which exhibits a prominent (001) orientation.[20]

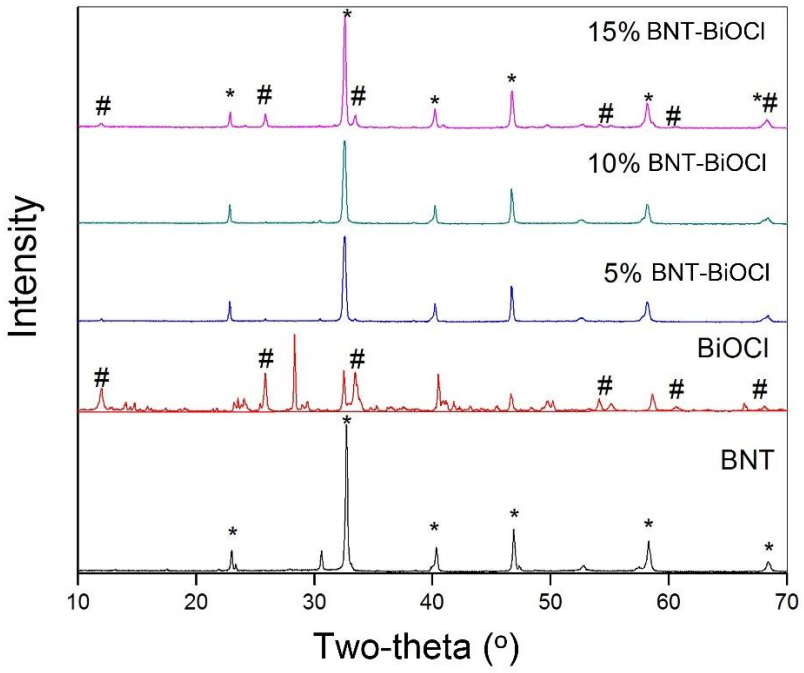

Figure 7.2: Powder X-ray diffraction patterns for all samples understudy.

7.4.2 X-ray photoelectron spectroscopy

To investigate the surface chemical composition of the prepared catalysts, XPS analysis was performed. Fig 7.3a, b and c display the XPS (survey) spectra for BNT, BiOCl and 15% BNT-BiOCl composite catalysts, respectively. Corresponding data for scanned peaks along with their respective binding energies (BEs) are reported in Table 7.1. The C 1s peak observed at ~284 eV can be attributed to the presence of a thin layer of adventitious C, which is inevitable in XPS

measurements of samples exposed to atmosphere. The surveyed spectrum was used to clearly detect the presence of all constituent elements in both pure and composite catalysts.

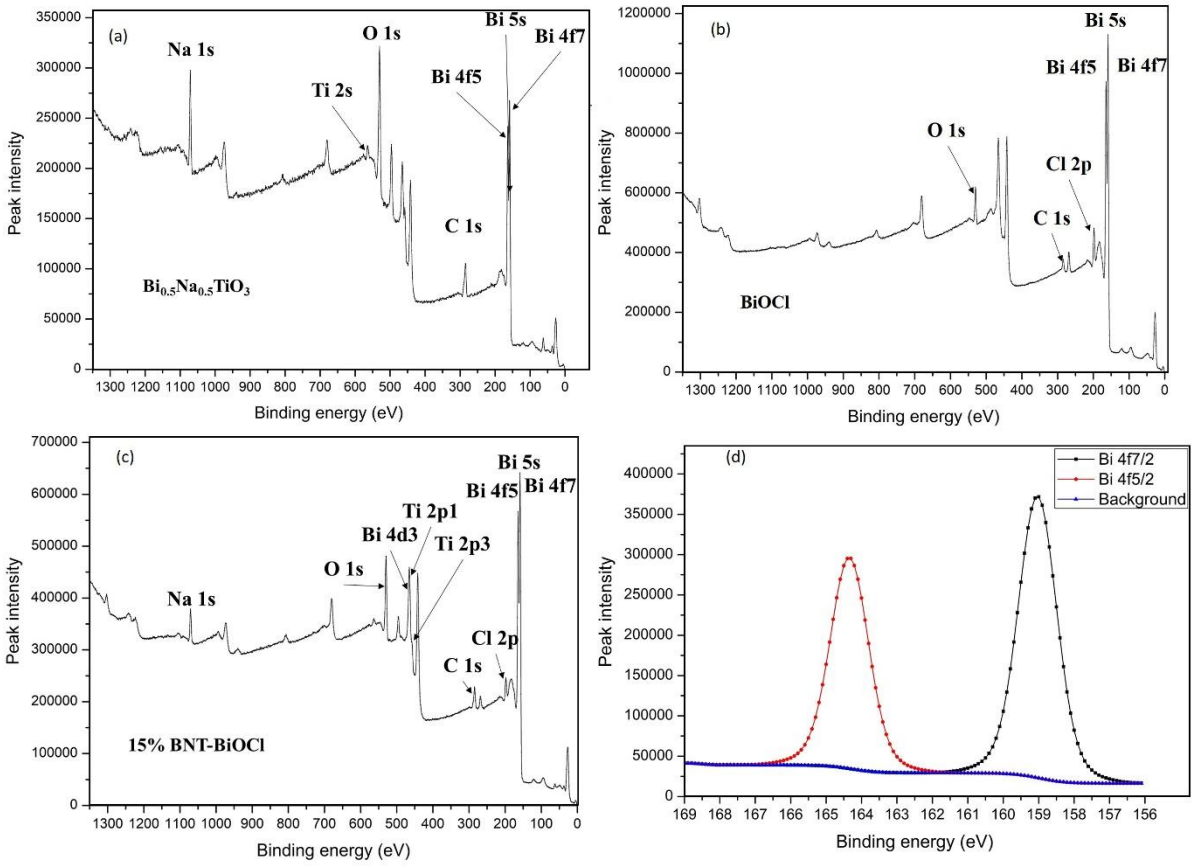

Figure 7.3: XPS survey spectrum for (a) pure $Bi_{0.5}Na_{0.5}TiO_3$, (b) pure BiOCl and (c) 15% BNT-BiOCl; (d) high-resolution scan for Bi 4f peaks.

However, the build-up of adventitious carbon on the catalyst adversely affected the XPS measurements. Primarily, even though the presence of Na in both BNT and BNT-BiOCl could be confirmed by the Na 1s peak observed at ~1071 eV; an in-depth spectrum for the same could not be obtained despite several scans. Fig 7.3d shows the shows the high-resolution XPS scan for Bi 4f orbitals. Two symmetrical peaks could be observed corresponding to binding energies of 159.1 and 164.4 eV for Bi $4f_{7/2}$ and Bi $4f_{5/2}$ orbitals, respectively. The two spin orbit components are separated by a binding energy difference of Δ5.3 eV, strongly indicating the presence of Bi^{3+} oxide. It is important to note that the binding energies of Bi^{3+} in the composite catalyst are similar to that of phase pure samples, suggesting a lack of change in the oxidation state of Bi post acid treatment. This observation stems from the fact that the BE values of Bi 4f orbitals are similar for both pure BNT and BiOCl. Hence, a transition from one to other cannot be detected using Bi orbitals alone.

Fig 7.4a shows the Ti 2p scan of 15% BNT-BiOCl, which is similar to that observed for pure BNT. The scan reveals a consistent presence of peaks at 458.5 and 464.2 eV, corresponding to Ti $2p_{3/2}$ and Ti $2p_{1/2}$ spins. Furthermore, a binding energy splitting value of ~Δ5.2 eV confirms the presence of Ti^{4+} oxide. Fig 7.4b displays the high-resolution scans for Cl 2p spectra of the 15% BNT-BiOCl sample. The Cl $2p_{3/2}$ and $2p_{1/2}$ peaks are located at 198 and 199.5 eV, respectively, which is characteristic of metallic chloride. However, the Cl $2p_{3/2}$ peak is shifted by a significant value of 0.5 eV towards lower binding energy compared to pure $BiCl_3$. This decrease in binding energy arises because of the higher electronegativity of Cl compared to O in BiOCl.

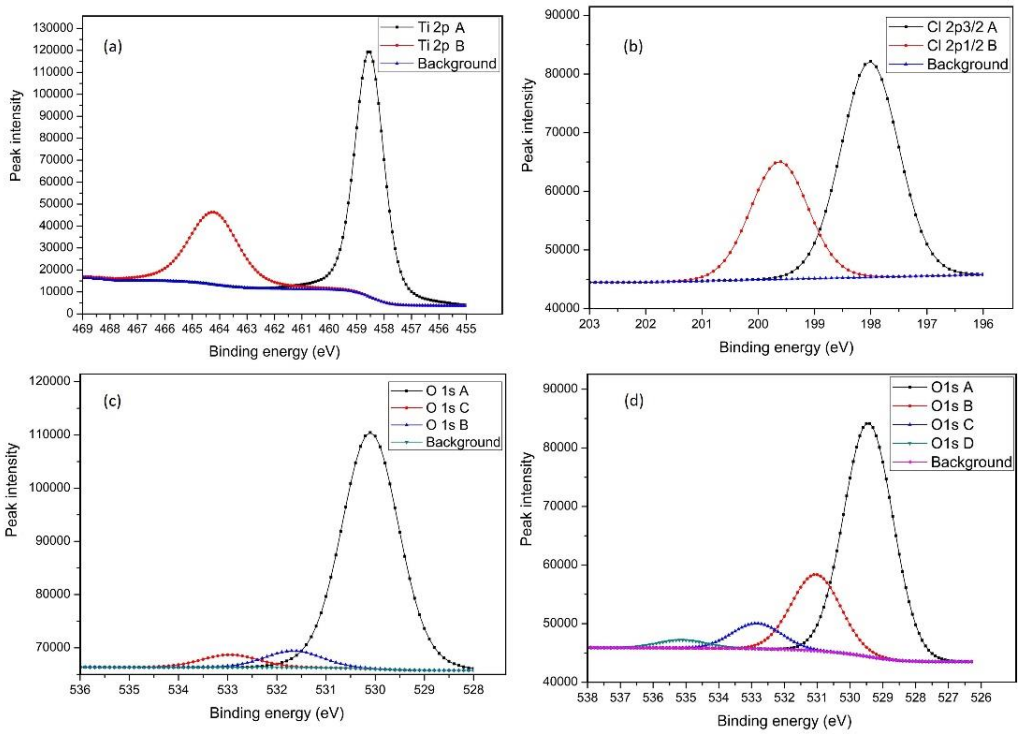

Figure 7.4: High resolution XPS spectra for (a) Ti 2p, (b) Cl 2p orbitals. O 1s plots for (c) BiOCl and (d) 15% BNT-BiOCl.

Finally, Fig 7.4c and d display the acquired O 1s spectra for BNT and 15% BNT-BiOCl catalysts, respectively. The largest peak designated as O 1s A was cantered at 530.1 and ~529.4 eV in BiOCl and the composite catalyst, respectively. Both these values are located in the BE range of 529-530 eV, which indicates a strong presence of metallic oxide. However, compared to the composite catalyst the O 1s A peak in BiOCl displays a shift of 0.5 eV towards higher BE. This corroborates well with shift observed in Cl $2p_{3/2}$ confirming the presence of lower electron density around O atoms in BiOCl owing to the higher electronegativity of Cl. This phenomenon is not observed for the composite sample, which could be attributed to the lower quantity of BiOCl compared to the parent BNT phase. The other two peaks in the O 1s spectrum

of BiOCl are located at 531.7 and 533 eV. The first peak lies in the range of (531.5–532 eV) and indicates the presence of CO_3^{2+} impurity on the surface, whereas the second peak corresponds to the presence of SiO_2 contamination. Similarly, three additional O 1s peaks are observed in the composite catalyst centered at 531, ~532.9 and ~535.2 eV. The latter two peaks can be attributed to the presence of SiO_2 (impurity) and overlap with Na KL2 auger peak. Given the overlapping nature of the peaks, further resolution is not possible. The presence of peak cantered at 531 eV could be attributed to either the presence of carbonates or alumina (Al_2O_3), both of which are possible impurities. However, given the strong intensity of the peak the presence of impurity alone is an unlikely explanation. Literature review does not indicate any other possible origin and hence, no explanation can be provided at present.

Table 7.1: XPS survey spectrum and corresponding peak locations for pure and composite catalysts.

Scan type	Binding energy (eV)	Additional note
$Bi_{0.5}Na_{0.5}TiO_3$ (BNT)		
Bi 4f7	158.16	
Bi 5s	161.67	
Bi 4f5	164.1	
C 1s	284.9	
O 1s	530.26	(~32% area is Na KL2)
Ti 2s	564.23	
Na1s	1071.02	(~3% area is Ti LM2)
BiOCl		
Bi 4f7	158.64	
Bi 5s	161.41	
Bi 4f5	164.5	
Cl 2p	198.16	
C 1s	284.55	
O1s	529.85	
15% BNT-BiOCl		
Bi 4f7	158.36	
Bi 5s	161.78	
Bi 4f5	164.18	
Cl 2p	197.96	

C 1s	284.72
Ti 2p3	458.26
Ti 2p1	463.46
Bi 4d3	466.2
O 1s	529.54
Na1s	1070.78

7.4.3 Raman spectroscopy

To complement the XPS and XRD data, confocal Raman spectroscopy was employed. All images were acquired at 5x magnification and 1% laser power, with a diffraction grating of 1800. Fig 7.5a, b, and c contain the Raman spectra for pure BNT, BiOCl and 15% BNT-BiOCl, respectively.

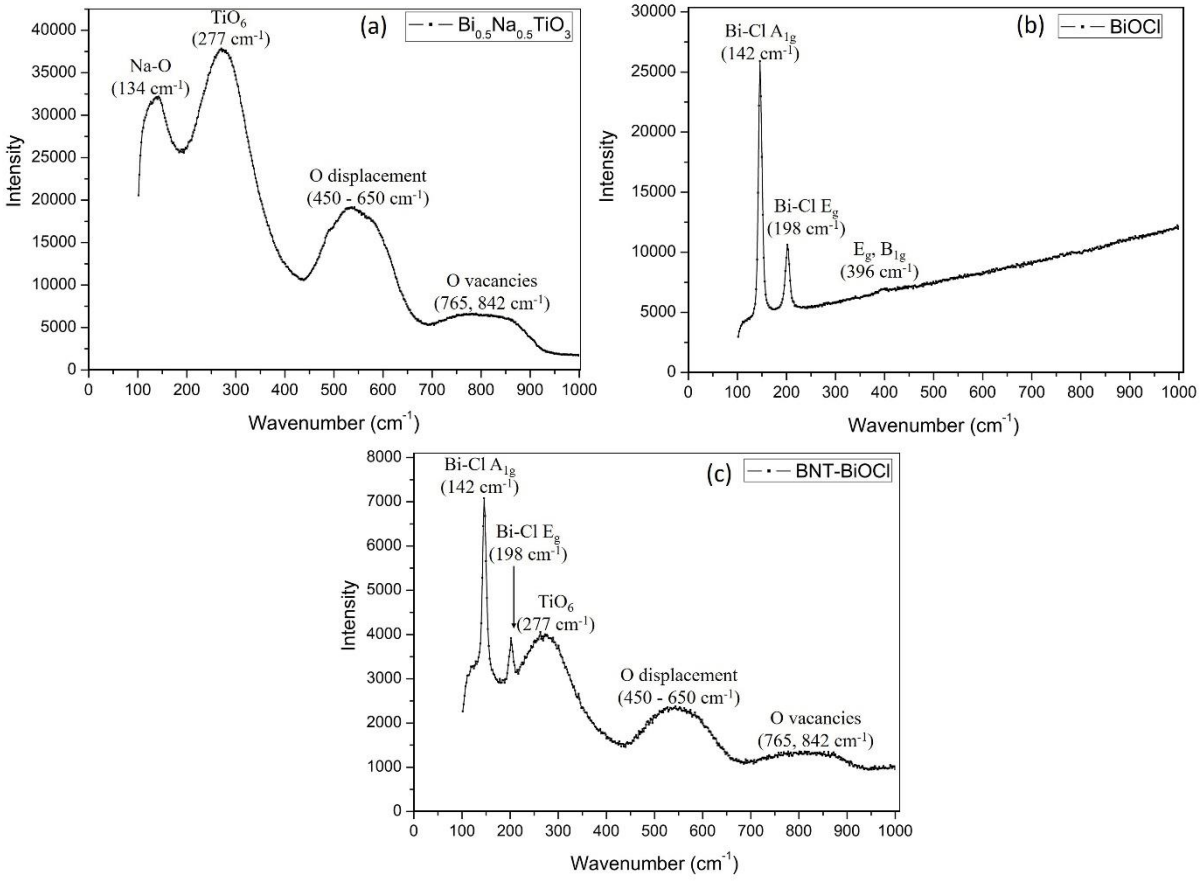

Figure 7.5: Raman spectra for (a) pure BNT, (b) pure BiOCl, and (c) 15% BNT-BiOCl.

The Raman spectra for pure BNT and BiOCl samples is in good agreement with that reported in literature.[16,24-26] BNT has six vibration modes, the first two modes observed at 130 and 279 cm^{-1} are associated with the presence of Na-O bond (A-site) and TiO_6 octahedra, respectively.

Both of these confirm the presence of ABO_3-type perovskite structure.[16,24,25] This is followed by modes observed due to presence of oxygen displacements (521 and 590 cm^{-1}) and oxygen vacancies (784 and 855 cm^{-1}). The peak broadening of the Raman spectra in BNT is often correlated to the small volume of the trigonal ferroelectric phase and lowering of symmetry.[24] Further, the absence of low frequency F_{2g} peak (30 cm^{-1}) indicates the lack of cubic phase, confirming the phase purity of the tetragonal ferroelectric structure.[24] Similarly, in pure BiOCl, only the peaks corresponding to the internal Bi-Cl stretching modes of A_{1g} (142 cm^{-1}) and E_g (198 cm^{-1}) could be observed.[20,26] The E_g and B_{1g} bands associated with the motion of oxygen atoms (396 cm^{-1}) were very weak. The Raman spectra acquired for 15% BNT-BiOCl composite, presented in Fig 7.5c, contains all the respective modes for the individual BNT and BiOCl phases. The lack of any additional modes indicate that the bond structure does not change after acid treatment and no additional phases are formed. The relatively higher intensity of the Bi-Cl stretching modes could be attributed to the enhanced scattering of the incident photons by the surface evolved BiOCl phase. This could also explain the lack of Na-O vibration mode, which is masked by the stronger signal from the Bi-Cl vibrations in the same vicinity. This data strongly indicates the presence of BiOCl phase on the surface of parent BNT phase in the composite catalyst.

7.4.4 Scanning electron microscopy imaging

All the characterization until this point show the evolution of phase and electronic structure of the as-prepared BNT-BiOCl. However, direct imaging of the particles is often required to confirm the evolution of microstructure and to determine the morphology of the resulting particles. Hence, SEM micrographs of the pure and treated BNT were obtained (Fig 7.6). Fig 7.6a reveals that the as-prepared BNT consist of well-defined cube-like particles with distinguishable edges and faces. The particle size distribution ranges between 0.8-2 µm with an average size of ~1 µm. Fig 7.6b displays the particles' morphology after being treated with HCl. It is easy to observe that treatment with acid distorts the original shape by creating etch-like features, which are clearly visible on the particle surfaces. Further, the presence of BiOCl is detected in the residual islands on the surface of BNT. Since the composite is still part of the original calcined powder, it is safe to assume that the generated BiOCl phase forms a heterojunction with the parent BNT phase.

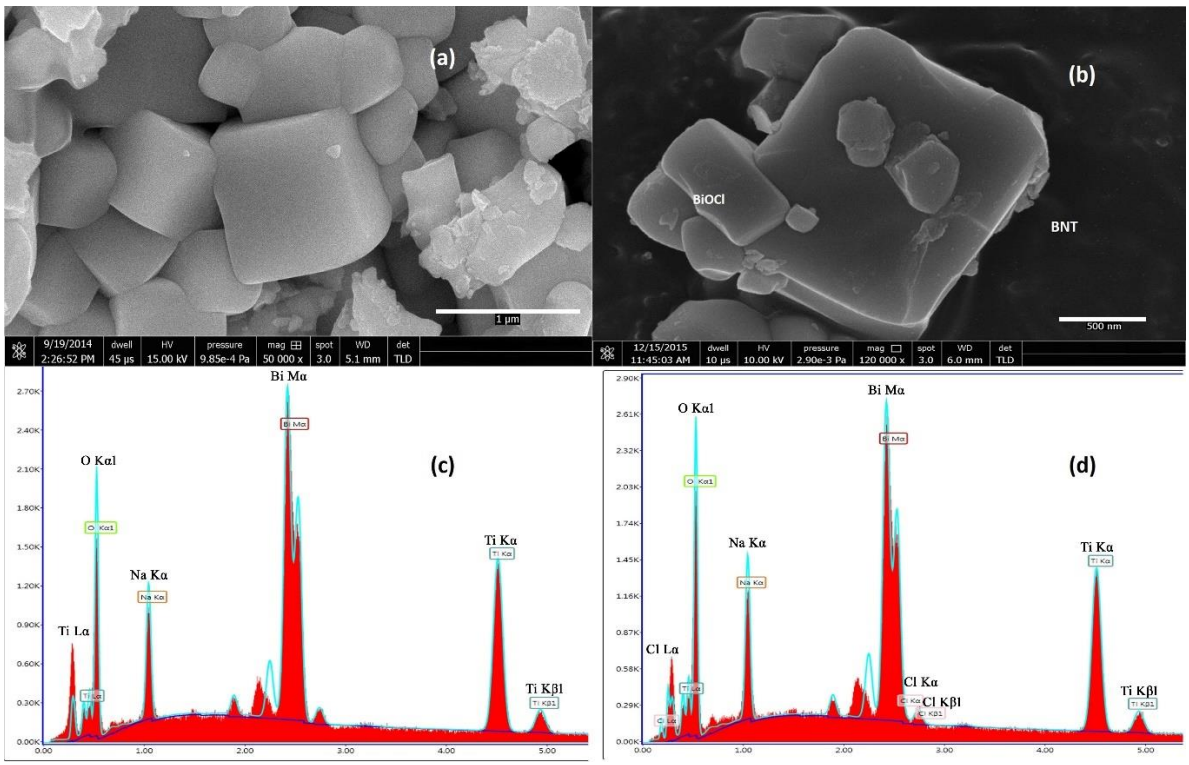

Figure 7.6: SEM micrographs of (a) pure and (b) treated (15% BNT-BiOCl) BNT samples and their corresponding EDX elemental mapping charts (below).

Elemental mapping was performed for area scans using energy dispersive X-ray (EDX) absorption spectroscopy for pure and treated BNT samples, reported in Fig 7.6c and d, respectively. EDX analysis confirms the original hypothesis of surface-grown BiOCl as a strong presence of Cl element was detected in the island-like structures while being almost negligible in other regions. This observation is in good agreement with results obtained from Raman spectroscopy. Notably, prolonged beam exposure in SEM has been previously reported to alter the surface morphology of BiOCl; as it is highly susceptible to melting under impinging electrons.[27]

7.4.5 Optical (UV/Vis and infrared) spectroscopy

UV/Vis diffuse reflectance and Fourier transform infrared spectroscopy analyses were conducted on all samples to determine the effect of progressive acid treatment on the BNT samples. All catalyst batches were studied using a full spectrum UV/Visible spectrophotometer in the reflectance mode. The diffuse reflectance spectroscopy (DRS) analysis reveals that formation of BiOCl does not interfere with the band positioning of BNT (Fig. 7.7a). A sharp drop in reflection is encountered for a wavelength of λ=420 nm, corresponding to a bandgap of 2.95 eV, which is in good agreement with the reported literature.[28] However, there is a stark difference between the reflection intensity beyond 400 nm for phase pure and acid-treated

samples. Compared to standard $BaSO_4$ internal reflectance standard, the untreated sample displays ~80% reflectivity in the visible region, whereas this number comes down to 60% for samples containing 5% and 10% BiOCl by weight. Furthermore, for the sample containing 15% BiOCl the reflectivity was further reduced to less than 55%. These plots reveal that the presence of BiOCl allows the composite to better absorb energy in the visible spectrum without affecting the band position. DRS data indicates a 25% improvement in absorption for 15% BNT-BiOCl compared to the untreated sample.

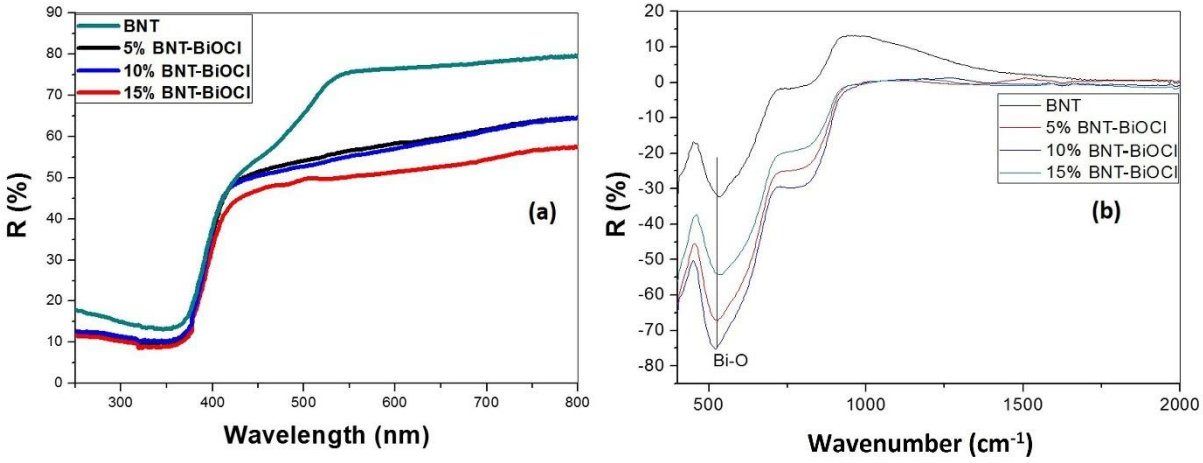

Figure 7.7: (a) Diffuse reflectance and (b) fourier transform infrared spectroscopy plots of the pristine and acid-treated BNT samples.

FTIR analysis was used to detect the presence of unreacted Cl^- impurities and other functional groups in the BNT-BiOCl heterostructures. Fig 7.7b shows the FTIR spectra of the pure BNT and BNT-BiOCl samples. The peak at approximately 523 cm^{-1} results from the symmetrical stretching vibration of the O–Bi bond, which is a characteristic peak of BiOCl. The intensity of band corresponding to Bi-O bond increases with the acid exposure time. This indicates an increased concentration of BiOCl sheets on the BNT surfaces, whereas an obvious shift of the absorption peak towards lower wavelength is observed associated with the stretching vibration of Bi-O bond. This is valent-symmetrical A_{2u}-type vibrations of Bi-O in BiOCl, representing the gradual compositional changes of the treated catalysts. The FTIR results are in good agreement with observation made using XRD, XPS, Raman and SEM analysis and further confirm the progressive formation of BiOCl phase with acid treatment.

7.5 Dye degradation experiments

The photocatalytic setup consisted of a pyrex glass vessel (100 mL) kept in a water-cooled temperature bath (25 °C). The setup was illuminated from above using a high-pressure mercury vapor lamp (125 W) kept at a distance of 15 cm and screened through a visible light cut-off

filter ($\lambda > 400$ nm). Described setup resulted in an equivalent (theoretical) illumination of 4.97×10^4 Lux at the surface of liquid. Primarily, to establish photocatalytic activity mineralization of Rh B solution (50 mL; 5 mg.L^{-1}) was employed as a model test. Absorbance data was acquired at $\lambda = 550$ nm with respect to the stock solution to determine percentage degradation. Fig 7.8a to c give different representations of the dye degradation parameters plotted as a function of time.

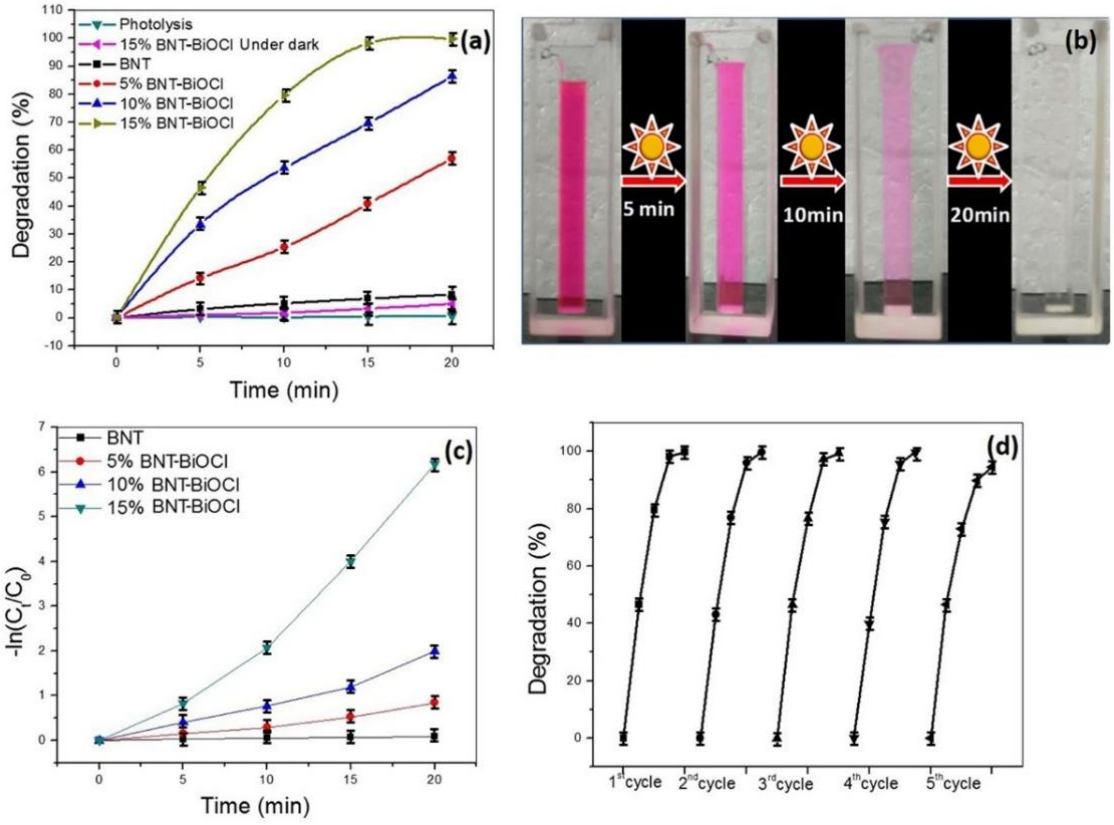

Figure 7.8: (a) Actual degradation of Rh B (%) plotted as a function of time for the tested samples; (b) observable de-colouration of Rh B solution in the presence of 15% BNT-BiOCl catalyst; (c) degradation rate constants for all samples corresponding to plots given in (a); and (d) reusability tests for 15% BNT-BiOCl composites.

Fig 7.8a describes the mineralization (%) with respect to the original concentration for various experimental setups. Control experiments were performed to analyse the change in dye concentration under pure photolysis/blank (no catalyst) and dark (no illumination) conditions. No change was observed in the dye concentration over a period of 20 min for photolysis experiments. Similarly, only minute changes were observed in the presence of untreated BNT and other catalysts in dark condition. Literature indicates that pure BiOCl is a poor visible light catalyst.[20] Hence, control experiments with BiOCl were not performed. This knowledge combined with the observation from dye degradation experiments confirm that the

mineralization observed under illuminated conditions can be solely attributed to photocatalysis in the presence of composite BNT-BiOCl. This is made even more evident by comparing the degradation curves observed for composite catalysts under visible light illumination (20 minutes). For 5% BNT-BiOCl a 50% degradation of the dye was observed, whereas for 10% BNT-BiOCl and 15% BNT-BiOCl samples 80% and 100% degradation could be achieved, respectively. The actual colour change at fixed time intervals has been depicted in Fig 7.8b, displaying complete mineralization (with a 15% BiOCl sample). In order to evaluate the apparent rate constant for degradation, the relative concentration ratio is plotted in Fig 7.8c. The rate constants for 15%, 10%, and 5% samples were calculated to be 0.36, 0.1, and 0.033 min^{-1}, respectively. Table 7.1 provides a comparative analysis of selected photocatalysts reported in the literature for degradation of Rh B. For reasons already discussed in section 5.7, a direct comparison between two different catalyst systems is not possible. Nevertheless, data listed in Table 7.1 provides a qualitative overview of different ferroelectric-, BiOCl-, and sensitized TiO_2-based systems which have reported visible light degradation of Rh B.

Table 7.1: Table lists recent selected examples of different ferroelectric-, BiOCl-, and TiO_2-based photocatalysts reported in literature for Rh B degradation.

Material	Catalyst conc. ($g.L^{-1}$)	Dye conc. ($mg.L^{-1}$)	Light source	Degradation (%)	Time (min)	Year	Ref
$BaTiO_3$-Ag	3	10	Solar simulator (AM 1.5G)	100	60	2015	[29]
Ag–AgCl–TiO_2/Pal	1.5	5	300 W Dy lamp (λ>400 nm)	100	20	2016	[30]
$Bi_2Fe_4O_9$/Bi_2WO_6	0.3	10	300 W Xe lamp (λ>420 nm; 155 mW cm^{-2})	100	90	2018	[31]
Poled $BaTiO_3$	0.5	10	300 W Solar simulator	44	90	2018	[32]
BiOCl/BiOI on rGO	0.25	10	350 W Xe lamp (λ>420 nm)	~100	9.61	2018	[33]
P25-C dots	0.68	15	84 W (λ>400 nm)	80	60	2019	[34]
$Bi_4Ti_3O_{12}$/BiOI	1	10	300 W Xe lamp (λ>420 nm)	100	12	2019	[35]
$BiFeO_3$/BiOCl	0.5	9.58	300 W Xe lamp (λ>420 nm)	60	75	2019	[36]
Au@$PbTiO_3$	1	9.58	500 W Hg-vapor lamp (λ>400 nm)	80	~210	2019	[37]
$BiFeO_3$	0.5	10	500 W Xe lamp	100	80	2019	[38]
BiOCl-Au	0.05	4.79	300 W Xe lamp (λ>420 nm)	93.8	20	2019	[39]
BiOCl/gC_3N_4 nanosheets	1	10	300 W Xe lamp (λ>420 nm)	~96	80	2019	[40]
$Bi_{0.5}Na_{0.5}TiO_3$-BiOCl	1	5	125 W Hg-vapor lamp (λ>400 nm)	100	~13	this study	

It is to be noted that photocatalysis is essentially a surface phenomenon and BiOCl is the active catalyst in the composite material. Since with prolonged acid treatment an increasing

concentration of BiOCl can be acquired on the surface, the correlation between the catalyst composition and degradation rates can be easily explained. Also, a decrease in particle size because of acid treatment would lead to increased activity owing to the enhancement in the specific surface area. Although the BNT particles are relatively large in the current work, their catalytic functionality can be clearly established.

Long term stability and resistance to photodegradation, anodic corrosion and poisoning are other important parameters for a practical catalyst. Hence, it is imperative to ascertain the reusability and long-term stability of the prepared catalyst. In this regard, Fig 7.8d displays the dye degradation results for 15% BNT-BiOCl for five consecutive cycles performed under similar experimental conditions. Before each cycle, the catalyst was recovered by centrifuging, washed repeatedly and dried in a vacuum oven at elevated temperature (80 ^{o}C) to rid of any stray dye molecules and moisture. The powder was then carefully weighed for any weight change and the experiment was repeated. The consistent performance of the composite catalyst indicates a lack of any unwanted galvanic reactions which could affect its reusability. Furthermore, for similar time frames and exposure conditions ~100% degradation was still observed even after five cycles, indicating the stability of the composites. This can be partly credited to the inertness of both the participating phases (BNT and BiOCl). BNT is an oxide perovskite (relaxor ferroelectric) and possesses high chemical stability, which is common to this class of compounds (oxide perovskites).[41] Similarly, BiOCl has been extensively investigated and reported for its chemical inertness in a wide variety of reaction medium.[42] Another important contributing factor could be the nature of phase evolution of BiOCl during fabrication process. BiOCl is formed at the surface of its parent phase BNT after suitable acid treatment. Hence, it possesses a strong bonding to the parent phase, which is often absent in similar catalysts prepared by two-step syntheses (surface deposition etc.). This bonding is expected to impart a good long-term stability to the composite material against loss of functionality through peeling, flaking or corrosion.

7.6 Discussion

Mechanism responsible for the improved photocatalytic activity of BNT-BiOCl along with the potential route for dye degradation is provided as follows.

7.6.1 Proposed band structure and improved photocatalytic activity

Despite both BNT (~3.0 eV) and BiOCl (>3.0 eV) having a large bandgap, the composite catalyst (BNT-BiOCl) displays significant photoactivity in the visible region. The bonding between BiOCl and BNT and the resulting visible-light activity of the composite can be

explained on the basis of heterojunction formation. A traditional bi-phasic heterojunction consists of a sensitizer (narrow bandgap) and the main catalyst (larger bandgap). Typically, materials capable of absorbing in the visible spectrum (CdS, Cu_2O) are used to generate charge carriers. Part of these charge carriers are then transferred to the main catalyst through the development of a Schottky junction owing to the difference in fermi energy at the interface. This Schottky or heterojunction can be of two types. A junction can be labelled as type-A if the conduction band (cb) of the sensitizer is located higher than that of main catalyst. In this case, the photogenerated electrons are transferred from the cb of the sensitizer to that of the catalyst. However, this is less than ideal as only a fraction of the desired oxidative species are generated. This arrangement is suitable for reaction proceeding through reduction such as water splitting or hydrogen evolution. Furthermore, the oxidation potential of holes is much greater, and the subsequently generated species are far more potent at achieving mineralization of organic pollutants. Hence, a higher availability of holes is of benefit for pollutant degradation, which can be achieved in a type-B junction. A type-B junction is created if the valence band (vb) of the sensitizer is lower than that of the primary catalyst. Such an arrangement allows some of the electrons from the vb of catalyst to be transferred to sensitizer. This creates an imbalance of charge which allows preservation of available holes in the catalyst vb, which can lead to direct reduction of adsorbed pollutants or help in the generation of hydroxyl radicals (see section 2.1.2).

This can be used to explain the improved photocatalytic activity of the BNT-BiOCl composite catalyst. Our studies indicate a lack of any significant photoactivity in BNT, which confirms that BiOCl is the active catalyst in this case. Despite lacking any sensitization activity, bonding of BNT and BiOCl creates a type-B heterojunction owing to the location of the respective vb edges, as depicted in Fig 7.9. BNT is a n-type semiconductor with a vb edge at 2.53 V, whereas BiOCl is a p-type semiconductor with vb edge at 2.4 V.[9,10,28,43] Similarly, the cb edges of BNT and BiOCl are located at -0.42 V and -1.1 V, respectively. Owing to band-bending at the heterojunction, BiOCl can partly absorb visible light and transfer energetic electrons to its cb, creating electron-hole pairs. Part of these electrons are then transferred to the cb of BNT. The process continues until any further flow is opposed by the growing depletion layer at the interface. Similarly, some of the holes from vb of BNT are transferred to vb of BiOCl until the generation of the depletion layer. Consequently, the excess holes are made available in the vb of BiOCl to migrate to the surface. A suitable charge imbalance extends the lifetime of these holes and reduces the chances of recombination. Moreover, the presence of BiOCl on the surface reduces the path length of the holes to the reaction medium (Fig 7.9). The presence of

a bulk polar vector in the parent BNT phase, its n-type nature, and presence of trap sites all combine to significantly reduce recombination and improve the availability of holes on the surface. There are only a few tests that can directly confirm the Stern-layer formation in free standing ferroelectric particles such as piezoresponse force microscopy[44] and second harmonic generation.[45] However, it is generally accepted that all ferroelectric particles above a critical size will display the formation of a Stern layer.[19,46] Furthermore, a study by Su et al. describes that the critical size for such ferroelectric particles could be well below 10 nm.[44] Since the BNT particles in this study are considerably larger (~1 µm), the presence of a Stern layer on the surface can be assumed. The bulk polar vector of ferroelectric phase accelerates and prolongs the separation of photogenerated charge carriers, and the formation of a Stern layer enables better surface adsorption of (polar) pollutants, which also contributes towards their accelerated degradation. A graphical representation of the concept is provided in Fig 7.9. All these factors work synergistically to produce the high photocatalytic activity observed in BNT-BiOCl.

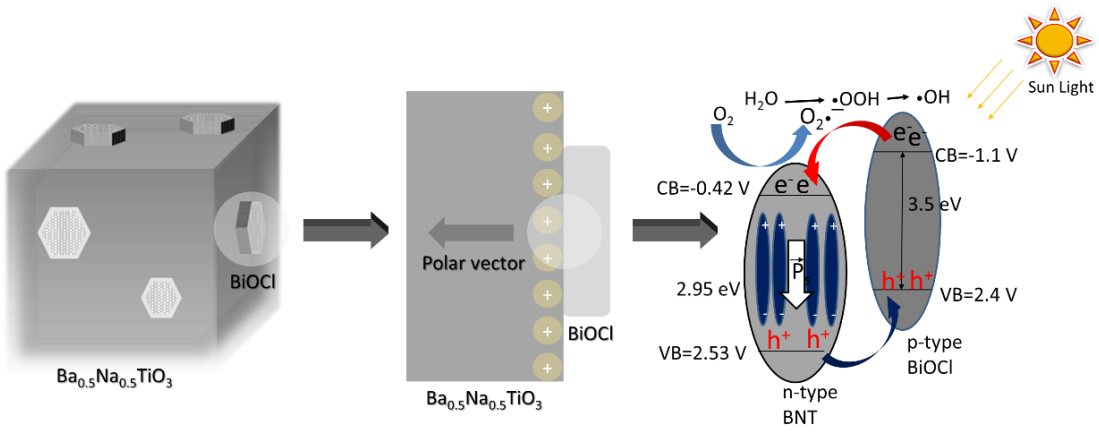

Figure 7.9: Mechanism for formation of type-B heterojunction between parent BNT and photoactive BiOCl phase and the effect of Stern layer formation on charge separation. Block arrows indicate magnified image of the highlighted area.

To further justify the proposed hypothesis, transient photocurrent measurements were performed for all prepared catalysts using chopped illumination with a 100-second cycle. Fig 7.10 shows the measured current activity for BiOCl, BNT and 15% BNT-BiOCl catalyst measured for a period of 10^3 seconds. As expected, BNT displays the least magnitude of photocurrent which agrees with its lack of photoactivity. BiOCl being a good photocatalyst displayed a variation of ~0.8 µA.cm^{-2} between the light and dark cycles. However, for the 15% BNT-BiOCl composite a peak photocurrent of 3.7 µA.cm^{-2} was observed with a difference of ~3 µA.cm^{-2} between the light and dark cycles. Comparatively, this amounts to a difference of 300% between pure BiOCl and the 15% composite, even though the latter contains far less

active catalyst (BiOCl) by weight. Sharp edges are present between the onset of illuminated and dark time intervals, whereas the photocurrent intensity is reproducible and stable. Since the photocurrent is a result of the transfer of photogenerated charge carriers minus the recombination at the electrolyte surface; these observations confirm that the photocurrent enhancement of the composite catalyst can be attributed to the higher separation efficiency and reduced recombination of the photo-induced electron–hole pairs at the heterojunction. All this reaffirms the advantages of BiOCl surface bonding with the ferroelectric phase. Thus, based upon the presented evidence, we can conclude that a non-photocatalytic (ferroelectric) material with poor activity can be used to introduce and enhance the visible-light performance of traditional UV-active materials.

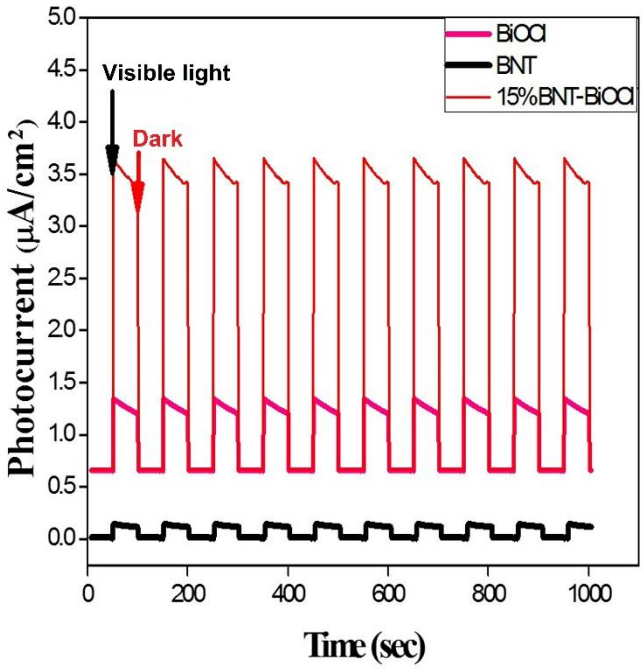

Figure 7.10: Transient photocurrent measurements for BNT, BiOCl, and 15% BNT-BiOCl.

7.6.2 Dye degradation mechanism

The degradation of Rh B can proceed through several different mechanisms in the presence of a composite photocatalyst. To investigate the primary REDOX species and thereby propose a degradation mechanism, the photocatalytic experiments were repeated in the presence of scavenging agents. Fig 7.11 displays the degradation achieved with different scavenging agents for the 15% BNT-BiOCl composite. When benzoquinone (BQ) was added to the mixture only a partial degradation (~60%) could be achieved within the standard time frame (20 minutes); whereas incorporation of isopropanol (IPA) had no effect whatsoever. However, the photoactivity of the catalyst was seriously hampered upon addition of sodium

ethylenediaminetetraacetic (Na-EDTA) and no degradation was observed. Upon subsequent washing and drying of the catalyst, its original performance was regained.

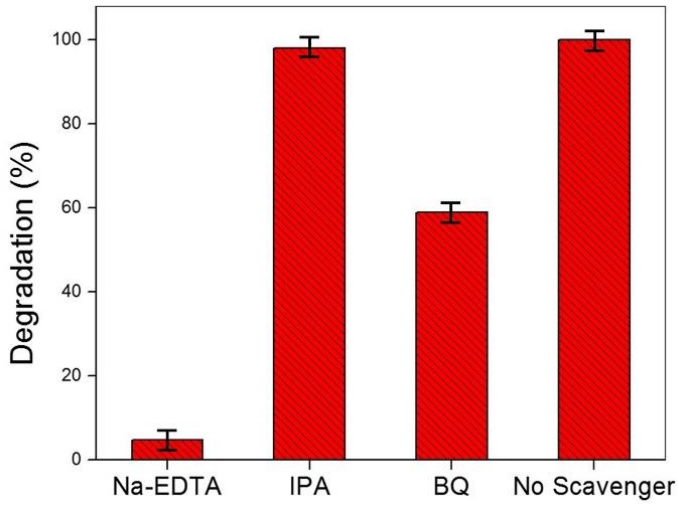

Figure 7.11: Scavenger test for photocatalytic degradation of Rh B over 15% BNT-BiOCl.

These observations support the assumption that holes are the primary REDOX species for the composite catalyst followed by superoxide radical. Hence, the degradation mechanism of Rh B in the solution can be represented as:

$$BiOCl + hv \rightarrow BiOCl^{*} \quad (7.2)$$

$$BiOCl^{*} \rightarrow h^{+}(BiOCl) + e^{-}(BNT) \quad (7.3)$$

$$2h^{+} + 2H_2O \rightarrow 2H^{+} + H_2O_2 \quad (7.4)$$

$$H_2O_2 \rightarrow 2OH^{\bullet} \quad (7.5)$$

$$Rh\,B + OH^{\bullet} \rightarrow Degradation\ products \quad (7.6)$$

7.7 Conclusions

A visible-light active $Bi_{0.5}Na_{0.5}TiO_3$-BiOCl based catalyst was successfully prepared by treating calcined BNT particles with dilute HCl. By varying the duration of acid treatment, different concentration (0-15 wt.%) of BiOCl phase could be obtained. BiOCl was observed to crystallize on the surface of parent BNT phase owing to a combination of etching and precipitation reaction. XRD was used to confirm the phase purity of the as-synthesized catalyst, whereas SEM (EDX) was used for mapping the particle size and phase distribution. XPS and Raman analysis helped to confirm that the composite catalyst consists of both BNT and BiOCl phases, and that acid treatment did not induce any changes in the oxidation states. DRS analysis of the BNT-BiOCl catalyst revealed the bandgap of the composite catalyst to be ~3.14 eV.

However, despite the large bandgap the catalyst was able to show high photoactivity in visible region as evident from degradation of Rh B. This observation was explained based on the formation of a type-B heterojunction between the BNT and BiOCl phases. The heterojunction improved charge separation and surface proximity of the BiOCl facilitated enhanced migration of holes to the catalyst surface. A confirmation of this concept was observed by the presence of a strong, sharp and reproducible photocurrent in the composite catalyst. Further, scavenger study indicates that holes (h^+) are the primary oxidative species responsible for dye-degradation. These results indicate that suitable bonding to a ferroelectric phase can induce visible-light activity even in a high bandgap and UV-active catalyst such as BiOCl. Such ferroelectric materials could also impart additional benefits such as piezocatalysis.[47] Hence, development and optimization of such photocatalysts could easily overcome the limitations of pure TiO_2, thereby making it easier to achieve commercial solar water-treatment technology.

7.8 Acknowledgements

I would like to acknowledge Dr. Himmat Singh Kushwaha (IIT Mandi) for providing the SEM images, the results from transient photocurrent measurements, and for his help with independent reproduction of the materials and experiments.

References:

1 S Girish Kumar and L Gomathi Devi, The Journal of physical chemistry A **115** (46), 13211 (2011).
2 Fang Han, Venkata Subba Rao Kambala, Madapusi Srinivasan, Dharmarajan Rajarathnam, and Ravi Naidu, Applied Catalysis A: General **359** (1), 25 (2009).
3 Zhuoxuan Li, Yang Shen, Yuhan Guan, Yuhan Hu, Yuanhua Lin, and Ce-Wen Nan, Journal of Materials Chemistry A **2** (6), 1967 (2014).
4 Ciara Byrne, Gokulakrishnan Subramanian, and Suresh C. Pillai, Journal of Environmental Chemical Engineering **6** (3), 3531 (2018).
5 Jingxiang Low, Jiaguo Yu, Mietek Jaroniec, Swelm Wageh, and Ahmed A Al-Ghamdi, Advanced Materials (2017).
6 Xiaoyan Liu, Yiguo Su, Qihang Zhao, Chunfang Du, and Zhiliang Liu, Scientific Reports **6** (2016).
7 Dongdong Lv, Dafeng Zhang, Qinzhao Sun, Jiandong Wu, Li Zhang, Xipeng Pu, Huiyan Ma, and Jianmin Dou, Nanotechnology **27** (38), 385602 (2016).
8 Yan Mi, Liaoyong Wen, Zhijie Wang, Dawei Cao, Rui Xu, Yaoguo Fang, Yilong Zhou, and Yong Lei, Nano Energy **30**, 109 (2016).
9 Zhiqiao He, Yuanqiao Shi, Chao Gao, Lina Wen, Jianmeng Chen, and Shuang Song, The Journal of Physical Chemistry C **118** (1), 389 (2013).
10 Seung Yong Chai, Yong Joo Kim, Myong Hak Jung, Ashok Kumar Chakraborty, Dongwoon Jung, and Wan In Lee, Journal of Catalysis **262** (1), 144 (2009).
11 Fajer Mushtaq, Miguel Guerrero, Mahmut Selman Sakar, Marcus Hoop, André M Lindo, Jordi Sort, Xiangzhong Chen, Bradley J Nelson, Eva Pellicer, and Salvador Pané, Journal of Materials Chemistry A **3** (47), 23670 (2015).

[12] Yu Yu, Changyan Cao, Hua Liu, Ping Li, Fangfang Wei, Yan Jiang, and Weiguo Song, Journal of Materials Chemistry A **2** (6), 1677 (2014).
[13] Fangfang Duo, Yawen Wang, Xiaoming Mao, Xiaochao Zhang, Yunfang Wang, and Caimei Fan, Applied Surface Science **340**, 35 (2015).
[14] Ankita Mathur, HS Kushwaha, Rahul Vaish, and Aditi Halder, RSC Advances **6** (97), 94826 (2016); Monisha Rastogi, Chris Bowen, H. S. Kushwaha, and Rahul Vaish, Materials Science in Semiconductor Processing **51**, 33 (2016); Monisha Rastogi, H. S. Kushwaha, and Rahul Vaish, Electronic Materials Letters **12** (2), 281 (2016).
[15] Monisha Rastogi, Aditya Chauhan, Himmat Singh Kushwaha, Ramachandran Vasant Kumar, and Rahul Vaish, Applied Physics Letters **109** (22), 223901 (2016); HS Kushwaha, Aditi Halder, D Jain, and Rahul Vaish, Journal of Electronic Materials **44** (11), 4334 (2015).
[16] Andrea Prado-Espinosa, Javier Camargo, Adolfo del Campo, Fernando Rubio-Marcos, Miriam Castro, and Leandro Ramajo, Journal of Alloys and Compounds **739**, 799 (2018).
[17] Ting Yu, Kin-Wing Kwok, and Helen Chan, presented at the Applications of ferroelectrics, 2006. isaf'06. 15th ieee international symposium on the, 2006 (unpublished); SJ Jeong, MS Kim, SM Jang, IS Kim, and M Saleem, presented at the Applications of Ferroelectric, International Symposium on Integrated Functionalities and Piezoelectric Force Microscopy Workshop (ISAF/ISIF/PFM), 2015 Joint IEEE International Symposium on the, 2015 (unpublished).
[18] Matthias Batzill, Energy & Environmental Science **4** (9), 3275 (2011); Li Li, Paul A Salvador, and Gregory S Rohrer, Nanoscale **6** (1), 24 (2014).
[19] Matt Stock and Steve Dunn, The Journal of Physical Chemistry C **116** (39), 20854 (2012); Yongfei Cui, Joe Briscoe, and Steve Dunn, Chemistry of Materials **25** (21), 4215 (2013).
[20] Jing Jiang, Kun Zhao, Xiaoyi Xiao, and Lizhi Zhang, Journal of the American Chemical Society **134** (10), 4473 (2012).
[21] Kan Li, Yanping Tang, Yunlan Xu, Yalin Wang, Yuning Huo, Hexing Li, and Jinping Jia, Applied Catalysis B: Environmental **140-141**, 179 (2013).
[22] Cao Sihai, Guo Chuanfei, Lv Ying, Guo Yanjun, and Liu Qian, Nanotechnology **20** (27), 275702 (2009); Sujuan Wu, Cong Wang, and Yinfang Cui, Applied Surface Science **289**, 266 (2014).
[23] Vinay P. Singh and Rahul Vaish, Journal of the American Ceramic Society **101** (7), 2901 (2018).
[24] I. G. Siny, E. Husson, J. M. Beny, S. G. Lushnikov, E. A. Rogacheva, and P. P. Syrnikov, Ferroelectrics **248** (1), 57 (2000).
[25] Hamza Lidjici, Brahim Lagoun, Mokhtar Berrahal, Mohamed Rguitti, Med Amine Hentatti, and Hamadi Khemakhem, Journal of Alloys and Compounds **618**, 643 (2015).
[26] Jinyan Xiong, Gang Cheng, Guangfang Li, Fan Qin, and Rong Chen, RSC Advances **1** (8), 1542 (2011); Yongqian Lei, Guanhua Wang, Shuyan Song, Weiqiang Fan, and Hongjie Zhang, CrystEngComm **11** (9), 1857 (2009).
[27] Sujuan Wu, Jianguo Sun, Shi-Ze Yang, Qiongyao He, Ling Zhang, and Lidong Sun, Inorganic chemistry **57** (15), 8988 (2018).
[28] Lu Wang and Wenzhong Wang, International Journal of Hydrogen Energy **37** (4), 3041 (2012).
[29] Yongfei Cui, Stephen M. Goldup, and Steve Dunn, RSC Advances **5** (38), 30372 (2015).
[30] Yanqing Yang, Ruixiang Liu, Gaoke Zhang, Lizhen Gao, and Weike Zhang, Journal of Alloys and Compounds **657**, 801 (2016).
[31] Bisheng Li, Cui Lai, Guangming Zeng, Lei Qin, Huan Yi, Danlian Huang, Chengyun Zhou, Xigui Liu, Min Cheng, Piao Xu, Chen Zhang, Fanglong Huang, and Shiyu Liu, ACS Applied Materials & Interfaces **10** (22), 18824 (2018).
[32] Yiqing He, Muwei Ji, Yao Hu, Qinghua Yang, Changxu Yan, Yuxiong Chen, Shengding Chang, Bo Li, and Jin Wang, Journal of Materials Chemistry C **6** (29), 7745 (2018).
[33] Xiangde Su, Jinjin Yang, Xiang Yu, Yi Zhu, and Yuanming Zhang, Applied Surface Science **433**, 502 (2018).
[34] Mohamed Mukthar Ali, J. S. Arya Nair, and K. Y. Sandhya, Dyes and Pigments **163**, 274 (2019).
[35] Amar Al-Keisy, Long Ren, Xun Xu, Weichang Hao, Shi Xue Dou, and Yi Du, The Journal of Physical Chemistry C **123** (1), 517 (2019).

[36] Jun Shang, Huige Chen, Tingzhen Chen, Xianwei Wang, Gang Feng, Mengwei Zhu, Yuxuan Yang, and Xusheng Jia, Applied Physics A **125** (2), 133 (2019).
[37] Chunying Chao, Yisha Zhou, Hao Li, Weiwei He, and Wenjun Fa, Applied Surface Science **466**, 274 (2019).
[38] Guoquan Huang, Ganghua Zhang, Zhipeng Gao, Jianwu Cao, Dezeng Li, Hong Yun, and Tao Zeng, Journal of Alloys and Compounds **783**, 943 (2019).
[39] Xudong Yan, Huamei Zhao, Tengfei Li, Wang Zhang, Qinglei Liu, Yang Yuan, Lujun Huang, Lulu Yao, Jiahao Yao, Huilan Su, Yishi Su, Jiajun Gu, and Di Zhang, Nanoscale **11** (21), 10203 (2019).
[40] Xianlong Zhang, Dong An, Dexin Feng, Fengbing Liang, Zhen Chen, Weimin Liu, Zhenzhen Yang, and Mo Xian, Applied Surface Science **476**, 706 (2019).
[41] Achim Neubrand, Reinhard Lindner, and Peter Hoffmann, Journal of the American Ceramic Society **83** (4), 860 (2000); M. A. Peña and J. L. G. Fierro, Chemical Reviews **101** (7), 1981 (2001).
[42] Ke-Lei Zhang, Cun-Ming Liu, Fu-Qiang Huang, Chong Zheng, and Wen-Deng Wang, Applied Catalysis B: Environmental **68** (3), 125 (2006); Liqun Ye, Kejian Deng, Feng Xu, Lihong Tian, Tianyou Peng, and Ling Zan, Physical Chemistry Chemical Physics **14** (1), 82 (2012); Norihito Kijima, Koichi Matano, Masao Saito, Tomo Oikawa, Tomohiro Konishi, Hiroyuki Yasuda, Toshio Sato, and Yuji Yoshimura, Applied Catalysis A: General **206** (2), 237 (2001).
[43] Haijing Lu, Lingling Xu, Bo Wei, Mingyi Zhang, Hong Gao, and Wenjun Sun, Applied Surface Science **303**, 360 (2014).
[44] Ran Su, Yajing Shen, Linglong Li, Dawei Zhang, Guang Yang, Chuanbo Gao, and Yaodong Yang, Small **11** (2), 202 (2015).
[45] Sava A. Denev, Tom T. A. Lummen, Eftihia Barnes, Amit Kumar, and Venkatraman Gopalan, Journal of the American Ceramic Society **94** (9), 2699 (2011).
[46] D. Tiwari, S. Dunn, and Q. Zhang, Materials Research Bulletin **44** (6), 1219 (2009).
[47] Mengye Wang, Biao Wang, Feng Huang, and Zhiqun Lin, Angewandte Chemie International Edition **58** (23), 7526 (2019).

Chapter 8

Conclusions and future prospects

This chapter summarizes and highlights the important observations and results reported in this study. The results acquired during the course of investigation have also uncovered some topics worthy of further analysis, which are also discussed here.

8.1 Conclusions

TiO_2-C composite particles were prepared through controlled hydrolysis of titanium alkoxide dissolved in excess alcohol. Partial hydrolysis enabled retaining of limited alkoxy groups thereby eliminating the need for an external carbon source. Three different alkoxides namely titanium IV butoxide, titanium IV isopropoxide, and titanium ethoxide were selected as Ti sources, whereas ethanol, isopropanol and butanol were selected as solvents. This enabled a systematic analysis of the effect of reagents on the size, morphology and amount of residual carbon in the samples.

It was observed that regardless of the reagent combination, the precipitated particles were composed of amorphous hydrates of Ti containing approximately 20 wt.% H_2O. These particles when calcined in a non-oxygenating atmosphere exhibited a range of colours varying from dark grey to black. XRD analysis indicated that the calcined particles were highly crystalline and composed mainly of anatase TiO_2 with some samples displaying peaks associated with either rutile or brookite phases. However, no other excess or anomalous peaks were observed. Characterization techniques such as EDX, Raman, and XPS spectroscopy revealed the presence of sp^2-hybridized carbon on the surface. Hence, the dark/black colour of the particles was attributed to the presence of a core-shell (TiO_2-C) structure. The amount of carbon in the samples was estimated using thermal analysis and was calculated to vary between 0.5 to 4.0 wt.%. Furthermore, SEM imaging revealed that depending on the solvent and precursor used, the average particle size varied from 300 nm to well over 10 µm with a concomitant change in specific surface area. It was observed that, regardless of the solvent used, there was a weak negative correlation between the molecular weight of the alkoxide and the size/surface area of the particles. However, no other correlation or trend could be established.

Reflectance spectroscopy indicated that the various TiO_2-C samples had significantly improved absorbance (≥50 %) in the visible spectrum with only a minor redshift (~0.2 eV) in the bandgap. Thereafter, these powders were tested for degradation of aqueous methylene blue under

simulated AM 1.5G sunlight. It was observed that the best sample batch offered 8.4 times faster rate of dye mineralization compared to a control sample of TiO_2 (calcined in air). Even the least active carbon-containing composite sample was still 4.6 times faster than control despite the reduced surface area. This test helped to establish the ameliorated catalytic performance of TiO_2-C samples over pristine TiO_2. Owing to the large disparity in the size of different catalysts, the apparent rate constants were normalized with respect to specific surface area. It was observed that the catalyst prepared using titanium IV butoxide and ethanol had the highest normalized rate constant among all samples. Hence, this combination was selected for further optimization.

In the subsequent study, the size of the primary precipitates was reduced through addition of aqueous KCl to the reaction mixture. It was observed that 0.1 M KCl produced stable particles which could be collected using a centrifuge, whereas increasing the salt concentration any further led to either colloidal particles (0.2 M KCl) or no precipitation (0.5 M KCl). The calcined particles were also observed to exhibit a core-shell (TiO_2-C) structure with an average crystallite size of ~10 nm and an agglomerated cluster size of ~100 nm. As previously defined, these composite nanoparticles were denoted as nanocomposites. The carbon content of the nanocomposites was observed to be in good agreement with those prepared through salt-free hydrolysis. However, reduction of the particle size increased the specific surface area of the nanocomposites by 25 times. These core-shell nanocomposites were tested for degradation of aqueous methylene blue, methyl orange, brilliant green and rhodamine B dyes. It was observed that degradation rates comparable to salt-free catalyst were achieved using only $1/5^{th}$ the amount (50 mg versus 10 mg), whereas the photo-activity was observed to be ~2 and 2.6 times better than control (air calcined) and commercial P25 catalysts under same conditions. A comparative analysis also revealed that the reported nanocomposites could easily perform at par or better than many state-of-art TiO_2-C-based materials reported in literature, and present an advantage of a facile preparation method.

The nanocomposites were further tested for degradation of two non-steroidal anti-inflammatory pharmaceutical compounds namely ibuprofen and diclofenac, and model pathogen gram-negative Escherichia coli bacteria. A considerably high degradation rate was observed for both compounds with an average 60 min required for complete degradation. Similarly, complete deactivation of bacteria could be achieved within a similar time period (~60 min), which was five times higher than with the control sample. These results confirmed that the rate of degradation is highly dependent on the type of dye molecule tested. Transient photocurrent measurement and electrochemical impedance spectroscopy revealed that the outer carbon

coatings not only increased visible light absorption but also improved the generation and separation of photogenerated charge carriers. The ameliorated performance was attributed to the delocalization of generated photoelectrons and sensitization produced by sp^2-hybridized carbon. Hence, the proposed technique was used for facile synthesis of an efficient TiO_2-C photocatalyst, which can be employed for the treatment of a broad range of water-borne pollutants under full solar spectrum.

The second part of the study reports on the synthesis and testing of various TiO_2 and Ni-based composites for visible light hydrogen evolution. Three compounds namely β-$Ni(OH)_2$, and its derivatives NiO and Ni_2P were selected owing to their proficiency as good electrocatalysts. TiO_2 nanocomposites with 1, 2.5, 5, and 10 wt.% Ni compounds were prepared through various routes including hydrothermal synthesis followed by solid-state reaction or salt-precipitation method. Various characterization techniques such as EDS, XPS, and XRD were used to determine the presence and phase purity of the prepared nanocomposites. It was observed that samples prepared using hydrothermal method had a relatively larger particle size (~300 nm) compared to salt-precipitated method owing to the low temperature processing of the latter, which could avoid particle agglomeration. Both phase pure and composite samples were tested for hydrogen evolution under visible light. No hydrogen was produced with pure water suggesting the need for sacrificial electron donors. Hence, a second set of experiments were performed using sodium ethylenediaminetetraacetic acid (Na-EDTA) (0.1 M, pH=4.5). In the presence of an electron donor significant hydrogen evolution was observed for $Ni(OH)_2$ and Ni_2P composites, whereas no hydrogen evolution was observed for pure TiO_2 or NiO-based catalysts. For $Ni(OH)_2$-based catalysts, the highest hydrogen evolution was observed for sample containing 2.5 wt.% cocatalyst (0.342 µM). However, for Ni_2P-based catalyst the samples prepared through salt-precipitation method displayed the highest rate for hydrogen production, which was observed to have a positive correlation with the wt.% of Ni_2P. A total hydrogen evolution of 0.981 and 0.993 µM could be achieved with samples containing 5 and 10 wt.% Ni_2P over a period of 4 h. The sample with 5 wt.% loading was selected for further analysis owing to the most hydrogen evolution per unit mass of active cocatalyst. A fresh reaction mixture was subjected to constant illumination for seven days and the amount of evolved hydrogen was measured. A steady rate of hydrogen production was observed (60.47 $\mu mol.h^{-1}.g^{-1}$), which confirmed the stability of the prepared catalyst over the tested time period.

The final section of the study deviates away from TiO_2 and reports on the synthesis and activity of a novel ferroelectric photocatalyst titanate. Ferroelectric $Bi_{0.5}Na_{0.5}TiO_3$ (BNT) was selected as the parent phase owing to its chemical affinity to BiOCl, which is an established

photocatalyst. BNT particles were prepared using solid-oxide reaction technique by calcination in air. The micrometre sized (~1 μm) particles were then treated with dilute HCl to achieve growth of BiOCl on the surface through nucleation-dissolution-recrystallization process. Four samples were prepared corresponding to 0 (pristine), 15, 30, and 60 min of acid treatment, in which the total BiOCl growth was observed to be dependent on the duration of the exposure. The as-prepared composite particles were observed to have a high bandgap (>3.0 eV) as estimated using diffuse reflectance spectroscopy. However, the presence of BiOCl was observed to improve visible light absorption by up to 30% for 15% BiOCl-BNT sample. These samples were then tested for degradation of aqueous rhodamine B under visible light. It was observed that despite the large particle size and high bandgap, the composite catalysts displayed fast dye degradation under visible spectrum ($\lambda > 400$ nm), and complete mineralization could be achieved in ~15 min under a (theoretically estimated) illumination of 4.97×10^4 Lux. The high visible light activity was attributed to the formation of a type-B heterojunction. This heterojunction improved charge separation and increased availability of holes in BiOCl for rapid reduction of dye molecules, as confirmed through independent transient photocurrent and scavenger tests. The presence of ferroelectric parent phase is also expected to impart further benefits such as Stern-layer formation. However, direct evidence for such activity was not observed. The stability of the composite catalyst was confirmed through repeated cycling for five consecutive runs, with no appreciable change in photocatalytic activity. This study serves as a proof-of-concept that integration of traditional photocatalyst with ferroelectric materials could be used to prepare stable and efficient visible-light active materials as an alternate to TiO_2.

8.2 Future prospects

In this study, the section regarding TiO_2 and carbon composites presents a facile method for preparation of TiO_2-C core-shell nanoparticles. These materials possess a high surface area and well-defined porosity which could benefit applications such as an electron transport material in solar cells,[1] electrode materials for fast-charging Na/Li-ion batteries[2] and solid-state capacitors;[3] as it improves contact with the electrolyte and provides sites for mass/charge transport. These are all applications that can benefit from a facile single-step preparation technique for producing TiO_2-C nanostructures. However, further investigation is required with respect to synthesis conditions and reagents to allow precise control over the shape and carbon content of the synthesized particles. Furthermore, the aim of this study was to develop a noble-metal-free composite material that can provide an efficient and stable performance for photocatalytic degradation of a wide range of water-borne pollutants. Preliminary

investigations have already indicated the potency of the prepared composites. However, only a limited set of isolated pollutants were tested. In a practical setting, it is quite rare to encounter isolated dye or pharmaceutical agents in contaminated water sources apart from select industrial discharges. Furthermore, recent research has suggested that catalyst behaviour can both be promoted and retarded/poisoned based on the nature and quantity of pollutants present in the mixture.[4] Hence, further research is required to analyse the effect of mixed pollutants on the performance of the as-prepared photocatalyst. In the same regard, optimization studies would also be beneficial to ascertain the best loading amount of the catalyst with respect to dye concentration. The effect of pH[5] and temperature[6] on the catalytic activity could also be explored to give a definite set of parameters to achieve maximum performance. It is well established that pH,[5] dye concentration[7] and temperature[6] all affect the rate of catalysis. In this study, all experiments were performed at room temperatures which is an ideal setting for performing photocatalysis without auxiliary temperature regulation equipment. However, a study by Fu et al. suggests that degradation of some pollutants could be accelerated with increase in temperature.[8] This could be beneficial for developing applications for targeted pollutants at or near source and warrants further research. Another important area for investigation is the effectiveness of the photocatalyst for inactivation of gram-positive bacteria. Gram-negative bacteria are easily attacked by radicals owing to their thinner cell wall. However, gram-positive bacteria are more resilient to attack by free radical and, hence, present more of a challenge for photo-inactivation.[9] The study should also be extended beyond model strains and field tests need to be performed to see the effect of as-prepared photocatalyst on live-unregulated pathogen strains. Given the large surface area and the presence of an outer carbon shell, the proposed catalyst could also be explored for degradation of gaseous pollutants[10] and to aid carbon capture[11] according to recently proposed techniques. Finally, it should be noted that water treatment using particulate systems is challenging as a large number of nanoparticles are left suspended in the treated water at the end of the photocatalytic process. These nanoparticles present a potential hazard and need to be removed to make the water potable. In this regard, several techniques such as centrifuging and filtration can be employed. However, a better solution is to suitably immobilize these particles either in a matrix[12] or a membrane,[13] which enables unhindered access to the photocatalyst along with ease of separation. Hence, techniques for proper immobilization and a suitable reactor design will also be required to achieve a practical photocatalytic water-treatment system. Each of these steps offers its own set of challenges, all of which could be a possible topic for further investigation.

The section dealing with hydrogen production is part of an ongoing investigation and the following experiments have already been planned in further work. Both the pristine and used catalysts will be analyzed using X-ray fluorescence (XRF) and XPS to determine the actual composition and oxidation states of the catalyst. The current nomenclature assumes 100% Ni deposition and conversion for each synthesis step, however actual amount may be different. Hence, XRF of pristine samples would help to establish the yield for different conversion processes and may also help to identify the cause for disparity between results obtained for samples prepared using different techniques. Thereafter, optimum Ni loading can be determined with respect to maximum hydrogen production. The instrument for performing XRF measurements on the powder samples is already installed in the materials chemistry lab and will be commissioned soon. In the same regard, performing nitrogen-sorption isotherms to determine specific surface area of the catalysts can also help to elucidate any existing relationship between the synthesis methods, effective area and hydrogen production rates of the catalysts. XPS analysis of the tested catalysts is another important characterization that will be performed. There is ample literature suggesting that metallic (Ni^0) is the active phase in any hydrogen evolution reaction regardless of the Ni compound used.[14,15] Ni^0 can be produced from reduction of Ni^{2+} in the presence of energetic photons and these metal nanoparticles serve as electron reservoirs thereby enabling hydrogen evolution.[15] However, majority of the studies supporting this conclusion have been performed in the presence of UV light. As the present studies were all performed under visible light, further analysis is required to confirm the state of Ni post reaction. XPS analysis of the used compounds will be able to certify whether the different Ni-based compounds undergo photo-reduction. XPS could also help to ascertain if the large amount of hydrogen evolution observed for Ni_2P-based catalysts is actually a result of the co-catalytic effect or auto-oxidation of Ni_2P. Similarly, photoelectrochemical tests such as electrochemical impedance spectroscopy (EIS) and transient photocurrent measurement (TPM) can provide useful information about the generation, separation and mobility of charge carriers in the composite samples. EIS is especially useful for determination of charge transfer efficiency and can also be used to determine the rate-limiting step in the photocatalytic hydrogen evolution reaction. Similarly, TPM analysis can be used to determine the separation efficiency of photogenerated charge carriers. Results from these analyses can be further supported by transient photoluminescent spectroscopy, which can provide information about the recombination rate of photogenerated charge carriers. To further determine the reason for improved visible light photoactivity of the prepared nanocomposites, accurate determination of the band structure and bandgap is necessary. In this regard, preliminary information can be quickly acquired using diffuse reflectance spectroscopy. However, further tests such as

ultraviolet photoelectron spectroscopy and Mott-Schottky plots are needed to determine the location of band edges. These tests can provide useful information about the shift in band edges and fermi level of pristine and Ni-TiO_2 composites. This information can also be used to determine other potential application of the prepared nanocomposites such as alcohol/aldehye reduction.[16] Finally, further studies with respect to different electron donors, effect of pH and catalyst/reagent concentration will be performed to optimize the rate of hydrogen evolution. Eventually, this study will provide a roadmap for further testing of potential electrocatalyst materials for photocatalytic hydrogen production/water splitting reactions.

The final section of the thesis is an attempt to explore other stable materials for environmental photocatalysis apart from TiO_2. In this direction, BNT-BiOCl is a surprising find in which the benefits of a high quantum efficiency photocatalyst (BiOCl) could be successfully combined with the benefits of a ferroelectric phase (BNT). As the results presented in this study are for large (~2 m) particles, there is ample scope of improvement through reduction of particle size. However, preliminary attempts to produce BNT-BiOCl nanocomposites have not been successful. Even extended treatment of BNT nanoparticles with different HCl concentrations did not result in any detectable BiOCl on the surface of the resulting particles. A systematic analysis could be undertaken to determine the effect of primary particle size on BiOCl formation and its eventual stability. Once optimized, these composites can be further tested for other important applications such as carbon capture[17] and degradation of gaseous pollutants.[18] In this regard, other recently proposed ABO_3-type oxide perovskites with reduced bandgap could also be explored as potential photocatalyst with in-built electric fields.[19,20] Poled-ferroelectric materials also have some other interesting applications such as piezocatalysis[21] and enhanced adsorption,[20] all of which can be combined to significantly improve the photocatalytic performance. These are all interesting areas of research and insights gained from such research can help to advance the field of photocatalysis towards successful commercialization.

References:

1 Hao Li, Weina Shi, Wenchao Huang, En-Ping Yao, Junbo Han, Zhifan Chen, Shuangshuang Liu, Yan Shen, Mingkui Wang, and Yang Yang, Nano Letters **17** (4), 2328 (2017).

2 Lingxing Zeng, Cheng Zheng, Lunchao Xia, Yaxian Wang, and Mingdeng Wei, Journal of Materials Chemistry A **1** (13), 4293 (2013); Seung-Min Oh, Jang-Yeon Hwang, C. S. Yoon, Jun Lu, Khalil Amine, Illias Belharouak, and Yang-Kook Sun, ACS Applied Materials & Interfaces **6** (14), 11295 (2014).

3 Huimin Zheng, Teng Zhai, Minghao Yu, Shilei Xie, Chaolun Liang, Wenxia Zhao, Shing Chi Ian Wang, Zishou Zhang, and Xihong Lu, Journal of Materials Chemistry C **1** (2), 225 (2013).

[4] Suzhen You, Yun Hu, Xingchen Liu, and Chaohai Wei, Applied Catalysis B: Environmental **232**, 288 (2018); Priyanshu Verma and Sujoy Kumar Samanta, Research on Chemical Intermediates **44** (3), 1963 (2018).

[5] Sung Kyu Maeng, Kangwoo Cho, Boyoung Jeong, Jaesang Lee, Yunho Lee, Changha Lee, Kyoung Jin Choi, and Seok Won Hong, Water Research **86**, 25 (2015).

[6] Sibo Wang and Xinchen Wang, Applied Catalysis B: Environmental **162**, 494 (2015).

[7] Khan Mamun Reza, ASW Kurny, and Fahmida Gulshan, Applied Water Science **7** (4), 1569 (2017).

[8] Xianzhi Fu, Louis A. Clark, Walter A. Zeltner, and Marc A. Anderson, Journal of Photochemistry and Photobiology A: Chemistry **97** (3), 181 (1996).

[9] Ahed Zyoud, Raed Alkowni, Omayma Yousef, Mazen Salman, Safaa Hamdan, Muath H. Helal, Sawsan F. Jaber, and Hikmat S. Hilal, Solar Energy **180**, 351 (2019).

[10] Guangxin Zhang, Zhiming Sun, Yongwei Duan, Ruixin Ma, and Shuilin Zheng, Applied Surface Science **412**, 105 (2017); Zahra Shayegan, Chang-Seo Lee, and Fariborz Haghighat, Chemical Engineering Journal **334**, 2408 (2018); Sammy W. Verbruggen, Journal of Photochemistry and Photobiology C: Photochemistry Reviews **24**, 64 (2015).

[11] Feiyan Xu, Jianjun Zhang, Bicheng Zhu, Jiaguo Yu, and Jingsan Xu, Applied Catalysis B: Environmental **230**, 194 (2018); Muhammad Tahir and NorAishah Saidina Amin, Applied Catalysis B: Environmental **162**, 98 (2015); Oluwafunmilola Ola and M. Mercedes Maroto-Valer, Journal of Photochemistry and Photobiology C: Photochemistry Reviews **24**, 16 (2015).

[12] Monisha Rastogi, Aditya Chauhan, Himmat Singh Kushwaha, Ramachandran Vasant Kumar, and Rahul Vaish, Applied Physics Letters **109** (22), 223901 (2016).

[13] M. Coto, S. C. Troughton, J. Duan, R. V. Kumar, and T. W. Clyne, Applied Surface Science **433**, 101 (2018); Lei Liu, Zhaoyang Liu, Hongwei Bai, and Darren Delai Sun, Water Research **46** (4), 1101 (2012).

[14] Ana L. Luna, Diana Dragoe, Kunlei Wang, Patricia Beaunier, Ewa Kowalska, Bunsho Ohtani, Daniel Bahena Uribe, Miguel A. Valenzuela, Hynd Remita, and Christophe Colbeau-Justin, The Journal of Physical Chemistry C **121** (26), 14302 (2017).

[15] Wan-Ting Chen, Andrew Chan, Dongxiao Sun-Waterhouse, Toshihiro Moriga, Hicham Idriss, and Geoffrey I. N. Waterhouse, Journal of Catalysis **326**, 43 (2015).

[16] Takeshi Morikawa, Takeshi Ohwaki, Ken-ichi Suzuki, Shinya Moribe, and Shozo Tero-Kubota, Applied Catalysis B: Environmental **83** (1), 56 (2008); Hatice Kasap, Christine A. Caputo, Benjamin C. M. Martindale, Robert Godin, Vincent Wing-hei Lau, Bettina V. Lotsch, James R. Durrant, and Erwin Reisner, Journal of the American Chemical Society **138** (29), 9183 (2016).

[17] Zhaoyu Ma, Penghui Li, Liqun Ye, Ying Zhou, Fengyun Su, Chenghua Ding, Haiquan Xie, Yang Bai, and Po Keung Wong, Journal of Materials Chemistry A **5** (47), 24995 (2017).

[18] Xiaoxia Wang, Qian Ni, Dawen Zeng, Guanglan Liao, Yanwei Wen, Bin Shan, and Changsheng Xie, Applied Surface Science **396**, 590 (2017).

[19] Yang Bai, Pavel Tofel, Jaakko Palosaari, Heli Jantunen, and Jari Juuti, Advanced Materials **29** (29), 1700767 (2017); Fang Chen, Hongwei Huang, Lin Guo, Yihe Zhang, and Tianyi Ma, Angewandte Chemie International Edition **58** (30), 10061 (2019).

[20] Li Li, Paul A. Salvador, and Gregory S. Rohrer, Nanoscale **6** (1), 24 (2014).

[21] Mengye Wang, Biao Wang, Feng Huang, and Zhiqun Lin, Angewandte Chemie International Edition **58** (23), 7526 (2019).